Clay minerals in Enhanced Oil Recovery; Implications for fines migration as a redox controlled process during Low Salinity Water Flooding

VASILOPANAGOS, CHRISTOS

Clay minerals in Enhanced Oil Recovery; Implications for fines migration as a redox controlled process during Low Salinity Water Flooding

Christos Vasilopanagos

A Thesis presented for the degree of Doctor of Philosophy

Department of Earth Sciences

University of Durham

England

October 2021

Clay minerals in Enhanced Oil Recovery; Implications for fines migration as a redox controlled process during Low Salinity Water Flooding

Submitted for the degree of Doctor of Philosophy

Abstract

In oil and gas exploration and production, the chemical and physical properties of reservoir clay minerals can have an effect on drilling operations, reservoir quality and oil recovery rates. Various methods have been used to optimize the recovery of oil from reservoirs, through technologies that are more economical, easier to apply and environmentally friendly, culminating in the development of low salinity water flooding (LSWF). LSWF is a chemical method whereby the concentration of cations, especially multivalent cations, in the injected water is carefully reduced and controlled. LSWF is used in secondary and tertiary enhanced oil recovery (EOR) operations. In this present study, we explore a new frontier in EOR research by examining the wettability and swelling capacity of reservoir clay minerals as a function of reduction extent. We investigate how changes in the redox state during a LSWF impact on the wettability of iron rich clay minerals. We make an attempt to map the roughness profile of the clay minerals, to be used as baseline for wettability and contact angle studies. For that, we introduce a novel approach to measuring the roughness with the use of Confocal Microscopy in combination with Atomic Force Microscopy (AFM) and White Light Interferometry (CCI). To further elucidate the behavior of clay minerals, we test the hydration of model clays, including swelling and non – swelling types, using infrared spectroscopy. Additionally we investigate how reduction extent impacts the surface hydration and water sorption by nitrogen BET and water vapor volumetry methods. We couple these studies with controlled humidity XRD scans of the clay minerals and measuring of the interlayer cation budget by means of the ICP-OES method. Building on the basic understanding of redox active clay mineral at the mineral level derived from the above studies, a polymer – coated silicon wafer is used as proxy to a sandstone, and anoxic – reduced conditions simulated by means of an experimental apparatus. This setup will allow direct visualization and modelling of the effects of reduction and re – oxidation within the context of low salinity water flooding, creating a better tool for understanding fines migration in EOR applications that could lead to optimizing the operations.

Declaration

The work in this thesis is based on research carried out at the Nano Geochemistry of Low Salinity Enhanced Oil Recovery, Department of Earth Sciences, and Durham University, United Kingdom. No part of this thesis has been submitted elsewhere for any other degree, diploma or other qualification and it is all my own work unless referenced to the contrary in the text. All parts of the thesis are my individual contribution.

How to Cite

Christos, Vasilopanagos. Clay minerals in Enhanced Oil Recovery; Implications for fines migration as a redox controlled process during Low Salinity Water Flooding, Department of Earth Science, Durham University, United Kingdom, 2021

Acknowledgements

A sincere and from the heart thank you to my supervisor professor Chris Greenwell (Durham), for being kind, sympathetic, a great mentor and the best supervisor I could have asked for. Chris, I will be forever grateful for what you did for me. Also, I would like to thank professor Cedric Carteret (Lorraine) for being an excellent co-supervisor and host while I was in Nancy, France and Dr. Anke Neumann (Newcastle) for co-supervising and giving useful pointers.

Also, many thanks to every technician, admin person and member of staff that was involved and helped with my work, at Durham University, Newcastle University, Lorraine University, BP Pangbourne Technology Center, Hutton Institute and Greewich University. Special thanks go to my sponsors, BP and NERC CDT in Oil&Gas and to the people that help keep these funding bodies up and running (Ian Collins and Bilal Rashid from BP and Morrow Lorna from CDT – Oil & Gas) and to my examiners, professor Matthew Jackson (Imperial) and Fred Worral (Durham) for the comments and feedback on my work.

I especially thank Nikos Apeiranthitis who has been the best friend during my time in Durham and my family for the love they have given me.

Thank you all!

Dedicated to

My family and friends

Table of contents

Chapter 1: Low Salinity Water Flooding Enhanced Oil Recovery, wettability and fines migration 1

1. Introduction 1

1.1 Low Salinity Water Flooding 4

1.2 Wettability alteration 6

1.3 The role of clay minerals in low salinity enhanced oil recovery 10

1.4 Fines migration induced by low salinity water flooding 14

1.5 Redox conditions of petroleum reservoirs 16

1.6 Aims and objectives 17

1.7 References 18

Chapter 2: Clay mineral hydration and swelling and effects of redox extent 26

2.1 Introduction 26

2.2 Clay minerals chemistry 26

2.2.1 Iron in clay minerals 28

2.2.2 Clay hydration 31

2.3 Effect of redox state on iron – bearing clay minerals 36

2.4 Aims and objectives 40

2.5 References 41

Chapter 3: Methods 48

3.1 Introduction 48

3.2 Methods used for surface characterization study 49

3.3 Measuring surface roughness of clay substrates 52

White light interferometry 58

Atomic force microscopy 59

Confocal microscopy 59

3.4 Methods used for clay wettability study of oxidized and reduced iron clays 60

3.5 Methods used for infrared spectroscopy studies 70

IR Spectroscopy data acquisition method 71

3.6 Methods used for adsorption studies 72

3.7 References 76

Chapter 4. Clay substrate surface characterization 79

4.1 Introduction 79

4.2 Surface texture 81

84
4.3 Materials and methods 84
4.4 Results 84
White light interferometry scans 84
AFM scans 90
4.5 Discussion 95
AFM measured roughness and wettability 95
White light interferometry roughness 95
4.6 Conclusions 96
4.7 References 97
Chapter 5. Wettability assessment of redox active clay minerals at the clay-crude oil interface using contact angles 101
5.1 Introduction 101
5.2 Materials and methods 103
5.2.1 Methods 105
5.3 Results 106
X – Ray diffraction patterns: 106
Mössbauer analysis: 110
Contact angle measurements: 110
5.4 Discussion 114
Clay mineralogy: 114
Surface texture: 115
Contact angle differentiation: 115
Wettability alteration: 116
Iron reduction effect: 116
Cation exchanges in oxidized and reduced states: 117
5.5 Conclusions 119
Future work: 120
5.6 References 121
Chapter 6. Infrared Spectroscopy Studies on Native and Reduced Clay Minerals: Implications for Hydration Changes as a Redox Controlled Process 124
6.1 Introduction 124
Nontronite NAu2 125
Illite IMt2 126
6.2 Materials and methods 128
Materials 128

Chemical reduction method 128
6.3 Results 131
Nontronite NAu2 MIR Infrared 131
Nontronite NAu2 NIR Infrared 134
Illite IMt2 MIR infrared: 137
Illite IMt2 NIR infrared 138
6.4 Discussion 140
Changes in the spectra of NAu2 after chemical reduction 140
Changes in the spectra of IMt2 after chemical reduction 142
6.5 Conclusions 144
Implications for EOR and Fines Migration in clastic reservoirs 144
6.6 Further work 145
6.7 References 145
Chapter 7. Effect of Redox State on Water Sorption by Swelling and Non-Swelling Clay Minerals 147
Abstract 147
7.1 Introduction 148
7.2 Materials and Methods 150
7.2.1. Clay mineral preparation 150
7.2.2 X-ray diffraction analysis 150
7.2.3 Water and nitrogen adsorption measurements 151
7.2.4 Composition analysis of clay minerals 152
7.3 Results 153
7.3.1. NAu-2 and IMt-2 Water Adsorption Isotherms 153
7.3.2 NAu-2 and IMt-2 Nitrogen BET Isotherms 155
7.3.3 X-ray Diffraction Analyses of Oxidised and Reduced NAu-2 and IMt-2 At Varying Relative Humidity 158
7.3.4. NAu-2 and IMt-2 charge-balancing cation composition 160
7.4 Discussion 161
7.4.1. Effect of Reduction and Clay Mineral Type on Water Vapour Adsorption of NAu-2 and IMt-2 161
7.4.2. Crystal Chemistry Controls on Hydration of NAu-2 and IMt-2 Upon Reduction 162
7.4.3. Effect of Clay Mineral Fe Reduction on Nitrogen Adsorption to NAu- 2 and IMt-2 164
7.4.4. Implications of increased adsorption as a redox function for fines migration 165
7.5 Conclusions 166
Acknowledgments 167

7.6 References 167
Supplementary material 171
Chapter 8. Microfluidics – a method for direct visualization of *in situ* iron reduction in a microfabricated sandstone proxy 175
8.1 Introduction 175
8.2 Creation of a Sandstone Proxy 179
8.2.1 Microfabrication – Process Overview 179
8.2.1.1 Selection of the photoresist material 182
8.2.1.2 Fluorescence of SU-8 184
8.3 Photomask creation 186
8.4 Sample preparation and scanning electron microscopy imaging 188
8.5 Complications and updated image processing 190
..... 193
8.6 Microfabrication; wafers 193
8.7 Creation of a microfluidic system; anaerobic flow cell and fluid flow apparatus 194
8.7.1 Anaerobic flow cell for microfluidics; designs and devices 195
8.7.2 Second flow cell; design and testing 200
8.7.3 Limitations of the flow cells 203
8.8 Sealing the micromodel; wafer bonding and advanced microfluidics flow cell 203
8.9 Microfluidics; apparatus – syringe pump, tubing, oxygen sensor, portable inert gas (nitrogen) tank and pressure gauge 205
8.9.1 Monitoring oxygen levels 206
8.9.2 Purging with nitrogen 207
8.9.3 Suggested setup, *in situ* reduction and visualization 207
8.10 Discussion 208
Sandstone proxy 208
Flow cell device 209
Visualisation of oil, fines and redox changes 209
8.11 Conclusions 210
8.12 Future work 211
8.13 References 213
Chapter 9: Summary of findings and future work 218
9.1 Introduction 218
9.2 Summary 218
9.2.1 Understanding engineered surface roughness of coated clay films 218
9.2.2 Understanding wettability at the clay-crude oil interface as a redox function 220

9.2.3 Infrared Spectroscopy studies on iron clays: Implications for hydration changes as a redox controlled process 220

9.2.4 Effect of redox state on water sorption by swelling and non-swelling clay minerals . 222

9.2.5 Creation of a flow-cell device for direct visualization of *in situ* iron reduction in a microfabricated sandstone proxy 225

9.3 Implications of results 226

9.4 Future work 227

9.5 References 229

Appendix A.1 230

Appendix B.1 237

..... 246

Chapter 1: Low Salinity Water Flooding Enhanced Oil Recovery, wettability and fines migration

1. Introduction

Energy demand is increasing and so is the need for petroleum. Oil recovery is achieved mainly by primary and secondary methods. Primary methods utilize the reservoir's own pressure to recover hydrocarbons, whereas the latter secondary methods induce a pressure recharge by means of water injection. Thomas (2008) mentioned that roughly 2×10^{12} barrels of light oil and 5×10^{12} barrels of heavy oil will be left inside petroleum reservoirs after all conventional methods of recovering oil are exhausted. From that time onwards, improved oil recovery (IOR) methods will become the only viable way of recovering oil worldwide. IOR is a generalized term used when the aim is the improvement, by any means, of oil recovery from an existing producing reservoir. Enhanced oil recovery (EOR) is a specific term used for a subcategory of IOR operations and describes methods with a focus on reducing oil saturation below the residual oil saturation (Thomas 2008, also see Figure 1.1).

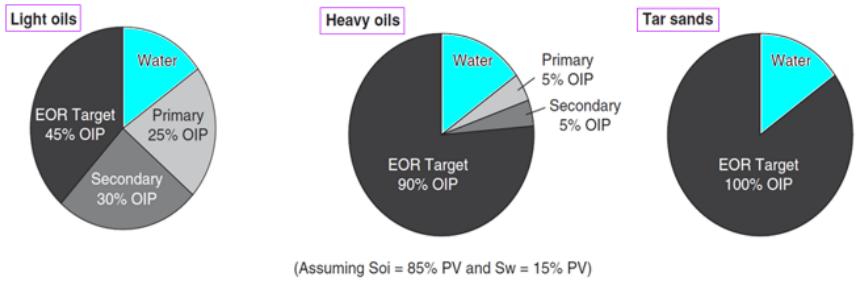

Figure 1.1. EOR target for different original oil in place (OIP) (modified after Thomas 2008).

Due to oil price uncertainty, the preference for EOR projects fluctuated from the 1980s until 2005 (Alvarado, Manrique 2010). In the United States specifically, there was a decline in EOR projects in the early 1980s, due to the drop of the oil price; an exception to that was polymer and immiscible CO_2 EOR projects that peaked in numbers in 1983 (Thomas et al 1988). Also, potential was seen in a polymer flooding application in North Burbank in the early 1980's (Moffit 1983). An oil price escalation led to an increase in EOR research that peaked in 1986 (Kokal, Al-Kaabi 2010), which was followed by a decrease due to a collapse in oil price in the early 2000s (Kokal, Al-Kaabi 2010).

During the early days of EOR development, low risk screening criteria in a reservoir attracted investors, whereas those that classified as higher risk were avoided. Projects that were eventually carried out were the ones with a significant capital investment already made (R.D. Thomas et al 1988). Chemical methods based EOR applications peaked in the mid-1980s with polymer flooding being the most used of all (Alvarado, Manrique 2010). Regardless of any advances made in the technology of EOR, their sensitivity to oil price instability created scepticism with regard to their suitability for operations and suggested that further research and development was necessary (Alvarado, Manrique 2010).

Until 2010, the contribution of EOR to the global oil production remained at moderate levels (Kokal, Al-Kaabi 2010), with some three million barrels/day produced as a result of EOR operations; 3.5% of the daily global production. This percentage could basically be attributed to thermal EOR methods (2 million barrels/day approx.), applied in Alberta (Canada), California (US), Venezuela, Indonesia, Oman, China and other countries (Kokal, Al-Kaabi 2010). The next major contributing EOR method was CO_2-EOR that produced one third of a million barrel per day, mainly from the US (Permian Basin) and Canada (Weyburn field) (Kokal, Al-Kaabi 2010). Other contributing EOR methods included injection of gas; a contribution of one third of a million barrel/day was made by this method (Kokal, Al-Kaabi 2010).

It has been suggested (Thomas et al 1988) that there are 3 defining factors that affect the popularity of EOR methods. Those are the price of oil, the economic success of a method and inertia. Within the context of optimizing hydrocarbon production and helping the energy transition go forward by lowering carbon emissions, the industry has shifted towards smarter and environmentally friendlier EOR methods.

BP successfully showed that oil bank production can be increased as a result of low salinity water flooding (LSWF) EOR and its subsequent increase in oil recovery, known as the low salinity effect (LSE). The LSE was achieved after a pilot testing in the Endicott field in Alaska, in 2008 (Vledder et al 2010; Seccombe et al 2010, Mahani et al 2011).

LSWF is a chemical EOR method whereby the concentration of cations, especially multivalent cations, in the injected water is carefully lowered and controlled. LSWF is used in secondary and tertiary EOR operations and the underpinning methods are not fully understood yet. Industry and academia have been studying the LSWF method using an array of different approaches (Bartels et al 2018, also see Figure 1.2). The former uses a top-to-bottom approach and the latter a bottom-up approach, meaning oil producers consider reservoir scale first and then scale down their research to the micro (making extensive use of core floods) and possibly nanoscale, whereas

academia, for the most part, works in a reversed way (Bartels et al 2018). The basic principle of the LSWF method is the injection of low salinity brine water that contains significantly less totally dissolved salts, mainly NaCl, than the formation water. The optimal salinity level, in parts per million (ppm), must be between 1500 to 5000 ppm to observe a LSE (Tang and Morrow 1999; Webb et al 2004; Zhang et al 2007.

As stated by Afekare and Radonjic (2007), owing to the complexity and number or process occurring involving oil droplets and/or mobilisation of fine particles, "Data interpretation does require deep understanding of particle physics and colloidal chemistry to explain LSE". This is why significant research has been done on LSWF EOR (Tang and Morrow 2005; McGuire et al 2005; Lager et al 2006; Lighthelm et al 2009; Austad et al 2010; Farzaneh et al 2017) and is still needed to elucidate the mechanisms that may cause the LSE that arise. The various mechanisms Proposed can be summarized as follows: drop of IFT (interfacial tension), fines migration, multi-component ion exchange, double layer expansion, desorption of organic material from clay due to local pH increase and the interaction of the low salinity water with polar compounds of crude oil leading to changes in the wettability of the rock.

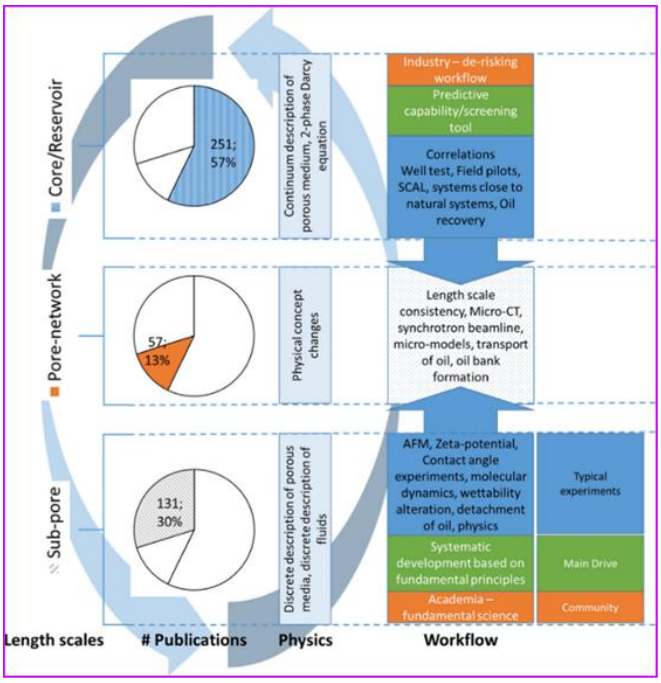

Figure 1.2 Different approaches and workflow on LSWF between academia and industry (modified after Bartels et al 2018).

1.1 Low Salinity Water Flooding

LSWFs, particularly in sandstone reservoirs, have been well studied over the last years. However, as forward prediction and extrapolation of results of LSWF in a specific rock has proven difficult, LSWF results are always estimated (Wang and Gu 2018). Early work on LSWF showed that fresh water is better than brine in sandstones with regard to improved recovery (Martin J.C. 1959) and was verified later again when fresh water was used instead of sea water for core flooding lab experiments (Bernard GG. 1967).

Sandstone composition and mineralogy; The composition of a sandstone consists of coarse silt – sized particles that make up a framework (Boggs 2009). Matrix can be found in a sandstone in size less than 0.03mm. Cementing material can also be present, which is the material formed after the formation of the matrix and holds together minerals and grains. Cementing material consists of authigenic minerals that take up the available space between the grains. In total they make up of 30% of the volume of a sandstone. The most common cementing materials are carbonate minerals, quartz and clay minerals. Framework grains include coarse and sand size silt that could vary between 0.03 and 2.0 mm. These grains are exclusively made of detrital particles that include quartz, feldspars, micas and heavy minerals (Boggs 2009). The matrix is usually made up of finer material that fills up spaces in between the grains of the framework. Similar to the framework grains, the matrix consists of silicates, feldspars, micas and clay minerals. These can have a size of 0.03 mm. In total, the matrix content can vary from trace amounts to a few tens of percent of the rock volume (Boggs 2009). Matrix in a sandstone is created from the late introduction of clay to interstitial spaces or from the alteration of unstable minerals such as feldspars or minerals rich in Fe, Mg (Boggs 2009). Silicate minerals found in sandstones are mainly quartz. High temperature varieties of quartz such as cristobalite – tridymite are not usually present in sandstones but may occasionally occur. Feldspars is another important category of minerals found in sandstones. They vary in content from a 10% for beach and dune sands to a 22% for river sands. Mica minerals are mainly found as muscovite and biotite in sandstones with muscovite being more abundant than biotite. They are hydrous K, Al sheet silicates; biotite can contain Fe and Mg. Chlorite can be present as detrital constituent of some sandstones in the form of hydrous Mg, Fe, Al sheet silicate that is similar to micas. Clay minerals is another category of detrital material found in sandstones that is of great significance to petroleum reservoirs due to their unique swelling ability. They can be found as matrix constituents and within argillaceous rock fragments. Lithic fragments can be found as detrital material. Their occurrence is controlled by the composition of the source rock. Most prevailing clasts of rock in a sandstone are fine – crystalline or fine grained clasts of parent rocks. Glass and material from volcanic activity are very common elements of sandstones. Other

detrital parts that constitute a sandstone include skeletal fragments of fossils and organic matter. The latter can be found in a size similar to that of silt clay, can vary greatly and reach up to the centimetre scale. They are either of plant or animal origin and they constitute 0.1 % of the entire sandstone.

The LSE was initially expressed as oil that becomes more mobilized as mixed-wet fines - a clay particle with oil and water attached to it, detach from pore walls during LSWF in sandstone cores (Tang and Morrow 1997). Studies have been dedicated to understanding the dominating mechanisms that result in increased mobilization of those mixed-wet fines, ultimately leading to increased oil recovery and the LSE. Lager and co-workers (2008 and 2011) showed that there is a change in the ionic composition of the effluent water, relative to the injected, after deployment of LSWF and suggested that this could be the mechanism responsible for the LSE. However, this cannot be the one mechanism responsible for the LSE as cation exchanges induced upon deployment of LSWF, lead to a delay in the LSE and therefore more pore volumes of water were needed (Suijkerbuijk et al 2013, Bartels et al 2018). In other studies the focus was on the changes in zeta potential (Nasralla and Nasr El Din 2014) and electric double layer as well as multicomponent ion exchange and local pH increases (Jackson M.D. et al 2016) and the Derjaguin–Landau–Verwey–Overbeek (DLVO) and the non-DLVO forces operating within the oil, brine, rock system during the LSWF (Ding and Rahman 2017) (see Fig 1.3 and section 1.3 for mechanisms inducing low salinity water flooding in sandstone reservoirs).

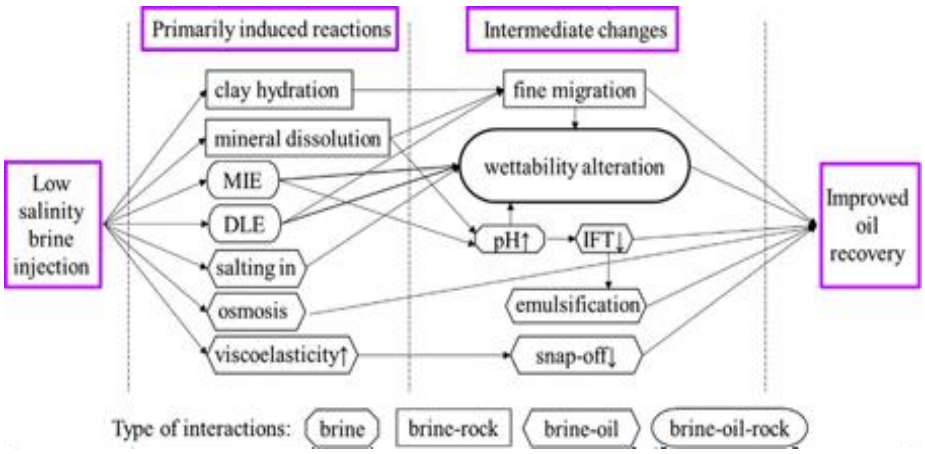

Figure 1.3. LWSF mechanisms in sandstone reservoirs (modified after Wang and Fu 2018).

Factors that change wettability were also brought forward as an important reason favouring the observed LSE in studies by Sheng J.J. (2014), Myint and Firoozabadi (2015), Shalabe and Segehrooni (2016). They suggested that understanding the wettability alteration (the preference of a surface to wet with one fluid relative to another) within the system should be the starting point of studies as wettability alteration leads to the LSE in sandstone reservoirs. Pouryousefy et al (2016) verified that wettability was a dominant factor in the additional oil recovery by LSWF by a coupled geochemical simulation study. They gave emphasis to ion exchange between the injected water (brine) and matrix (reservoir) system and crude oil. However, they mentioned that ion exchange is not fully responsible for the LSE and that there are other reasons to consider too. Building on previous studies, Zeinijahromi and co–workers (2015) suggested that fines migration induced by wettability alteration is an important mechanism for the LSE. By changes in the wetting state of the mineral surfaces due to interfacial tension alterations in combination with swelling of clay particles upon LSWF deployment, fines become mobilized in relation to the amount of salts present in the injected water. However, it should be noted that the downside of migration of fines is potential production loss due to formation damage where the fines aggregate and then restrict the permeability of the reservoir rock, preventing oil flow (Bennion D. et al 1998; Blume et al 2002). As a more general observation Al-Saedi et al (2018) concluded that EOR is achieved by clay swelling, allowing the fine clay particles to detach more readily with associated bound oil, and fines migration and that both of these are enhanced by low salinity (Lever and Dawe 1984).

1.2 Wettability alteration

Typically seawater, or water of lower salinity than the formation water, is injected into the reservoir rock. The aim is the displacement of the original oil in place (OOIP) and an increase in oil recovery (Wang and Fu 2018). The salinity of the injected brine is usually kept at 5000 ppm NaCl, whereas a typical formation water salinity is in the range of 55000 to 85000 ppm of dissolved salts and NaCl. After injection, the low salinity effect is expressed through flow parameters such as the permeability, defined as the fluid volume that passes through a medium in a unit time under a pressure gradient and capillary forces that are interfaces at the fluid-gas-solid interface capable of minimizing the surface energy at the interface. Upon LSWF deployment, permeability increases and capillary forces decrease (Bartels 2018).

The condition for successfully deploying LSWF is mixed wetness at the initial reservoir rock surfaces (Afekare and Radonjic 2017). LSWF improves the wettability of a formation by making it shift from mixed-wet to water-wet (Figure 1.4). As a result, oil mobility is increased by means of lower adhesion between the rock-oil-injected water interface. The expression of a wettability

change by means of lower adhesion has been proven experimentally with contact angle measurements (for phobic fluids, a droplet forms rather than wetting occurring) at the crude oil-mineral surfaces (Jiménez-Ángeles and Firoozabadi 2016).

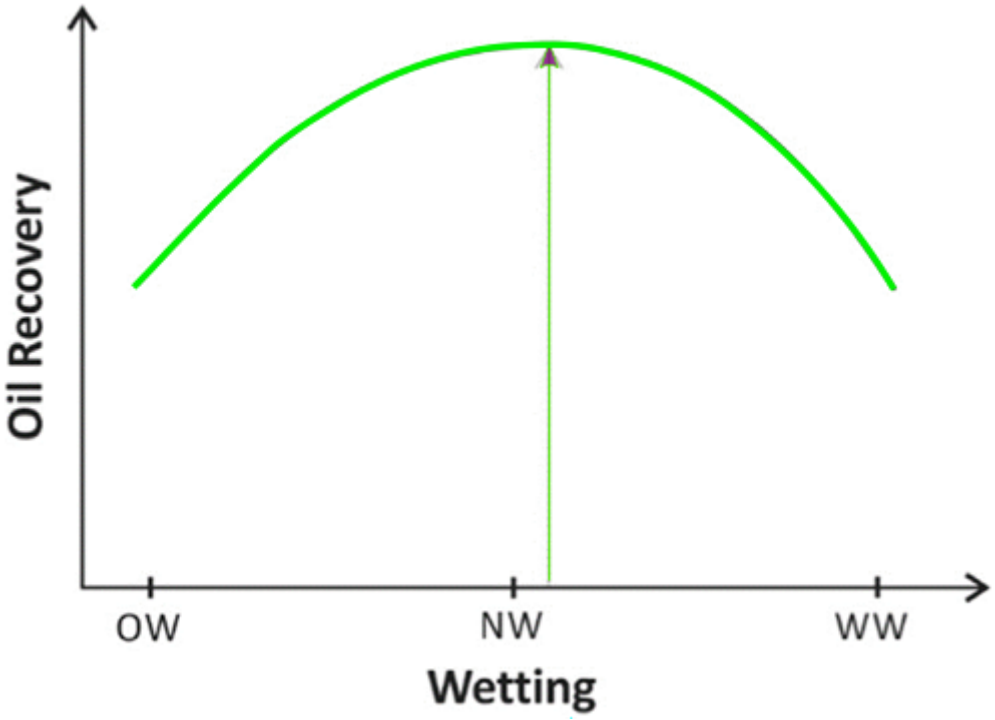

Figure 1.4. Wetting conditions and Oil Recovery. OW: oil – wet, NW: neutral – wet, WW: water – wet (modified after Strand et al 2016)

Underpinning controls on changes in wettability are: oil properties such as viscosity and API gravity, mineral surfaces such as those of quartz, clay and other mineral phases of sandstones, cation exchange capacity (i.e. the measure of the amount of cations that are retained on particle surfaces), electrical charge and surface groups, the composition and pH conditions of the formation water (Drummond C, Israelachvili J. 2004; Suijkerbuijk B et al 2012). According to Jackson and co – workers (2016) in order to achieve the LSE through wettability alteration in sandstone reservoirs, one of the following changes should occur:

- a change in the primary wetting state of the rock to mixed – wet state; changes in the reservoir's initial oil wet state will be induced after deploying a controlled salinity waterflood resulting in shifting the wetting state towards intermediate wet.
- a change in the wettability displayed in the mineral surfaces towards a more water – wet state after LS brine injection; crude oil wetting phase will be diminished and replaced by a water wet phase, leading to the mobilization of OIP.

The wettability of a matrix rock has achieved a chemical equilibrium after millions of years of crude-oil-brine-rock (COBR) interactions. During secondary oil recovery, the COBR interactions reach steady state after initial water flooding has been carried out for some time.

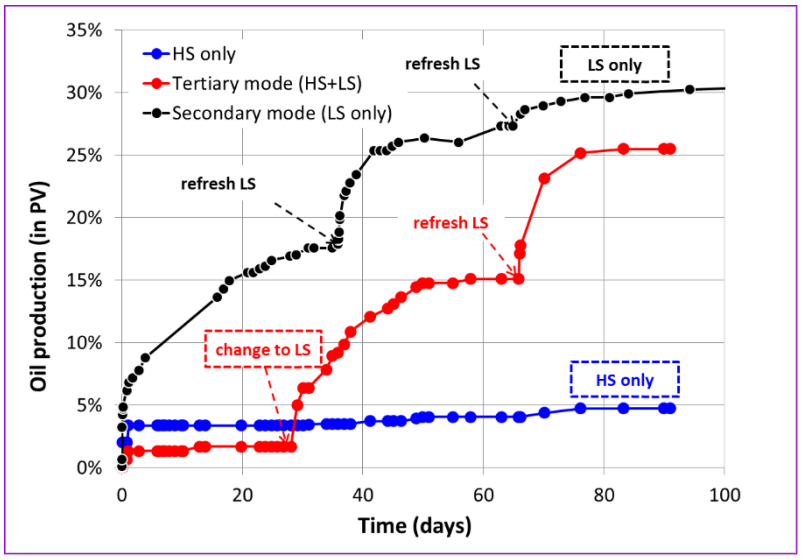

Figure 1.5. *Oil production r*esults generated by Amott testing. Tertiary mode: sample 1, in red, HS and LS; secondary mode: sample 2, in blue, HS only; sample 3, in black, LS, modified after Sorop et al 2015.

LSWF is a process that aims at changing the equilibria between oil, brine and rock so that an improvement in oil recovery can be achieved (Strand et al 2016). The suggestion that the thermodynamic equilibrium maintained by the COBR system during LSWF has to be disturbed is in agreement with earlier studies (Morrow N. 1990; Hirasaki 1991; Lager et al 2008). Buckley and Morrow (1990) and Didier et al (2015) showed that the equilibrium phase is a reversible phase and reversal can be achieved by the reactions that cause proton exchange. A change in pH can trigger these proton exchanges. Aqueous reactions and the dissolution of minerals and precipitation are followed by the exchange of ions in the COBR system also leading to changes in wettability. These reactions are also dependent on the rate of the injection (Pouryousefy et al 2016). Pouryousefy et al (2016) suggested that in order for ionic bonds to break and for a change in wettability to occur, there must be an outside force greater than the chemical bond (Fig. 1.6). That force can be a disjoining pressure which can be explained as a repulsion force coming from the DEL previously described by Hirasaki G.J (1991). Buckley and Liu (1998) showed that low ionic water with 5800 ppm NaCl with varying pH 4-8 can alter wettability to more water wet in sandstone cores. This suggested that free clay swelling is a practical way of approaching swelling

potential of clays. The swelling potential can then accurately be used as an indicator of volume change and wettability change.

Multicomponent ion exchange as a factor affecting wettability: It is the replacement of formation ions that exist in the water molecules that are attached to the clay sites, with ions of injected brine (Afekare and Radonjic 2017). These cations can also be replaced by crude oil organics (Afekare and Radonjic 2017) (Fig. 1.6). Pope and co – workers (1978) tested this theory on EOR in the 1970s. It was more successfully tested on aquifers by Valocchi et al (1981).

Lager et al (2007) mentioned that due to the different selectivity that natural exchangers such as clay minerals display, different cations will distribute different sorbed/ solute concentration ratios. They found that Ca^{2+} and Mg^{2+} contents were lower in different wells, after the injection of water and they attributed that to ion exchange and adsorption. BP studied salinity floods and noticed a significant decrease in Ca^{2+} and Mg^{2+} in the effluent compared to the injected brine. That led to the conclusion that Ca^{2+} and Mg^{2+} were significantly adsorbed by the reservoir rock and clay minerals present (Lager et al 2007). Based on the previously mentioned results, the MIE was established as the main mechanism of LSE.

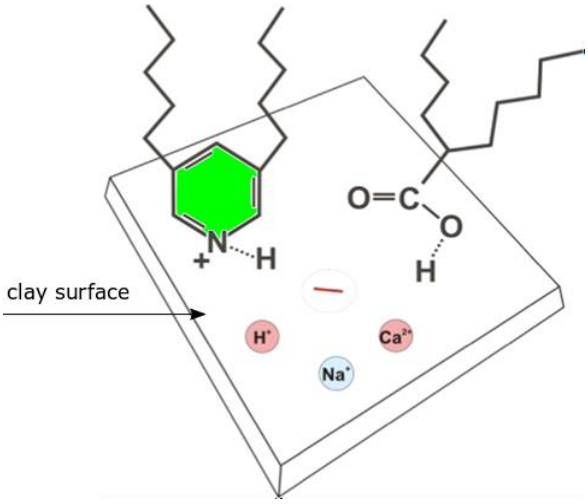

Figure 1.6. Brine active cations and polar acidic/ basic constituents of crude oil trying to occupy the active negative sites on the clay surface during LSWF (modified after Strand et al 2016).

1.3 The role of clay minerals in low salinity enhanced oil recovery

In sandstone reservoirs, the importance of clay minerals for oil recovery is thought to be significant by various researchers. Clastic reservoirs consist of quartz, which bears a negative charge in the pH 5-9 of the formation water and clays make up 3-25 wt% of the minerals in the reservoir rock. Most commonly, clay minerals in a sandstone reservoir are kaolinite, mica-illite and low swelling clays (Strand et at 2016). Montmorillonite is also a 2:1 swelling clay, commonly encountered in sandstone reservoirs (Strand et al 2016). Clay structures are explained in detail in the next chapter.

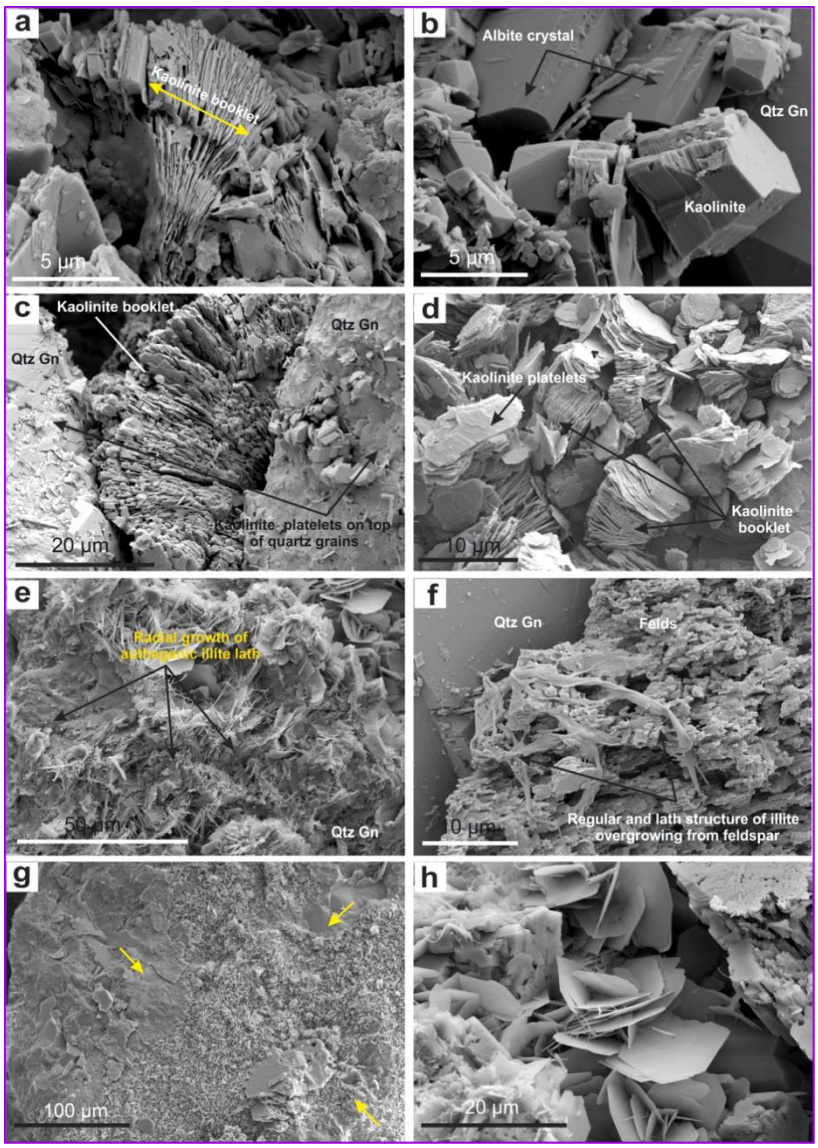

Figure 1.7. SEM micrographs of the clay matrix in Berea sandstone samples. a) kaolinite coatings seen as "booklet". b) Kaolinite crystals in contact with an albite feldspar and detrital quartz grain. c) Pore-filling and authigenic kaolinite. d) Aggregated kaolinite. e) Illite crystals seen in a hairy-like morphology. f) Illite crystals overgrowing from a K-feldspar grain g) Chlorite region show mixed between chlorite and another clay mineral (yellow arrows). h) Enlarged area from (g) showing chlorite crystals. Qtz=quartz. Modified after Kareem et al 2017.

Effect on permeability: Different clay minerals will lead to different microporosity of the reservoir rock. Hurst and Nadeau (1995) suggested that a matrix that is clay – rich contains a significant amount of void space and that the clay matrix can work as a buffer to fluid flow. The permeability can be different based on which clay mineral – cement is present, since the difference in composition will be also displayed in the way they are distributed in pore network (Stalder 1973; Howard et al 1992). In a sandstone reservoir, the significance of clay minerals lies in their ability to promote or retard chemical compaction. Chlorite specifically can help with the preservation of reservoir quality by forming a coating around surfaces and stop quartz cementation (Worden and Morad 2003). Clay minerals placed tangentially at the grain surfaces have a lower impact on permeability than the ones that are perpendicularly emplaced (Pallatt et al 1984; Kautorowicz 1990). Clay coating can reduce permeability, whereas if small – sized aggregates of clay are present in the reservoir these will be insignificant to the permeability unless they are well distributed in the pore network (Whetton and Hawkins 1970). Another way clay minerals can affect reservoir quality is by being present as pseudomatrix inside the pore rock. In this case the pseudomatrix can work as buffer and reduce the permeability. Chlorite can prevent quartz cementation, thus become beneficial to the permeability (Worden and Morad 2003).

The effect on permeability manifests itself by a reduction of capillary forces by the clay – sized particles. They cause a reduction of the pore area available for fluid to flow through. It has been argued that non-swelling clay mineral illite can cause permeability reduction by a factor of up to 30, when compared to a sand that has no illite. The effect on microporosity is evident by a lower rock resistivity caused by the conducting path presented by the water being hindered by filled microporosity (Worden and Morad 2003). An effect on capillarity (i.e. the liquid's tendency to fall or rise due to the applied surface tension) occurs when dispersed or structural clays cause an increase in capillary retention of a medium that is water – wet (Worden and Morad 2003).

Effect on wettability: Puntervold et al (2018) suggested that extra oil production from LSWF EOR is dependent on the amount of clay minerals in the reservoir since clays are responsible for the first stage of wetting as they coat pores and exposed quartz surfaces. Clays are important in LSWF due to the fact that they act as cation exchangers since the structural negative charges on the clay minerals must be charged balanced by cations (Strand et al 2016). The idea that clays are important to LSWF as cation exchangers has also been supported by Gomari and Joseph (2017), who point out that clay particles have a negative charge, and therefore can adsorb oil leading the matrix rock to a more oil-wet state. Clay minerals, although less than other minerals in number in a reservoir, do take up a lot of space of the surface area and in that way affect the wettability disproportionately to their volume. Mobilisation of these clay minerals ultimately leads to their

migration together with oil particles attached to them. Kim and Lee (2017) studied the changes in permeability due to the presence of clay minerals during LSWF. They showed that, in the absence of clay minerals, no improvement was made in oil recovery. When clay minerals were present without connate water (i.e. water trapped inside pores during deposition time), they were released from the pore walls and transported the oil droplets, increasing the recovery by 3% during the second stage of testing.

Clay mineral content can display different results regarding swelling and permeability reduction (Aksu et al 2015). The physical effect of clay minerals has been studied for many years, early studies conducted by Krumbein and Monk (1943) showed that the characteristics of sediments in terms of clay content and type can significantly affect permeability. Perry and Hower (1970), Malmberge and Smith (2012), Mahmoud et al (2018) studied the effect of clay mineral content on wettability of sandstone reservoirs and suggested that the quality of the reservoir can be affected by the adsorption of polar compounds or the deposition of organic matter in crude oil. The adsorption, they suggested, was enhanced by the presence of clays. A clay can become oil wet due to adsorption (Somenon and Rodke 1983), as well as change properties, including the double layer expansion, clay surface, cation exchange capacity and sensitivity to water.

Clay minerals can also alter the wettability indirectly by causing changes in the capillary pressure and permeability as shown by Anderson (1986) and Anderson (1987) by means of swelling, dispersion and cation exchange causing blockages and reduced permeability. (1989) also showed that clay mineral content can affect reservoir quality when alkaline solutions are introduced to the matrix rock. Their work showed that the crude oil contact angle in Saudi sandstone cores increase aligned well with the increase in clay content inside sandstones, highlighting the importance of clay minerals.

A study by Hendry et al (2009) showed that swelling of clay minerals in a reservoir increased the diffusion coefficient (De) value under confining pressure for a clay-rich medium. They found that their results were different than those that came from the field scale test and they attributed that to a possible swelling of the samples that they used. A question that arises from any lab study though, is whether the measurements performed can realistically represent *in situ* values and if so, to what extent (Xiang and Mazurek 2016).

Sharifipour and co – workers (2017) showed that oil recovery can be affected by low salinity water flooding due to swelling of clays (see Fig. 1.7). Clay swelling can cause more oil to be bypassed in the system after flooding. Aksu et al (2015) conducted core flood experiments and used X-ray and micro-computed tomography (Micro – CT) to study the swelling of clay minerals *in situ* and how it

affects unconsolidated porous media. They showed that different clays swell differently. For example, montmorillonite increases in volume by 39% due to swelling. Kaolinite only increases its volume by 15% after swelling, causing a concomitant effect in oil recovery.

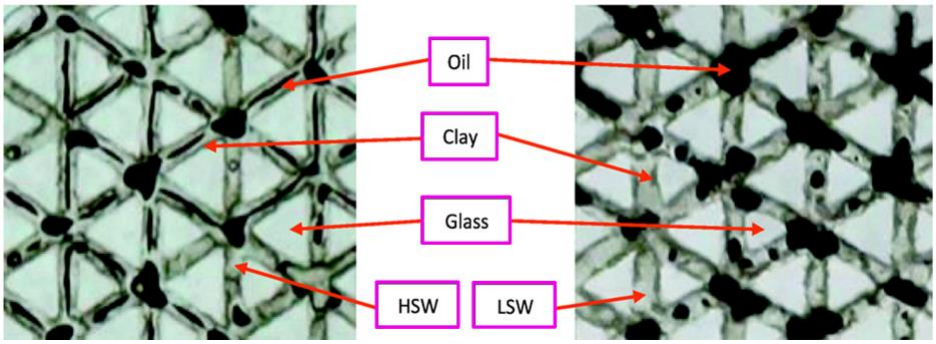

Figure 1.8. Clay swelling and capturing of oil (modified Sharifipour et al 2017).

1.4 Fines migration induced by low salinity water flooding

The difference between salinities of the formation and injected water induces wettability alteration. Subsequently, fines migration is induced as a direct effect of changes in layer charge and cation type relative to clay minerals present (see section 1.4), leading to an increased sweep efficiency by means of a decrease in water flux and its diversion into zones not yet flooded with water (Borazjani et al 2017). The zones that have not been flooded with low salinity water, become the lowest resistance pathway, after the zones that were flooded lose permeability (Abdelmoneim and Nasr El Din 2018).

Fines migrate as colloids or suspensions (Oliveira et al 2014). A reduction of permeability is a result of the fines migration. The fines are transported via the carrier fluid. Also Oliveira et al (2014) stated that "The permeability stabilization occurs after the arrival of the last mobilized fine at the core outlet". Their results also showed that permeability was stable again after achieving more than one pore volume. The time needed for the stabilization was found to decrease as the rate of the flow increased (Oliveira et al 2014). Based on Oliveira and co – workers (2014), critical salinity was the absolute necessary salinity needed by the fines in order to be detached

Physical factors affecting fines migration: From the physical aspect of fines migration, the migration is directly proportional to their diameter. Oliveira et al (2014) suggested that the carrier velocity is critical for fines migration and that the higher it is, the smaller the transition time, since the latter is in proportion with the force of dragging. The force of dragging is responsible for

moving fines close to the walls of the pore. Also, the authors suggested that the higher the velocity of fluid, the less the transition time, or the higher the particle drift speed. Fines attach to the quartz grain when the attaching torque is greater than the detaching torque. Kinetic factors also greatly regulate the migration of fines and are primarily affected by the size of the fine (Oliveira et al 2014). A fine can be detached and/ or mobilized when the detaching torque is greater than the attached one. Also, a particle can do the same as a result of the velocity that causes an increase of the physical forces related to the fine (drag or lift, see Figure 1.7).

Chemical factors affecting fines migration: With regard to the chemical aspect of fines migration, salinity of the injected brine causes a decrease in the electrostatic force between OIP and clay minerals, when it is decreased, leading to a decreased attaching torque (Oliveira et al 2014). Temperature and pH increase can cause weaker electrostatic force, thus the attaching force is weakened and fines migration favored (Miranda and Underdown 1993).

To measure and model the migration of fines, mathematical models regarding the formulation of detachment transport and capturer were used by Russell and Bedrikovetsky (2018). They suggested that drag and lift forces are the most common forces with regard to the movement and detachment of particles by the moving fluid that can cause detachment (Russell and Bedrikovetsky 2018). The simulations that Russel and Bedrikovetsky (2018) ran showed that porous medium permeability following fines migration will be location dependent. Also, they highlighted two important variables in fines migration that are: impedance and injected salinity. Based on their results, they summed up the rest of the important factors for fines migration. According to them, these are: temperature, pH and Eh, time and pressure of the injected brine, the physical properties of fines and the overall heterogeneity of the reservoir. Nhattacharya et al 2016, showed that with decreasing salinity there is a decreasing electrostatic force provoking fines migration (also supported by Kia et al 1987).

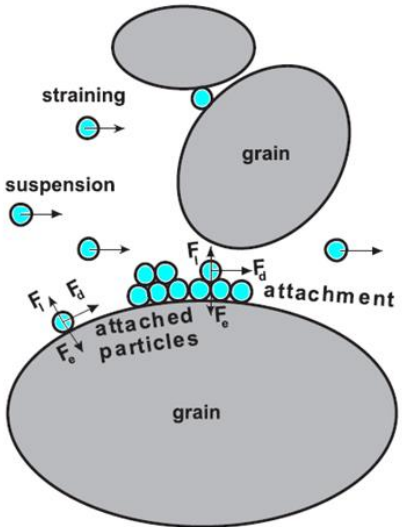

Figure 1.7. Physical properties of fines – detachment from grains, migration in carrier water, attachment to grains and straining from thin pores (modified after Oliveira et al 2014).

1.5 Redox conditions of petroleum reservoirs

Overall, it can be said that redox conditions in petroleum reservoirs have been traditionally examined in relation to the types of bacteria present and their effect on petroleum quality. It is well understood that petroleum reservoirs exist in anaerobic conditions that favor microbial populations comprised of sulfate reducing bacteria (Voordouw et al 1996; Magot et al 2000; Dong et al 2014), facultative anaerobic bacteria (Nazina et al 1995) and anaerobic ammonium-oxidizing (anammox) bacteria (Li et al 2010). These organisms thrive under anoxic reservoir conditions due to their ability to enzymatically reduce redox active elements such as ferric iron, carbon dioxide or sulfate (Liebensteiner et al 2014). The existence of such organisms significantly factors into biodegradation, free oxygen consumption and the perpetuation of reducing conditions inside reservoirs. The reducing conditions aided by the existence of microorganisms inside petroleum reservoirs are thought to vary relative to the chemical and physical characteristics of the ecosystem (Magot et al 2000). Temperature is also important in terms of sustaining bacterial growth (Stetter et al 1993a). For instance, deep oil reservoirs with a temperature range between/over 130-150 °C do not easily sustain bacterial growth. Another factor that affects bacterial populations inside oil reservoirs is the composition of formation water along with pH. The existing ions in the formation water act as electron donors that fuel important metabolic activities of bacteria allowing them to live and grow within petroleum reservoirs (Barth 1991). Early experimental work on crude oil in anaerobic shallow sand aquifers showed hydrocarbon degradation due to microbial activity that was primarily caused by methanogenesis and reduction of present redox active species (i.e. Fe^{3+} and Mn^{4+}). There is scarcity of literature with regards to

redox conditions of petroleum reservoirs that is separate from studies that revolve around bacterial populations and biodegradation. In this research we aim to a take a step further towards understanding how redox conditions impact iron clay minerals and their potential migration inside sandstone petroleum reservoirs during LSWF EOR.

1.6 Aims and objectives

In this present study, we explore a new frontier in LSWF EOR research by examining the wettability, swelling capacity and hydration state of reservoir clay minerals as a function of reduction extent, with many natural clay minerals containing Fe and oil reservoirs shifting from reduced to oxidised conditions upon production.

Within the context of fines mobility and migration inside clastic reservoirs, we investigate how changes in reduction extent impact on the wettability of iron rich clay minerals. We aim to understand the following: a) how does the wettability of iron bearing clay minerals change relative to changes in their reduction state – clays are important regulators of a reservoir's wetting state as previously mentioned. It has been shown (Yesufu-Rufai et al 2021 and Apeiranthitis PhD thesis 2021) that reduction of iron clays alters the wetting properties of clay minerals. Based on these previous studies dedicated on the wetting of clays minerals, we hypothesize that reduction of iron clays will induce less wetting of crude oil on the clay surface along with an increase in water wetting b) how is the cation exchange capacity (CEC) changed and what kind of cation substitutions occur as a result of iron clay reduction and how the enthalpy of hydration of the clay minerals is affected – CEC significantly factors in surface hydration of clay minerals and subsequently to their swelling capacity (Stucki et al 1984). Stucki et al (1984) saw an increase in CEC of smectite clays upon iron reduction. High CEC is thought to induce permeability decrease (Basin and Labrid 1991). Based on an understanding gained by their findings we aim to investigate further and we hypothesize that clay bulk composition and purification methods will have an effect on the CEC upon reduction c) what is and how is the hydration state of iron clays in reduced conditions affected at the surface and in their bulk – clay hydration is directly linked to surface properties. Pervious study by Stucki et al (2000) showed a dehydrated interlayer upon iron reduction. We hypothesize that iron reduction will induce dehydration in the interlayer due to changes in the occupying cation, and d) how does the sorption properties of the reduced clay minerals compare to those in oxidized conditions. Sorption of clay minerals is an important property responsible for maintaining or changing equilibrium between the solid – liquid interface in hydrous systems. Research by Kostka et al (1999) has shown that surface area decreases upon

iron reduction. We hypothesize that surface area changes will depend on clay bulk chemistry and purification methods and potentially be different when testing native – as received clay minerals.

Additionally, a significant part of this study was dedicated to developing a flow cell apparatus to study fines migration *in situ* as a function of redox state. Having understood how redox state effects hydration of clay minerals and wettability, the subsequent impact on fines migration, detachment and mobilisation of fines can be better understood by *in situ* visualization. Unfortunately, owing to CoVID 19, there was not time to fully finish the cell and test it with the samples previously characterised.

1.7 References

1. Abdelmoneim, S. S., and H. A. Nasr-El-Din. "Effect of low salinity waterflooding on sweep efficiency in multilayered clay-rich sandstone reservoirs." In *SPE Improved Oil Recovery Conference*. OnePetro, 2018.
2. Afekare, Dayo A., and Mileva Radonjic. "From mineral surfaces and coreflood experiments to reservoir implementations: Comprehensive review of low-salinity water flooding (LSWF)." *Energy & fuels* 31, no. 12 (2017): 13043-13062.
3. Aksu, I., E. Bazilevskaya, and Z. T. Karpyn. "Swelling of clay minerals in unconsolidated porous media and its impact on permeability." *GeoResJ* 7 (2015): 1-13.
4. Al-Saedi, Hasan, Patrick Vane Brady, Ralph Flori, and Peyman Heidari. *Novel Insights into Low Salinity Water Flooding Enhanced Oil Recovery in Sandstone With/Without Clays*. No. SAND2018-0830C. Sandia National Lab.(SNL-NM), Albuquerque, NM (United States); Sandia National Laboratories, null, 2018.
5. Al-Shalabi, Emad W., and Kamy Sepehrnoori. "A comprehensive review of low salinity/engineered water injections and their applications in sandstone and carbonate rocks." *Journal of Petroleum Science and Engineering* 139 (2016): 137-161.
6. Alvarado, Vladimir, and Eduardo Manrique. *Enhanced oil recovery: field planning and development strategies*. Gulf Professional Publishing, 2010.
7. Anderson, William G. "Wettability literature survey-part 6: the effects of wettability on waterflooding." Journal of petroleum technology 39, no. 12 (1987): 1605-1622.
8. Anderson, William. "Wettability literature survey-part 2: Wettability measurement." *Journal of petroleum technology* 38, no. 11 (1986): 1246-1262.

9. Austad, Tor, Alireza RezaeiDoust, and Tina Puntervold. "Chemical mechanism of low salinity water flooding in sandstone reservoirs." In *SPE improved oil recovery symposium*. OnePetro, 2010.
10. Bartels, W. "Pore scale processes in mixed-wet systems with application to low salinity waterflooding." PhD diss., UU Dept. of Earth Sciences, 2018.
11. Bartels, W-B., H. Mahani, S. Berg, and S. M. Hassanizadeh. "Literature review of low salinity waterflooding from a length and time scale perspective." *Fuel* 236 (2019): 338-353.
12. Barth, S. S., K. B. Williams, S. J. Gibson, and L. B. Elliott. "Rapid identification of gram negative bacteria by carbon source oxidation, abstr. C-211." In *Abstr. 91st Gen. Meet. Am. Soc. Microbiol*, p. 377. 1991.
13. Bazin, Brigitte, and Jean Labrid. "Ion exchange and dissolution/precipitation modeling: application to the injection of aqueous fluids into a reservoir sandstone." *SPE reservoir engineering* 6, no. 02 (1991): 233-238.
14. Bennion, D. B., D. W. Bennion, F. B. Thomas, and R. F. Bietz. "Injection water quality-a key factor to successful waterflooding." *Journal of Canadian Petroleum Technology* 37, no. 06 (1998).
15. Bernard, George G. "Effect of floodwater salinity on recovery of oil from cores containing clays." In *SPE California Regional Meeting*. OnePetro, 1967.
16. Bhattacharya, S. S., J. Paitaridis, A. Pedler, A. Badalyan, Y. Yang, T. Carageorgos, P. Bedrikovetsky, D. Warren, and N. Lemon. "Fines mobilisation by low-salinity water injection: 3-point-pressure tests." In *SPE International Conference and Exhibition on Formation Damage Control*. OnePetro, 2016.
17. Blume, Theresa, Noam Weisbrod, and John S. Selker. "Permeability changes in layered sediments: Impact of particle release." *Groundwater* 40, no. 5 (2002): 466-474.
18. Boggs Jr, Sam, and Sam Boggs. *Petrology of sedimentary rocks*. Cambridge university press, 2009.
19. Borazjani, S., A. Behr, L. Genolet, A. Van Der Net, and P. Bedrikovetsky. "Effects of fines migration on low-salinity waterflooding: analytical modelling." *Transport in Porous Media* 116, no. 1 (2017): 213-249.
20. Buckley, J. S., and Norman R. Morrow. "Characterization of crude oil wetting behavior by adhesion tests." In *SPE/DOE Enhanced Oil Recovery Symposium*. OnePetro, 1990.
21. Buckley, J. S., and Y. Liu. "Some mechanisms of crude oil/brine/solid interactions." *Journal of Petroleum Science and Engineering* 20, no. 3-4 (1998): 155-160.

22. Didier, Mathilde, Annabelle Chaumont, Thibaut Joubert, Igor Bondino, and Gérald Hamon. "Contradictory trends for smart water injection method: Role of pH and salinity from sand/oil/brine adhesion maps." In *Proceedings of the International Symposium of the Society of Core Analysts*, pp. 16-21. 2015.
23. Ding, Hongna, and Sheik Rahman. "Experimental and theoretical study of wettability alteration during low salinity water flooding-an state of the art review." *Colloids and Surfaces A: Physicochemical and Engineering Aspects* 520 (2017): 622-639.
24. Dong, Yiran, Charu Gupta Kumar, Nicholas Chia, Pan-Jun Kim, Philip A. Miller, Nathan D. Price, Isaac KO Cann et al. "H alomonas sulfidaeris-dominated microbial community inhabits a 1.8 km-deep subsurface C ambrian S andstone reservoir." *Environmental microbiology* 16, no. 6 (2014): 1695-1708.
25. Drummond, Carlos, and Jacob Israelachvili. "Fundamental studies of crude oil–surface water interactions and its relationship to reservoir wettability." *Journal of Petroleum Science and Engineering* 45, no. 1-2 (2004): 61-81.
26. Farzaneh, S. Amir, Andrew Carnegie, Mehran Sohrabi, John R. Mills, Juliana M. Facanha, and Ben Sellers. "A case study of oil recovery improvement by low salinity water injection." In *Abu Dhabi International Petroleum Exhibition & Conference*. OnePetro, 2017.
27. Hendry, M. Jim, S. Lee Barbour, Brigitte EJ Boldt-Leppin, Laura J. Reifferscheid, and Leonard I. Wassenaar. "A comparision of laboratory and field based determinations of molecular diffusion coefficients in a low permeability geologic medium." *Environmental science & technology* 43, no. 17 (2009): 6730-6736.
28. Hirasaki, G. J. "Wettability: fundamentals and surface forces." *SPE formation evaluation* 6, no. 02 (1991): 217-226.
29. Howard, James J., and William E. Kenyon. "Determination of pore size distribution in sedimentary rocks by proton nuclear magnetic resonance." *Marine and petroleum geology* 9, no. 2 (1992): 139-145.
30. Hurst, Andrew, and Paul H. Nadeau. "Clay microporosity in reservoir sandstones: an application of quantitative electron microscopy in petrophysical evaluation." *AAPG bulletin* 79, no. 4 (1995): 563-573.
31. Jackson, Matthew D., Dawoud Al-Mahrouqi, and Jan Vinogradov. "Zeta potential in oil-water-carbonate systems and its impact on oil recovery during controlled salinity water-flooding." *Scientific reports* 6, no. 1 (2016): 1-13.

32. Jiménez-Ángeles, Felipe, and Abbas Firoozabadi. "Contact angle, liquid film, and liquid–liquid and liquid–solid interfaces in model oil–brine–substrate systems." *The Journal of Physical Chemistry C* 120, no. 22 (2016): 11910-11917.
33. Kantorowicz, J. D. "The influence of variations in illite morphology on the permeability of Middle Jurassic Brent Group sandstones, Cormorant Field, UK North Sea." *Marine and Petroleum Geology* 7, no. 1 (1990): 66-74.
34. KAREEM, RIKAN, and ALI MOHAMMED. "Nano Geochemistry of Low Salinity Enhanced Oil Recovery." PhD diss., Durham University, 2017.
35. Kia, S. F., H. S. Fogler, and M. G. Reed. "Effect of pH on colloidally induced fines migration." *Journal of colloid and interface science* 118, no. 1 (1987): 158-168.
36. Kim, Changkyun, and Jeonghwan Lee. "Experimental study on the variation of relative permeability due to clay minerals in low salinity water-flooding." *Journal of Petroleum Science and Engineering* 151 (2017): 292-304.
37. Kokal, Sunil, and Abdulaziz Al-Kaabi. "Enhanced oil recovery: challenges & opportunities." *World Petroleum Council: Official Publication* 64 (2010): p64-69.
38. Kostka, Joel E., Jun Wu, Kenneth H. Nealson, and Joseph W. Stucki. "The impact of structural Fe (III) reduction by bacteria on the surface chemistry of smectite clay minerals." *Geochimica et Cosmochimica Acta* 63, no. 22 (1999): 3705-3713.
39. Krumbein, W. C., and G. D. Monk. "Permeability as a function of the size parameters of unconsolidated sand." *Transactions of the AIME* 151, no. 01 (1943): 153-163.
40. Lager, A., K. J. Webb, C. J. J. Black, M. Singleton, and K. S. Sorbie. "Low salinity oil recovery." *An experimental investigation, presented at the Society of Core Analysts. SCA, Trondheim, Norway* (2006).
41. Lager, A., K. Webb, and J. Seccombe. "Low salinity waterflood, Endicott, Alaska: Geochemical study & field evidence of multicomponent ion exchange." In *IOR 2011-16th European Symposium on Improved Oil Recovery*, pp. cp-230. European Association of Geoscientists & Engineers, 2011.
42. Lager, Arnaud, Kevin J. Webb, C. J. J. Black, Mike Singleton, and Kenneth S. Sorbie. "Low salinity oil recovery-an experimental investigation1." *Petrophysics-The SPWLA Journal of Formation Evaluation and Reservoir Description* 49, no. 01 (2008).
43. Lever, Andrew, and Richard A. Dawe. "Water-sensitivity and migration of fines in the hopeman sandstone." *Journal of Petroleum Geology* 7, no. 1 (1984): 97-107.

44. Li, Hui, Shuo Chen, Bo-Zhong Mu, and Ji-Dong Gu. "Molecular detection of anaerobic ammonium-oxidizing (anammox) bacteria in high-temperature petroleum reservoirs." *Microbial ecology* 60, no. 4 (2010): 771-783.
45. Liebensteiner, Martin G., Nicolas Tsesmetzis, Alfons JM Stams, and Bartholomeus P. Lomans. "Microbial redox processes in deep subsurface environments and the potential application of (per) chlorate in oil reservoirs." *Frontiers in microbiology* 5 (2014): 428.
46. Ligthelm, Dick Jacob, Jan Gronsveld, Jan Hofman, Niels Brussee, Fons Marcelis, and Hilbert van der Linde. "Novel waterflooding strategy by manipulation of injection brine composition." In *EUROPEC/EAGE conference and exhibition*. OnePetro, 2009.
47. Magot, Michel, Bernard Ollivier, and Bharat KC Patel. "Microbiology of petroleum reservoirs." *Antonie van Leeuwenhoek* 77, no. 2 (2000): 103-116.
48. Mahani, Hassan, T. G. Sorop, P. J. Van den Hoek, A. D. Brooks, and Marcel Zwaan. "Injection fall-off analysis of polymer flooding EOR." In *SPE reservoir characterisation and simulation conference and exhibition*. OnePetro, 2011.
49. Mahmoud, Ahmed Abdulhamid, and Hasan Al-Hashim. "Insight into the mechanism for oil recovery using EDTA chelating agent solutions from clayey sandstone rocks." *Journal of Petroleum Science and Engineering* 161 (2018): 625-635.
50. Malmberg, E. W., and L. Smith. "Suntech, Incorporated." *Improved Oil Recovery by Surfactant and Polymer Flooding* (2012): 275.
51. Martin, John C. "The effects of clay on the displacement of heavy oil by water." In *Venezuelan annual meeting*. OnePetro, 1959.
52. McGuire, P. L., J. R. Chatham, F. K. Paskvan, D. M. Sommer, and F. H. Carini. "Low salinity oil recovery: An exciting new EOR opportunity for Alaska's North Slope." In *SPE western regional meeting*. OnePetro, 2005.
53. Miranda, R. M., and D. R. Underdown. "Laboratory measurement of critical rate: a novel approach for quantifying fines migration problems." In *SPE Production Operations Symposium*. OnePetro, 1993.
54. Morrow, Norman R. "Wettability and its effect on oil recovery." *Journal of petroleum technology* 42, no. 12 (1990): 1476-1484.
55. Myint, Philip C., and Abbas Firoozabadi. "Thin liquid films in improved oil recovery from low-salinity brine." *Current Opinion in Colloid & Interface Science* 20, no. 2 (2015): 105-114.

56. Nasralla, Ramez A., and Hisham A. Nasr-El-Din. "Double-layer expansion: is it a primary mechanism of improved oil recovery by low-salinity waterflooding?." *SPE Reservoir Evaluation & Engineering* 17, no. 01 (2014): 49-59.
57. Nazina, Tamara N., Anna E. Ivanova, Igor A. Borzenkov, Sergei S. Belyaev, and Michail V. Ivanov. "Occurrence and geochemical activity of microorganisms in high-temperature, water-flooded oil fields of Kazakhstan and Western Siberia." *Geomicrobiology Journal* 13, no. 3 (1995): 181-192.
58. Oliveira, Maira A., Alexandre SL Vaz, Fernando D. Siqueira, Yulong Yang, Zhenjiang You, and Pavel Bedrikovetsky. "Slow migration of mobilised fines during flow in reservoir rocks: laboratory study." *Journal of Petroleum Science and Engineering* 122 (2014): 534-541.
59. Pallatt, Nadia, Jeff Wilson, and Bill McHardy. "The relationship between permeability and the morphology of diagenetic illite in reservoir rocks." *Journal of Petroleum Technology* 36, no. 12 (1984): 2225-2227.
60. Perry, E. D., and John Hower. "Burial diagenesis in Gulf Coast pelitic sediments." *Clays and Clay minerals* 18, no. 3 (1970): 165-177.
61. Pouryousefy, Ehsan, Quan Xie, and Ali Saeedi. "Effect of multi-component ions exchange on low salinity EOR: Coupled geochemical simulation study." *Petroleum* 2, no. 3 (2016): 215-224.
62. Puntervold, Tina, Aleksandr Mamonov, Zahra Aghaeifar, Gunvor Oline Frafjord, Gyrid Marie Moldestad, Skule Strand, and Tor Austad. "Role of kaolinite clay minerals in enhanced oil recovery by low salinity water injection." *Energy & fuels* 32, no. 7 (2018): 7374-7382.
63. Rezaei Gomari, Sina, and Nikhil Joseph. "Study of the effect of clay particles on low salinity water injection in sandstone reservoirs." *Energies* 10, no. 3 (2017): 322.
64. Russell, Thomas, and Pavel Bedrikovetsky. "Colloidal-suspension flows with delayed fines detachment: Analytical model & laboratory study." *Chemical Engineering Science* 190 (2018): 98-109.
65. Sayyouh, M. H. "Secondary vs. Tertiary oil recovery from a two-dimensional porous media by microemulsion flooding." (1989).
66. Seccombe, Jim, Arnaud Lager, Gary Jerauld, Bharat Jhaveri, Todd Buikema, Sierra Bassler, John Denis et al. "Demonstration of low-salinity EOR at interwell scale, Endicott field, Alaska." In *SPE improved oil recovery symposium*. OnePetro, 2010.

67. Sharifipour, Milad, Peyman Pourafshary, and Ali Nakhaee. "Study of the effect of clay swelling on the oil recovery factor in porous media using a glass micromodel." *Applied Clay Science* 141 (2017): 125-131.
68. Sheng, James J., and Ke Chen. "Evaluation of the EOR potential of gas and water injection in shale oil reservoirs." *Journal of Unconventional Oil and Gas Resources* 5 (2014): 1-9.
69. Somenon, W. H., and C. J. Rodke. "Role of clay in EOR of petroleum from some California sand." *J. Pet. Technol* 35, no. 3 (1983): 643-654.
70. Stalder, P. J. "Influence of crystallographic habit and aggregate structure of authigenic clay minerals on sandstone permeability." *Geologie en Mijnbouw* 52, no. 4 (1973): 217-220.
71. Stetter, Karl Otto, R. Huber, E. Blöchl, M. Kurr, R. D. Eden, Me Fielder, H. Cash, and I. Vance. "Hyperthermophilic archaea are thriving in deep North Sea and Alaskan oil reservoirs." *Nature* 365, no. 6448 (1993): 743-745.
72. Strand, Skule, Tina Puntervold, and Tor Austad. "Water based EOR from clastic oil reservoirs by wettability alteration: A review of chemical aspects." *Journal of Petroleum Science and Engineering* 146 (2016): 1079-1091.
73. Stucki, Joseph W., D. C. Golden, and Charles B. Roth. "Effects of reduction and reoxidation of structural iron on the surface charge and dissolution of dioctahedral smectites." *Clays and Clay Minerals* 32, no. 5 (1984): 350-356.
74. Stucki, Joseph W., Jun Wu, Huamin Gan, Peter Komadel, and Amos Banin. "Effects of iron oxidation state and organic cations on dioctahedral smectite hydration." *Clays and Clay Minerals* 48, no. 2 (2000): 290-298.
75. Suijkerbuijk, B. M. J. M., H. P. C. E. Kuipers, C. P. J. W. Van Kruijsdijk, S. Berg, J. F. Van Winden, D. J. Ligthelm, H. Mahani et al. "The development of a workflow to improve predictive capability of low salinity response." In *IPTC 2013: International Petroleum Technology Conference*, pp. cp-350. European Association of Geoscientists & Engineers, 2013.
76. Suijkerbuijk, B. M., J. P. Hofman, Dick Jacob Ligthelm, Julija Romanuka, Niels Brussee, H. A. van derLinde, and A. H. Marcelis. "Fundamental investigations into wettability and low salinity flooding by parameter isolation." In *SPE Improved Oil Recovery Symposium*. OnePetro, 2012.
77. Tang, G. Q., and Norman R. Morrow. "Salinity, temperature, oil composition, and oil recovery by waterflooding." *SPE Reservoir Engineering* 12, no. 04 (1997): 269-276.

78. Thomas, R. D., J. F. Pautz, and M. P. Madden. *Applications of EOR (enhanced oil recovery) technology in field projects: Project BE2, Milestone 3, FY 88: Topical report*. No. NIPER-366. National Inst. for Petroleum and Energy Research, Bartlesville, OK (USA), 1988.
79. Thomas, Sara. "Enhanced oil recovery-an overview." *Oil & Gas Science and Technology-Revue de l'IFP* 63, no. 1 (2008): 9-19.
80. Valocchi, Albert J., Robert L. Street, and Paul V. Roberts. "Transport of ion-exchanging solutes in groundwater: Chromatographic theory and field simulation." *Water Resources Research* 17, no. 5 (1981): 1517-1527.
81. Vledder, Paul, Julio Carrera Fonseca, Terence Wells, Ivan Gonzalez, and Dick Ligthelm. "Low salinity water flooding: proof of wettability alteration on a field wide scale." In *SPE Improved Oil Recovery Symposium*. OnePetro, 2010.
82. Voordouw, Gerrit, Stephen M. Armstrong, Monika F. Reimer, Benjamin Fouts, Anita J. Telang, Y. I. N. Shen, and Diane Gevertz. "Characterization of 16S rRNA genes from oil field microbial communities indicates the presence of a variety of sulfate-reducing, fermentative, and sulfide-oxidizing bacteria." *Applied and Environmental Microbiology* 62, no. 5 (1996): 1623-1629.
83. Wang, Zhenjun, and Simin Gu. "State-of-the-art on the development of ultrasonic equipment and key problems of ultrasonic oil prudction technique for EOR in China." *Renewable and Sustainable Energy Reviews* 82 (2018): 2401-2407.
84. Webb, K. J., C. J. J. Black, and I. J. Edmonds. "Low salinity oil recovery–The role of reservoir condition corefloods." In *IOR 2005-13th European Symposium on Improved Oil Recovery*, pp. cp-12. European Association of Geoscientists & Engineers, 2005.
85. Whetten, John T., and James W. Hawkins Jr. "Diagenetic origin of graywacke matrix minerals." *Sedimentology* 15, no. 3-4 (1970): 347-361.
86. Worden, Richard, and Sadoon Morad, eds. *Clay mineral cements in sandstones*. Vol. 19. John Wiley & Sons, 2009.
87. Xiang, Y., T. Al, and Martin Mazurek. "Effect of confining pressure on diffusion coefficients in clay-rich, low-permeability sedimentary rocks." *Journal of contaminant hydrology* 195 (2016): 1-10.
88. Yesufu-Rufai, Sherifat, Maja Rücker, Steffen Berg, Sarah F. Lowe, Fons Marcelis, Apostolos Georgiadis, and Paul Luckham. "Assessing the wetting state of minerals in complex sandstone rock in-situ by Atomic Force Microscopy (AFM)." *Fuel* 273 (2020): 117807.
89. Zeinijahromi, Abbas, Vadim Ahmetgareev, Alexander Badalyan, Rais Khisamov, and P. Bedrikovetsky. "Case study of low salinity water injection in Zichebashskoe field." (2015).

Chapter 2: Clay mineral hydration and swelling and effects of redox extent

2.1 Introduction

The importance of clay minerals in sandstone reservoirs in terms of the success of EOR operations and more specifically LSWF, has already been brought forward in Chapter 1 - enhanced oil recovery, LSWF and the factors underpinning those techniques have been explained. A lot of these factors either are directly a result of changes occurring at clay mineral surfaces or indirectly, like fines migration. Understanding what causes clay mineral surfaces to swell/detach is critical and to do so requires a look at the structure and properties of those clay minerals. This chapter is dedicated to the properties of pore lining, pore filling and grain coating clay minerals that are important for the overall wettability of a sandstone reservoir. Within the context of redox active clay minerals and the effects redox extent has on swelling and non-swelling clay types, the hydration state and swelling of clay minerals is explained. Moreover, the specific effects of chemical reduction on iron clay minerals are elaborated on.

2.2 Clay minerals chemistry

In this thesis, the main focus is on ferruginous clay minerals with high and low iron content. *Smectite*: The iron rich smectite is usually nontronite. It forms on abyssal plains, in deep ocean basins, near mid – ocean ridges. Silica content can be high due to biogenic silica present in these environments. Iron owes its presence to the existence of Fe – oxyhydroxides in combination with a low organic matter (Worden and Morad 2003). Water molecules and cations sit between the 2:1 layers of the smectite. The chemical formula of smectite is $(OH)_4Si_8Al_4O_{20}$ - NH_2O (interlayer). Smectite consists of the following elements in corresponding contents (%): SiO_2, 66.7%; Al_2O_3, 28.3%; and H_2O, 5%. The interlayer material is not included (Murray 2006).

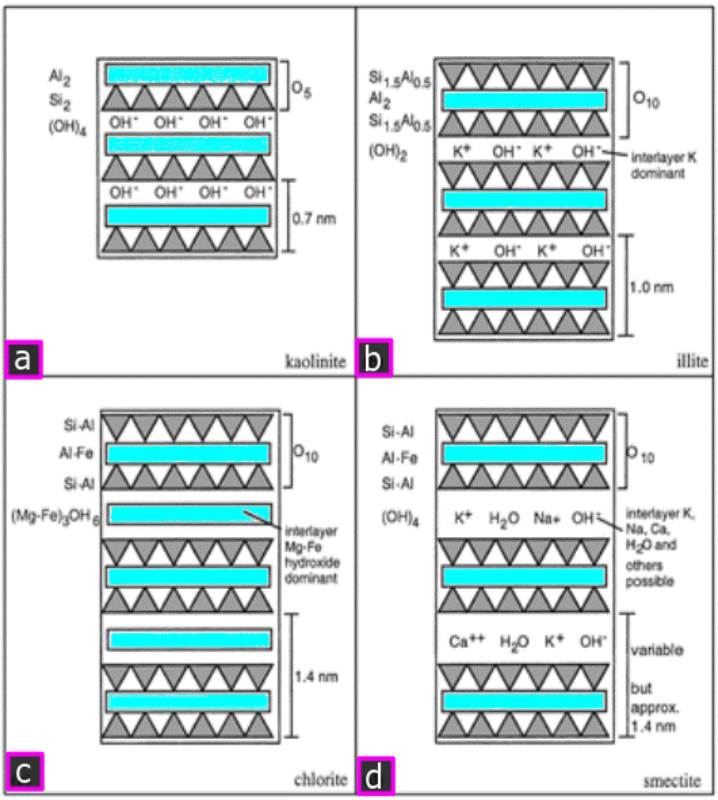

Figure 2.1. Structures of the most common clay minerals in sandstone reservoirs; (a) kaolin, (b) illite (c) chlorite and (d) dioctahedral smectite. Blue bars indicate interlayer space, gray triangles indicate Si –O_2 layers (modified after Worden et al 2013).

Specifically nontronite NAu-2 has molecular formula of $M^{+}_{0.72}[Si_{7.55}Al_{0.45}][Fe_{3.83}Mg_{0.05}]O_{20}(OH)_4$ with an octahedral Fe^{3+} speciation and a composition of NAu-2 (%) is SiO_2: 56.99, Al_2O_3: 3.4, Fe_2O_3: 37.42, MgO: 0.34, CaO: 2.67, Na_2O: 0.11, K_2O: 0.02 (Keeling et al 2000). Montmorillonite SCa3 has chemical composition of (%)SiO_2: 52.8 Al_2O_3: 15.7, TiO_2: 0.181, Fe_2O_3:1.06, FeO: <0.10, MnO: 0.03, MgO: 7.98, CaO: 0.95, Na_2O: 0.92, K_2O: 0.03,P_2O_5: 0.02 and a stoichiometry of: $(Mg_{.45}\ Ca_{.15}\ Na_{.26}\ K_{.01})[Al_{2.55}\ Fe(III)_{.12}\ Mg_{1.31}\ Ti_{.02}\ ][Si_{7.81}\ Al_{.19}]O_{20}(OH)_4$, Octahedral charge: -1.29, Tetrahedral charge: -0.19,Interlayer charge: -1.48, unbalanced charge: 0.00 and M representing the interlayer cation (data taken from the Clay Minerals Repository (also see methods chapter).

Illite: Illite belongs to the mica group and is a potassium mica (Grim et al 1937). Potassium sits in the hexagonally structured oxygens of the tetrahedral sheet, creating a structure with a strong ionic bond. As a result the layers are held together leaving no space for water to penetrate which is unlike what happens in smectites. Illite displays a difference compared to other well – crystallized micas, by including a lesser amount of trivalent aluminum in the tetrahedral sheet.

Moreover, illite structure consists of about one – sixth of trivalent aluminium as a substitute for Si^{4+}. Illite IMt-2 has a chemical formula of $K_{0.7}Na_{0.01}(H_2O)_{0.42}(Al_{1.53}Fe^{2+}_{0.06}Fe^{3+}_{0.19}Mg_{0.28})_{\Sigma=2.06}(Si_{3.44}Al_{0.56})O_{10}(OH)_2$ and a composition of IMt-2 (%): SiO_2: 49.3, Al_2O_3: 24.25, TiO_2: 0.55, Fe_2O_3:7.32, FeO: 0.55, MnO: 0.03, MgO: 2.56, CaO: 0.43, Na_2O: 0, K_2O: 7.83, P_2O_5: 0.08, LOI: 8.02, with 76% Fe^{3+} and 24% Fe^{2+} (Nieto et al 2011).

Table 2.1. Swelling and non – swelling clay minerals and of their dominant elements. Basal spacing is the distance from a plain in layer that corresponds to a plane in another layer that is set in parallel relative to the first layer. A set of two values is given to smectites corresponding to basal spacing before and after interlayer hydration (Modified after Velde 1992).

	Dominant elements	**Basal spacing (Å)**	
Swelling types			
Smectites			
Montmorillonite	Al (Mg, Fe^{2+} minor)	17	10
Nontronite	Fe^{3+}	17	10
Mixed layer minerals*		10-17	<10
Non-swelling types			
Illite	K, Al (Fe, Mg minor)	10	

2.2.1 Iron in clay minerals

In sediments, the total Fe content is about 3.9 mass % with a Fe(III)/Fe(II) ratio is 1.35 (Ronov and Yaroshevsky, 1969; Garrels and Mackenzie, 1972; Sibley and Wilbrand, 1977). The presence of iron is controlled by the following factors: Its own abundance in the environment found, its ability to form compounds in Fe^{2+} and Fe^{3+} forms, its similarity of its ionic radii to other major elements, its ability to exist both in chalcophile and lithophile groups and that it is prone to bond with other elements in insoluble hydrolysates. Iron is heavily regulated by its mobility in the Fe^{2+} form. Iron comes from the weathering of secondary minerals such as: sulphides (pyrite, marcasite), clay minerals (smectites) or from carbonates. Meijer and van der Plas (1980) have shown that the stacking regularity, the interlayer water and the specific surface area are also parameters directly

linked to the presence of iron in clay minerals. That has also been verified in a number of studies conducted by other workers (Stucki and co-workers). When a change in Fe occurs surface parameters such as the surface area and water sorption change due to the redistribution of the lattice of the iron clay. Cation exchanges at surface and in the bulk triggered by a change in the clay-fluid system, resulting in a change in Fe reduction extent and it moving to new domains, act as regulators of water retention, altering the above parameters. Iron is prevalent in soils and soil formation processes and its size can vary from 10 – 100 nm giving it a large surface area. It displays a range of morphologies and can differ significantly from samples created in the lab. Iron can form as oxides inside pores and fill up the void space of sediments. In order for this to happen, the iron content has to be such that allows for mineral formation and precipitation. The bonding with the constituents of the matrix, such as quartz crystals, is very solid. To disrupt the chemical equilibria of iron cemented minerals, the dissolution of iron is necessary (Stucki 1988).

According to Stucki and co – workers (1988) the redox potential can control the oxidation state of iron and, to an extent, the distance it will travel. Iron content in sedimentary environments can vary from 0.7 to 55% mass. An average content is 3.8% mass as was suggested by Lindsay (1988). Iron m-magnesium silicates that bear the Fe^{2+} form, are present in sediments and weathering of these minerals can cause iron release. As a result the released iron will be oxidised and precipitate in its divalent form, paired with oxyhydroxides. Iron oxide minerals have structures that consist of hexagonal planes of oxygen atoms, placed one of top of each other, arranged in a hexagonal or cubic order. Iron sits mostly in the octahedral sheet between the hexagonal planes and in some occasions it can also be found inside the tetrahedral sheets.

Iron in the clay structure: Iron content in smectites can vary greatly but all contain some iron in their structure. Nontronite has been well studied first by Hoffman et al (1933) and then Edleman and Favajee (1940) and then extensively in more recent studies (Grim 1962, Matson et al 1983, Keeling et al 2000, Stucki et al 2012, Ndzana et al 2018). These workers described the structure of nontronite as that of inverted tetrahedra caused by an unsuitability in the pairing of a Si – rich tetrahedral sheet and a Fe – rich octahedral sheet. In the more recent studies, nontronite has been shown to consist of two silicate sheets separated by one gibbsite sheet in a layer type 2:1 (Grim, 1962), with alkali metal cations occupying the interlayer. The cations' function is to compensate for the charge imbalance caused in the mineral layers (Huang et al 2018). The deficit is caused when Si is replaced by Al or Fe in the tetrahedral sheet, or when Al is substituted by Mg or Fe in the sheet of gibbsite (Matson et al 1983, Shi et al, 2013 and Huang et al 2018). These substitutions occur during the formation stage of the clay mineral in its natural environment

(Mukherjee 2013). Nontronite displays crystals that form groups of 6 layers as shown by Enggleton (1977). In the illite structure, ferric iron sits in the place of the aluminium octahedral replacing Al^{3+} (Malathi et al 1969). Iron can change its properties in place. This ability of iron can cause alteration of the properties of the clay mineral itself, separating iron from other parts of the clay minerals. The Fe present can change its oxidation state, which effectively changes the charge on layer and amount/type of cations. It can also change the di/trioctahedral site distribution. The properties that can be altered due to the presence of iron in clay minerals, can be summarized in Table 2.2. The difference between dioctahedral and trioctahedral minerals is in the number of available positions, octahedrally coordinated, that are occupied by cations. Two positions are occupied in the dioctahedral clay by two trivalent cations and three in the trioctahedral by three divalent cations.

Table 2.2 Effects of structural Fe on smectites, symbols signify positive (+), negative (-), and no (0) correlation between the property and Fe. ? = unknown, octa=octahedral, tetra=tetrahedral (Modified after Stucki 1988).

		Dioctahedral	
Property	Octa Fe(III)	Tetra Fe(III)	Octa Fe(II)
Layer Charge/ cation exchange capacity	0	+	+
Swelling in Water	(-)	?	(-)
Crystallographic b-dimension	+	+	+
Surface Area	?	?	(-)
Color	yellow brown	?	blue, green, blue-gray
Chemical and thermal stability	(-)	(-)	(-)

		Trioctahedral	
Property	Octa Fe(III)	Tetra Fe(III)	Octa Fe(II)
Surface Charge/cation exchange capacity	0	+	+
Swelling in Water	?	?	?
Crystallographic b-dimension	+	+	+
Surface Area	?	?	?
Color	yellow brown	?	green blue
Chemical and thermal stability	(-)	?	+

2.2.2 Clay hydration

The Derjaguin, Landau, Verwey, and Overbeek (DLVO; Derjaguin and Landau 1941; Verwey and Overbeek 1948) theory is useful for the prediction of swelling by means of utilizing the balance of electrostatics. The electrostatic double layer and van der Waals forces are two independent entities that can be imposed on an interacting distance between two particles. The negatively charged clay sheets repel each other, but are also attracted to the interlayer cations. At a surface level, the relative hydration enthalpy of the cations and how well they bind with the sheets versus the water is also important in terms of understanding hydration (Underwood et al 2016; Anderson et al 2010).

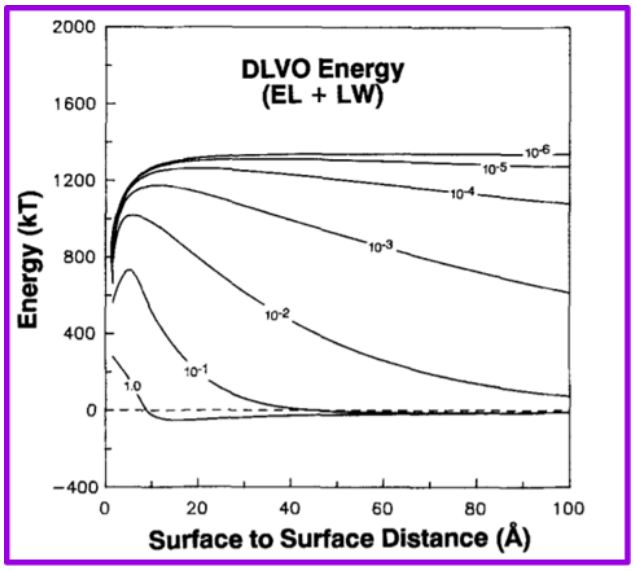

Figure 2.2. DLVO *energy curves generated for 1 n*m hectorite particles *showing* energy maximum at small inter-particle distances (Modified after Van Oss et al 1990*)*

The expansion of the interlayer as a result of hydration was brought forward as an important process of clay hydration in the works of Hofmann and Bilke (1936), Grim et al (1937), Hendricks and Jefferson (1938), Hendricks et al (1940), Mering (1946) and Mooney and co – workers (1952). The X-Ray diffraction analysis of the interlayer spacing of montmorillonites conducted by those workers, indicated a correlation between *d* (001) and water content of the clay. In later studies, the saturating cation present in the clay structure became identified as an important controlling factor in clay hydration, specifically in smectite clays, along with the layer charge of the clay sheets (Halitim et al 1984). In their study, Halitim and workers, measured the effect of water potential in homoionized clay after saturating montmorillonites with Na, Ca and Mg cations. Clay swelling occurs in micro, meso and macro porosity scales that correspond to the below 2 nm length scale,

the 2 – 50 nm length scale and the above 50 nm length scale, respectively (Figure 2.3) (Salles et al 2009).

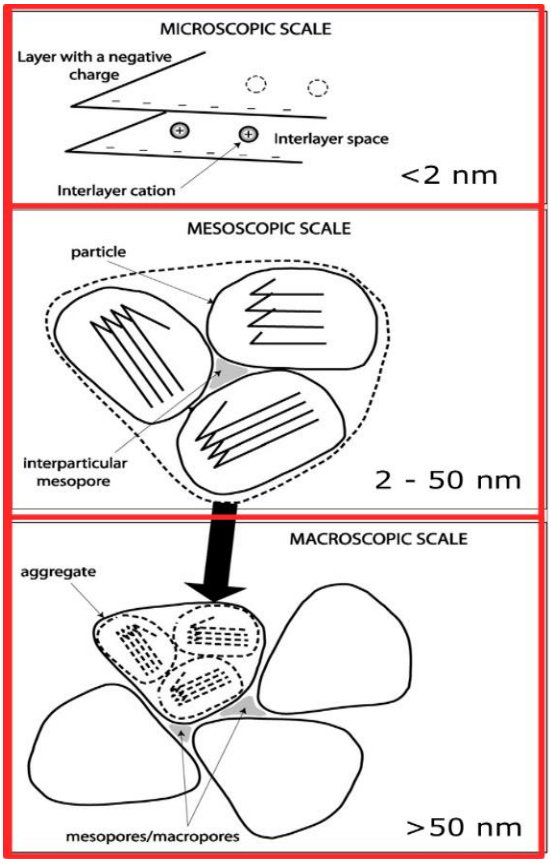

Figure 2.3. A multiscale representation of the hydration for clay montmorillonites (modified after Sébastien et al 2005; Salles et al 2009).

Smectite hydration: The mechanism of smectite clay hydration can be divided into separate successive events as follows (see Fig.2.5). The initial step consists of the hydration of the clay particles externally, followed by gradual interlayer expansion (Barshad 1952, Salles et al 2009). Interlayer expansion begins with separation of silicate surfaces with the interlayer cation remaining in place and ends with the breaking of the cation – oxygen surfaces bonds due to water – oxygen surfaces interactions (Barshad 1952). Once interlayer water layers have taken up the existing interlayer space, further hydration in this region increases interlayer distance, otherwise known as crystalline swelling (Salles et al 2009). The interlayer cations are subsequently detached from the silicate sheets followed by the creation of a final multimolecular layer of water forming in the exterior of clay particles (Barshad 1952).

Previous studies that looked at swelling of smectites such as, montmorillonite (Cases et al 1992) and sodium nontronite (Suquet et al 1987), suggested that under different partial pressures, hydration occurs in different parts of the clay, supporting what was previously mentioned by Barshad (1952). Namely, in the pressure range between 0 and 0.25 kPa, adsorption occurs on the tactoid surfaces of the clay – external liquid phases, isotropic in nature. Water molecules are adsorbed by interlamellar spaces (Cases et al 1992), leading to an opening in the interlayer. This opening can continue until pressure (p/p_0) values of 0.72 or higher, corresponding to a *c* – axis expansion between 9.5 - 12.49 Å (Fig. 2.4).

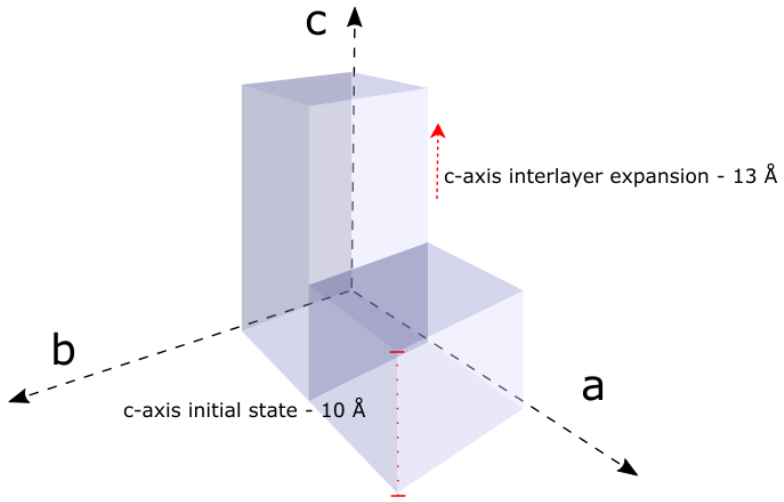

Figure 2.4. Hydration and expansion of interlayer on the c-axis of a swelling clay mineral upon applying pressure.

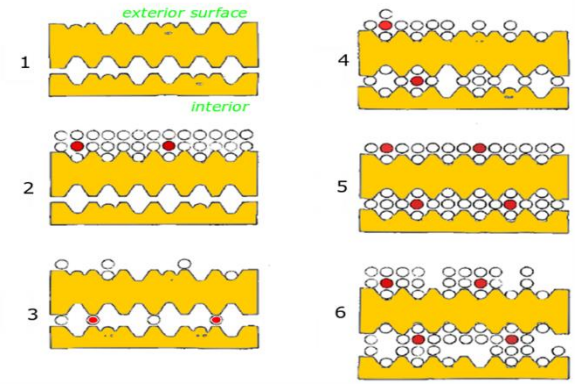

Figure 2.5. Representation of smectite clay hydration and expansion of interlayer. White dots indicate water molecules, red dots indicate exchangeable cations. Anhydrous phase (1), beginning of hydration (2), initial expansion (3), advanced hydration (4,5) and subsequent expansion (6); modified after Barshad 1952).

Illite hydration: Given that the interlayer cation is a dominating controlling factor in clay hydration, potassium (K^+) – rich clays, such as illite IMt – 2, have limited capacity for interlayer expansion. As an interlayer cation, potassium has been shown to cause diffused and weak intensities in the interlayer *d* (001) spacing as well as low water content in grams of H_2O per gram of clay in K^+ - saturated montmorillonites and illites (Barshad 1952). Any water uptake by illite can therefore not be attributed to the interlayer cation. Early studies on illite hydration were primarily focused on the extra water that exists in its structure. Assuming that hydration occurs within the interlayer of illite with the H_3O^+, Brown and Norrish (1952) showed that interlayer charge of illites is similar to that of muscovite – approximately 1.00 per half unit cell of $[O_{10}(OH)_2]$. That finding was later supported by White and Burns (1963). Other workers suggested that extra water is present in the interlayer space as neutral H_2O (Hower and Mowatt 1966, Gaudette et al 1965). That suggestion contradicted that of Nelson (1956) that had suggested illites have an anhydrous interlayer. Brindley (1965) suggested that extra water found in illites may be due to "chemically altered hydrous surfaces". To this day, there is no consensus regarding illite's water content. Illite can be thought as a mixed clay, mimicking both swelling and non – swelling clays in terms of hydration.

Clay hydration can also be probed with the use of infrared spectroscopy (see Chapters 3 and 6 references therein). The relative bending or stretching of the clay mineral's functional groups can be estimated according to its chemical type and could be affected by the specific bonding, degree of isomorphic substitution and nature of cations sitting near OH^- groups (Keeling, J.L.et al. 2000).

In the case of hydration of clay minerals, the structural OH^- groups and their vibrations/overtones become important during the interpretation of the spectra (Fig. 2.6).

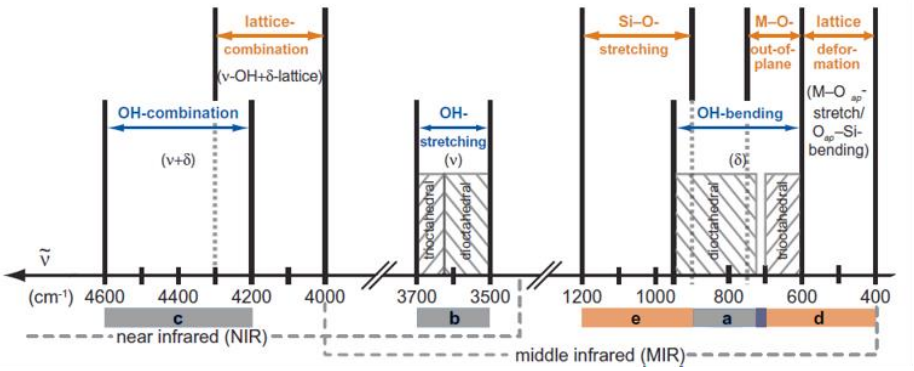

Figure 2.6. IR spectra in the mid- and near- infrared and the key-vibrating groups of clay minerals (Modified after Neumann et al 2011).

The movements of the hydroxyls are expressed as stretching and/or bending vibrations in the mid-IR (MIR) region, between 4000 – 1600 cm^{-1} and as overtones in the near-IR (NIR) region, between 8000 – 4000 cm^{-1} (Balan and Kloprogge 2017). The basic bands in the MIR that exist in the 4000 – 400 cm^{-1} region are the OH^- and Si – O. The MIR area covers the fundamental stretching (υ) and bending (δ). Absorption of OH^- in the IR region can be usually seen between the 3700 and 3500 cm^{-1} areas (Farmer 1974b; Gates 2005; Petit 2006; Gates et al 2017). In the MIR infrared spectrum, the 3000 – 3600 cm^{-1} region is of particular significance as it is the main region where the effect of reduction on the hydroxyl groups can be visualized. Hence, the effect of reduction on the clay minerals' hydration state becomes visible by monitoring the vibrations of the OH^- bands in this region.

In the NIR infrared, overtones in the OH^- structural group are first expressed as (2υ(OH)) at 7060 cm^{-1} and as a combination of stretching and bending modes (ν(OH)+δ(OH)) expressed at 4600 – 4300 cm^{-1} (Bishop et al 1994; Madejova´ and Komadel, 2001).Another way of dividing the respective bands is the following: water bending in clay minerals can be seen in the 1500 – 1700 cm^{-1} region, water stretching (weakly bound water) is visible in the 2800 – 3500 cm^{-1} and strongly bound water in the 3500 – 3600 cm^{-1} region in the MIR spectrum. Overtones are seen in the NIR spectrum between the 4000 – 5000 cm^{-1} and 5000 – 7000 cm^{-1} that correspond to OH^- stretch and bending H_2O combinations.

Clay dispersions in hydrated conditions: Clay particles within a solution are considered as colloidal micelles, the stability of which affects the flocculation and dispersion of the clay suspensions (Hauser 1945). Clay crystals have a negative charge either due to ion exchange or an unbalanced lattice. In the process of balancing their charge, especially in the presence of water, their cations will hydrate leading to the creation of the diffuse electric layer (Fig. 2.7). Clay dispersions depend heavily on the ion distribution inside the diffuse layer of every clay particle. By means of reducing the electrokinetic potential within a dispersion, an ion will cause a decrease in the stability of suspension. The opposite will occur in the presence of ions that favor the diffuse electric layer (dispersing agents). When the diffuse layers of two particles approach each other, the repulsive force between the two particles increases (Kim and Lee 2017).

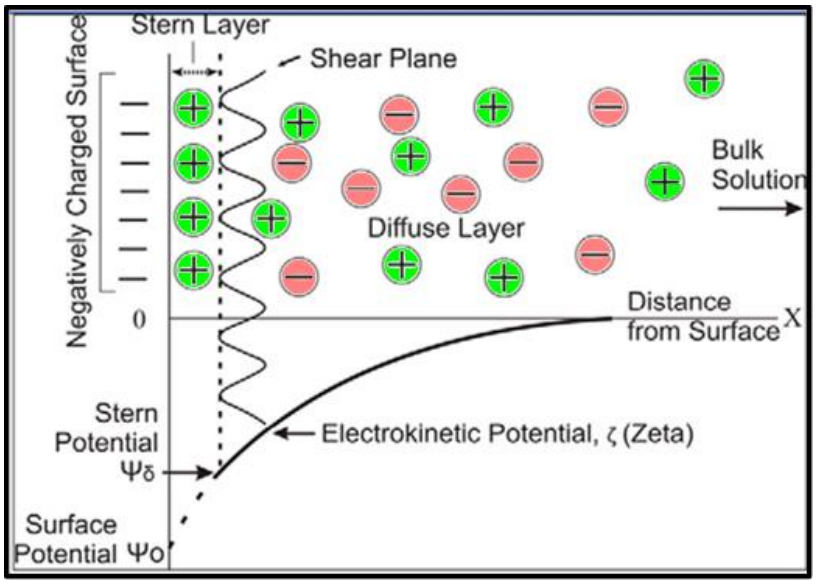

Figure 2.7 The Double electric layer (modified after Wilson et al 2016)

2.3 Effect of redox state on iron – bearing clay minerals

The important things in governing clay hydration and thus swelling/dispersion are clay layer charge and cation amount/type. A redox change will change both of these giving more charge and cations and possibly different ions depending on the environment. This section explores the effect of reduction/oxidation in more detail. Iron reduction is responsible for changes in structural and

colloidal properties (Yan and Stucki 1999). The interpretation of redox profiles can be achieved with the use of the Nernst equation (Gorski et al 2013). The modified version of the Nernst equation used in redox profiles is as follows:

$$E_H = E_H^{\emptyset} - \frac{1}{\beta} * \frac{RT}{nF} ln \frac{\{Fe^{2+}\}}{\{Fe^{3+}\}} \text{ (2.1)},$$

where β takes values between 0 and 1, R is the universal gas constant, T is temperature in Kelvins, F is the Faraday constant and a, the number of transferred electrons in a half reaction, with the brackets denoting activities.

Iron reduction in clays alters their structure due to the size and charge difference between Fe^{3+} and Fe^{2+} (Yan and Stucki 1999). Structural reduction of Fe in iron bearing clays is measured as the ratio Fe^{2+}/Fe_{total} (Gorski et al 2013). As reduction potential (Eh) values become more negative, structural Fe^{3+} becomes Fe^{2+}. The reduction of octahedral iron in partially swelling clays is achieved by electron transferring from the reducing agent (dithionite) to the Fe^{3+}. The transfer is followed by loss of water and gaining of H^+ from the solution. The ratio of de – protonation and re – protonation is 2:1 as shown in the work of Lear and Stucki (1985). Reduction of structural iron in smectites also leads to iron migrating from *cis* to *trans* octahedral sites that significantly changes the structure of the clay mineral by means of altering the Gibbs free energy of the interlayer water (Lear and Stucki 1985). In smectite clays such as nontronites and montmorillonites and mica – like clays such as illite, cations that have low enthalpy of hydration ($\Delta H_{hydration}$) such as K^+, NH_4^+, Rb^+ and Cs^+ can create interlayers that are dehydrated. Cations with high $\Delta H_{hydration}$ such as Ca^{2+}, Mg^{2+} and Sr^{2+} have the opposite effect by producing expanded interlayers due to their higher affinity for water molecules (Shawhney 1972). In their work Lear and Stucki showed that during reduction the loss of hydroxyls previously bonded with interlayer cations, ultimately leads to a less hydrated interlayer (Lear and Stucki 1989).

Cation fixation and affinity is an important mechanism for the hydration state of clays (Khaled and Stucki 1991). Khaled and Stucki (1991) showed that chemical reduction of Fe^{3+} to Fe^{2+} causes cation fixation and the collapse of the clay layers that ultimately trap cations in the interlayer. In addition, surface charge density is increased after the reduction of structural iron due to significant collapse of the clay structure, leading to a decrease in surface area and further dehydration (Stucki, Golden and Roth (1984); Lear and Sucki (1985); Kostka, Wu and Stucki 1999). The proposed scheme for the structural protons, solution and clay phases can be described by the following equations.

$$m(Fe^{3+})_x + me^- \rightarrow m(Fe^{2+})_x \text{ (2.2)},$$

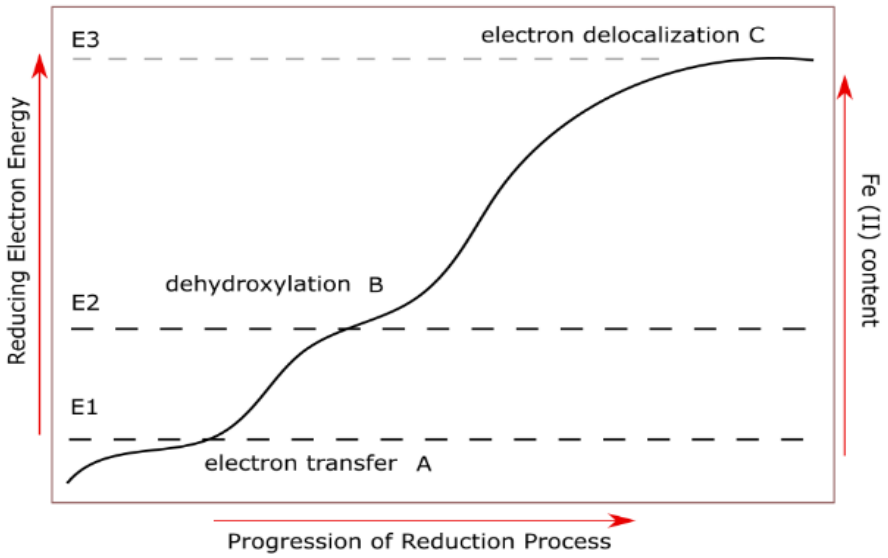

Figure 2.8. Stages of energy of reducing electrons during reduction of structural Fe^{3+} by SO_4^{2-} radicals in smectites (modified after Gan, Stucki and Bailey 1992).

$$2n(OH*^{-})_x \rightarrow n(O^{2-})_x + n(H*_2O)_s \text{ (2.3), and}$$

$$n(O^{2-}) + n(H^{+})_s \rightarrow n(OH^{-})_x \text{ (2.4),}$$

where the stoichiometric coefficients are given as m and n (m > n > 0), solution and clay phases as x and s subscripts respectively and structural protons as H* (Lear and Stucki 1985). The prediction of an increase in surface charge due to structural iron reduction, is possible with the use of these equations. A conceptual model for the energy of reducing electrons is shown in Figure 2.8 (modified after Gan, Stucki and Bailey 1992).

Iron reduction: When chemical reduction is performed on iron clays, sodium dithionite is added to the aqueous clay in solution (see Chapter 3), and it is disproportioned into sulfoxylate free radicals (Komadel, Madejová and Stucki 2006). As a result, its electron activity increases along with the capacity for reducing (Fialips et al 2002). As shown by Drits and Manceau (1992), sodium dithionite ($Na_sS_sO_4$) has electron redox potential Ɛ°= -1,12 V and its SO_4^{2-} member can fully reduce iron (Komadel et al 1990) by successfully approaching the charged clay surfaces (Gan, Stucki and Bailey 1992). Gran, Stucki and Bailey (1992) also demonstrated that $Na_sS_sO_4$ has the ability to reduce iron from the basal surfaces and not from the edges of the clay structure as has been previously proposed by Rozenson and Kallai (1976a).

Chemical reduction of structural iron in iron – bearing clays can alter their structural and colloidal properties. Free SO_4^{2-} radicals of dithionite induce the reduction of Fe^{3+} by entering the structure of the clay through its basal domains. A de – stabilization of energy equilibrium in the crystal lattice of the clay forces layers to re – adjust to reach new equilibrium states. The many changes in clays during chemical reduction, are followed by changes in physical properties of clays such as swelling pressure and specific surface area (Lear and Stucki 1989; also see Chapter 7 and references therein). The color change associated with chemical reduction is due to intra- and inter valence transfers of electrons that involve Fe^{2+} and Fe^{3+} as well as O_2 and Fe^{3+} charge changes (Lahav and Banin 1968 and Sherman and Vergo 1988). The intervalence electron charge transfer transition (IVCT) between Fe species is seen in the UV-Visible spectrum at 700 to 750 nm (Stucki 1987). The compensation of layer charge is possible due to dehydroxylation. The relationship between the excess electrons captured by octahedral Fe is as follows:

$$M\,(Fe^{3+})_x + a(Z^{-q})_x + (m\text{-}a)e^- = m(Fe^{2+})_x + a(Z^{1-q})_x \quad (2.5),$$

Where Z^{-q} is an electron donor in the clay that, upon reduction, gives up one electron that finds a way to arrive at a Fe site, thus achieve reduction.

A schematic example of clay dehydration after reduction of iron clay visualized with the use of infrared spectroscopy can be seen in Figure 2.9. Following the structural rearrangements described above, trioctahedral ferrous iron groups take up the domains of smectite (nontronite), leading to dehydration by means of dehydroxylation in the smectite's octahedral sheet (open circle in Figure 2.9,b). The MIR and NIR spectra can be measured for the regions where cations share hydroxyl groups (Neumann et al 2011).

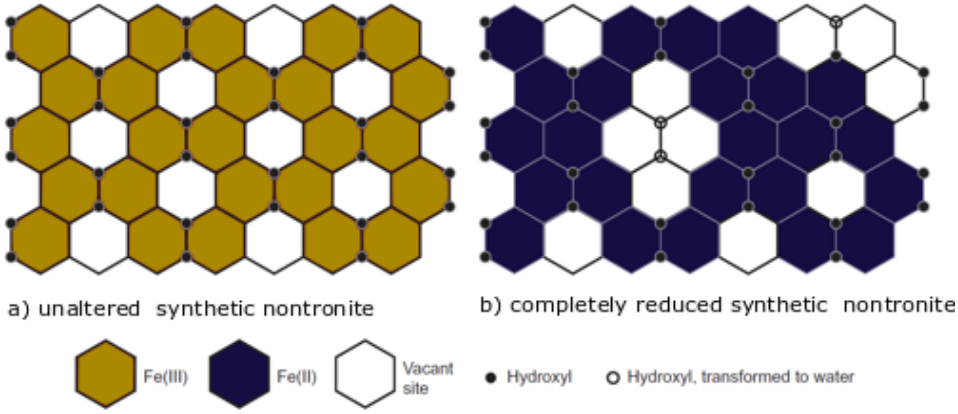

Figure 2.9 Cationic arrangement of unaltered synthetic nontronite (a) and fully reduced trans-vacant synthetic nontronite (b) based on IR studies (modified after Neumann et al 2010).

Loss of the structural OH^- groups and dehydration induced by reduction has been suggested by workers in the past (Stucki and Roth 1977, Lear and Stucki 1985, Kallai 1997, Drits and Manceau 2000, Neumann et al 2011). In the NIR spectra, dehydration has been previously seen around the 4200 – 4600 cm^{-1} region, indicating changes in the combination of OH^- stretch combination and OH^- deformation of FeFeOH (Frost et al 2001; Neumann et al 2011). The peaks seen at 5200 cm^{-1} are possibly a continuation of the the structural (ν+δ) OH combination that occurs around 4500 cm^{-1} (Madejova et al 2017). Moreover, it has been suggested in a number of studies that loss of water is a reversible process. Rehydration is achieved by rehydroxylation, once IR spectra is similar to the initial spectra (Komadel et al 1990, Fialips et al 2002, Dong et al 2003, Lee et al 2006, Ribeiro et al 2009, Neumann et al 2011). An overall preservation of the silicate structure is also concomitant of partial rehydration of smectites (Stucki et al 1984a; Komadel et al 1995; Ribeiro et al 2009, Neumann et al 2011).

2.4 Aims and objectives

So far the theory of clay structure and properties has been explained and their relation to iron has been elaborated on. Structural changes occurring upon reduction in terms of clay hydration and swelling have been mentioned relative to different clay types. In the following chapters we aim to understand and better constrain the changes in clay surface and bulk properties upon reduction. The literature suggests that dehydration is directly linked to Fe reduction alongside a decrease in

CEC and cation exchanges. At surface, decreased sorption capacity by means of a smaller specific surface area is evident upon reduction, indicating a less water wet clay in all domains. It is critical to understand how un-altered, as received clay minerals behave when reduced to allow a more precise comparison with realistic reservoir conditions. As very little has been published on these items in previous years, we aim to couple hydration studies in the bulk and at surface using as received clay minerals of both swelling and non-swelling types. Due to the low iron content, a significant gap in the literature exists, with regard to non-swelling type (i.e. illite), that is however an important clay mineral present in many sandstone reservoirs.

2.5 References

1. Anderson, R. L., I. Ratcliffe, H. C. Greenwell, P. A. Williams, S. Cliffe, and P. V. Coveney. "Clay swelling—a challenge in the oilfield." *Earth-Science Reviews* 98, no. 3-4 (2010): 201-216.
2. Balan, E., and J. T. Kloprogge. "Theoretical Aspects of Infrared and Raman Spectroscopies." In *Developments in Clay Science*, vol. 8, pp. 6-33. Elsevier, 2017.
3. Barshad, Isaac. "Absorptive and swelling properties of clay-water system." *Clays and Clay Minerals* 1, no. 1 (1952): 70-77.
4. Bishop, Janice L., Carle M. Pieters, and John O. Edwards. "Infrared spectroscopic analyses on the nature of water in montmorillonite." *Clays and clay minerals* 42, no. 6 (1994): 702-716.
5. Brindley, G. W. "Clay-organic studies. X. Complexes of primary amines with montmorillonite and vermiculite." Clay Minerals 6, no. 2 (1965): 91-96.
6. Brown, George, R. Greene-Kelly, and Keith Norrish. "Organic derivatives of montmorillonite." *Clay Minerals Bulletin* 1, no. 7 (1952): 214-220.
7. Derjaguin, B., and L. Landau. "The theory of stability of highly charged lyophobic sols and coalescence of highly charged particles in electrolyte solutions." *Acta Physicochim. URSS* 14, no. 633-52 (1941): 58.
8. Dong, Hailiang, Joel E. Kostka, and Jinwook Kim. "Microscopic evidence for microbial dissolution of smectite." *Clays and Clay Minerals* 51, no. 5 (2003): 502-512.
9. Drits, V. A., and A. Manceau. "A model for the mechanism of Fe3+ to Fe2+ reduction in dioctahedral smectites." *Clays and Clay Minerals* 48, no. 2 (2000): 185-195.

10. Edelman, CH T., and J. Ch L. Favejee. "On the crystal structure of montmorillonite and halloysite." *Zeitschrift für Kristallographie-Crystalline Materials* 102, no. 1-6 (1940): 417-431.
11. Eggleton, R. A. "Nontronite: chemistry and X-ray diffraction." *Clay Minerals* 12, no. 3 (1977): 181-194.
12. Farmer, Victor Colin. *Infrared spectra of minerals*. Mineralogical society, 1974.
13. Fialips, Claire-Isabelle, Dongfang Huo, Laibin Yan, Jun Wu, and Joseph W. Stucki. "Infrared study of reduced and reduced-reoxidized ferruginous smectite." *Clays and Clay minerals* 50, no. 4 (2002): 455-469.
14. Frost, Ray L., Oliver B. Locos, Huada Ruan, and J. Theo Kloprogge. "Near-infrared and mid-infrared spectroscopic study of sepiolites and palygorskites." *Vibrational Spectroscopy* 27, no. 1 (2001): 1-13.
15. Ganguly, A. K. "Base Exchange Capacity of Silica and Silicate Minerals." *The Journal of Physical Chemistry* 55, no. 9 (1951): 1417-1428.
16. Garrels, Robert M., and Fred T. MacKenzie. "A quantitative model for the sedimentary rock cycle." *Marine Chemistry* 1, no. 1 (1972): 27-41.
17. Gates, Will, J. Theo Kloprogge, Jana Madejova, and Faïza Bergaya. *Infrared and Raman spectroscopies of clay minerals*. Elsevier, 2017.
18. Gates, Will. "Infrared spectroscopy and the chemistry of dioctahedral smectites." *The Application of Vibrational Spectroscopy to Clay Minerals and Layered Double Hydroxides* (2005): 126-168.
19. Gaudette, H. E., J. L. Eades, and R. E. Grim. "The nature of illite: Clays and clay minerals." In *Proc. of the 13th Natl. Conf. on Clays and Clay Minerals*, pp. 33-49. 1965.
20. Gorski, Christopher A., Laura E. Klüpfel, Andreas Voegelin, Michael Sander, and Thomas B. Hofstetter. "Redox properties of structural Fe in clay minerals: 3. Relationships between smectite redox and structural properties." *Environmental science & technology* 47, no. 23 (2013): 13477-13485.
21. Grim, R. E., J. E. Lamar, and W. F. Bradley. "The clay minerals in Illinois limestones and dolomites." *The Journal of Geology* 45, no. 8 (1937): 829-843.
22. Grim, Ralph Early, Roger Hammond Bray, and William Frank Bradley. "The mica in argillaceous sediments." *American Mineralogist: Journal of Earth and Planetary Materials* 22, no. 7 (1937): 813-829.
23. Grim, Ralph Early. "Applied clay mineralogy." (1962).

24. Halitim, Amor, Michel Robert, Daniel Tessier, and René Prost. "Influence des cations échangeables (Na+, Ca++, Mg++) et de la concentration saline sur le comportement physique (rétention en eau, conductivité hydraulique) de la montmorillonite." *Agronomie* 4, no. 5 (1984): 451-459.
25. Hauser, Ernst A. "Colloid chemistry of clays." *Chemical reviews* 37, no. 2 (1945): 287-321.
26. Hendricks, Sterling B., and Lyle T. Alexander. "A qualitative color test for the montmorillonite type of clay minerals." *Journal of the American Society of Agronomy* 32 (1940): 455-458.
27. Hendricks, Sterling B., and Merrill E. Jefferson. "Structures of kaolin and talc-pyrophyllite hydrates and their bearing on water sorption of the clays." *American Mineralogist: Journal of Earth and Planetary Materials* 23, no. 12 (1938): 863-875.
28. Hofmann U, Endell K, Wilm D (1933) Kristallstruktur und quellung von montmorillonit. (Das tonmineral der bentonittone). Zeitschrift für Kristallographie 86: 340-348
29. Hofmann, U. "„and Bilke." *W „Kolloid* 77 (1936): 238-51.
30. Hower, John, and Thomas C. Mowatt. "The mineralogy of illites and mixed-layer illite/montmorillonites." *American Mineralogist: Journal of Earth and Planetary Materials* 51, no. 5-6 (1966): 825-854.
31. Huamin, Gan, Joseph W. Stucki, and George W. Bailey. "Reduction of structural iron in ferruginous smectite by free radicals." *Clays and Clay Minerals* 40, no. 6 (1992): 659-665.
32. J.M. Cases, I. Bérend, G. Besson, M. François, J.P. Uriot, F. Thomas and J.E. Poirier
33. Keeling, John L., Mark D. Raven, and Will P. Gates. "Geology and characterization of two hydrothermal nontronites from weathered metamorphic rocks at the Uley graphite mine, South Australia." *Clays and Clay Minerals* 48, no. 5 (2000): 537-548.
34. Khaled, Eid M., and Joseph W. Stucki. "Iron oxidation state effects on cation fixation in smectites." *Soil Science Society of America Journal* 55, no. 2 (1991): 550-554.
35. Kim, Changkyun, and Jeonghwan Lee. "Experimental study on the variation of relative permeability due to clay minerals in low salinity water-flooding." *Journal of Petroleum Science and Engineering* 151 (2017): 292-304.
36. Komadel, Peter, Jana Madejova, and Joseph W. Stucki. "Reduction and reoxidation of nontronite: Questions of reversibility." *Clays and Clay Minerals* 43, no. 1 (1995): 105-110.
37. Komadel, Peter, Jana Madejová, and Joseph W. Stucki. "Structural Fe (III) reduction in smectites." *Applied Clay Science* 34, no. 1-4 (2006): 88-94.

38. Komadel, Peter, Paul R. Lear, and Joseph W. Stucki. "Reduction and reoxidation of nontronite: Extent of reduction and reaction rates." *Clays and Clay Minerals* 38, no. 2 (1990): 203-208.
39. Kostka, Joel E., Jun Wu, Kenneth H. Nealson, and Joseph W. Stucki. "The impact of structural Fe (III) reduction by bacteria on the surface chemistry of smectite clay minerals." *Geochimica et Cosmochimica Acta* 63, no. 22 (1999): 3705-3713.
40. Lahav, N. T., and A. Banin. "Tactoid rearrangement and the optical density of montmorillonite suspensions during Na-Ca exchange reaction." *Journal of Colloid and Interface Science* 26, no. 2 (1968): 238-240.
41. Langmuir, 8 (1992), pp. 2730-2739
42. Lantenois, Sébastien, Bruno Lanson, Fabrice Muller, Andreas Bauer, Michel Jullien, and Alain Plançon. "Experimental study of smectite interaction with metal Fe at low temperature: 1. Smectite destabilization." *Clays and Clay Minerals* 53, no. 6 (2005): 597-612.
43. Lear, Paul R., and Joseph W. Stucki. "Effects of iron oxidation state on the specific surface area of nontronite." *Clays and Clay Minerals* 37, no. 6 (1989): 547-552.
44. Lear, Paul R., and Joseph W. Stucki. "Intervalence electron transfer and magnetic exchange in reduced nontronite." *Clays and Clay Minerals* 35, no. 5 (1987): 373-378.
45. Lear, Paul R., and Joseph W. Stucki. "Role of structural hydrogen in the reduction and reoxidation of iron in nontronite." *Clays and clay minerals* 33, no. 6 (1985): 539-545.
46. Lee, Kangwon, Joel E. Kostka, and Joseph W. Stucki. "Comparisons of structural Fe reduction in smectites by bacteria and dithionite: An infrared spectroscopic study." *Clays and Clay Minerals* 54, no. 2 (2006): 195-208.
47. Lindsay, Willard L. "Solubility and redox equilibria of iron compounds in soils." In *Iron in Soils and Clay Minerals*, pp. 37-62. Springer, Dordrecht, 1988.
48. Madejová, J., W. P. Gates, and S. Petit. "IR spectra of clay minerals." In *Developments in clay science*, vol. 8, pp. 107-149. Elsevier, 2017.
49. Madejova, Jana, and Peter Komadel. "Baseline studies of the clay minerals society source clays: infrared methods." *Clays and clay minerals* 49, no. 5 (2001): 410-432.
50. Malathi, N., and Saraswat IP. "Mössbaur Studies of Iron in Illite and Montmorillonite." *Journal of the Physical Society of Japan* 26, no. 3 (1969): 680-683.
51. Matson, Ernest A., Mark M. Brinson, D. Dawn Cahoon, and Graham J. Davis. *Biogeochemistry of the sediments of the Pamlico and Neuse River estuaries, North Carolina*. Water Resources Research Institute of the University of North Carolina, 1983.

52. Meijer, E. L., and Leendert van der Plas. *Relative stabilities of soil minerals*. No. 80-16. Veenman, 1980.
53. Mering, J. "On the hydration of montmorillonite." *Transactions of the Faraday Society* 42 (1946): B205-B219.
54. Mukherjee, Swapna. "Clays and their Constituents–Definitions and a Brief Overview." *The Science of Clays* (2013): 3-22.
55. Murray, Haydn H. *Applied clay mineralogy: occurrences, processing and applications of kaolins, bentonites, palygorskitesepiolite, and common clays*. Elsevier, 2006.
56. Ndzana, Georges Martial, Li Huang, Jin Bo Wang, and Zhi Yi Zhang. "Characteristics of clay minerals in soil particles from an argillic horizon of Alfisol in central China." *Applied Clay Science* 151 (2018): 148-156.
57. NELSON, B. W. "The Illites from Some Northern Ohio Shales", Clays and Clay Minerals, 4th Conf., Nat'l Acad. Sci.-Nat'l Res. Council. Pub. 456, 116,(1956).
58. Neumann, Anke, Sabine Petit, and Thomas B. Hofstetter. "Evaluation of redox-active iron sites in smectites using middle and near infrared spectroscopy." *Geochimica et Cosmochimica Acta* 75, no. 9 (2011): 2336-2355.
59. Petit, S. "Fourier transform infrared spectroscopy." *Developments in Clay Science* 1 (2006): 909-918.
60. Mooney, R. W., A. G. Keenan, and L. A. Wood. "Adsorption of water vapor by Montmorillonite. I. Heat of desorption and application of BET theory1." Journal of the American Chemical Society 74, no. 6 (1952): 1367-1371
61. Ribeiro, Fabiana R., José D. Fabris, Joel E. Kostka, Peter Komadel, and Joseph W. Stucki. "Comparisons of structural iron reduction in smectites by bacteria and dithionite: II. A variable-temperature Mössbauer spectroscopic study of Garfield nontronite." *Pure and Applied Chemistry* 81, no. 8 (2009): 1499-1509.
62. Ronov, A. B., and A. A. Yaroshevsky. "Chemical composition of the earth's crust." *The Earth's crust and upper mantle* 13 (1969): 37-57.
63. Rozenson, I., and L. Heller-Kallai. "Reduction and oxidation of Fe3+ in dioctahedral smectites-1: Reduction with hydrazine and dithionite." *Clays and Clay Minerals* 24, no. 6 (1976): 271-282.
64. Salles, Fabrice, Jean-Marc Douillard, Renaud Denoyel, Olivier Bildstein, Michel Jullien, Isabelle Beurroies, and Henri Van Damme. "Hydration sequence of swelling clays: Evolutions of specific surface area and hydration energy." *Journal of colloid and interface science* 333, no. 2 (2009): 510-522.

65. Sawhney, B. L. "Selective sorption and fixation of cations by clay minerals: a review." *Clays and clay minerals* 20, no. 2 (1972): 93-100.
66. Sherman, David M., and Norma Vergo. "Optical (diffuse reflectance) and Mössbauer spectroscopic study of nontronite and related Fe-bearing smectites." *American Mineralogist* 73, no. 11-12 (1988): 1346-1354.
67. Shi, Li-Na, Yan Zhou, Zuliang Chen, Mallavarapu Megharaj, and Ravi Naidu. "Simultaneous adsorption and degradation of Zn 2+ and Cu 2+ from wastewaters using nanoscale zero-valent iron impregnated with clays." *Environmental Science and Pollution Research* 20, no. 6 (2013): 3639-3648.
68. Sibley, Duncan F., and John T. Wilband. "Chemical balance of the Earth's crust." *Geochimica et cosmochimica acta* 41, no. 4 (1977): 545-554.
69. Stucki, Joseph W. "Structural iron in smectites." In *Iron in soils and clay minerals*, pp. 625-675. Springer, Dordrecht, 1988.
70. Stucki, Joseph W., Bernard A. Goodman, and Udo Schwertmann. *Iron in soils and clay minerals*. Vol. 217. Springer Science & Business Media, 2012.
71. Stucki, Joseph W., PHILIP F. Low, Charles B. Roth, and D. C. Golden. "Effects of oxidation state of octahedral iron on clay swelling." *Clays and Clay Minerals* 32, no. 5 (1984): 357-362.
72. Suquet, H. E. L. I. E. N. E., and Henri Pezerat. "Parameters influencing layer stacking types in saponite and vermiculite: A review." *Clays and Clay Minerals* 35, no. 5 (1987): 353-362.
73. Underwood, Thomas, Valentina Erastova, and H. Chris Greenwell. "Ion adsorption at clay-mineral surfaces: the Hofmeister series for hydrated smectite minerals." *Clays and Clay Minerals* 64, no. 4 (2016): 472-487.
74. Velde, Bruce. *Introduction to clay minerals: chemistry, origins, uses and environmental significance*. Vol. 198. London: Chapman & Hall, 1992.
75. Verwey, Evert Johannes Willem, Jan Theodoor Gerard Overbeek, and K. Van Nes. *Theory of the stability of lyophobic colloids: the interaction of sol particles having an electric double layer*. Elsevier Publishing Company, 1948.
76. White, Joe L., and Allan F. Burns. "Infrared spectra of hydronium ion in micaceous minerals." *Science* 141, no. 3583 (1963): 800-801.
77. Wilson, M. J., L. Wilson, and M. V. Shaldybin. "Clay mineralogy and unconventional hydrocarbon shale reservoirs in the USA. II. Implications of predominantly illitic clays on the physico-chemical properties of shales." *Earth-Science Reviews* 158 (2016): 1-8.

78. Worden, Richard, and Sadoon Morad, eds. *Clay mineral cements in sandstones*. Vol. 19. John Wiley & Sons, 2009.
79. Yan, Laibin, and Joseph W. Stucki. "Effects of Structural Fe Oxidation State on the Coupling of Interlayer Water and Structural Si− O Stretching Vibrations in Montmorillonite." *Langmuir* 15, no. 13 (1999): 4648-4657.
80. Yan, Laibin, and Joseph W. Stucki. "Effects of Structural Fe Oxidation State on the Coupling of Interlayer Water and Structural Si− O Stretching Vibrations in Montmorillonite." *Langmuir* 15, no. 13 (1999): 4648-4657.

Chapter 3: Methods

3.1 Introduction

This chapter covers the methods, instrumentation and principles used for conducting the experiments presented in Chapters 4, 5, 6 and 7. These are divided into 4 subsections and described, each corresponding to a results chapter (Chapters 4-7). The first section covers the method for casting clay films, the microscopy methods used to measure surface roughness of the clay substrates and the additional clay purification method used to prepare clay substrates. The second covers the instrumentation used for iron clay reduction, measuring contact angles onto clay substrates and the contact angle method. The third covers the principles of infrared spectroscopy used for measuring clay hydration. The fourth covers the principles of water and nitrogen adsorption and relative humidity XRD methods used for measuring sorption of the two gas phases onto the oxidized and reduced clay minerals as well as clay swelling. The methods and instrumentation presented in Chapter 8 are not included, as those were part of a standalone development process that aimed at the creation of the microfluidic flow cell device. Therefore the respective methods and instrumentation are only included in Chapter 8.

The clay minerals used throughout the PhD work were the following: Clay minerals were purchased from the CMR, Chantilly, VA, USA. Nontronite NAu-2, illite IMt-2 and montmorillonite SCa-3 were bought in batches of 100 grams and were ground until a fine consistency was achieved. . Nontronite NAu-2 has the reported composition: SiO_2: 56.99, Al_2O_3: 3.4, Fe_2O_3: 37.42, MgO: 0.34, CaO: 2.67, Na_2O: 0.11, K_2O: 0.02, yielding a structural formula of $M^+_{0.72}[Si_{7.55}Al_{0.45}][Fe_{3.83}Mg_{0.05}]O_{20}(OH)_4$ with an octahedral Fe^{3+} speciation (Keeling et al 2000). The illite IMt-2 has a reported composition (%) of: SiO_2: 49.3, Al_2O_3: 24.25, TiO_2: 0.55, Fe_2O_3:7.32, FeO: 0.55, MnO: 0.03, MgO: 2.56, CaO: 0.43, Na_2O: 0.05 K_2O: 7.83, P_2O_5: 0.08, LOI: 8.02, with 76% Fe^{3+} and 24% Fe^{2+}, yielding a structural formula of $K_{0.7}Na_{0.01}(H_2O)_{0.42}(Al_{1.53}Fe^{2+}_{0.06}Fe^{3+}_{0.19}Mg_{0.28})_{\Sigma=2.06}(Si_{3.44}Al_{0.56})O_{10}(OH)_2$ (Nieto et al 2010). The montmorillonite SCa-3 has chemical composition as follows (%): SiO_2: 52.8 Al_2O_3: 15.7, TiO_2: 0.181, Fe_2O_3:1.06, FeO: <0.10, MnO: 0.03, MgO: 7.98, CaO: 0.95, Na_2O: 0.92, K_2O: 0.03, P_2O_5: 0.02, LOI: 21.2> STRUCTURE: (Mg 0.45 Ca 0.15 Na.26 K 0.01)[Al2.55 Fe(III)0.12, Mg 1.31 Ti.02][Si7 0.81 Al -.19]$O_20(OH)_4$, Octahedral charge:-1.29, Tetrahedral charge:-0.19, Interlayer charge:-1.48, Unbalanced charge:0.00 (CMS data, also see Chapter 7 for full quantitative XRD and fraction analysis of the samples).

3.2 Methods used for surface characterization study

Contact and non – contact surface texture measuring techniques were used order to verify the consistency and reproducibility of the method for creating the clay – glass substrates. The techniques allowed the characterization of the roughness profile of the clay substrates. Atomic Force Microscopy in the Department of Physics, Durham University, Confocal Microscopy in the Biosciences Department, Durham University and White Light interferometry at the BP Technology Center, Pangbourne UK, proved the consistency and reproducibility of the method for clay substrate preparation and excluded surface roughness defects from being a controlling factor for later experiments. Each method is described in more detail in the following pages.

Clay purification treatment method; Clay substrates were created using both purified and non-purified clay samples. The purification was performed in Dr Anke Neumann's laboratory, in Newcastle University, at the Department of Environmental Engineering. The method was first developed by Brown et al (1956) and revised by A. Neumann.

The first phase consisted of size fractionation of the clays. For that, 15 g of clay minerals were kept in suspension in 1 L of 1 M NaCl and placed on a stir plate and stirred overnight. The suspension was then centrifuged in 250 mL Sorvall Dry – Spin centrifuge tubes (PP) in a FiberLite F14B rotor on Beckman J2 – 21M centrifuge, at 1000 rpm, 10 °C for 15 minutes (Figure 3.1). The clear supernatant was decanted and the remaining solids were re – suspended in 1 L DI water. The new solution was stirred overnight.

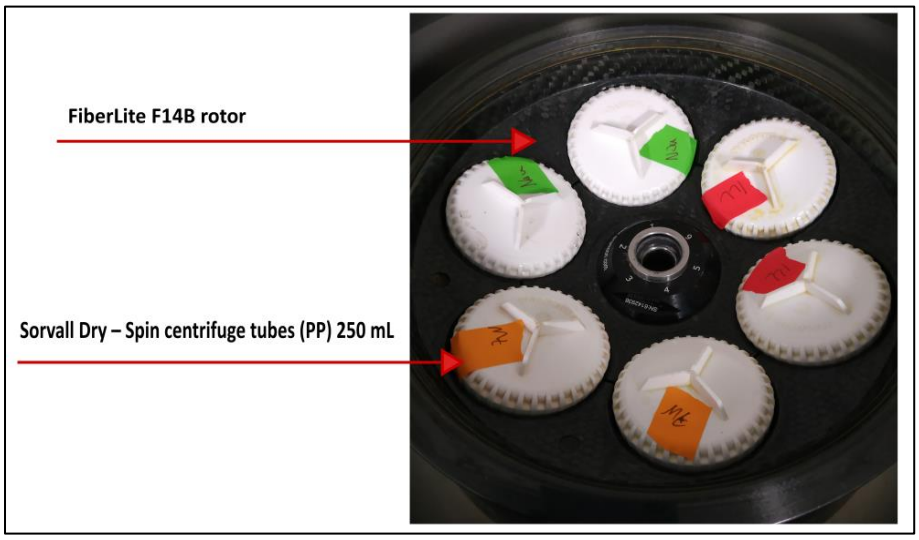

Figure 3.1. 250 mL Sorvall Dry – Spin centrifuge tubes (PP) in a FiberLite F14B rotor on Beckman J2 – 21M centrifuge.

Corning centrifuge tubes (PP) of 250 mL were filled with the solution to the 125 mL mark and are then centrifuged in a Beckman GPKR centrifuge swing bucket rotor. Centrifuging happened at 500 rpm, 16 °C for 8.5 minutes. After centrifuging the solution, the sediment was above 2 µm and the supernatant contained the less than 2 µm fraction of the clay. Depending on the amount of sediment it might be useful to be re – suspended in DI water overnight and then centrifuge again inside the Corning centrifuge tubes at the same conditions. This step was optional.

The remaining supernatant was then centrifuged in 250 mL Corning centrifuge tubes (PP) that were filled with the solution to the 125 mL mark, in a Beckman GPKR centrifuge swing bucket rotor. Centrifuging happens at 2000 rom, 16 °C for 8.5 minutes. The remaining sediment is now 0.5 – 2 µm in size fraction and the supernatant contains less than 0.5 µm fraction. Re – suspension of sediment in DI water over night and centrifugation might be necessary, depending on the remaining sediment.

The centrifugation speed and the duration of centrifugation was calculated based on the following mathematical relationship:

$$T_m = \frac{6.3*10^9*\eta\ log_{10}\left[\frac{R}{S}\right]}{N^2 D^2 \Delta s}, \quad (3.1)$$

where T_m is sedimentation time, n is the viscosity (measured in poise and temperature dependent), R is the distance from the axis of rotation to the top of suspension, N is the

revolutions per minute (rpm), D is the clay particle diameter (µm) and Δs is the difference is density between solvated particle and suspension liquid (2.65 g/cm^3 and 0.999 g/cm^3 respectively).

The second phase of clay treatment consisted of homo – ionization. Into the clay suspension, 58.44 g of NaCl were added and stirred overnight. The suspension was then centrifuged in 250 mL Sorvall Dry – Spin centrifuge tubes in a FiberLite F14B rotor on a Beckman J2 – 21 M centrifuge at 1000 rpm and at 10 °C for 15 minutes. The supernatant was then decanted. The remaining solids were re – suspended 2 times in 1 L 1 M NaCl and stirring over night as well as centrifuging was repeated. The solids were re – suspended again for another two times in 1 l DI water and then centrifuged inside the Sorval Dry – Spin centrifuge tubes.

The third and final phase of the treatment process consisted of the purification of clay minerals. The clay solids from the previous phase were re – suspended in 1 L of DI water and stirred overnight. The suspension was then centrifuged in 250 Ml Sorvall Dry – Spin centrifuge tubes (PP) at speed of 8000 rpm, at 10 °C for 5 minutes. The supernatant was then saved and the solids were re –suspended in a small volume of DI water. Centrifugation and re – suspension steps were repeated 2 to 3 times until the supernatant and solids had the same color. The remaining fraction of the solid clay represented the purified fraction of the clay.

In order to remove solids, DI water was added to to make the volume up to 1 L and the solution was kept in suspension overnight. The steps of centrifugation and visual checking of the solid and liquid phase were repeated until the solid was fully free of impurities (white or red streaks in the sediments), while the supernatant was kept separate from the cleaned fraction. The clean fraction was centrifuged in 250 mL Sorvall Dry – Spin centrifuge tubes (PP) in a FIberLite F14B rotor on the Beckman J2 -21M centrifuge at 12000 rpm, at 10 °C for 60 minutes and the supernatant saved.

The solids were scraped into small plastic culture dishes that had a diameter of 10 cm and were freeze – dried overnight after being sealed with ParaFilm®. The solids were afterwards pulverized in an agate mortar and kept in a plastic bottle that was well sealed and dry.

The various clay minerals behaved differently when they underwent purification process. The amount of clay fraction that was left at the end of purification varied, thus different clay minerals had to undergo the process for a different amount of times until enough material was accumulated for further use. It was shown that NAu2 and SCa3 produced the most amount of purified clay whereas IMt2 produced the least, making the accumulation of enough material difficult as the process had to be repeated many times (Figure 3.2).

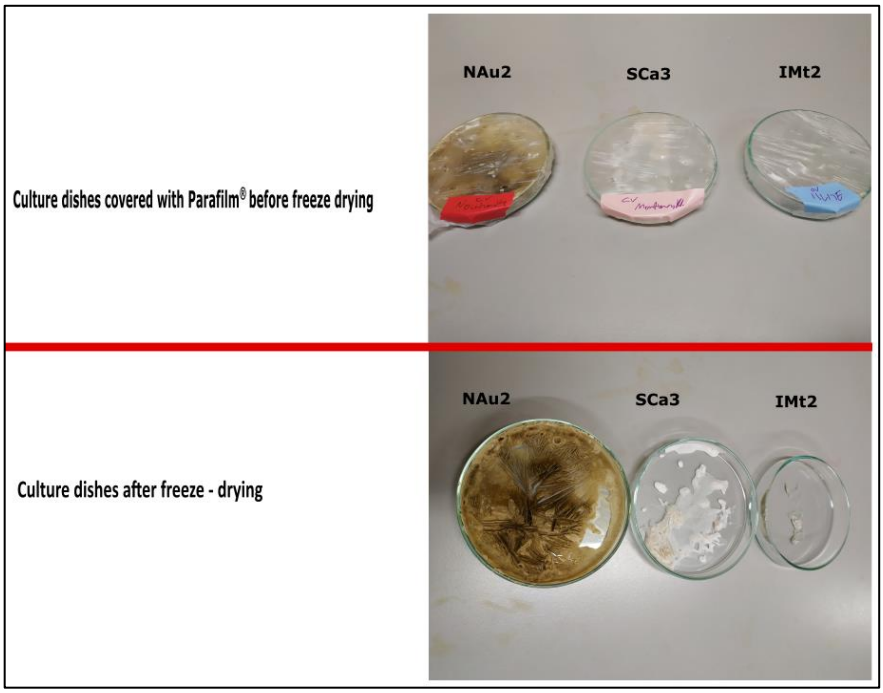

Figure 3.2. Prepared culture dishes containing fully treated clays before and after freeze – drying. The total amount of residual treated clay varies significantly between NAu2, SCa3 and IMt2 clay minerals.

3.3 Measuring surface roughness of clay substrates

Surface roughness of the clay films was measured by means of contact and non-contact measurements to prove the validity as well as the reproducibility of the method. Once consistency among the roughness profiles of the clay substrates was proven, these were used for follow on wettability experiments (Chapter 5).

1.Atomic force microscopy; The first method for studying the surface texture of the clay substrates was the Bruker Multimode atomic force microscopy (AFM) equipped with a Nanoscope V controller, at Durham University, Department of Physics. Data gained were processed with the JPKSPM Data Processing software.

AFM is a contact based technique that can be used to assess the roughness of a surface by mapping its topography, using a tip that is attached to a cantilever. The AFM is different from the optical microscopy in that it does not require the use of lenses or a light source. This technique

only uses a tip that can perform various moves on different modes. The resolution is typically 30 µm in the x, y and z axis. Essentially, the AFM measures the force between the sample and the tip (Fig 3.3). The deflection emitted from the cantilever during scanning is measured and a three – dimensional image of the sample can be constructed based on the emission. In order for the deflection to be converted into an image, signals from the detector are put together to calculate the signal emitted by the deflection. Ultimately a three – dimensional topographic map of the surface can be created (Johnson et al 2009).

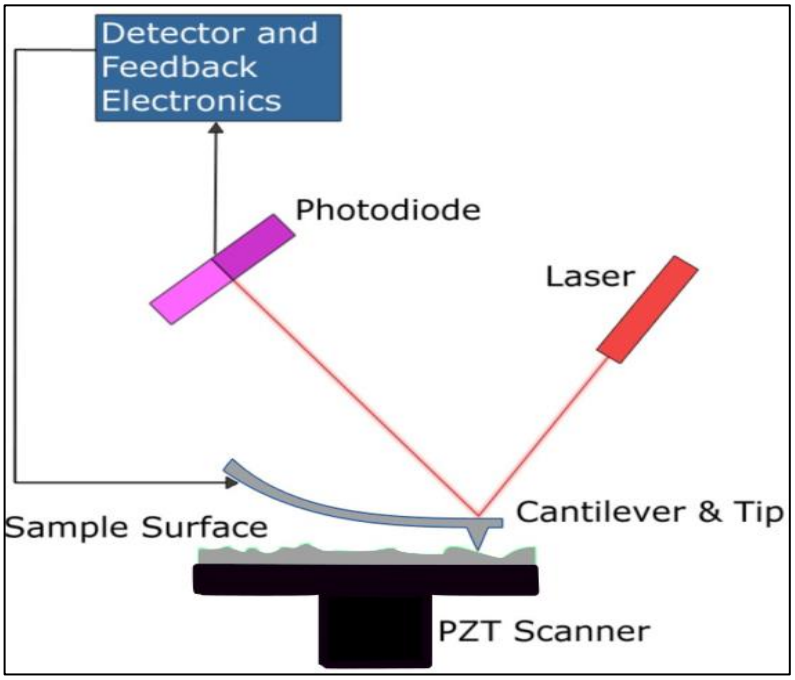

Figure 3.3. Setting of the AFM's photodiodes; the laser spot position can be calculated in two directions (Cubillas and Anderson, 2014, modified).

The AFM offers three options of scanning mode; contact mode, non – contact mode and tapping mode (Hansma et al 1993, also see Fig. 3.4). For the purposes of this study, two modes were used to measure roughness; constant force mode and quantitative imaging (QI mode). In Contact mode of operation the cantilever deflection under scanning reflects repulsive force acting upon the tip. The tip moves while touching the surface. Adjustments to the height of the cantilever can be made during contact mode. If the height of the cantilever remains unchanged during the scan, then the imaging performed is called constant height. The degree of deflection of the cantilever is controlled by the setpoint value – low setpoint value, means a low imaging force. The height

position is updated based on a time constant and the proportional gain value. Both values are responsible for the speed in which the system responds to the changes in the height.

Quantitative Imaging mode is based on force spectroscopy imaging. It allows for the measuring of height and adhesion and mechanical properties by recording a force distance curve for every pixel of an image. The tip performs a series of approaches and retractions to create the distance curve. Surfaces that can change due to a contact force mode due to stickiness or relative softness, are more suitable for the use of the QI, since there is no lateral forces during the movement of the cantilever. The main difference between QI and constant force mapping is in the algorithm of the motion of the tip as well as the sample rate (Figure 3.4).

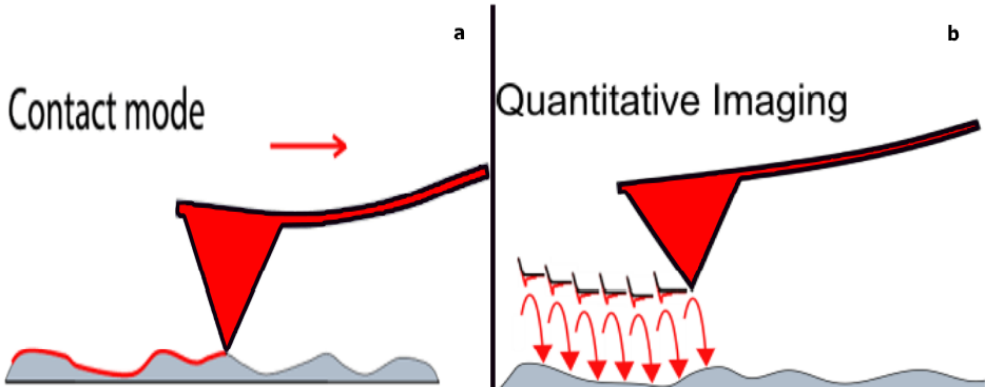

Figure 3.4. Difference in probe movement between Contact mode (a) and Quantitative Imaging (QI) (b) (images taken from JPK NanoWizard® AFM Handbook Version 6.0 and modified).

2.White Light Interferometry; The second technique used to measure the surface topography of the clay substrates was White Light Interferometry, using the Talysurf Coherence Correlation Interferometry (CCI) 6000 by Taylor Hobson, at the BP Technology Center, in Pangbourne UK. Data acquired were processed with the Taylor Hobson software package. The benefit that this technique provided can be attributed to the fact that there was no contact between a tip or stylus with the substrate surface, allowing for no alteration of the topography. Also, larger areas were scanned allowing for a better representation of the surface topography. The resolution is typically in the 400-1000 µm range in the x,y axis and in the 100 µm in the z axis. Samples were analyzed at Pangbourne Tehcnology center, BP, London.

White light interferometry is used as a non – contact optical technique to measure the roughness of a surface due to the long coherence length of laser light. A white laser light works as a source

that can easily help with obtaining interference fringes. By vertical – scanning of a sample in depth, a 3 D image can be produced. Various intensities can be seen when scanning along the Z – axis at a given point. The different intensities will yield a specific interference pattern that is unique for every scanned area. The height at every point can be calculated based on the peaks of visibility along the Z – axis. Therefore, a surface profile can be created based on the measured surface heights (Hariharan, P. 1996).

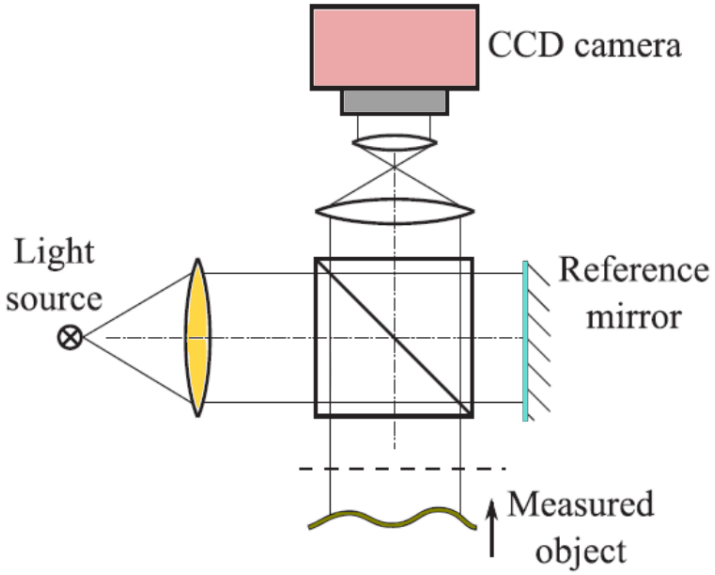

Figure 3.5. White Light Interferometer set-up. A Michelson interferometer with light source and a diode that emits light – typically LED, incandescent or superluminescent. The mounted CCD camera detects the output of the interferometer, the object measured replaces one of the mirrors, whereas the other one is used as reference that specifies the plane of reference in the object shown as a dashed line (Modified after Pavel Pavliček and Erik Mikeska 2019).

The Talysurf CCI 6000 used for roughness measurements and the creation of a 3 D profile of the surface topography of the clay substrates (Fig 3.5). The instrument has a vertical range (Z) of 100 µm (standard) 400 µm (optional) 10 mm (optional) and a vertical resolution over 100 µm range of 0.1 Å (10 pm) and noise floor of 0.5 Å (50 pm). It measures in X, Y and Z axis in an area of 360 um^2 to 7.0 mm^2 and has a number of measurement points of 1.048.576 (1024 x 1024 pixel array). It has mounted magnification lenses of × 2.5, × 5, × 10, X 20 and × 50 with a working distance (mm) of 10.3, 9.3, 7.4, 4.7 and 3.4 respectively. Also a measurement area (mm) of 7.0 × 7.0, 3.6 × 3.6, 1.8 × 1.8, 0.9 × 0.9, and 0.36 × 0.36 for each of the lenses respectively.

For the measurements the × 20 lens and a working distance of 4.7 mm were used as was proved to be the most suitable working distance for the samples at hand after trials. The scanned area had a 800 × 800 μm size in the X, Y axis. In total 4 scans per sample were performed, moving from left to the right side of the sample while keeping the distance between the scans constant at 1 mm. The samples tested were created using the same technique previously described in Section 1.3.3. NAu2, Sca3 and Imt2 batches were used for the scans. No specific preparation of the samples was necessary to perform the testing in the CCI Talysurf 6000. The samples were placed one by one at a horizontal stage and the positioning was adjusted accordingly.

Raw data were processed using the TalyMap Platinum software package to exclude noise and optimize the image. Initial 800 x 800 micron areas were zoomed to 400 × 400 microns to fit the ISO 4287 standard. Gaussian filter was applied automatically by the TalyMap Platinum software and the primary arithmetic mean deviation of the roughness profile, Ra, was calculated.

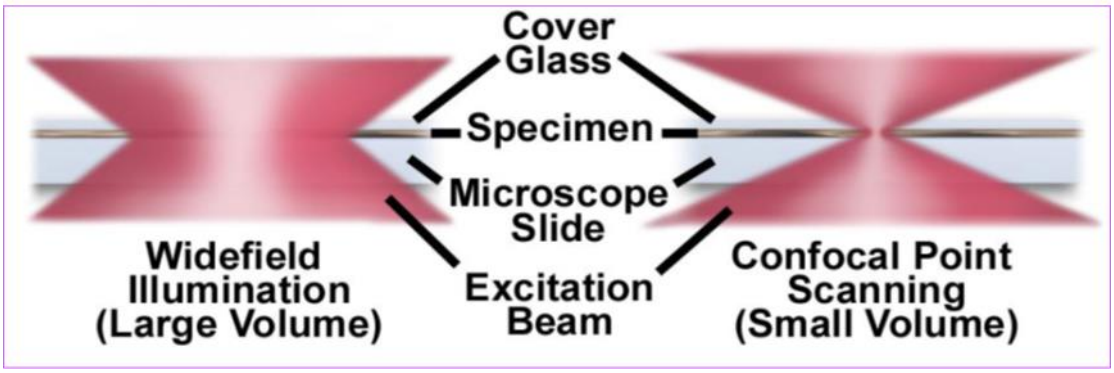

Figure 3.6. Large volume illumination seeon in typical widefield microscopy on the left; small volume illuminated seen through a single confocal point during last scanning confocal microscopy (modified after Claxton, Fellers and Davidson 2006).

3. Confocal Microscopy for characterizing surface fluorescence intensity of the clay substrates; Confocal microscopy is a method vastly used in the field of life and biological sciences for imaging biological samples such as cells and tissue. It is a non – contact technique that uses fluorescent or reflected light. Light from a light source works as an excitation beam that is focused through the microscope objective. The illumination source fills the objective rear aperture by first expanding (Fig. 3.6). Then the lens system allows it to be focused in a spot at a focal plane as seen in Figure 3.7. The illumination point range can vary in size from 0.25 to 0.8 μm and 0,5 to 1.5 μm for the highest intensity (Claxton, Fellers and Davidson 2006). The objective gathers and previews the emitted light. Through a pinhole aperture, the emitted light reaches a photomultiplier tube

located on the other side of the pinhole. Scattered light outside the focal plane is blocked by the screen (Nwaneshiudu et al 2012). The benefits of using confocal microscopy include the ability to acquire more precise and detailed images and virtual sections. Imaging a stack of planes in the Z axis helps with the creation of a more accurate 3 D profile of a sample. Samples were measured at the Department of Biosciences, at Durham University.

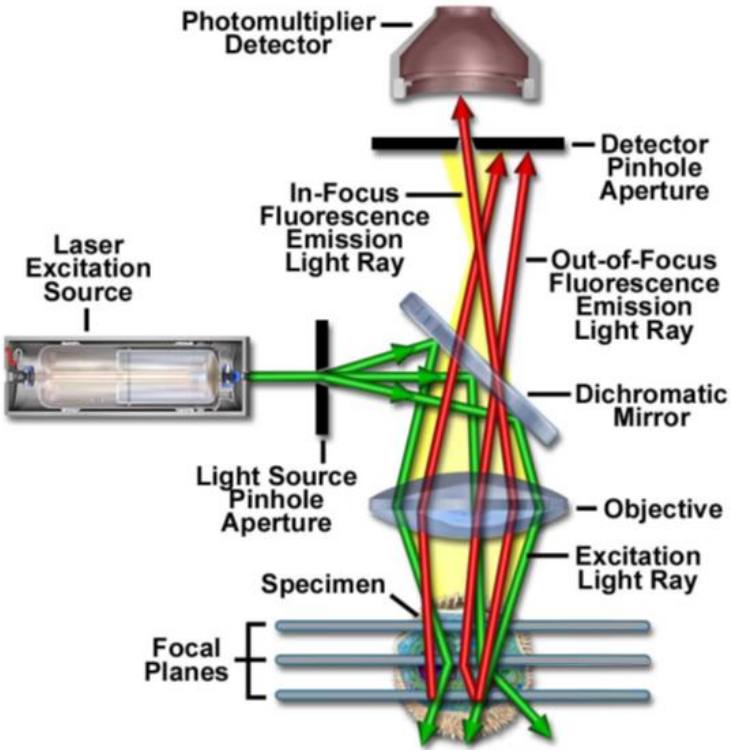

Figure 3.7. Components of a laser scanning confocal microscope during epi – fluorescent laser scanning (modified after Claxton, Fellers and Davidson 2006).

Measurements were taken using a ZEISS 800 Confocal Microscope in Airyscan mode, at Durham University, at the Department of Biosciences. This is a novel approach to measure surface texture that utilizes fluorescence intensity of a material to create the fluorescence intensity map of its surface. Data gained were processed with ImageJ and ZEN Blue Microscope software to create the fluorescence intensity profiles of the substrates.

Airyscan mode was used to scan the substrates. Its principle lies in the use of a multi – point detector that allows for quick readout tones with low noise (Fig. 3.8) The optical axis is in line with the central detector whereas the rest of the detectors are in displacement from the optical axis (Figure 3.8). The images produced by the multi – point detectors represent different phases of one confocal image. These single images are displaced against each other (Weisshart 2014).

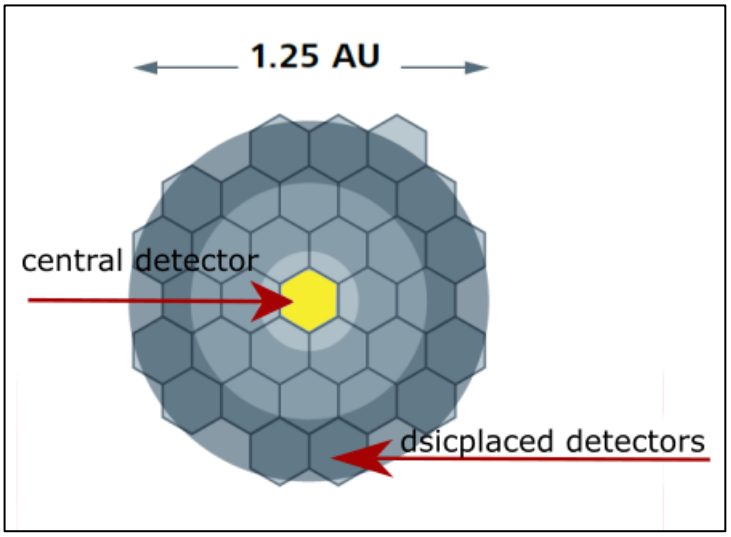

Figure (3.8). Airyscan central and displaced detectors in an eye arrangement; 1,25 Airy Units (AU) are used for higher resolution applications (Modified after Weisshart 2014).

White light interferometry*;* The first method for studying the surface texture of the clay substrates was white light interferometry, using the Talysurf Coherence Correlation Interferometry (CCI) 6000 by Taylor Hobson, at the BP Technology Center, in Pangbourne, UK. NAu-2, Sca-3 and IMt-2 substrates were made (see Section 5.2.1) and used for the scans. Data acquired were processed with the Taylor Hobson software package. The benefit that this technique provided can be attributed to the fact that there was no contact between a tip or stylus with the substrate surface, allowing for no alteration of the topography during measurements (see Section 3.2 in Chapter 3). An additional benefit arises as CCI Talysurf allowed the scanning of large areas assisting with the representation of the surface topography. For the measurements here, the × 20 objective lens and a working distance of 4.7 mm were used. The scanned area had a 800 × 800 micron size in the X, Y axis. In total 4 scans per sample were performed, moving from left to the right side of the sample while keeping the distance between the scans constant at 1 mm. The samples were placed one by one at a horizontal stage and the positioning was adjusted accordingly. Raw data were processed using the TalyMap Platinum software package to exclude noise and optimize the image. Initial 800 * 800 µm areas were zoomed to 400 * 400 microns to fit the ISO 4287 standard. Gaussian filter was applied automatically by the TalyMap Platinum software and the primary arithmetic mean deviation of the roughness profile, Ra, was calculated.

Atomic force microscopy*;* The second technique used to measure the surface topography of the clay substrates was the Bruker Multimode AFM equipped with a Nanoscopic V controller, in Durham University, in the Department of Physics under the supervision of Dr. Pablo Cubillas. Data gained were processed with the JPKSPM Data Processing software. Batches of three clay substrates were prepared for each mineral. Nine 30 × 30 µm areas in the x, y axis for every clay coated glass slide sample were scanned. To create an accurate roughness map of the area, the surface of the clay-coated films were marked using aT5482 Deluxe diamond scribing pen. Three areas on each sample were marked and the distance between areas was kept at approximately 1 cm. The scanning started by placing the sample under the Bruker Multimode AFM microscope and taking three measurements along every diamond mark on the sides of the sample.

Nontronite NAu-2 and montmorillonite SCa-3 substrates were scanned using constant force mode in 512 × 512 pixel images, with a pixel ratio of 1:1. Scan speed (line rate) was kept constant throughout the measurements. The scans were at a line rate between 0.2 to 0.4 Hz; 0.3 Hz on average. The half scan time was kept constant at 1.497 seconds and the tip velocity at 20.03 µm/s. Total time for a complete image scan was 28.44 minutes. Quantitative Mode was used for the IMt-2 samples, due to the sensitivity of their surface texture to the tip of the cantilever shown during constant force mode. An initial trial using constant force mode resulted in movement of material on the surface of the IMt-2 samples, altering the topography of the coated substrate, making it impossible to take accurate measurements. Nine 30 × 30 micron scans with a resolution of 256 × 256 pixels and a 1:1 pixel ratio were performed in Quantitative Imaging (QI) mode. The Z length was at approximately 500 nm and the set point around 0.40 V. The Z range for the QI measurements was kept between 0 and 6.5 µm with an average value of 4 nm. The total time for a complete image scan was approximately 21 minutes.

Confocal microscopy*;*

The third method for measuring surface texture was using a ZEISS 800 Confocal Microscope used in Airyscan mode (see Chapter 3), at Durham University, at the Department of Biosciences. This was a novel approach to measure surface texture that utilizes fluorescence intensity of a material to create the fluorescence intensity map of its surface. Data gained were processed with ImageJ and ZEN Blue Microscope software to create the fluorescence intensity profiles of the substrates.

Airyscan mode was used to scan the substrates. Twelve 50 × 50 micron areas in the X-Y axis on the NAu-2, IMt-2 and SCa-3 substrates were scanned. The Z – stack consisted of 48 slices at a height of 17.86 µm, for NAu-2 and IMt-2 19 µm for SCa-3 respectively. Image size was 682 × 682 pixels and the scaled image size was 50.771 × 50.71 µm. Bit depth was at 8 Bit. The microscope was an

Axio Imager Z2 with a Plan – Apochromat 20× / 0.8 M27 objective lens. The excitation wavelength was 493 nm and the emission wavelength was at 517 nm. No reflector was used. The contrast method was fluorescence, with a pinhole adjusted at 5.00 AU / 181 µm. The laser wavelength was calibrated at 488 nm: 2.00%, with an enabled laser blanking and a frame scan mode. The scan zoom was kept at 6.3, with 0 rotation. Pixel time was at 3.10 µs, line time at 2.48 ms and frame time at 1.69 s. For the imaging, the Airyscan device was used, with a director type GaAsP-PMT, detector gain 897 V, 0 detector offset and 1.0 detector digital gain.

3.4 Methods used for clay wettability study of oxidized and reduced iron clays

1.1 XRD analysis: For bulk (whole sample) quantitative analysis samples were wet ground for 12 minutes (in ethanol or water) in a McCrone mill and spray dried to produce random powder specimens (Hillier, 1999). X-ray powder diffraction (XRPD) patterns are typically recorded over a range of 65°2θ or more using either Cu or Co radiation, the actual range being instrument dependent is given on the scans. Quantitative analysis was made by a normalised full pattern reference intensity ratio (RIR) method as described in Omotoso et al (2006) and Butler and Hillier (2021). Unless stated otherwise, expanded uncertainty using a coverage factor of 2, (i.e. 95% confidence) was given by ± X0.35, where X = concentration in wt%, (e.g. 30 wt.% ±3.3) (Hillier 2003). Note also, that for phases present at the trace level (<1%) there may also be uncertainty as to whether or not the phase is truly present in the sample. This is both phase and sample dependent. It arose because at trace concentrations identification is often based on the presence of a single peak and the judgement of the analyst in assigning that peak to a likely mineral or phase.

For semi-quantitative analysis of clay minerals based on their basal reflections, clay fractions of <2 µm were obtained by timed sedimentation, prepared as oriented mounts using the filter peel transfer technique and scanned from near 2 or 3°2θ to 45°2θ using either Cu or Co radiation, the actual range being instrument dependent is given on the scans. Typically, three scans are made, one in the air-dried state, one after glycolation, and one after heating to 300°C for one hour. Clay minerals identified were quantified using a mineral intensity factor approach based on calculated XRPD patterns (Hillier et al 2003). Unless otherwise stated, for clay minerals present in amounts >10 wt% uncertainty is estimated as better than ±5wt% at the 95% confidence level.

1.2 RH-XRD method: X-ray powder diffraction patterns were produced at the James Hutton Institute, Craigiebuckler, Aberdeen, Scotland. The patterns were recorded on a Panalytical Xpert Pro diffractometer using Fe filtered, Co Kα, radiation, and an X-celerator position sensitive

detector with active length set to 2.12°. Specimens were mounted in powder cavity holders in an Anton Paar XRK 900 reactor chamber and purged with N_2 gas at various relative humidities controlled by an external Sycos H gas humidifier. Automatic divergence and antiscatter slits were set to illuminate a constant 6mm wide area of the specimen and patterns were collected from 3-15°2Θ counting for 250 seconds per 0.017° step so that each scan took approximately 30 minutes to collect. Successive runs were made from low to high humidity, and prior to each run the specimen was equilibrated at the given relative humidity for one hour.

2.Preparation of glass slides for thin films: Glass is an excellent proxy for a real silicate rock found in sandstone reservoirs and provides an inexpensive and quick way of measuring adhesion phenomena. It also presents a flat surface for creating films on. As clay minerals are too small to look at contact angles on individual crystals, and mounting on quartz grains is impractical, a thin film needs to be formed. The method easily provides reproducible substrate materials for measuring adhesion forces that allow very high control of their surface. Microscope glass slides (Thermo Scientific), of a size 76 mm by 26 mm, thickness 1.0 to 1.2 mm and plain finish were prepared using the following method: repeatedly washed with deionized water, dried by hand and then washed with acetone three times. This process purified the surface of the glass by removing any excess of dust or other surface impurities that may have been detrimental to glass coating. Insufficient coating can occur when the surface is not thoroughly cleaned to allow sufficient surface activation. Inadequately altering the surface chemistry of the glass can lead to weak charges on the surface of the glass that are incapable of bridging the different materials (clay and glass). Therefore it is possible that when subsequentlty put in contact with another solution, such as contact angle measurements, the clay material will be easily dispersed.

3.Preparing clay mineral dispersions: Clay powders was weighed using a Kern Analytical Balance scale and 0.3 g of ground clay minerals were added to glass screw neck specimen bottles (Fisher Scientific) that have a volume of 28 mL, a height of 96 mm and a metric outer diameter of 23 mm. Once the clay was placed inside the vial, 28 mL of purified water (~17 Ω) was added to the vial until the brim was reached (Figure 3.9.c). The vial was then shaken by hand to create a relatively homogeneous mixture of clay and water. The vial was then placed inside a sonicator, Fisher Scientific FB-120, with an amplitude of 20 kHZ and was sonicated for 45 minutes to maximize homogeneity.

4.Casting thin films: After 45 minutes, the vial was taken out of the sonicator and the homogenized solution was placed inside a Falcon 50mL Conical Centrifuge Tube (Fisher Scientific) along with the prepared glass slides. The centrifuge tubes were then placed inside a Panasonic Electric Oven, of an effective capacity 97 L, a rated voltage of AC 230 V and a rated frequency of 50 Hz, at 70 °C for approximately 48 hours, or until fully dry. The clay substrates are shown in Figure 3.9.d. The films were created at the Department of Chemistry, at Durham University.

5.Calculation of sodium dithionite for applying iron clay reduction method; For the reduction of structural iron in NAu2 the amount of sodium dithionite is calculated based on the following: The amount of iron is first converted into mMol/g by dividing 23 wt % by 100 and by 55.845 amu – the atomic weight of iron. The derived value is converted to mMol after multiplied by 1000. A reaction with dithionite gives away two electrons. Every Fe^{+3} takes up one electron every time the reaction takes place. Therefore for any reduction, half of dithionite per Fe^{+3} cation in the reaction is needed. The derived value is divided by 2 and multiplied by the percentage of the desired reduction extent. The amount of sodium dithionite needed for reducing structural iron in IMt2 was similarly calculated.

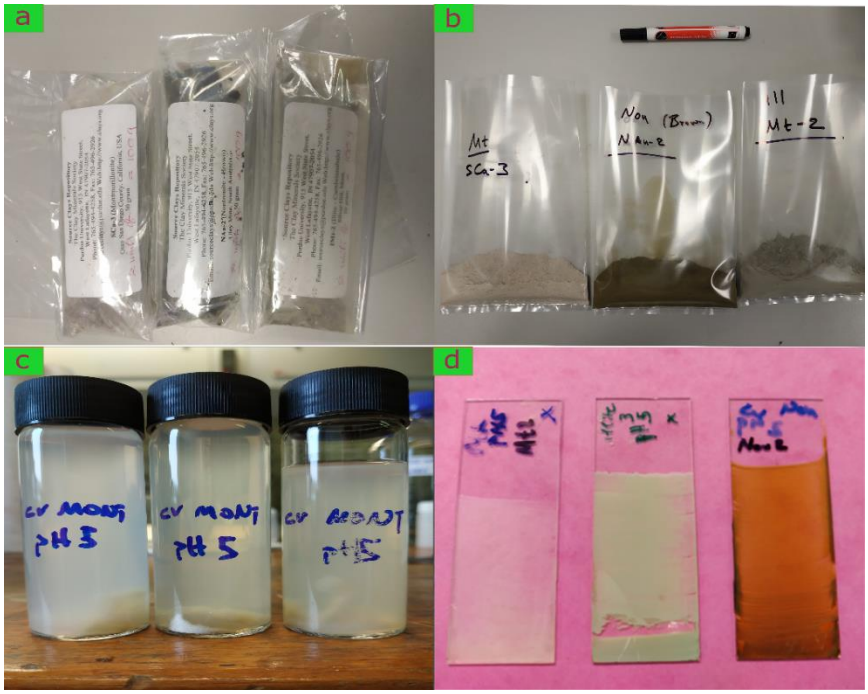

Figure 3.9. Sourced clays from the CMR (a), ground clays (b), montmorillonite clay suspensions before sonication (c), clay films (d).

Chemical reduction of iron clay minerals by sodium dithionite method; To reduce the structural iron in clays the following were placed inside the glovebox: 500 mL glass bottles with a magnetic stirrer bar, 1 g of powdered clay mineral, 1.32 g sodium citrate with a molecular weight of 258.07 g/mol and 9.24 g of sodium bicarbonate with a molecular weight of 84.007 g/mol, that were used as buffers to prevent producing acidity that could affect the clay surface. Also, a bottle of 1 L of de – oxygenated de – ionized water, a stirrer plate with heating function and a thermometer. Finally, two 250 mL centrifuge tubes with o – rings, Teflon PTFE tape and an empty 1 L glass for aqueous waste.

The reducing agent used is sodium dithionite (174.107 g/mol) (Sigma Aldrich). The amount of reducing agent used varied according to the desired degree of reduction; 40 mg (2.2 mmol) of sodium dithionite reduced 0.46 mmol of iron according to a 1:2 stoichiometry. For further reduction, the amount of sodium dithionite was increased according to the 1:2 stoichiometry. For a full reduction, the amount of sodium dithionite necessary equalled three times the mass of the clay mineral.

Once the amount of dithionite needed was calculated in mmol, the value was converted to mols when divided by 1000 and multiplied by 174.1 g, which is the atomic mass number of dithionite, to give the final value in mg. That value represented the amount of dithionite needed to reduce one gram of iron bearing clay by a desired percentage. In the case of clay films, 0.3 g of clay coat the glass slides, therefore any derived dithionite value was multiplied by 0.3 to calculate the final amount of dithionite in mg needed. Based on those calculations, the amount of sodium dithionite used for NAu2 partial reduction (30%) was 0.172 g – considering minor impurities of the non–size fractionated NAu2, for 1 g of clay and 0.053 g for 0.3 g of clay. Similarly, sodium dithionite for IMt2 was calculated to be 0.054 g for 1 g of clay and 0.0162 g for 0.3 g of clay.

Clay reduction method was divided in steps are as follows: 500 mL DI water was added to the solids in the 500 mL glass bottle, then with a stirrer the solution was kept in suspension overnight to create a homogenous mixture. Once homogenization was achieved, the hot plate was turned on and the 500 mL bottle was placed on top. The temperature of the suspension was monitored with a thermometer. Once the temperature reached 70 °C, sodium dithionite was added to the suspension. The suspension was then stirred for 2 to 4 hours at 70 °C and then transferred into the 250 mL centrifuge tubes. The bottles were then sealed with Teflon PTFE tape and centrifuged at 10000 rpm for 10 minutes at 10 °C. Afterwards, the centrifuge tubes were transferred back into the glovebox. The solids were put inside the 1 M NaCl solution bottle and were re –suspended

overnight. The suspension was centrifuged again at 10000 rpm, for 10 minutes at 10 °C and the reduced solids were placed inside plastic Corning® centrifuge tubes.

Clay reduction was performed at Newcastle University, at the Department of Environmental Engineering, in Dr Anke Neumann's laboratory. The method of reduction of iron – rich clay minerals with the use of chemical reducing agent sodium dithionite described below, is an adapted version of a method suggested by Stucki et al (1984), further refined by Neumann and co – workers (2011). The reduction was performed in a four – handed anaerobic glovebox by Glovebox Systemtechnik GmbH that maintains an inert atmosphere of 100% nitrogen.

For the reduction of clay coated substrates, a modified version of the previous technique was used. The clay coated slides were put inside glass vials containing sodium citrate and sodium bicarbonate. The amount of buffers was adjusted relative to the amount of solution used. The glass films were placed inside the solution were gradually heated up to 70 °C as seen in Figure 3.10. Once the desired temperature was reached, sodium dithionite was added and the substrates were left inside the vials for 4 hours in order for the reduction to be complete. After that time the solution was discarded and the reduced glass slides remained inside the glass vials to dry overnight. The clay substrates were partially reduced to 30% and 50% as shown in Mössbauer spectra (Chapter 5). Chemical reduction was performed at Dr. Anke Neumann's laboratory, at the department of Environmental Engineering, at Newcastle University.

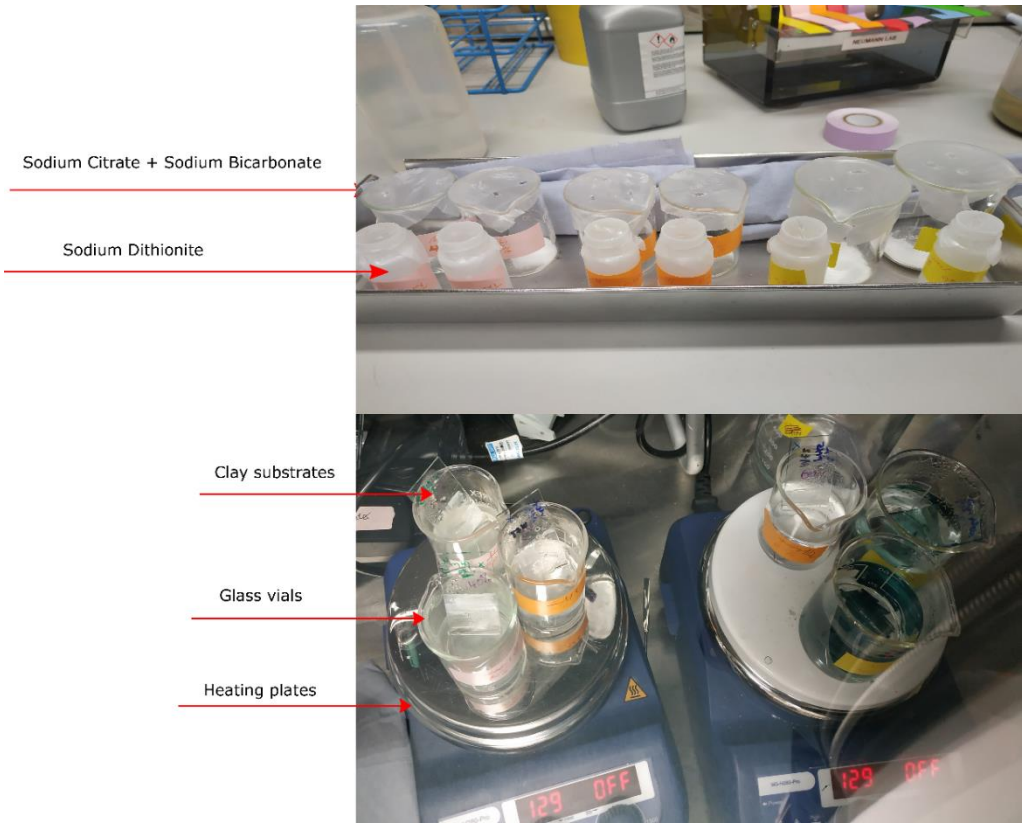

Figure 3.10 Upper half shows buffers Sodium Citrate and Sodium Bicarbonate and the reducing agent sodium dithionite, as part of sample preparation for clay substrates reduction outside the glovebox. Lower half shows clay substrates being reduced inside the glovebox; in dark blue color indicative of a reduced NAu-2.

6. Mössbauer spectroscopy. It is a nuclear spectroscopy for the adsorption of gamma rays and the recoil free emission in solids. The function of this spectroscopic method is based on the ability of atoms to vibrate, hence produce recoil-free events (Fig. 3.11). This occurs when the lowest quantize vibrational mode is higher than the recoil energy. The spectra are typically measured in transmission mode. The emitted gamma rays follow a periodic movement, successively with different velocities. Thus, the radiation is transmitted by the absorber (i.e. sample) and is recorded as the energy. In the case of phylosilicates, such as clay minerals, the spectra consist of an iron doublet for every oxidation state and for every structural site. Samples were ran at the department of Environmental Engineering, at Newcastle University.

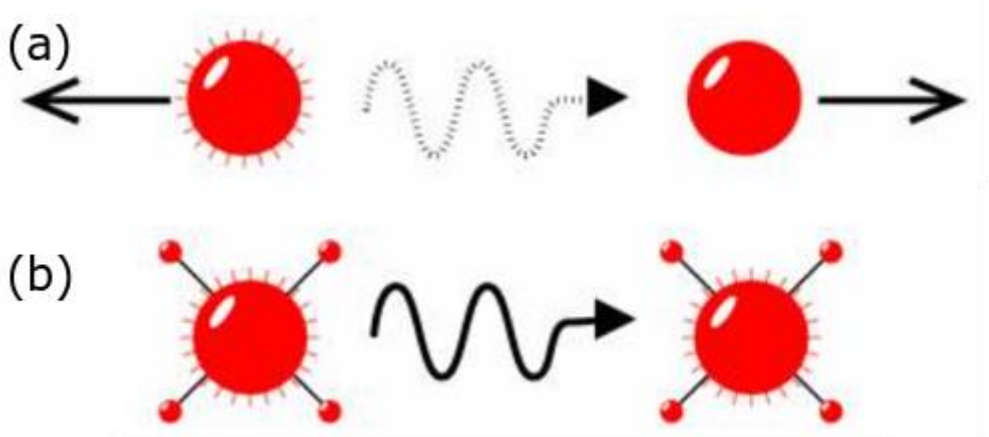

Figure 3.11 particles in recoil adsorption/emission of gamma rays (a) and emssions in crystal lattice (b).

7.Sessile Drop method; There are various methods for measuring surface tension and wettability based on contact angle measurements. The methods utilize different drops such as pendant, sessile or captive bubble. Two major forces alter the shape of the drops; these are surface tension that minimizes surface and gravitational force. The latter can flatten a sessile drop or elongate a pendant drop (Yuan and Lee 2013). Measurements were taken at Department of Chemistry, Durham University.

The sessile drop method is the simplest and most time – efficient method for measuring wettability (Fig. 3.12). To take measurements, the Ramé-Hart contact angle goniometer was used. A fixed microsyringe assembly mounted on top of a 3 – axis stage was manually used to introduce crude oil droplets. The Eppendorf™ epTIPS™ (Fischer Scientific) pipettes with a 4.6 cm length were used to introduce crude oil droplets of approximately 1 µL in volume. *Sessile drop contact angle measurement method:* A fixed microsyringe assembly mounted on top of a 3 – axis stage was manually used to introduce crude oil droplets (see Table 5.1 for gas chromatography analysis of the crude oil in chapter 5). The clay films tested were coated with NAu2 nontronites, IMt2 illites

and SCa3 montmorillonites. All substrates were partially reduced - 30% and 50% for the NAu2 and IMt2 respectively, using sodium dithionite. The SCa3 montmorillonite was used as a control mineral due to its negligible percentage of structural iron. The contact angle measurements were taken for the clay coated films and crude oil interface. The number of crude oil droplets averaged 5 per sample, both for the oxidized and the reduced samples. Oxidized samples were measured in ambient conditions, at 20 °C and 30% relative humidity. Reduced NAu2, IMt2 and SCa3 samples were measured inside a plastic portable glovebox (Lab – Bubble™), in which the entire contact angle goniometer could be housed. An anoxic environment was achieved after removing the oxygen by purging nitrogen gas into the glovebox. Oxygen levels were monitored using an oxygen sensor Gas Alert O2 by Gas Monitor Point. Several batches of clay substrates were made and tested with the sessile drop method to obtain a sufficient number of values to allow comparison. In total, 28 clay films were tested.

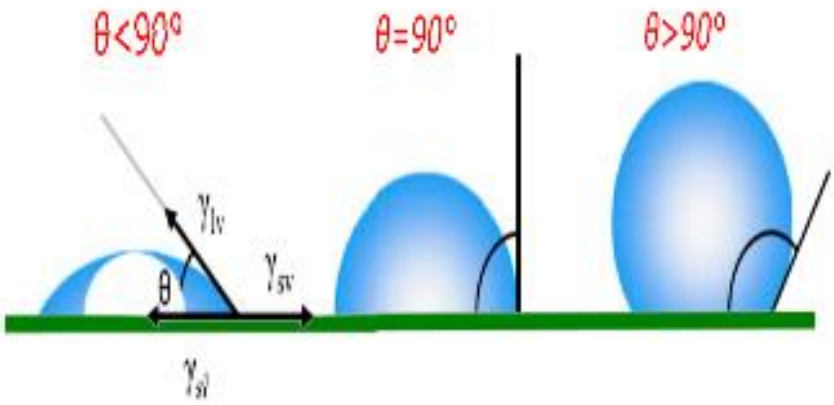

Figure 3.12. Sessile droplets of an ideal liquid in different shapes and contact angles on a smooth surface (Modified after Yuan and Lee 2013).

As indicated by Treiber and Owens (1972), to accurately measure the wettability using the sessile droplet method, a flat, homogeneous surface (i.e. quartz, calcite or clay coated substrates) is needed. When contact angle increases the wetting of the surface decreases. When the contact angle between the liquid and the solid exceeds 90°, the surface is considered hydrophobic.

8.Ramé-Hart contact angle goniometer set up and calibration. The goniometer is an instrument frequently used to measure contact angle and provides a quick and relatively inexpensive way to measure wettability. The model used for the measurements was the Ramé-Hart Model 260. The goniometer consists of the following parts: A microsyringe fixture and assembly, illuminator, a fiber bundle, a 3 – Axis stage, an optical bench, a bubble level and levelling legs, a levelling stage, a camera and a Z, X, Y axis focus. The apparatus for the experiment consists of a light source with adjustable light intensity and a computer that runs the Ramé-Hart contact angle software (Figure 3.13).

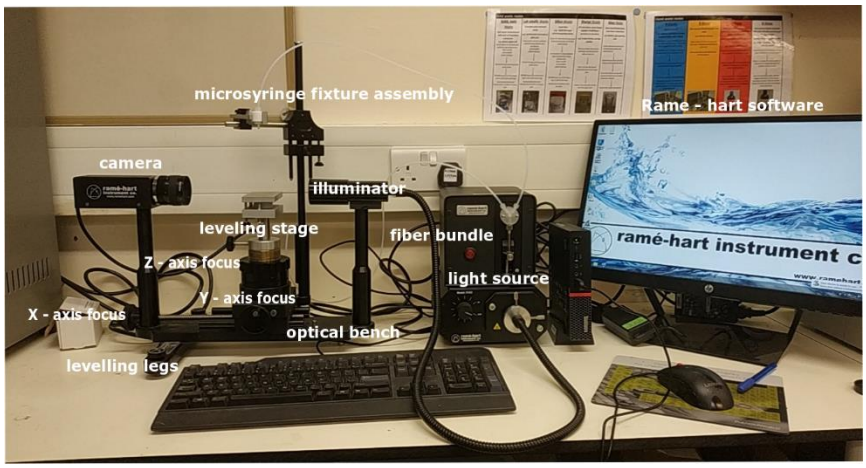

Figure 3.13. Setup of the Ramé-hart Contact Angle Goniometer.

The instrument requires calibration of the total magnification system before every run to ensure optimal settings are used for the test substrate under study. Calibration is performed by the measuring of a spherical object. Figures 3.14, 3.15 show the options for calibration.

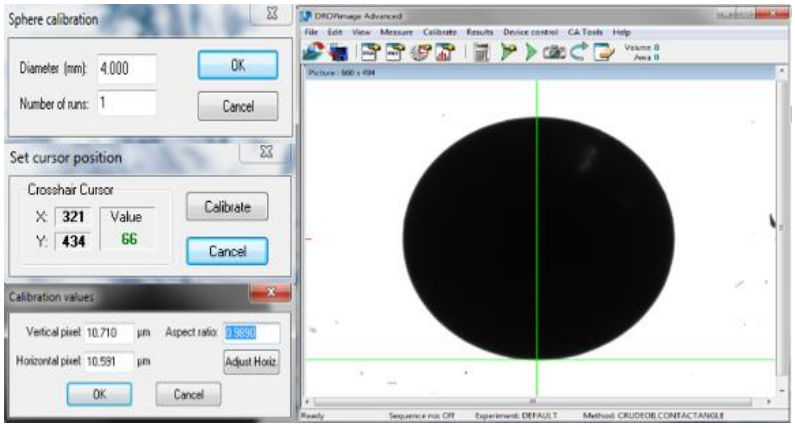

Figure 3.14. Sphere calibration software options for crude oil contact angle measurements. Green cross indicates baseline calibration. The baseline cross makes a selection of where the direction of the contact angle baseline is.

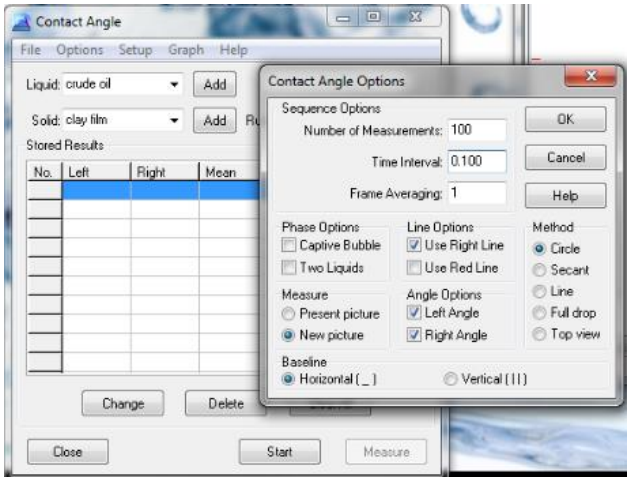

Figure 3.15. Selection of software options for contact angle measurements for the crude oil/clay film interface. Number of measurements is 100 at a time interval of 0.1 sec; elapsed time between each measurement is 0,1 sec.

3.5 Methods used for infrared spectroscopy studies

Infrared spectroscopy principle is based on analyzing the transition dipole moment. The electric dipole moment is controlled by the molecule's nuclei and location of electrons. Dipole changes are the key selection rule of IR spectra (Atkins and de Paula 2006). Infrared Spectroscopy obtains the IR spectra of the measured mineral. That is the fraction of the reflection or transmission of light intensity as a function of light frequency. The light frequency is expressed in wavenumber units (cm^{-1}) and is related to the refractive index and geometry of the mineral. IR spectroscopy studies were conducted at the Laboratory of Physical Chemistry and Microbiology for Materials and the Environment University of Lorraine (LCPME), Nancy, France, under the supervision of professor Cedric Carteret.

The IR method for studying the structural fingerprint of clay minerals is directly linked to the ability of crystals to vibrate. Any atom within a crystal has its individual position that can be defined as a vector and calculated based on the following equation:

$$\overrightarrow{R_{ak}} = \vec{R}_a + \overrightarrow{r_k} + \overrightarrow{u_{ak}}, \quad (3.2)$$

where $\overrightarrow{R_{ak}}$ is vector of the lattice, r_k is the atom's atomic coordinates and u_{ak} a displacement from a hypothesized equilibrium position (Balan and Kloprogge 2017). Each individual atom (k) can experience a force (F) that can have any direction (a) in the Cartesian coordinates system. This force can be calculated based on the equation:

$$F_{aka} = -\frac{\partial E_{pot}}{\partial R_{aka}}, \quad (3.3)$$

where E_{pot} is the system's potential energy (i.e short range and long range interactions between atoms) surface. Systems can be divided in low and high symmetry with corresponding different energies and structural fingerprints. In equilibrium conditions, the potential energy is zero. There are three types of vibration modes; stretching (υ), bending (δ) and the combination of the two (υ + δ). The different vibration modes cause various changes to the bond lengths (after stretching) and to angles (after bending). Inside a crystal lattice, the internal modes vibrate at higher frequencies, classifying as hard modes. Typical examples are the Si – O stretching at $\bar{\nu} \approx 1000$ cm^{-1} and the O – H stretching at $\bar{\nu} \approx 3600$ cm^{-1}. The hydroxyl parts of hydrous minerals vibrate at higher stretching frequencies due to the small mass of hydrogen, making them sensitive to the surroundings of the OH^- group, the strength of hydrogen bond (Ryskin, 1974) and to the substitutions of cations (Farmer 1974b; Besson and Drits, 1997a).

Specifically for the IR studies presented in Chapter 6, the MIR spectra measured corresponded to the 1400 – 3600 cm^{-1} region and to the 4200 – 7100 cm^{-1} region. Within the context of measuring

clay hydration-dehydration, emphasis was given to the vibrations and overtones of the OH^- bands (see Chapters 2, 6).

The samples were taken to the LPCME, CNRS (Centre National de la Recherche Scientifique), at the University of Lorraine, Nancy, France and were prepared for IR Spectroscopy analysis in the laboratory of professor Cedric Carteret. Further preparation of the native oxidized clay samples was not necessary. The reduced samples were first centrifuged at 1000 rpm, 20 °C for 10 minutes (LCPME, CNRS FR); the solids (reduced clay) were collected and the supernatant was discarded. The reduced clays were then placed under vacuum for 2 days until completely dry. Once the samples were dry and no presence of water was evident, they were milled by hand until their texture was fine to very – fine inside an anaerobic chamber.

IR Spectrometer; The Thermo Electron 8700 Nikolet FTIR spectrometer was used to acquire the spectra of the oxidized and reduced samples. It has a wavenumber precision of 0.01 cm^{-1}, 0.125 cm^{-1} optical resolution and peak-to-peak noise below 8.68 x 10^{-5} absorbance units. It uses a high-intensity ETC EverGlo (20 – 9600 cm^{-1}, low to high) (ThermoFischer) mid-IR source that can be computerized so that it provides options for NIR and far-IR analyses. It uses a Ge-on-KBr beamsplitter that cover a region between 350 – 7800 cm^{-1}. It has a wavenumber precision of 0.01 cm^{-1}, 0.125 cm^{-1} optical resolution and peak-to-peak noise below 8.68 x 10^{-5} absorbance units. Data processing and graphs were made using OriginLab (2019) software.

IR Spectroscopy data acquisition method: Oxidized, reduced and reduced samples were put inside the 8700 Nikolet FTIR Spectrometer's sample holder one at a time and their spectra were measured after in-situ exposure of each sample to air, vacuum and relative humidity conditions (RH%) in the following order: Air – spectra measured right after the sample was placed inside the sample holder. After the air measurement, the sample chamber was purged with nitrogen for 5 minutes using the nitrogen tank (see Figure 6.1 – chapter 6, shows the setup used for measuring the spectra). All measurements were taken at room temperature of 20 °C; no heating of the sample holder was performed.) to discard any excess of air. The sample was then put under vacuum conditions using the setup seen in Figure 6.1 and was left to equilibrate under vacuum for 30 minutes before the spectra were measured again. Measurements under different humidity conditions (RH%) were taken after resetting RH% conditions by adjusting the water and nitrogen chambers accordingly (see Figure 6.1). Before each RH% measurement, 30 minutes of equilibrium time were allowed.

For the acquisition of the NIR spectra, 35 mg of powdered clay were placed inside the IR sample holder. For the acquisition of the MIR spectra, 10 mg of clay mixed with 200 mg of KBr were milled together until homogenous and placed inside the sample holder.

3.6 Methods used for adsorption studies

1.Water vapor method; The determination of a clay's textural changes occurred by water volume sorption, is achieved with the calculation of the specific surface area (SSA). The SSA is defined as the portion of the surface area of the clay that is available to adsorb (Kuila, Prasad 2013) and is by definition in proportion with the amount of sorption of the volume of water vapor by the clay. Samples were ran at the Laboratory of Physical Chemistry and Microbiology for Materials and the Environment University of Lorraine (LCPME), Nancy, France. An increase uptake of water vapor by the clay is followed by an increase in the SSA. To calculate the SSA the following equation is used:

$$n_{ads}=n_m \frac{C_{BET}X}{(1-X)(1-(C-1)X)} \quad (3.4),$$

whereas the relative humidity (RH) is given as X, n_{ads} represents the adsorbed molecules, C_{BET} represents the energetic constant that indicates water affinity and n_m represents adsorbed molecules in the monolayer. The C_{BET} is the sorption energetic constant that expresses the heat produced due to water adsorption on the clay, calculated by the following equation:

$$C_{BET}X=\exp\left(\frac{-E_{ads}-E1}{RT}\right) \quad (3.5),$$

whereas E_{ads} represents the energy of the adsorbed water molecules and $E1$ the energy required for water liquefaction. The $-E_{ads}$-$E1$ is the difference between the enthalpy of hydration, per layer, versus the energy of free water. In the case of swelling clays, adsorption isotherms are valid only when their surface area is constant. If the surface area varies then the final isotherm is derived from adding different isotherms that correspond to various surface areas (Salles et al 2009).

1.*Nitrogen BET method*; Estimation of the SSA requires the use of gas adsorption, typically N_2, for the quantitative analysis of gas that is necessary for the creation of a monolayer and subsequently multilayer on the clay's surface. After gas injection takes place, the known area of the clay is used as reference for the measurement of the total area of the sample including the inert gas. The adsorption isotherm is generated for a range of pressures (P/P_0) at a temperature of 77 K. The

desorption isotherm is generated after measuring the volume of gas removed during gradual pressure drop.

The BET measures both the size of the pores and the surface area. When nitrogen gas is not present, no layers of inert gas are created. A layer of one molecule thick (monolayer) is expected to be formed after gas molecules are present. After nitrogen saturation has occurred, layers of multiple – molecule thickness (multilayer) are formed. The principles of the Brunauer-Emmett-Teller (BET) method are based on a previous model proposed by Langmuir (1918), used in equilibrium conditions in adsorbent – adsorbate systems to determine the kinetics relative to adsorption. The theory of the more evolved BET model is based on the following. The surface is homogeneous and lateral interactions do not occur between molecules. Moreover, adsorption energy is the same for all sites and adsorption can occur in an infinite amount of layers whereas in Langmuir's theory was only limited to one monolayer. Based on the type of material, the generated isotherms can vary in type. In general, there are five distinct types of isotherms described by Brunauer, L. Deming, E. Deming and Teller (1940) suggesting creation of mono or multi layers at different pressures and constant temperature.

The calculations of BET specific surface area require the use of the following equation:

$$\frac{1}{X[\left(\frac{P_0}{P}\right)-1]} = \frac{1}{X_m C} + \frac{C-1}{X_m C}\left(\frac{P}{P_0}\right) \quad (3.6),$$

where the weight of gas (N_2) is X, P/P_0 is the relative pressure, X_m is the weight of adsorbate and C is the BET constant. Plotting of the BET occurs as a linear plot of

$$\frac{1}{X[\left(\frac{P_0}{P}\right)-1]} \quad (3.7),$$

in the y axis and of P/P_0 in the X axis. For the plotting of the BET of the clay samples, multipoint BET, using a minimum of three data points was used. The slope *s,* the intersect *i* of the linear regression line and the weight of the monolayer X_m were calculated by the following equations:

$$= \frac{C-1}{X_m C}, \; i = \frac{1}{X_m C} \quad (3.8) \text{ and}$$

$$X_m = \frac{1}{s+i} \quad (3.9),$$

respectively. Once the BET measurement was produced for the monolayer adsorption volume, the following equation is used for the determination of the BET surface are per unit mass of the sample:

$$S_{total} = \frac{X_n N A_{cs}}{M} \quad (3.10),$$

whereas A_{cs} is the cross sectional area of the adsorbate, M is the molecular weight of the adsorbate and N the Avogadro's number. Ultimately, the SSA is calculated by dividing S_{total} by the weight of the sample *W*, using the equation:

$$S = \frac{S_{total}}{W} \quad (3.11),$$

Type I gas isotherms indicate micropores with a surface that is mainly found inside micropore structures. These types of pores fill up at early stages of gas injection and once filled, the remaining external surface available for adsorption is very little. Type II is generated when pore diameter is larger than that of micropores with inflection point appearing at the time of the creation of a monolayer. Type III isotherms are generated when the occurring interaction of adsorbate with a preexisting adsorbed layer is greater than its interaction with the surface available for adsorption. Type IV isotherms are generated when adsorption takes place inside a porous material with pore size ranging from 1.5 to 100 nm, with an increased uptake occurring as an increase in the slope at higher pressures. In this type of isotherm, the point of infection is present close to the time that the monolayer is completed. Finally, Type IV isotherms occur when there is limited interaction between the adsorbate and absorbed (Fig. 3.16).

Complete water vapour adsorption–desorption isotherms at 298 K and N_2 adsorption–desorption isotherms at 77 K were obtained using a MicrotracBEL Belsorp-Max volumetric adsorption analyzer equipped with three pressure sensors (133 kPa, 1.33 kPa and 13.3 Pa). The samples were initially outgassed at 100 °C under vacuum (~3×10^{-6} Pa) for 20 h. In the case of the water vapour isotherm, a long acquisition time (7 days per isotherm) was required because of slow hydration kinetics. The weight of the samples used for each measurement was approximately 0.15 g.

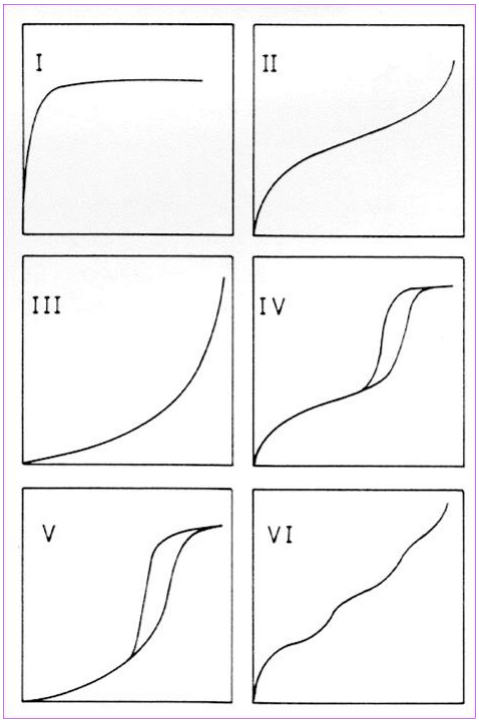

Figure 3.16. Types of isotherms generated for the sorption of a material (modified after Sing et al 1985)

A schematic representation of the apparatus of the setup for water and nitrogen is seen bellow (Fig. 3.17).

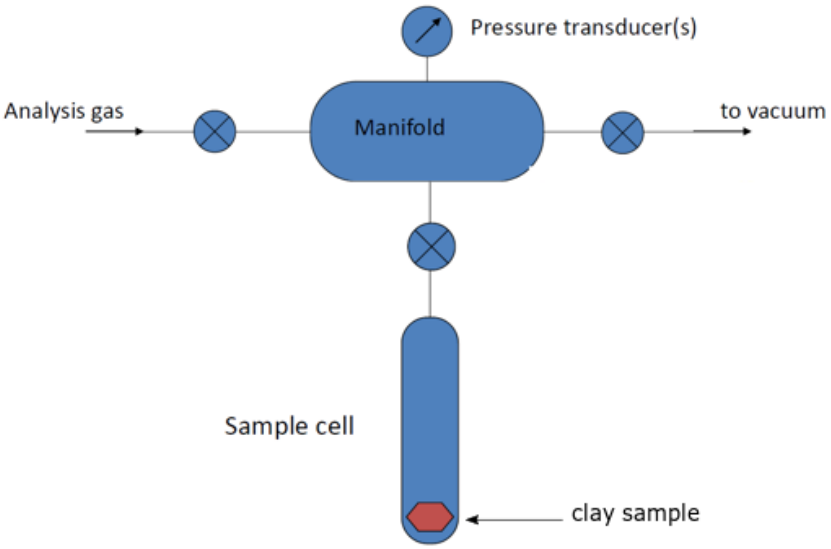

Figure 3.17. Schematic representation of the apparatus for measuring sorption of the gaseous phases, water vapor and nitrogen.

3.7 References

1. Balan, E., and J. T. Kloprogge. "Theoretical Aspects of Infrared and Raman Spectroscopies." In *Developments in Clay Science*, vol. 8, pp. 6-33. Elsevier, 2017.
2. Besson, G., and V. A. Drits. "Refined relationships between chemical composition of dioctahedral fine-grained mica minerals and their infrared spectra within the OH stretching region. Part I: Identification of the OH stretching bands." *Clays and Clay Minerals* 45, no. 2 (1997): 158-169.
3. Brown, B. E., and M. L. Jackson. "Clay mineral distribution in the Hiawatha sandy soils of northern Wisconsin." *Clays and Clay Minerals* 5, no. 1 (1956): 213-226.
4. Brunauer, Stephen, Lola S. Deming, W. Edwards Deming, and Edward Teller. "On a theory of the van der Waals adsorption of gases." *Journal of the American Chemical society* 62, no. 7 (1940): 1723-1732.
5. Butler, Benjamin M., and Stephen Hillier. "Automated full-pattern summation of X-ray powder diffraction data for high-throughput quantification of clay-bearing mixtures." *Clays and Clay Minerals* 69, no. 1 (2021): 38-51.

6. Claxton, Nathan S., Thomas J. Fellers, and Michael W. Davidson. "Laser scanning confocal microscopy." *Encyclopedia of Medical Devices and Instrumentation* 21 (2006): 1-37.
7. Engelmann, R., T. Anhut, I. Kleppe, and K. Weisshart. "Airyscanning: Evoking the full potential of confocal microscopy." *Imaging Microsc* 3 (2014): 20-21.
8. Farmer, Victor Colin. *Infrared spectra of minerals*. Mineralogical society, 1974.
9. Hansma, Helen G., Robert L. Sinsheimer, Jay Groppe, Thomas C. Bruice, Virgil Elings, Gus Gurley, Magdalena Bezanilla, Iris A. Mastrangelo, Paul VC Hough, and Paul K. Hansma. "Recent advances in atomic force microscopy of DNA." *Scanning* 15, no. 5 (1993): 2
10. Hariharan, P., and Maitreyee Roy. "Interferometric surface profiling with white light: effects of surface films." *Journal of modern optics* 43, no. 9 (1996): 1797-1800.
11. Hillier, S., M. J. Roe, J. S. Geelhoed, A. R. Fraser, J. G. Farmer, and E. Paterson. "Role of quantitative mineralogical analysis in the investigation of sites contaminated by chromite ore processing residue." *Science of the Total Environment* 308, no. 1-3 (2003): 195-210.
12. Hillier, Stephen. "Quantitative analysis of clay and other minerals in sandstones by X-ray powder diffraction (XRPD)." *Clay mineral cements in sandstones* (1999): 213-251.
13. Johnson, Daniel, Nidal Hilal, and W. Richard Bowen. "Basic principles of atomic force microscopy." In *Atomic force microscopy in process engineering*, pp. 1-30. Elsevier Ltd, 2009.
14. Kuila, Utpalendu, and Manika Prasad. "Specific surface area and pore-size distribution in clays and shales." *Geophysical Prospecting* 61, no. 2-Rock Physics for Reservoir Exploration, Characterisation and Monitoring (2013): 341-362.
15. Langmuir, Irving. "The adsorption of gases on plane surfaces of glass, mica and platinum." *Journal of the American Chemical society* 40, no. 9 (1918): 1361-1403.
16. Nwaneshiudu, Adaobi, Christiane Kuschal, Fernanda H. Sakamoto, R. Rox Anderson, Kathryn Schwarzenberger, and Roger C. Young. "Introduction to confocal microscopy." *Journal of Investigative Dermatology* 132, no. 12 (2012): 1-5.
17. Omotoso, Oladipo, Douglas K. McCarty, Stephen Hillier, and Reinhard Kleeberg. "Some successful approaches to quantitative mineral analysis as revealed by the 3rd Reynolds Cup contest." *Clays and Clay Minerals* 54, no. 6 (2006): 748-760.
18. Peter Atkins, P., and J. De Paula. *Atkins' physical chemistry*. OUP Oxford, 2014.
19. Recommendations, I. U. P. A. C. "Reporting physisorption data for gas/solid systems with special reference to the determination of surface area and porosity." *Pure Appl. Chem* 57, no. 4 (1985): 603-619.

20. Ryskin, Ya I. "The vibrations of protons in minerals: hydroxyl, water and ammonium." *The infrared spectra of minerals* (1974): 137-182.
21. Salles, Fabrice, Jean-Marc Douillard, Renaud Denoyel, Olivier Bildstein, Michel Jullien, Isabelle Beurroies, and Henri Van Damme. "Hydration sequence of swelling clays: Evolutions of specific surface area and hydration energy." *Journal of colloid and interface science* 333, no. 2 (2009): 510-522.
22. Sing, Kenneth SW. "Reporting physisorption data for gas/solid systems with special reference to the determination of surface area and porosity (Recommendations 1984)." *Pure and applied chemistry* 57, no. 4 (1985): 603-619.
23. Treiber, L. E., and W. W. Owens. "A laboratory evaluation of the wettability of fifty oil-producing reservoirs." *Society of petroleum engineers journal* 12, no. 06 (1972): 531-540.
24. Yuan, Yuehua, and T. Randall Lee. "Contact angle and wetting properties." In *Surface science techniques*, pp. 3-34. Springer, Berlin, Heidelberg, 2013.

Chapter 4. Clay substrate surface characterization

4.1 Introduction

Contact angle is impacted by surface roughness (Oliver et al 1980; Drelich et al 1996; Miwa et al 2000). As shown in previous studies, roughness is impacted by particle size, dispersion of solution and film purification methods, ultimately affecting wettability. In this study, casted clay films are compared before chemical reduction in terms of their surface roughness and a roughness profile is created. The aim of this test was to understand and constrain the roughness parameter and its impact on the clay films prior to wettability measurements. This study aims at the overall characterization of the topography of the clay substrate as well as to verify the consistency and reproducibility of the method for creating the clay – glass substrates. That is to gain an understanding of how the roughness parameter affects the wettability at the clay-crude oil interface. To constrain roughness in different scales, relative to the follow on wettability experiments, various methods were used.

Atomic force microscopy was used as it allows for a measuring surface roughness with a tip (i.e. contact method – see measuring surface roughness in the surface roughness section, chapter 4). Due to the low coverage achieved with the AFM and to better constrain larger area of the clay surfaces, CCI Interferometry was used (i.e. 800 × 800 in the x,y axis was covered). Confocal microscopy was used as a supplementary method – following experimental work performed internally by our sponsor, BP (information not disclosed) and the promising results confocal microscopy has shown to have, a confocal microscope was used.

Contact and non – contact surface texture measuring techniques were used for baseline studies on the surface texture of swelling nontronite NAu-2, non-swelling illite IMt-2 and swelling montmorillonite SCa-3 clay films cast on glass substrates. Details on the method for substrate creation are found in detail in methods chapter. The techniques essentially allowed the characterization of the engineered roughness profile of the clay substrates. Atomic force microscopy in the Department of Physics, Durham University, confocal microscopy in the Biosciences Department, Durham University and white light interferometry at the BP Technology Center, Pangbourne UK, where the selected methods for this study.

Namely, the basic methods for obtaining the roughness profile were atomic force microscopy, which is a contact – based method and white light interferometry – a non–contact method for characterizing surface texture. Confocal microscopy was used as a complementary and novel approach to characterize the surface texture of the substrates. In the following sections, the term roughness is introduced, imaging of the clay substrates at different scales is shown and the various

topographic features are displayed. The collected data and their interpretation give a quantitative estimation of the topography of the substrates that were created using the methods subsequently used in Chapter 5. This characterization should not be considered as a way of obtaining a definitive surface texture profile for clay substrates prepared by other methods.

Like any other manufacturing method, clay substrate creation has limitations and an embedded degree of error that ultimately leads to different nano and micro – topographies and roughness between substrates. It has been well understood by previous studies that roughness is interconnected with wetting behavior of surfaces (Oliver, Huh and Mason, 1980; Drelich, Miller and Good, 1996; Miwa et al., 2000; Volpe et al., 2002). Surface roughness can impact on wetting by means of affecting drop sizes (Drelich et al 1995). This has been shown to be true experimentally by Drelich and Miller (1994) and Drelich (PhD thesis, 1993). At the interface between a liquid and a solid that has roughness, a metastable configuration is possible that can produce different contact angles. Roughness, mainly responsible for this metastable condition, can therefore produce advancing and receding angles and a three-phase contact line between a gas, a liquid and a solid phase (Good 1952; Johnson and Dettre 1964; Johnson and Dettre 1970; Neumann 1974; Eick et al 1975; Huh and Mason 1977). With regards to the wetting of clay minerals and the surface chemistry of clays, nano – roughness is proven to vary relative to the clay's cation affinity (Ballah et al 2016, see details below). These previous studies are expanded on in Section 4.2. The importance of surface roughness for contact angle measurements has been shown both experimentally and by modelling (Wenzel 1936; Volpe et al 2002). Wenzel suggested that upon adding the roughness parameter, the wettability is increased owing to added adhesion forces at the surface. When a liquid penetrates a surface, it will be governed by the surface roughness profile and the surface chemistry of the solid. The droplets will be typically up to three times larger than the surface roughness features. When drops are combined across a surface uninterrupted and between the grooves of a surface that is known as heterogeneous wetting (Cassi and Baxter 1944). Clay films have a roughness directly linked to their interlayer cation (Zabat et al 2015). Using montmorillonites, they showed that roughness is decreased when the monovalent clays were exchanged for divalent cations and ultimately trivalent cations using first Li, Na and Cs and later on Mg and Al cations for their study. Lee and Yen (1999) measured the surface roughness of metal and organic cation exchanged Ca-montmorillonites by measuring the D fractal value derived from nitrogen BET plots. Their assessment showed that with larger exchanged cations, surface irregularities (i.e. roughness) is less, indicating a smoother surface, whereas in the case of organo-montmorillonites, the surface topography was unaltered.

Surface roughness that causes a modification in a wetting surface, is the ratio of the surface areas (Wenzel 1936). The equation that relates specific interfacial energy and roughness, that also includes contact angle,

$$r(S_s - S_{SL}) = S_L \cos \vartheta \quad (3.1),$$

Whereas, roughness is r and is defined as the ratio between the area of surface and the smooth area. Surface roughness can also be named the degree of average heights (elevation) in a given profile (of a clay film). However, there is no consensus as to what is the absolute numerical value of roughness (Wenzel 1949).

The characterization presented here goes beyond the scope of elucidating the links between cation – nano-roughness and clay wetness – clay roughness. Instead, it aims to provide a description of the main features between the different scales of measured areas on the clay substrates. This sets the basis for further experiments (Chapter 5) by excluding macro – roughness from being a controlling factor in the observed contact angle results.

4.2 Surface texture

Casting clay films is a proven method for measuring wettability ta the mineral level before upscaling. Specifically, spin coating has been used for wettability and adhesion studies. Spin coating is a technique for creating thin films of an initially dispersed liquid that becomes solidified into a coating. In terms of scale, coatings range from nanometres to microns. The size depends on the velocity of spinning (Bantignies et al 1997). Ballah et al (2016) used smectite (montmorillonite and nontronite) films to understand their interplay with water in the presence of different interlayer cations. The technique they used were previously described by Wu (2001) – a glass surface was purified using distilled water and acetone and then 1.5 ml of 3 g/L clay suspensions were left to dry at 46% relative humidity for several hours. In a previous study, and similar to the method later used by Wu, van Duffel et al (1999) created laponite clay films by using clay dispersions by stirring for a minimum of 48 h before the films were left to dry. Their research constrained the surface roughness by means of AFM microscopy coupled with simplified modelling of film formation. Key parameter found to minimize roughness was the extensive stirring, whereby the dispersed solution was homogenized. More recent work (Santha, PhD thesis, 2018) was focused on the surface roughness of kaolinite clay fims and its effect on crude oil wetting by means of white light interferometry. Kaolinite (KGa1b) was mixed with distilled water with a pH of 9.8 and sonicated using a sonicator probe at 40% amplitude and allowed to rest before it was centrifuged again at 3000 rpm for 5 min. Santha showed that longer sonication times

(i.e. 16 min instead of initial 8 min) were needed for a better coverage of the glass film by a kaolinite clay.

According to the CEN, Comité Européen de Normalisation and the ISO, the International Organization for Standardization, specific geometrical product specifications (GPS) exist that help with the categorization of surface texture (i.e roughness). Specific rules and procedures have to be followed to categorize the texture of a surface (i.e. the use of a contact technique – tip or stylus). Using strict engineering terms, roughness is assessed according to the EN ISO 4288. The ISO 4288 was created by the Technical Committees ISO/TC 57, ISO/TC 3, ISO/TC 10 and the Subcommittee SC 5. Definitions found in the ISO 3274, ISO 4287, ISO 12085, ISO 13565 and ISO 13585 – 3 were used for the introduction of basic parameters associated with surface texture. Roughness expresses any irregularities that are embedded in a process of production of a material. Since the clay substrates were created in a laboratory, their roughness may be evaluated using ISO recognised characterization methods. When the roughness is superimposed on a part of a texture it is called waviness that is caused by noise and vibration during the manufacturing process (see Fig 4.1). The overall form of a surface is the shape from which the features of roughness and waviness are excluded. The most common roughness value used is the roughness average, Ra.

The main parameters are R – parameters, calculated on the roughness profile, P – parameters calculated on the primary profile and motif parameters, calculated as peak – valley – peak combination for the specific profile length.

A parameter estimate is the estimate of a parameter's value, calculated relative to the length of a sample. The average parameter estimate is calculated by taking the arithmetic mean of all the sampling lengths. Any parameter defined over the evaluation length is the estimate of the parameter's value. That is achieved by measuring data from an evaluation length that is of equal value to the standardized number of sampling lengths. For measuring curves, measurement data from a curve are used. For the calculation of the roughness average (Ra) values, the following equation is used:

$$R_a = \frac{1}{5}\sum_j R_{a\,j}, \quad (4.1)$$

where Ra is the deviation of the arithmetic mean for a specific length.

In order to accurately make a decision on whether the studied surface meets the specification criteria, the following are taken into account: the number of the sampling lengths within the evaluation lengths and the number of the lengths that were evaluated.

Before the measurement test of the surface texture, a visual inspection is necessary to identify areas of defects and areas where a more detailed study is needed. Areas that appear smoother require more sophisticated testing using various analytical methods. Once the measurement is taken, a comparison is made based on the ISO values found in Table 4.1.

Table 4.1. The roughness sampling lengths for non – periodic roughness profiles (modified after BS ISO 4288:1996).

***Ra* (µm)**	**Roughness sampling length *lr* (mm)**	**Roughness evaluation length *ln* (mm)**
(0.006) < *Ra* ≤ 0.02	0.08	0.4
(0.02) < *Ra* ≤ 0.1	0.25	1.25
0.1 < *Ra* ≤ 2	0.8	4
2 < *Ra* ≤ 10	2.5	12.5
10 < *Ra* ≤ 80	8	40

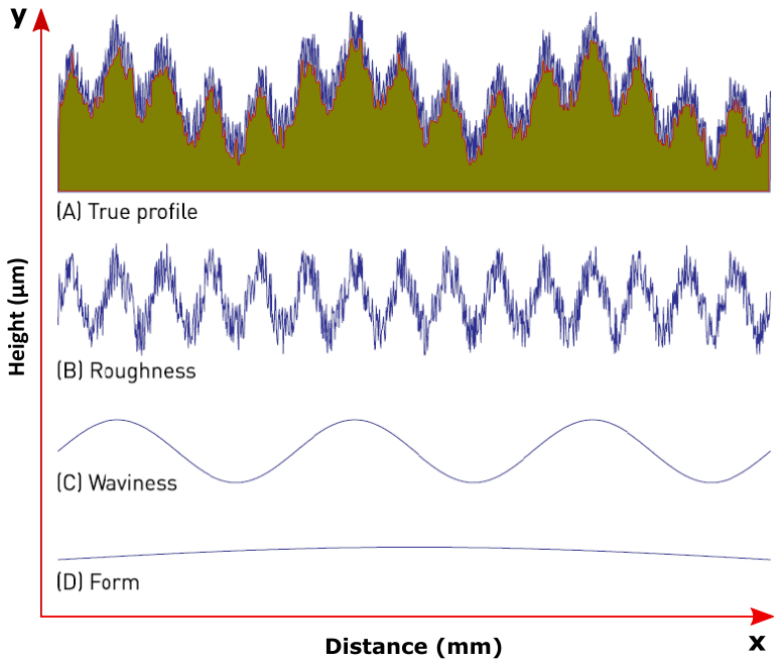

Figure 4.1. 2D surface profile of surface texture combining roughness, waviness and form (figure taken from © Taylor Hobson Ltd, A fundamental guide to the measurement of surface finish 7th Edition, 2004, modified).

4.3 Materials and methods

The clay minerals used were nontronite Nau-2, illite IMt-2 and montmorillonite SCa-3 and have been previously described in the methods chapter. Clay coating was performed as described in methods Chapter 3. The methods used for surface characterization were atomic atomic force microscopy, CCI interferometry and confocal microscopy and were previously described in the methods chapter.

4.4 Results

White light interferometry scans*;* The surface texture of NAu-2, SCa-3 and IMt-2 clay films was first tested with the CCI Talysurf 6000 Interferometer in 800 × 800 µm scans. To fit ISO 4287 standards, 400 * 400 µm areas were measured and cross sections as well as 2 D profiles were extracted. Primary Ra values were calculated based on the extracted profiles after a Gaussian filter was applied.

The 2 D profiles of NAu-2 that were extracted from the 400 × 400 µm area, fit the ISO 4287 and provided the primary Ra values. They show the topographic highs and lows of the selected cross section in µm. NAu-2 films have primary Ra values that vary between 0.00025 in NAu-2 – 1 to 0.00048 in NAu2 – 2. The topography of the NAu-2 films varies in terms of the shape of the coating. The coating appears as aggregates that vary in quantity. Most are found in NAu-2 – 2 substrate as can be seen visually in Figure 4.2. Despite the different shapes of the coated material, there is no significant variation in the primary roughness values.

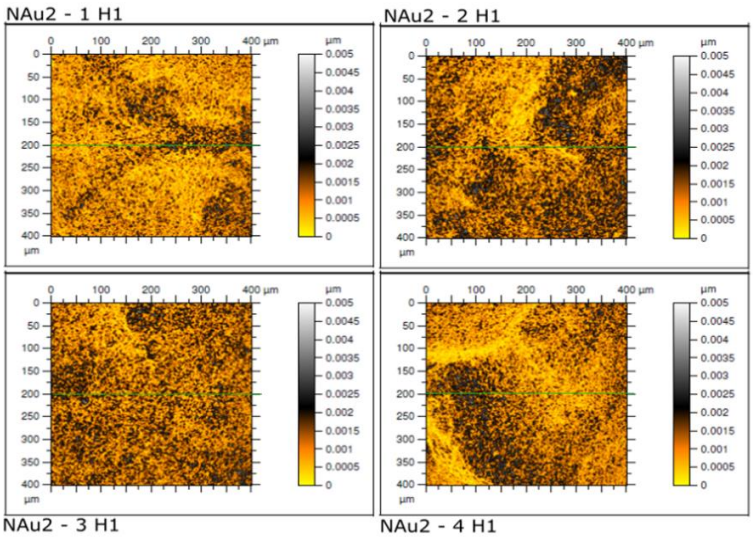

Figure 4.2. Zoomed area of 400 × 400 um for roughness measurements according to ISO 4287 for NAu-2 films in the H1 position – 0.4 mm evaluation length. Images were processed with the TalyMap Platinum software. Brown and gray scales were used to identify the differences in topography between the highest and lowest topographic points.

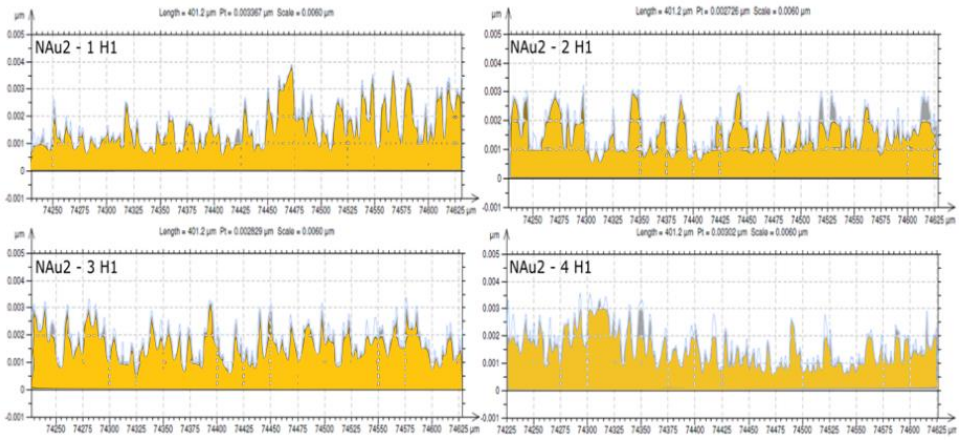

Figure 4.3. Extracted profile through the 400 × 400 µm zoomed area with a centerline along the X axis for the NAu-2 substrates. Primary Ra values were obtained based on these profiles. Selected cross sections are shown in green in Figure 4.2.

The 2 D profiles of SCa-3 were extracted from the 400 × 400 um area and provided the primary Ra values. They show the highs and lows of the topography of the selected cross section (µm). The primary Ra values show a lowest value of 0.000106 µm in SCa-3 – 4 and a highest of 0.000274 µm in Sca-3 – 2 (see Table 4.2). The coating of the surface does not show a significant variation in height (i.e. peaks) among the substrates. Most variations can be seen in white yellow as scattered material that represents higher topographic points, mainly in SCa-3 – 3 (Fig. 4.5). Primary roughness does not change significantly in the substrates.

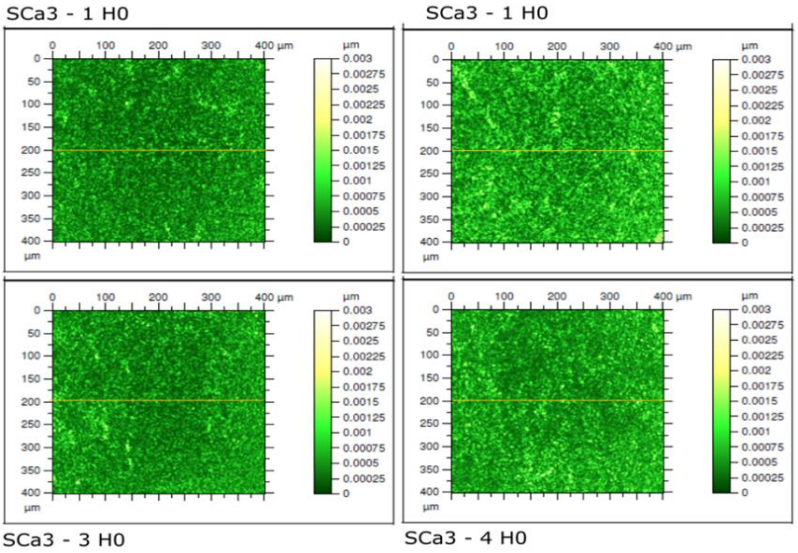

Figure 4.4. Zoomed area of 400 × 400 µm for roughness measurements according to ISO 4287 for SCa-3 substrates in the H0 position – 0.4 mm evaluation length. Images were processed with the TalyMap Platinum software. Green and light yellow scales were used to identify the differences in topography between the highest and lowest topographic points.

Similarly, 400 × 400 µm areas were scanned to fit the ISO 4287 standard so that an approximation of the Ra values can be obtained for IMt-2 (Fig. 4.6). The respective highs and lows seen in the extracted 2 D profile are shown in appendix A.1. The coating appears in different shapes; for IMt-2 – 1 and IMt-2 – 3 coatings valleys appeared across, or in the center of, the substrate's surface whereas IMt-2 – 2 and IMt-2 – 4 have scattered accumulations of coating (Fig.4.5).

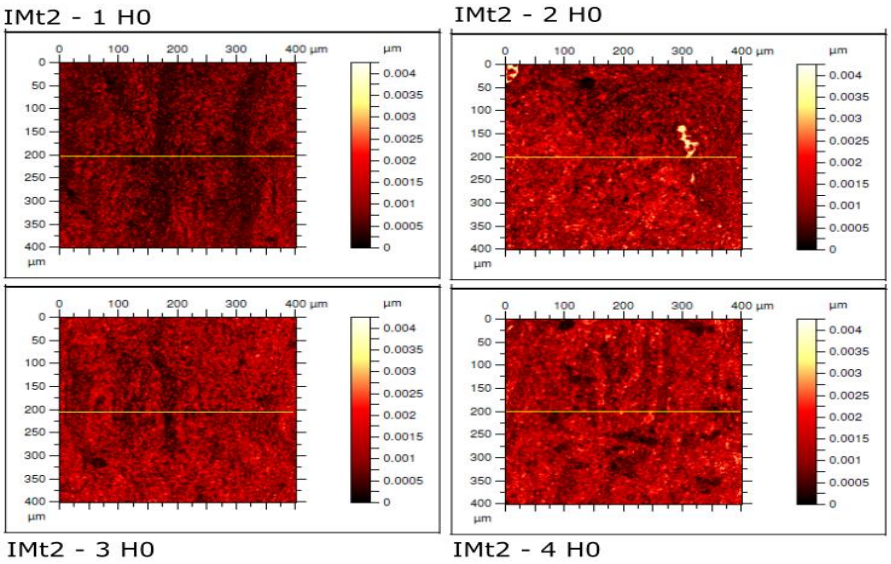

Figure 4.5. Zoomed area of 400 × 400 µm for roughness measurements according to ISO 4287 for IMt-2 substrates in the H0 position – 0.4 mm evaluation length. Images were processed with the TalyMap Platinum software. Red and light yellow scales were used to identify the differences in topography between the highest and lowest topographic points. Yellow lines indicate selected cross sections for the extraction of 2 D profiles.

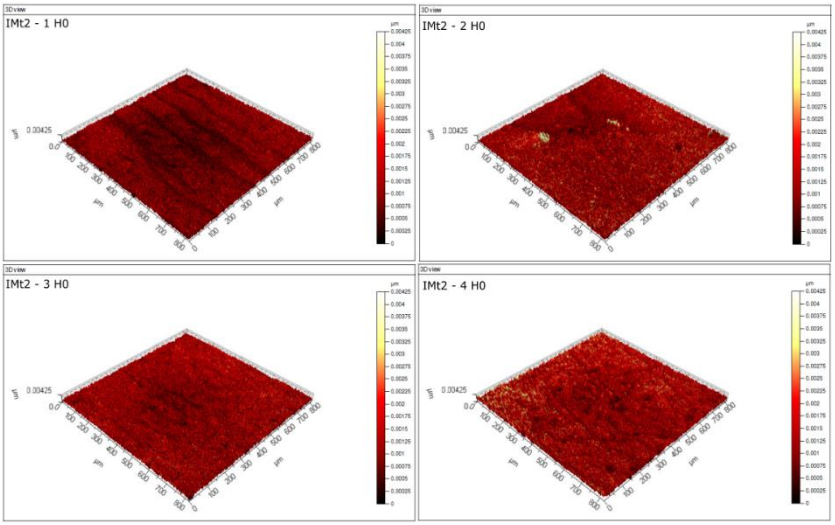

Figure 4.6. 3 D view of IMt2 substrates in the H0 position in a 800 × 800 um area in the X, Y axis. The height difference in topography can be seen by the change in colors. Red shades show lower topography and light yellow shades show higher topography. All substrates have been coated differently, showing variation in shape and form of surface texture. IMt2 – 1 shows valleys that run through the entire profile, IMt-2 – 2 shows small scattered peaks (in white yellow) and accumulated material in specific areas, IMt-2 – 3 show small valleys mainly in the central part of the surface and IMt2 – 4 shows larger peaks (in light yellow) that are spread unevenly throughout the surface of the clay film.

AFM scans; The results for AFM scans are as follows: Constant force mode showed that NAu-2 – 1 and NAu-2 – 2 have similar primary Ra values that average 58.45 and 78.9 µm respectively. Their 2 D and 3 D profiles correlate well, proving consistency over the two samples. NAu-2 – 3 shows small variation in primary Ra values compared to the other two substrates. NAu-2 – 3 substrate appears to be relatively rougher, averaging a primary Ra value of 253 nm. That can be seen in the imaging of NAu-2 – 3, which displays as wavy coatings as opposed to NAu-2 – 1 and NAu-2– 2 where the shape is more irregular and the features are spikes instead of waves (Fig. 4.7).

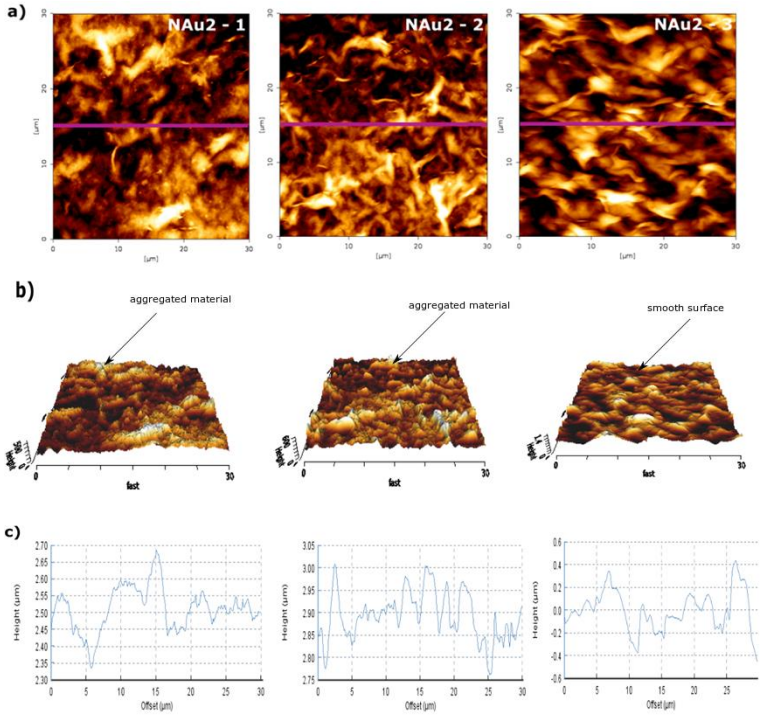

Figure 4.7. AFM surface topography results for NAu-2 – 1, NAu-2 – 2 and NAu-2 – 3. Primary roughness profile can be seen in a) 2D 30 × 30 micron scanned areas with similarly distributed material throughout the NAu2 glass coated batch. Substrate NAu-2 – 3 shows a wavy profile that is different from the other two, b) 3D topographic images of the NAu-2 coated slides – height is between 1 and 4 um throughout the batch and c) cross – section profiles of the NAu-2 coated slides (selected cross sections shown in purple) show similar primary roughness values for NAu-2 – 1 and NAu-2 – 3 and only a rougher surface for NAu2 – 3. All three substrates have similar topographies with peaks and lows that correlate to different shades of brown. Light brown shows topographic peaks and dark brown shows a lower topography.

Constant force mode showed that SCa-3 – 1 and SCa-3 – 2 have similar primary Ra values that average 134.65 and 153.18 respectively. SCa3 – 3 has a primary Ra of 262.2 nm giving it a relatively rougher texture than the SCa-3 – 1 and SCa-3 – 2. Similarities in surface texture are clear in SCa-3 – 1 and SCa-3 – 2 in the 2 D profiles. The first two substrates show patches of clay material almost equally coating the glass surface, whereas SCa-3 – 3 shows that the material has coated the surface in waves, forming a different surface texture. That is also shown in the 3 D images of SCa-3 substrates. The wavy – darker profile shows an increased primary Ra compared to SCa-3 – 1 and SCa-3 – 2 (see Fig. 4.8).

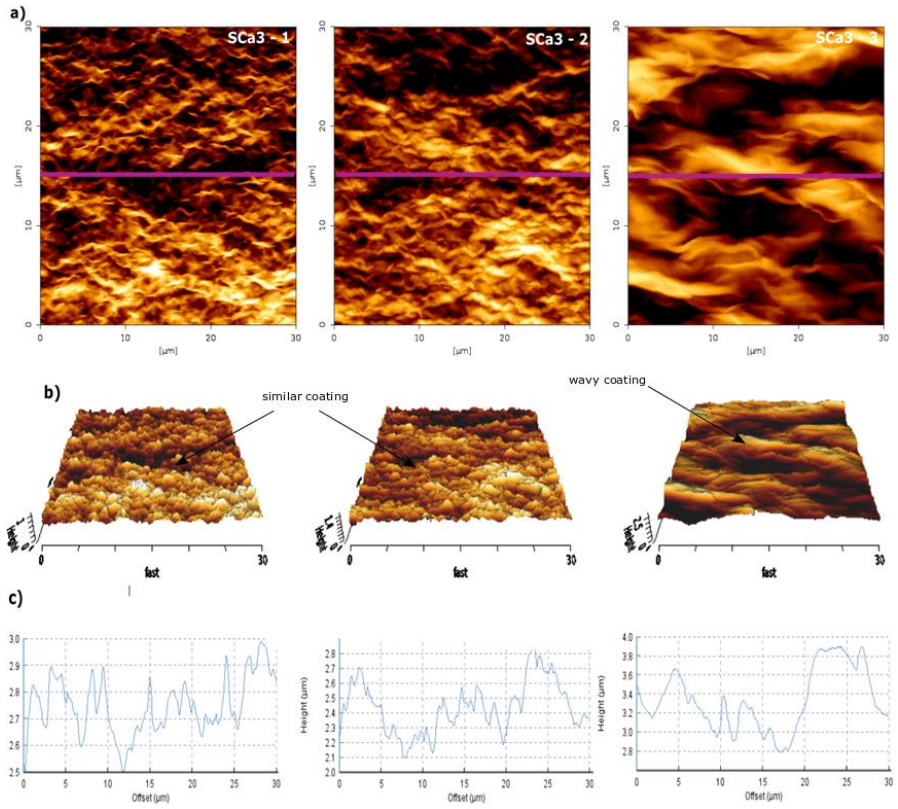

Figure 4.8. AFM surface topography of SCa3 – 1, SCa3 – 2 and SCa3 – 3. Primary roughness profile can be seen in a) 2 D 30 x 30 micron scanned areas with the coated material distributed similarly between the first two substrates and forming a wavy form in SCa3 – 3, b) 3D topographic images of the SCa3 coated slides – height varies between 1 and 3 um throughout the entire batch and c) cross – section profiles of the SCa3 coated slides show similar topographic height values for SCa3– 1 and SCa3 – 2 and only elevated height values for SCa3 – 3. Different shades of brown show higher (dark brown) and lower (light brown) topographies.

Quantitative Imaging mode used for IMt2 showed primary Ra values that average 114.17 and 81.83 µm for IMt-2 – 1 and IMt-2 – 2 and 79.66 µm for IMt-3. All substrates have similar texture. IMt-2 – 1 appears to have an elevated primary Ra. A small variation between the coated material can be seen between the first two substrates and IMt-2 – 3 (Fig. 4.9).

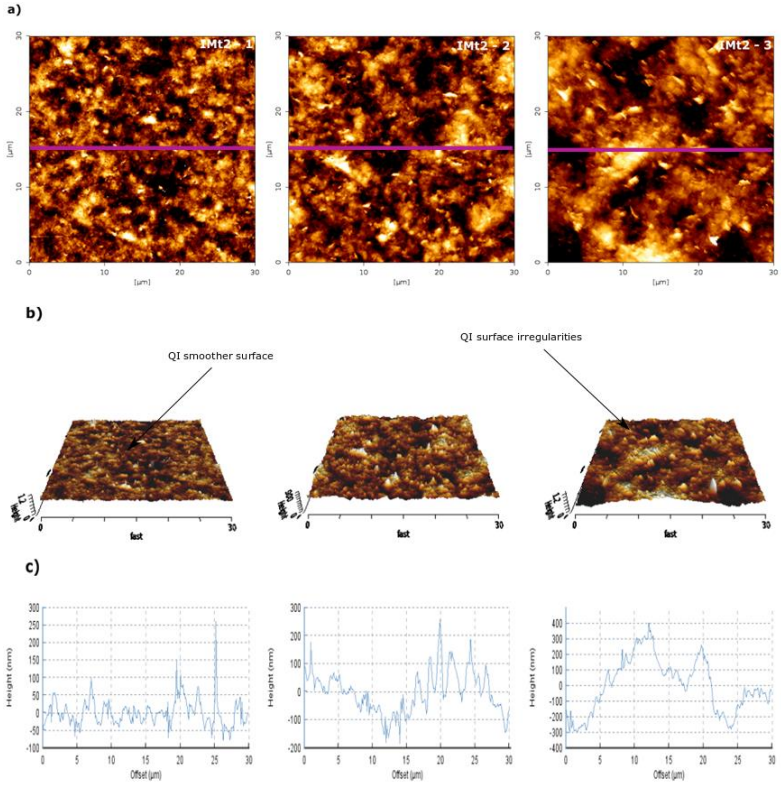

Figure 4.9. AFM surface topoghraphy for IMt-2 – 1, IMt-2 – 2 and IMt-2 – 3. Primary roughness profile can be seen in a) 2 D 30 × 30 micron scanned areas with the coated material distributed similarly in the batch, b) 3D topographic images of the IMt-2 coated slides – height varies between 50 and 250 nm for IMt-2 – 1 and IMt-2 – 2 and from 50 to 400 nm for IMt-2 - 3 c) cross – section profiles of the IMt-2 coated slides show similar height values for all substrates. Different shades of brown show higher (dark brown) and lower (light brown) topographies.

Confocal microscopy scans; For the confocal microscopy, the ZEISS 800 LSM in Airyscan mode was used to obtain the fluorescence intensity profiles of the SCa-3, IMt-2 and NAu-2 substrates. Twelve 50 × 50 areas per sample were scanned and the data were processed with ImageJ and ZEN Blue

Microscope software. The SCa-3 substrates average fluorescence intensities that have values up to 750 Arbitrary Units (AU). Substrates SCa-3 – 1 and SCa-3 – 2 have similar intensity values whereas SCa-3 – 3 averages 300 AU. The intensity profiles do not vary significantly. All three substrates have peaks and lows that are seen throughout their surface, making them easily comparable.

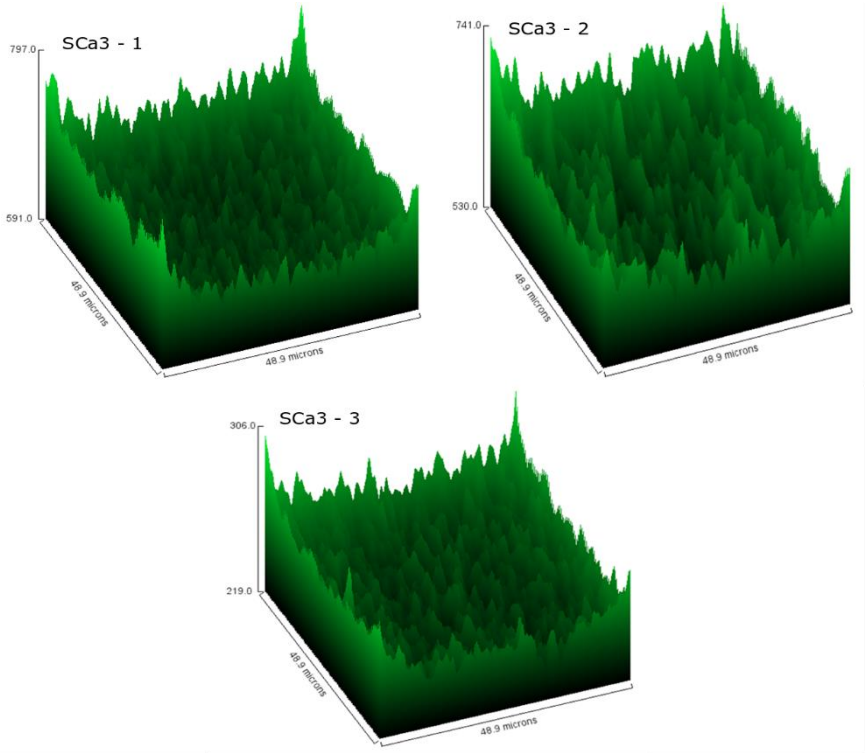

Figure 4.10. Average fluorescence intensity profiles of the SCa-3 substrate surfaces. SCa3 – 1 and SCa3 – 2 average very similar fluorescence intensities, whereas SCa3 – 3 averages are lower.

Similarly, data show very little difference in fluorescence intensity values between IMt-2 – 1 and IMt-2 – 3 (Fig 4.11). The average fluorescence intensity of IMt-2 – 1 and IMt-2 – 3 values reach up to 580 AU and 500 AU respectively. However, the distribution of intensity is dissimilar between the substrates. IMt-2 -1 shows even distribution of the intensity with more peaks appearing in the 3 D profile, whereas IMt-2 – 3 has less intensity peaks. IMt-2 – 2 has significantly less fluorescence intensity that does not exceed 15 AU. NAu2 substrates have the lowest fluorescence intensity values. NAu-2 – 1 and NAu-2 – 3 average 20 AU and NAu-2 – 2 average intensity does not exceed 12 AU. In terms of the intensity's distribution, all three substrates have a relatively flat surface with few peaks (Fig.4.12).

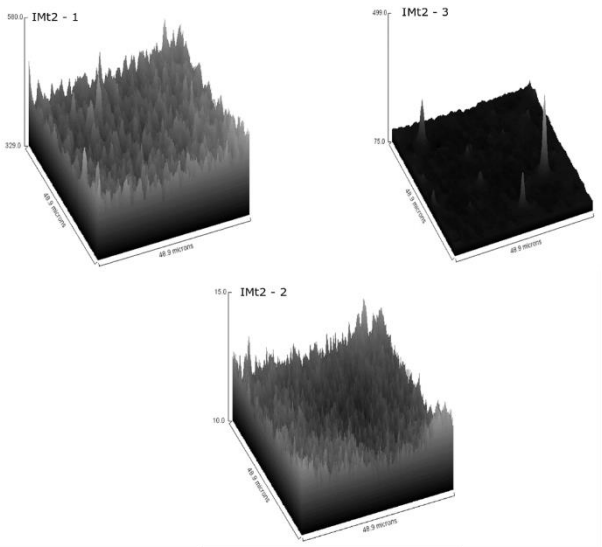

Figure 4.11. Fluorescence intensity profiles of the IMt-2 substrates.

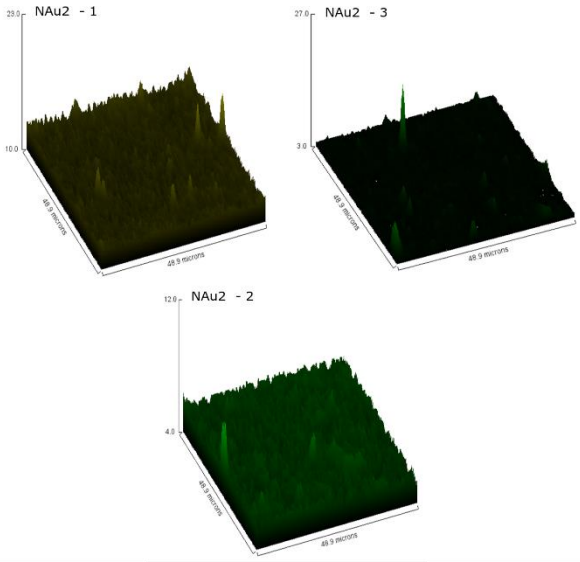

Figure 4.12. Fluorescence intensity profiles of NAu-2 substrates.

4.5 Discussion

The method for preparing clay substrates includes defects that can alter the surface texture. One defect is caused by the drying rate flaw embedded in the preparation process. The rate of evaporation of water inside the electric oven can be different for each clay – water solution. That is due to adhesive forces between the molecules of water and clay that are different for every clay, expressed as a clay – water potential. Estimation of steady – state evaporation rates in soils and clays (Ripple, Rubin, Hylckama, 1970) and models for calculating the humidity during evaporation in water – soils systems (Stewart and Broadbridge, 1998) show that evaporation and humidity vary significantly depending on the saturated conductivity of the soils. Assuming all other factors are well constrained and cross contamination during the making of the substrates is avoided, a fast evaporation rate can create patches of clay at some parts of the glass slide and a smoother surface at other parts. A slow evaporation rate will allow for a more evenly distributed material throughout the glass slide.

AFM measured roughness and wettability; Surface roughness measured with AFM provides detailed understanding of topography using a contact technique. The uniformity shown is at the 30×30 μm scale. Numerous scans were needed to give a better representation of the entire film. As has been shown by other studies (Ballah et al 2016, Santha PhD thesis 2018 and Yesufu Rufai et al 2020) AFM works very well for clay films to address topographic discrepancies between initial and latter stages of the wetting state. When used as baseline study to constrain what controls roughness, it has been shown (studies above) that changes in roughness induced by altering redox state, interlayer cations and brine composition, can change the wettability. Post reduction stages showed a lower adhesion force between sandstone and polar components in the above study by up to 70% using a -NH_2 functionalized tip (Yesufu-Rufai et al 2020).That is induced by textural changes owing to changing redox state and water capacity properties. Ballah et al (2016) showed there is a decrease in r (μm) values as particle size was decreasing (from 3 to 1.3 μm for topographic heights 0.68 to 0.66 μm respectively). Our values are in the nm scale, showing relative consistency between two out of three clay films in each mineral group. Potentially, discrepancies seen in the third film of each group will not induce significant changes in contact angles (see Chapter 5).

White light interferometry roughness; The method allowed for a larger scale measurements that cover areas closer to the millimeter scale. As a result the roughness parameter measured using these scans can be more accurately related to the follow on wettability measurements (see chapter 5). Santha (PhD thesis, 2018) used the same method for probing the surface roughness of

kaolinite clay films and proved consistency among the clay films using 800 × 800 µm scans. Using her study as a basis, the CCI scans produced results that are more realistic in terms of size.

Confocal microscopy; This stand-alone method was used as a novel approach to verify surface discrepancies between clay films and provided intermediate sized scans. By using the range of techniques a reasonably full picture of clay thin film structure was therefore obtained. The method was used for measuring coverage of fluorescence, hence, full or, even, good fluorescence coverage was linked to an even roughness profile.

Limitations embedded in the process; It is important to distinguish between roughness found in natural environments such as clay nano – surfaces in rocks and roughness expressing irregularities caused by a manufacturing process. The methods described throughout this chapter focus on the engineered roughness. AFM scans do not follow the ISO standards for measured areas. That is due to the limitation embedded in the machine, allowing for the largest scans to be 30 × 30 microns in the X, Y axis. ISO standards were followed when using the CCI Talysurf Interferometer since the instrument allowed for 800 × 800 micron scan areas in the X, Y axis. Confocal Microscopy was only used as a novel and complementary method to the other two surface characterization methods. Since a confocal microscope only measures emitted light intensity and not topographic heights, ISO standards do not apply. With no previous work ever done exclusively on the fluorescence intensity of clay minerals under a confocal microscope, this method can be a stand – alone, for surface characterization. Since the measured roughness is not real roughness based on ISO characterization and because this chapter focuses on characterizing engineered roughness, the measured values are called primary roughness Ra.

Engineered roughness can change upon chemical reduction of clay thin films, owing to the surface changes occurring mainly at the surface of the clay (Stucki 2011). Therefore, measuring clay films at a post-reduction state becomes problematic. In addition, contact with a wetting fluid can influence the measurements owing to the dynamic interplay between phases.

4.6 Conclusions

The methods for measuring the surface texture of the substrates provided results on the engineered primary surface roughness Ra. The AFM data provided a detailed set of results for 30 × 30 µm scans in the X, Y axis. The scans proved a relative consistency of the method across the substrates was achieved at least in two out of three coated glass slides. Due to the small size of the scanned area, the characterization was focused on features in the micro – scale. The CCI Talysurf Interferometer method provided results that again focused on a more realistic size in the

micro – scale, measuring 800 × 800 μm areas in the X, Y axis. The values were subjected to ISO characterization and indicated that they are bellow any ISO standard. Therefore the values cannot be classified as roughness values. However consistency was proven across all substrates with small discrepancies between them. Surface texture features show significant variation across the samples that is not followed by varied primary Ra values. Moreover, fluorescence intensity was used as a mean to identify the degree of even – uneven distribution of material across the clay substrates. Confocal microscopy confirmed that clay minerals fluoresce. More specifically, NAu-2 nontronite, IMt-2 illite and Sca-3 montmorillonite fluoresce at different intensities with NAu-2 being the least fluorescent and SCa-3 fluorescing the most. Based on this finding it can be said that the produced clay substrates share similar fluorescence intensities throughout each batch. Combined with the AFM and white light interferometer results, fluorescence intensity is a complementary method that proved the relative consistency of the produced substrates. However, to prove definitive consistency of a method, a large number of specimens is necessary and a statistical mean of their features (roughness) is needed. Due to the limited number of clay substrates prepared in the laboratory, the lack of a statistical mean and the primary Ra values bellow any ISO standard, this surface texture characterization only provides a baseline roughness profile. Good between sample consistency was attained for coverage and roughness, the coating method was considered appropriate for contact angle measurements, but in some systems (Illite samples) then the in sample roughness varied and thus different spots on the same slide may vary.

4.7 References

1 Ballah, J., M. Chamerois, S. Durand-Vidal, N. Malikova, P. Levitz, and L. J. Michot. "Effect of chemical and geometrical parameters influencing the wettability of smectite clay films." *Colloids and Surfaces A: Physicochemical and Engineering Aspects* 511 (2016): 255-263.

2 Bantignies, J-L., C. Cartier Dit Moulin, and Herve Dexpert. "Wettability contrasts in kaolinite and illite clays: characterization by infrared and X-ray absorption spectroscopies." *Le Journal de Physique IV* 7, no. C2 (1997): C2-867.

3 Cassie, A. B. D., and S. Baxter. "Wettability of porous surfaces." *Transactions of the Faraday society* 40 (1944): 546-551.

4 Della Volpe, C., D. Maniglio, M. Morra, and S. Siboni. "The determination of a 'stable-equilibrium'contact angle on heterogeneous and rough surfaces." *Colloids and Surfaces A: Physicochemical and Engineering Aspects* 206, no. 1-3 (2002): 47-67.

5 Drelich, J., and J. D. Miller. "A critical review of wetting and adhesion phenomena in the preparation of polymer-mineral composites." *Mining, Metallurgy & Exploration* 12, no. 4 (1995): 197-204.

6 Drelich, Jaroslaw Wieslaw. "The role of wetting phenomena in the hot water process for bitumen recovery from tar sand." PhD diss., The University of Utah, 1993.

7 Drelich, Jaroslaw, and Jan D. Miller. "The effect of solid surface heterogeneity and roughness on the contact angle/drop (bubble) size relationship." *Journal of colloid and interface science* 164, no. 1 (1994): 252-259.

8 Drelich, Jaroslaw, Jan D. Miller, and Robert J. Good. "The effect of drop (bubble) size on advancing and receding contact angles for heterogeneous and rough solid surfaces as observed with sessile-drop and captive-bubble techniques." *Journal of colloid and interface science* 179, no. 1 (1996): 37-50.

9 Eick, J. D., R. J. Good, and A. W. Neumann. "Thermodynamics of contact angles. II. Rough solid surfaces." *Journal of Colloid and Interface Science* 53, no. 2 (1975): 235-248.

10 Good, Robert J. "A thermodynamic derivation of Wenzel's modification of Young's equation for contact angles; together with a theory of Hysteresis1." *Journal of the American Chemical Society* 74, no. 20 (1952): 5041-5042.

11 Huh, C., and S. G. Mason. "Effects of surface roughness on wetting (theoretical)." *Journal of colloid and interface science* 60, no. 1 (1977): 11-38.

12 Johnson Jr, R. E., and R. H. Dettre. "Contact angles and monolayer depletion." *The Journal of Adhesion* 2, no. 1 (1970): 3-15.

13 Johnson Jr, Rulon E., Robert H. Dettre, and Dale A. Brandreth. "Dynamic contact angles and contact angle hysteresis." *Journal of Colloid and Interface science* 62, no. 2 (1977): 205-212.

14 Keeling, John L., Mark D. Raven, and Will P. Gates. "Geology and characterization of two hydrothermal nontronites from weathered metamorphic rocks at the Uley graphite mine, South Australia." *Clays and Clay Minerals* 48, no. 5 (2000): 537-548.

15 Lee, Cheng-Chung, and Yi-Jun Jen. "Influence of surface roughness on the calculation of optical constants of a metallic film by attenuated total reflection." *Applied optics* 38, no. 28 (1999): 6029-6033.

16 Miwa, Masashi, Akira Nakajima, Akira Fujishima, Kazuhito Hashimoto, and Toshiya Watanabe. "Effects of the surface roughness on sliding angles of water droplets on superhydrophobic surfaces." *Langmuir* 16, no. 13 (2000): 5754-5760.

17 Neumann, A. W. "Contact angles and their temperature dependence: thermodynamic status, measurement, interpretation and application." *Advances in colloid and interface science* 4, no. 2-3 (1974): 105-191.

18 Nieto, Fernando, Marcello Mellini, and Isabel Abad. "The role of H3O+ in the crystal structure of illite." *Clays and Clay Minerals* 58, no. 2 (2010): 238-246.

19 Oliver, J. P., C. Huh, and S. G. Mason. "An experimental study of some effects of solid surface roughness on wetting." *Colloids and surfaces* 1, no. 1 (1980): 79-104.

20 Ripple, C. D., Jacob Rubin, and T. E. A. Van Hylckama. *Estimating steady-state evaporation rates from bare soils under conditions of high water table*. US Geological Survey, Water Resources Division, 1970.

21 SANTHA, NIPADA (2019) Understanding Clay-Oil-Brine Interactions at the Nano-scale: Implications for Low-Salinity Enhanced Oil Recovery, Durham theses, Durham University. Available at Durham E-Theses

22 Stewart, J. M., and P. Broadbridge. "Calculation of humidity during evaporation from soil." *Advances in water resources* 22, no. 5 (1999): 495-505.

23 Stucki, Joseph W. "A review of the effects of iron redox cycles on smectite properties." *Comptes Rendus Geoscience* 343, no. 2-3 (2011): 199-209.

24 Van Duffel, Bart, Robert A. Schoonheydt, Cees PM Grim, and Frans C. De Schryver. "Multilayered clay films: atomic force microscopy study and modeling." *Langmuir* 15, no. 22 (1999): 7520-7529.

25 Wenzel, Robert N. "Resistance of solid surfaces to wetting by water." *Industrial & Engineering Chemistry* 28, no. 8 (1936): 988-994.

26 Wenzel, Robert N. "Surface roughness and contact angle." *The Journal of Physical Chemistry* 53, no. 9 (1949): 1466-1467.

27 Wu, Wenju. "Baseline studies of the clay minerals society source clays: colloid and surface phenomena." *Clays and Clay Minerals* 49, no. 5 (2001): 446-452.

28 Yesufu-Rufai, Sherifat, Maja Rücker, Steffen Berg, Sarah F. Lowe, Fons Marcelis, Apostolos Georgiadis, and Paul Luckham. "Assessing the wetting state of minerals in complex sandstone rock in-situ by Atomic Force Microscopy (AFM)." *Fuel* 273 (2020): 117807.

29 Zabat, M., R. Harba, and H. Van Damme. "Fractal analysis of surface roughness of montmorillonite clay self-supported films: Effects of exchanged cations and of mechanical

tensile stress." *Colloids and Surfaces A: Physicochemical and Engineering Aspects* 486 (2015): 38-44.

Chapter 5. Wettability assessment of redox active clay minerals at the clay-crude oil interface using contact angles

5.1 Introduction

In this experiment the wettability of clay minerals with regard to the clay – crude oil interface is tested as a function of the reduction extent (Eh) of structural iron inside clay minerals. A change in reduction extent of iron – bearing clay minerals can alter their structure and colloidal properties, cause changes in the hydration state of the interlayer, cation affinity and surface charge (Yan and Stucki 1999) and potentially in the wettability of the clay (see Chapter 2: Literature, for more information on the mechanisms and results of iron reduction in clay minerals).

The wettability of clay minerals is important to sandstone petroleum reservoirs as it can control the wetting state of a surface where original oil in place (OOIP), formation water or brine can be adhered to (Morrow 1990). In the Low Salinity Water Flooding operations for Enhanced Oil Recovery, optimal results are achieved when the wetting state is intermediate to water – wet (Jackson et al 2016, Strand et al 2008). By examining the wettability alterations as a function of Eh, the behavior of the wetting state of the clay can be better understood.

Clastic reservoirs consist of swelling and non-swelling types of clay minerals that are important for wettability. Clay minerals regulate wettability according to their affinity towards acidic and basic molecules. Consequently, they can be responsible for controlling water-wet, oil-wet or intermediate-wet conditions. Ultimately, wettability alterations are followed by the migration of fines (i.e. clay mineral and oil particle colloids) inside clastic reservoirs (see Chapter 2: Literature Review and references therein). Within this context, constraining the wettability of clay minerals is fundamental in order to understand the effect it has on the migration of fines within a clastic reservoir.

To assess the wettability, various methods have been used in the past, with the most widely used being that of contact angle measuring. The values derived from the measurements provide an indication of the mechanical equilibrium between the solid, liquid and vapor phases of a system as was first described by Thomas Young (1832) (see Chapter 3: Methods and references therein). Two major forces alter the shape of the drops applied on a solid surface; these are surface tension and gravitational force.

Previous work on assessing the wettability of both sandstone rocks and homogeneous clay films has been done by a number of researchers: Contact angles between air-water-sandstone reservoir samples that had been pre-treated with crude oil, were measured by Borysenko and co-workers (2009) with the use of the sessile drop method. The sandstones used were rich in clay minerals kaolinite and illite. The measured contact angle values of water were 10-30 degrees for hydrophilic and 120 degrees for hydrophobic sandstone samples respectively. Contact angle of diesel oil was measured (44 degrees) to assess the wettability of Polish shale reservoir samples by Ksiezniak and co-workers (2015) using the method of capillary rise showing that it almost doubled the contact angle of water (80 degrees). Janczuk et al (1989) measured the wettability of kaolinite as a function of its exchangeable cations by means of the sessile contact angle method. In their work, they measured contact angle of water and diiodomethane on kaolinite, each time saturated with one of the following cations: H^+, Na^+, K^+, Mg^{2+}, Ca^{2+}, Ba^{2+}, Al^{3+}. Their results indicated that the wettability as expressed through contact angle values was affected by the type of cation present in the clay's structure. Highest contact angle values, indicating less wetting, were measured for the Ca^{2+}, 32 degrees for diiodomethane and Ba^{2+}, 34 degrees for diiodomethane, saturated kaolinites. Water contact angle values were measured for the Al^{3+} and K^+- 28 and 26 degrees respectively. Another study on kaolinite clay films by Lebedeva et al (2010) showed that, kaolinite clay films aged in brines, in low, neutral and high pH values, exhibit changes in wettability relative to sodium chloride concentration and/or pH. In their study they used the captive bubble method (see Chapter 3: Methods) to measure advancing and receding contact angles of crude oil. Advancing and receding contact angles of decane and water on kaolinite clay films aged in different salinity brines have been also measured by Lebedeva and Foden (2010), showing wettability alterations as a function of salinity. In the case of a kaolinite aged in calcium chloride brine, the wetting of kaolinite shifts towards more water-wet conditions. In a more recent study by Wei and co-workers (2018) the wettability was measured with the use of the contact angle method applied to flat quartz slides, using the captive bubble method and capillaries. Their results indicated that the wettability was less (higher contact angles) in the case of flat surface contact angles and a clear positive effect of low salinity brine on wettability.

A recent study by Yesufu-Rufai et al (2020), dealt with wettability changes within sandstone core samples as a redox function. In their study, they measured wettability changes between redox active sites within the core and polar components ($-NH_2$ and –COOH) with the use of atomic force microscopy before and after introducing a reducing agent, sodium dithionite, to the sandstone cores. Their results showed that adhesion decreased after sodium dithionite was used. Although the method these workers used for assessing the wettability was different from contact angle

measurements, the results were indicative of the importance of redox conditions with regards to the wettability inside clastic cores.

The aim of this study is to understand how the wettability of iron bearing clay minerals change relative to changes in their reduction state. The experiments presented in this chapter were conducted to measure the difference in the clay wettability and crude oil before and after a reduction extent change using contact angle measurements. The sessile drop method was used to gain understanding of wettability at a monolayer mineral level (i.e. using casted clay flims). Due to an increased demand by our industry sponsor, BP, to investigate wettability changes relative to reduction states of clay minerals at mineral level and to upscale with follow on experiments, this method was used due to its simplicity and time-efficiency.

A difference in wettability was evident in samples in which structural iron was reduced, when compared to the unaltered samples. The clay material was sourced from the Clay Minerals Repository, Chantilly VA, USA and the admixed phases and their proportions of each batch was tested using XRD analysis in Newcastle University, at the School of Natural and Environmental Sciences Chemical Crystallography. The degree of clay reduction was verified with the use of Mössbauer spectroscopy in Newcastle University, at the department of Environmental Engineering, in Dr Anke Neumman's laboratory. Surface adhesion was studied by means of contact angle measurements. These were taken with the use of a Ramé-art Contact Angle Goniometer, in the Department of Chemistry, Durham University.H The sets of data were obtained using the sessile drop method technique that was first described by Bashforth and Adams in 1892. In the following sections, the selection of clays along with XRD and ICP data for testing their purity and cation constitution is presented. The protocol for chemical reduction of structural iron followed is given along with Mössbauer fitted curves that verify the Fe^{2+} - Fe^{3+} ratio after reduction. Three sets of contact angle measurements are shown for NAu2 nontronite, IMt2 illite and SCa3 montmorillonite clays. To conclude, the effects of iron reduction on clay wettability are interpreted within the following context: the XRD measurements and purity of the samples, cation exchange due to reduction and interlayer cation, the effect of reduction and the visual changes based on the Mössbauer analyses of the clay mineral and the textural characterization of the clay films.

5.2 Materials and methods

Materials: The clay minerals were sourced from the Clay Minerals Repository, Chantilly VA, USA. In total, two smectites and one non – smectite clay were used for this experiment. Nontronite

NAu-2, illite IMt-2 and montmorillonite SCa-3 have been described in methods chapter. Nontronite and illite have chemical compositions as shown in Table 5.1. Clay iron reduction was performed in a solution of buffers, sodium citrate and sodium bicarbonate and reducing agent sodium dithionite purchased from Sigma Aldrich. The crude oil used was provided by BP. Gas chromatograpy details of the crude oil are given in Table 5.2

Table 5.1 Concentration (wt%) of major elements in the NAu2 and IMt2 clay minerals as these were sourced from the CMR, Chantilly, VA, USA.

Mineral name	**moisture (%) at** 105 °C	**Al_2O_3**	**Fe_2O_3**	**P_2O_5**	**SiO_2**	**TiO_2**	**sum**
Nontronite NAu2	11.5	2.1	32.3	0.01	47.1	0.1	81.61
Illite IMt2	1.8	20.2	6.2	0.08	57	0.79	84.27
Exchangeable cations		CaO	MgO	MnO	Na_2O	K_2O	
Nontronite NAu2		1.4	0.72	0.002	0.22	0.03	2.37
Illite IMt2		0.39	2.1	0.03	0.08	7.5	10.10

Table 5.2. Gas chromatography analysis results of crude oil (provided by BP) in a; polar components of crude oil (BP) in b (Modified after Kareem 2017).

Hydrocarbon type (C<36)	**wt%**	**Physical properties of C<36**	
Normal paraffins	12.27	Density (25 °C)	0.8793
Isoparaffins	12.72	Viscosity (40 °C)	41.71
Aromatics	0.784		
Naphthenes (C<17<C<25)	7.535		
Aromatics (C17<C<25)	10.22		
Unknwon (C<25)	14.36		
$C36^+$	36.77		

Polar components

Total acidic number (TAN) (-)	1.2 mg KOH/g

Total basic Number (TBN) (+)	0.52 mg KOH/g

5.2.1 Methods

Clay mineral preparation: The sourced material (Figure 5.1.a) was first ground using a Retsch RM 100, 230 V and 50 Hz, mortar grinder with a feed size below 8 mm and final fineness below 10 microns, at Durham University, Department of Earth Sciences. When each batch of clay was adequately ground (see Chapter 3) for approximately 15 minutes or until fine powder consistency was achieved. The preparation of glass slides, clay mineral dispersions and casting thin clay films can be found in Chapter 3: Methods and a sub-set of the same clay films were assessed for uniformity of deposition and roughness in Chapter 4. In addition, chemical reduction method and sessile drop method for measuring wettability have been described in detail in the methods chapter.Contact angle measurements were first taken in oxic-atmospheric conditions and then in anaerobic conditions.

5.2.1.1 Clay mineral analysis

X-Ray Diffraction analysis: The bulk mineralogy of each batch of clays was tested using X–ray diffraction (XRD) analysis. Our industry sponsor, BP, were interested in building on this research, and in turn, asked for a scale-up. However, due to time limitations, trying to scale up the clay purification process was not feasible. Therefore the as received clay material was used instead of the size fractionated. Therefore, the clays used were the native non–homoionized and non–size fractionated NAu-2, IMt-2 and Sca-3. Above 2 micron fragments were included along with the initial set of interlayer cations. Fragments of oxides, typically found inside the clays were included. Samples NAu-2 and IMt-2 were prepared at the James Hutton Institute, Aberdeen, UK, by professor Steven Hillier and miss Helen Pendlowski and by X-ray Mineral Services Ltd, North Wales (Figure 5.1).

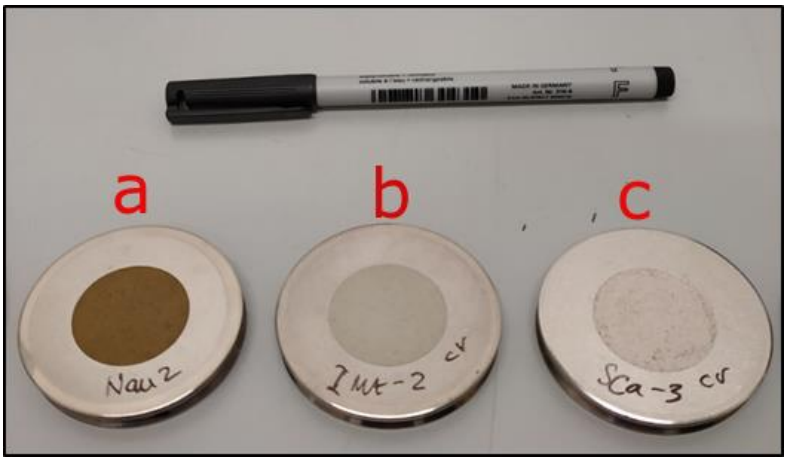

Figure (5.1). Ground oxidised clay mineral samples prepared for X – ray powder diffraction analysis; a) dark brown nontronite NAu – 2; b) gray illite IMt – 2; c) light gray montmorillonite.

Mössbauer spectroscopy: Curves were generated and the degree of clay reduction extent was verified with the use of relative adsorption – velocity fitted curves. Spectral analysis of the reduced samples verified the degree of reduction for IMt-2 and NAu-2 samples (Figure 5.3). The analysis was performed by using the Mössbauer cryosystem with a fitted ^{57}Co source, detector and a 336 temperature controller (LakeShore), at Newcastle University, Department of Environmental Engineering using a portion of the reduced clay minerals (typically 0.1 g of reduced iron clay is used without any prior sample preparation) .

5.3 Results

X – Ray diffraction patterns:

Results of the analysis of the bulk material are given in Table 5.3. Additionally, XRPD patterns, with the main phases identified in the samples by reference to patterns from the International Centre for Diffraction Database (ICDD), are provided for reference (Butler and Hillier 2021; Hillier 1999; Hillier 2003, Omosoto et al 2006). Results of clay fraction analysis are provided in Table 5.4. The patterns are in agreement with previous XRD phase analysis studies on native clays found in literature reports (see Fig. 5.2). The IMt-2 pattern corresponds well with the bulk mineralogy suggested by Marsh and co – workers (2018). Analysis of the clay size fraction of IMt-2, confirms the dominant illite. Small changes are apparent between air-dried, glycolated and heated traces,

suggesting a small amount of expandable (smectite like) layers. However, the proportion of these is estimated at 5% or less and 'illite' (the pragmatic definition of which allows up to 10% expandable layers) is definitely an appropriate identification. A trace amount of kaolinite is also indicated in the clay fraction but again at a level that leaves some uncertainty over identification. A trace of chlorite is also indicated, and it is possible that the main peak tentatively assigned to kaolinite could also be from chlorite. Some quartz and anatase also look to be present in the clay size fraction. Its pattern confirms agreement with prior literature (Gaillhanou et al 2017). It therefore classifies as 1M/1Md polytype (Haines and van der Pluijm 2008). Sample NAu-2 consists almost entirely of a dioctahedral smectite with an 060 peak position that indicates it is very rich in Fe and consistent with the expected 'nontronite'. Note the ICDD database PDF pattern shown is not a particularly good match but this is due the generally poor quality of clay mineral patterns in the ICDD database. The only other mineral detected in the specimen examined is minor/trace quartz. Analysis of the clay size fraction of NAu-2 shows it to consist entirely of dioctahedral smectite, the relative intensities of the basal reflections in being consistent with a very Fe-rich variety such as nontronite. The NAu-2 pattern confirms the existence of the main phase being that of nontronite followed by some minor phases of quartz and plagioclase. Biotite exists in very minor phases and is therefore considered undetectable. This pattern is in agreement with the one given by Keeling and co – workers (2000). They also reported minor phases of talc, ilmenite and goethite

with the dominant one being that of nontronite. The SCa-3 pattern is showing montmorillonite as the main phase, followed by minor phases of cristobalite and albite (Table 5.5, 5.6) (Liu et al 2018).

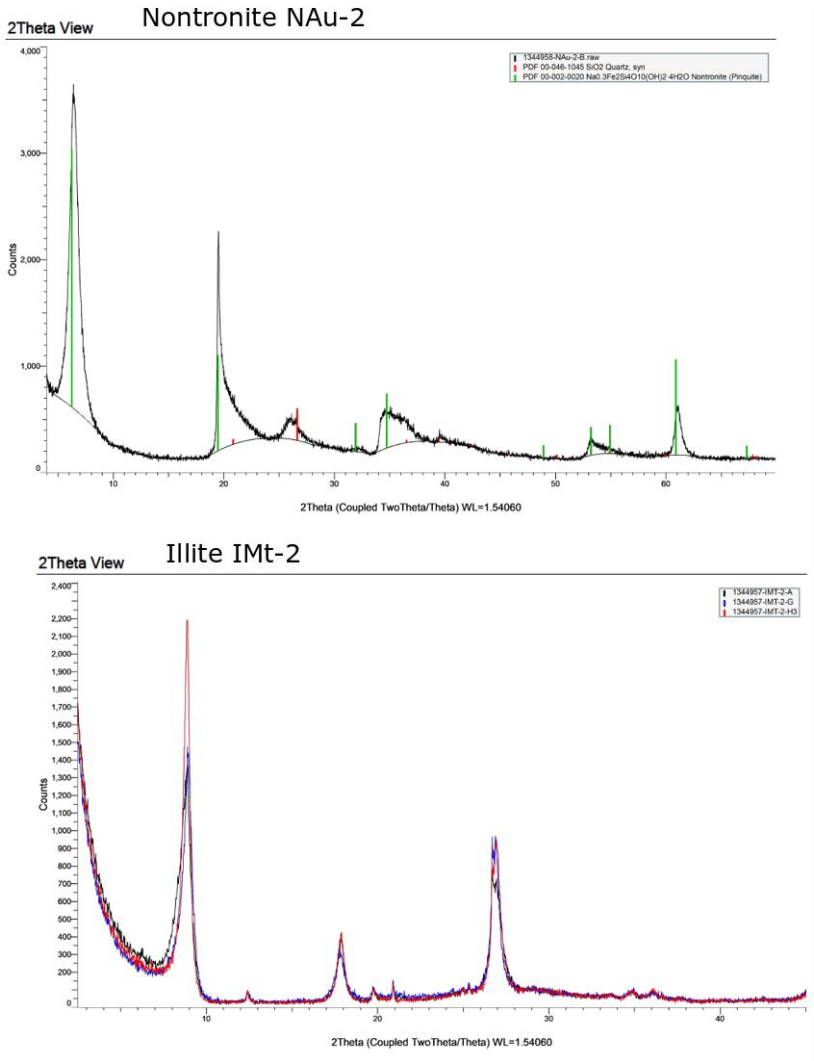

Figure 5.2. Quantitative XRD patterns of nontronite NAu-2 and illite IMt-2

The SCa-3 pattern is showing montmorillonite as the main phase (see Fig 5.3) was generated by Quantitative X-ray diffraction (XRD) analysis, undertaken by X-ray Mineral Services Ltd, North Wales. It showed mainly montmorillonite phase followed by minor phases of cristobalite and albite (see Table 5.3, 5.4) (in agreement with Liu et al 2018).

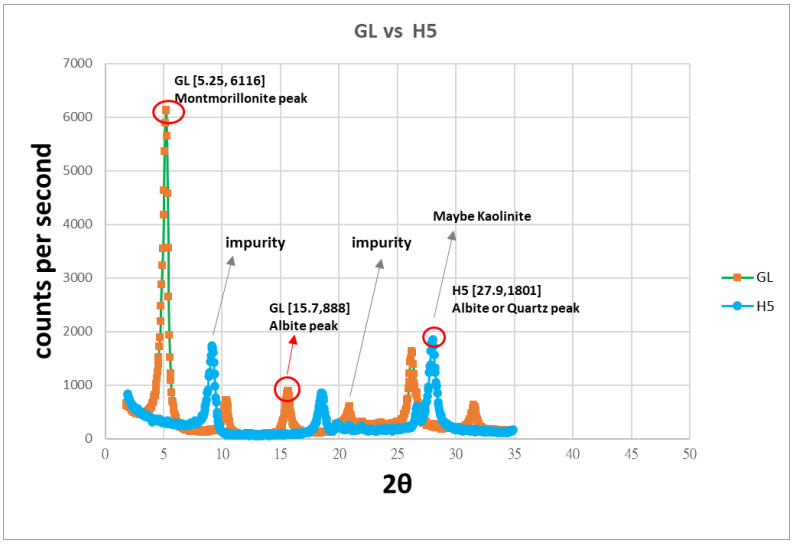

Figure 5.3. XRD oriented filter data shows multiple types of clay minerals within the SCa-3 sample and non-clay mineral impurities. (GL) Glycolated sample (H5) heated at 550°C.

Table 5.3 XRDP bulk mineralogy (weight %) by RIR method.

Sample	**Quartz**	**k-feldspar**	**plagioclase**	**Calcite**	**Anatase**	**Illite/mica**	**Kaolinite**	**Nontronite**	**total**
IMt-2	17.1	4.9	0.3	0.3	0.6	76.3	0.5	-	100
NAu-2	0.5	-	-	-	-	-	-	-	99.5

Table 5.4 Relative percentage of clay minerals in the < 2 µm clay size fraction.

Sample	**Chlorite**	**Kaolinite**	**Illite**	**Smectite**
IMt-2	Trace?	1	99	-
NAu-2	-	-	-	100

Table 5.5 XRDP bulk mineralogy of SCa-3 (weight %)

Sample	**Anatase**	**Quartz**	**Plagioclase**	**k-feldspar**	**Kaolinite**	**Illite**	**Montmorillonite**	**Total non-clay**
SCa-3	-	6.4	4.5	4.3	-	5.4	79.5	15.2

Table 5.6 Relative percentage of clay minerals in the < 2 µm clay size fraction.

Sample	**Wt% <2 µm**	**Smectite**	**Illite /smectite**	**Illite /mica**	**Kaolinite**	**Chlorite**	**Quartz**	**k-feldspar**	**Calcite**	**Dolomite**	**Anatase**	**Pyrite**	**total**
SCa-3	31.9	100	0	0	0	0	Trace	0	0	0	0	0	100

Mössbauer analysis:

The spectra verify a Fe^{2+} - Fe^{e+} ratio of 46.44 – 53.56% and 28.03 – 71.96 for IMt2 and NAu2 samples respectively after reduction.

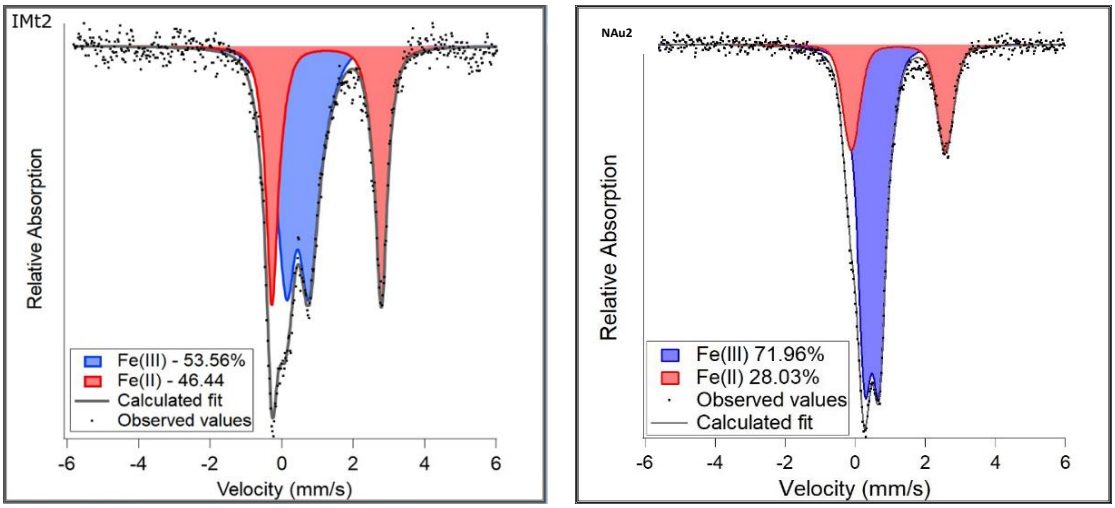

Figure 5.4. Mössbauer spectra of 50% (left) and 30% (right) reduced IMt2 and NAu2 minerals, respectively.

Contact angle measurements:

Contact angle values were obtained in pairs of left and right values for a total of 28 clay coated films (see Table 5.7). An average of those values was calculated for each measurement for every clay film. In the case of a large discrepancy between left and right angle values (usually greater than 10°), the smallest angle was selected. The final contact angle value would then be the average of the 100 readings of either the left or the right measured angle. Schematically this can be seen in Figure 5.5 – Figure 5.7. The derived values were then averaged again and the final contact angle value used for plotting, would represent the average value of all angle readings for each clay film. The plotting of the final averaged value was then done against the number of each set of contact angle measurements taken for every clay film (Figure 5.5 – Figure 5.7), ranging from 1-7 values for

NAu2, 1-6 for IMt2 and 1-5 for SCa3. Error bars indicate the discrepancies between each set of contact angle measurements obtained for each clay film.

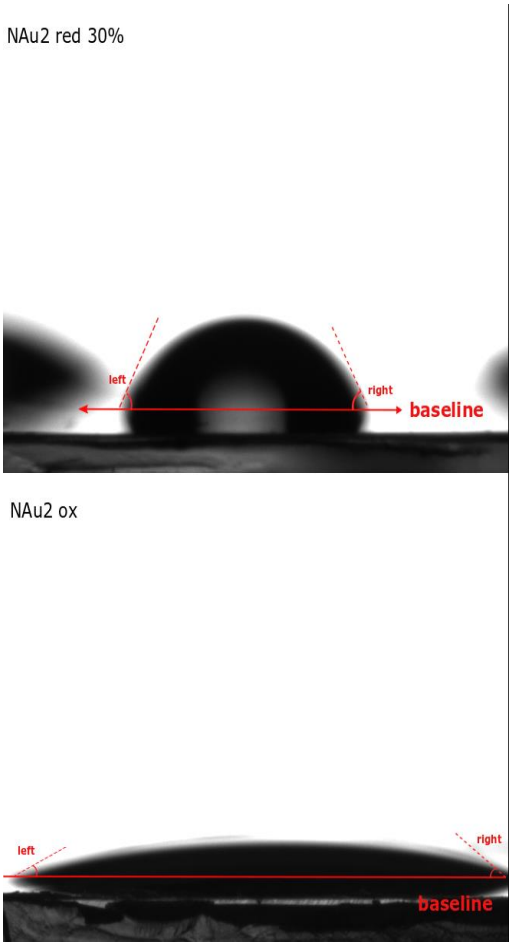

Figure (5.4). Left and right angles of crude oil droplets on oxidized and 30% reduced nontronite NAu2 substrates. The baseline was always re – adjusted before each measurement was taken.

Table 5.7: Contact angle measurements for the oxidized and reduced nontronite (NAu-2), illite (IMt-2) and montmorillonite (SCa-3). Montomorillonite SCa-3 contact angles were measured with air and nitrogen as the gas phase.

Sample	**Contact angle-oxidized (average of five crude oil droplets per clay** film)	**St. deviation**	**Contact angle-reduced (average of five crude oil droplets per clay film)**	**St. deviation**
Nontronite (NAu2)	21.8	2.4	32.4	2.4
	21.1	1.8	31	1.3
	22.3	2	33	1.6
	23	2.1	33	2
	21	1.7	34	0.4
Illite (IMt2)	25.6	0.7	32.8	2.2
	24	3	33.2	2.4
	25.2	-	32.2	1.8
	25.1	1.8	31.2	1.3
	24.2	-	32.7	1.9
Montomrillonite (SCa3)	**Contact angle crude oil droplet (5 point average) in air**	**St. deviation**	**Contact angle crude oil droplet (5 point average) in nitrogen**	**St. deviation**
	22.7	2.1	23.5	2
	23.3	3	24.5	2.1
	24.3	1.1	23.1	2.2
	24.6	-	23.1	0..8

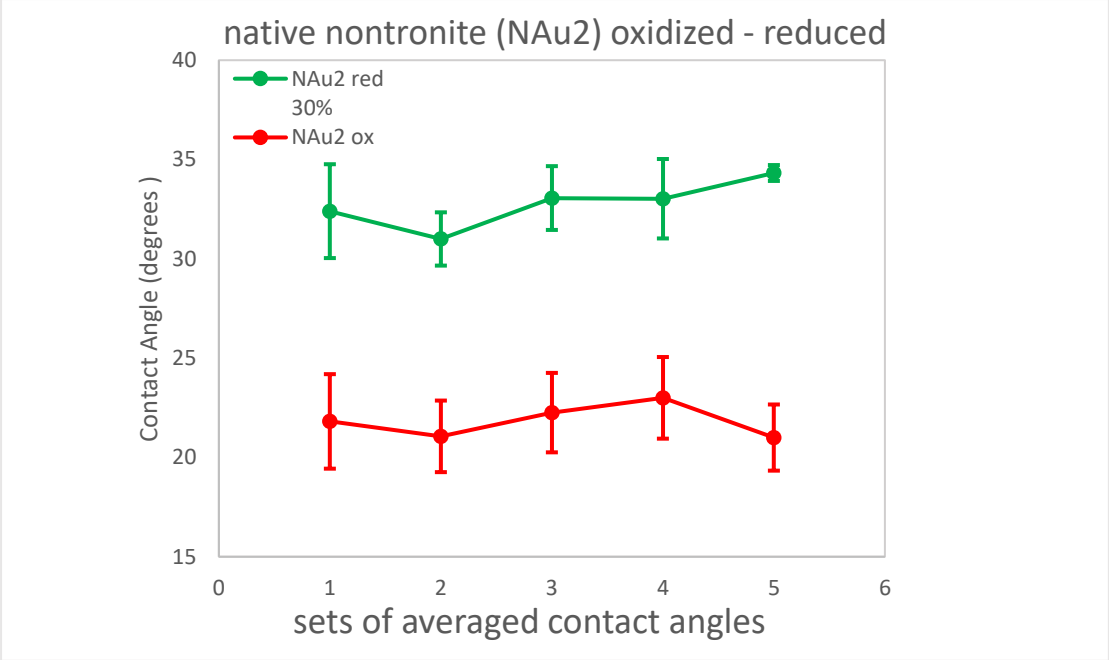

Figure (5.5). Contact angles of crude oil on nontronite (NAu2) films in oxidized and reduced – anoxic conditions. Error bars indicate the discrepancies between each set of contact angle measurements obtained for each clay substrate.

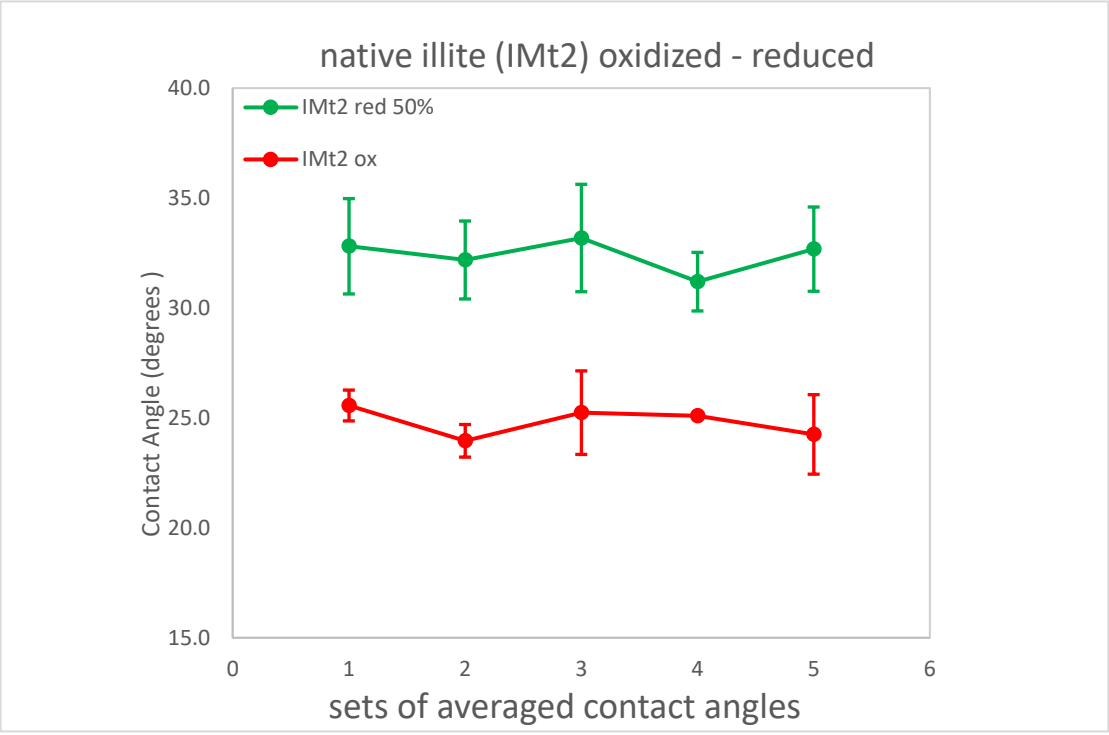

Figure (5.6). Contact angles of crude oil on illite (IMt2) films in oxidized and reduced – anoxic conditions. Error bars indicate the discrepancies between each set of contact angle measurements obtained for each clay substrate.

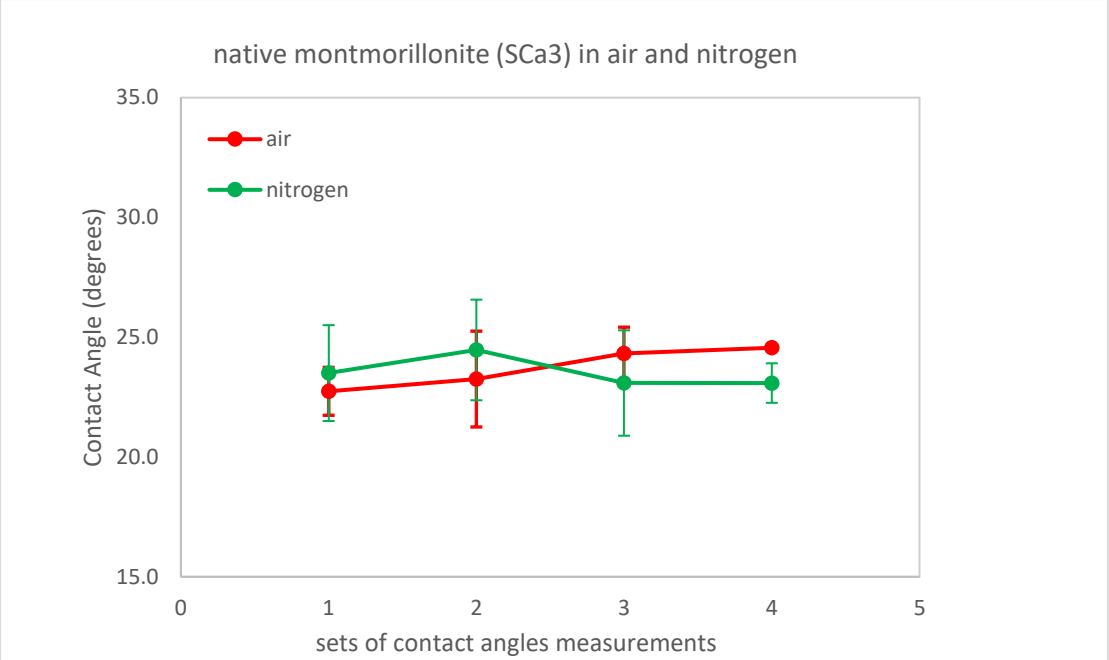

Figure (5.7). Contact angles of crude oil on montmorillonite (SCa3) films in oxidized and reduced – anoxic conditions. Error bars indicate the discrepancies between each set of contact angle measurements obtained for each clay substrate.

5.4 Discussion

Clay mineralogy:
The major and minor phases of the clay minerals in their oxidized state were identified using XRD analysis. Their admixed phases and their proportions were verified and found to correspond well with literature reports and verify purity of the samples (see Section 5.3 and references therein).

Partial chemical reduction was achieved as was measured with Mössbauer spectroscopy. In addition to the Mössbauer spectra, visual changes were evident in the clay mineral post-reduction and particularly in nontronite NAu-2 by means of color change (see Chapter 3: Methods, Section 3.3, Figure 3.10), indicating the change in iron reduction extent. Visual changes between oxidized and reduced smectites is an observation in agreement with the work of O'Loughlin et al (2020). After fully chemically reducing NAu-2 samples using a reducing agent citrate-bicarbonate-dithionite (cbd), they saw distinct color changes upon reduction – chemically reduced NAu-2 was blue in color. NAu-2 and SCa-3 are similar in terms of structure and exchangeable cation composition (see ICP-OES in Chapter 7). Key in this study is that both clays show a similar CA when oxidized but where NAu-2 changes significantly on reduction, SCa-3 does remains the same as very

low iron does not allow for control over the reduction extent. NAu-2, will pick up Na and some cation exchange will occur in illite as well upon chemical reduction. Overall, it would seem as illite has uptaken Na but due to relatively little structural iron present, it can be assumed that the Na is what may drive the contact angle change.

Surface texture:

It has been well understood by previous studies that roughness is interconnected with the wetting behavior of surfaces (Oliver, Huh and Mason 1980; Miller et al 1996; Miwa et al 2000; Volpe et al 2002). In terms of the engineered roughness of the clay films, three methods for surface characterization were used (see appendix), both contact (Atomic Force Microscopy) and non-contact (CCI Interferometry, Confocal Microscopy), to constrain their engineered roughness profile (see Chapter 4). The results (see appendix 4.1) were generated prior to the reduction of the clay films and the measuring of contact angles. The values were subjected to ISO characterization in accordance with the CEN, Comité Européen de Normalisation and the ISO, the International Organization for Standardization, specifically the EN ISO 4288 and indicated that they are bellow any ISO standard. Roughness values were therefore classified as "primary roughness values", $Ra_{primary}$ and were only used for the purpose of verifying a degree of consistency among the produced clay films. Using the $Ra_{primary}$ values derived from AFM and CCI Interferometry, along with the mapped fluorescence intensities of the clay films (see Chapter 4 for details), relative consistency was proven across all substrates with small discrepancies between them.

Contact angle differentiation:

In oxidized conditions, contact angles for all three clay minerals seem to be similar and in the range of 20-24 degrees. That is a considerable consistency among the values, indicating that crude oil wetting is relatively the same across both types of clays (i.e. smectite and non-smectite) and that roughness consistency was achieved in the making process. Although subtle variations of roughness (see appendix A.1) were present in the oxidized group samples, contact angles remained consistent throughout, indicating the roughness discrepancies, at the nm scale, did not account for a change in wetting. Apeiranthitis (PhD thesis, 2021) measured crude oil contact angles in oxidized smectite NAu-2 films and recorded similar values (25°), thus there is consistency among this present study and his.

Wettability alteration:

The contact angle measurements indicated that less surface tension occurs at the surface of the clay films post-reduction. In the three-phase system which characterizes the system under study; i.e. clay film, crude oil and nitrogen as the vapor phase or air in the case of oxidizing conditions, the angle between the solid and liquid increased. Due to the scarcity in contact angle measurements taken under reduced conditions, using the specific swelling and non-swelling types of clay minerals, a comparison between these findings and literature is problematic. However, in the most recent study by Apeiranthitis and co-workers (2021, manuscript in preparation), it has been shown that under complete iron reduction of redox active swelling and non-swelling types (i.e. nontronite NAu1 and illite IMt2) contact angles increased, indicating a less oil-wet surface, proving consistency between these findings and theirs. In their study they reported values of 10 – 15 degrees higher contact angles between crude oil and clay films for the reduced samples, compared to the oxidised, using the sessile drop method.

Previous published work on the changes of wettability as a function of chemical reduction (Yesufu-Rufai et al., 2020), has shown a decrease in wettability at the redox active mineral – oil interface. With the use of sodium dithionite as a reducing agent, the AFM measured adhesion between the Bandera brown sandstone and various polar and non-polar oils, the rock surface-oil adhesion was shown to decrease as a redox function. Adhesion between a functionalized tip and the sandstone's surface was improved upon reduction (by 70%).

Iron reduction effect:

iron – bearing clay mineral reduction, plays a key role for the equilibrium between clay layers and their interfacial water and cations. Reduction of structural iron de – stabilizes this equilibrium, forcing both the interlayer and the other clay layers to re – adjust to reach the new equilibrium state interlayer separation (Yan and Stucki 2000). The SO_4^{2-} free radicals transfer electrons to $Fe^{3+,}$ causing the crystal structure to destabilize due to the increased number of negative charge, which requires more cations which then increases attractive forces between the interlayer cations and layers. A further reduction would cause partial dehydroxylation and activation of Al sites inside the crystal lattice of the clay. Ultimately, during reduction, electrons in contact with structural iron (Fe^{3+}) reduce it to Fe^{2+}, reforming the structure of the clay (Gan, Stucki and Bailey 1992) (see more details on clay reduction mechanisms and subsequent changes in clay properties in Chapter 2). Contact angle values show the SCa-3 is not changed, with no Fe, providing a control. Changes occur where structural Fe is present. The change is as dramatic whether both for the rich and the poor iron clays (NAu and IMt-2). It can therefore be assumed that the reason of change in

wettability is unlikely to be just about the charge or amount of interlayer/surface ion. To answer this, the cation needs to be explored.

Cation exchanges in oxidized and reduced states:
In oxidized conditions the NAu2, with a calcium cation-rich interlayer and surface sites, shows crude oil contact angle values ranging from 21-23 degrees. The potassium-rich IMt-2 illite shows crude oil contact angle values ranging from 24-25.6 degrees and the sodium-rich SCa3 smectite shows crude oil contact angles between 22.7-24.6 degrees. Given that the relative humidity conditions remained unaltered (RH 30% at room temperature) during the testing and that surface roughness was excluded from being a controlling factor (see Chapter 4), the interlayer cation should account for the changes in wettability at the interface between clay surface, crude oil and air as the vapor phase.

The effect of cation on the wetting of clay substrates has been previously shown by Ballah and co-workers (2016). They suggested that water droplets wet smectite coated glass surfaces differently relative to the interlayer cation present using the static sessile drop contact angle method. Contact angles were higher for the K and Ca rich samples (29 and 28 degrees) and lower for Li samples (26), when 1 M of NaCl was probed. Their results are dissimilar to ours (21 to 25 degrees approx.) indicating less water wetting in oxidized conditions compared with crude oil wetting. Although in this present study crude oil wetting was tested onto the clay substrates, the findings of the above mentioned workers are indicative of the implications that the interlayer cation and subsequent layer charge have on the enthalpy of clay hydration and wettability. Crude oil appeared to wet the clay surfaces in the order of NAu-2 < SCa-3 < IMt-2.

In reduced conditions, a concentration of the cations (mmol cation/ mmol Si) occurs as a general trend favouring dehydration and cation exchange in both nontronite NAu-2 and illite IMt-2 (see ICP-OES analyses in Chapter 7). This is consistent with the literature in the case of chemically reduced smectites, specifically nontronites (Garfield) and their changes on cation concentrations (Stucki 2011; also see Chapter 2: Literature Review and references therein). A sodium increase is a direct effect of the exchange in both NAu2 and IMt2 clay minerals as a result of chemical reduction using buffer agents sodium citrate, sodium bicarbonate and reducing agent sodium dithionite. There is scarcity of literature about the cation exchange capacity of the IMt2 with regards to reduction states, due to its low iron not allowing for extensive control over the redox state. However, the changes in the wettability are shown through the increase in crude oil contact angles of both redox states. More specifically crude oil contact angle onto nontronite NAu-2 was in the range of 31-34 degrees after reduction and the respective crude oil contact angle of IMt-2 was 31.2-33.2 degrees. There was no observed change in the crude oil contact angle values at the

SCa-3 coated glass substrate – crude oil – nitrogen (vapor phase) interface. Since chemical reduction was not possible in the montmorillonite due to its near-zero iron content, the measurement was only taken in any potential effect of the nitrogen atmosphere conditions used in the reduced sample contact angle measurements, relative to the oxidised undertaken in air.

The amounts of the cation constituents were successfully changed due to electrons from the reducing agent, in the form of SO_4^{2-} free radicals, donated to NAu-2 and IMt-2 respectively (see Chapter 2 for effects of sodium dithionite on clay minerals), favouring dehydration (Stucki 2011). Cation exchange capacity (CEC) for both iron clays was increased (93.97 from 64.04 meq/100 g for NAu-2 and 182.25 from 178.86 meq/100 g for IMt-2, also see Chpater 7). For the illite, although the clay mineral's surface was dehydrated as a result of reduction, the IMt2 remained K-bearing. Being the low iron (6.2 wt% iron) mineral, IMt-2 did not allow for a complete redistribution of its sites via cation exchanges.

Different reduction extents were achieved for NAu-2 (28%) and IMt-2 (46%), that account for different iron contents (23 wt% for NAu-2 and 7 wt% for IMt-2) and therefore the effects of chemical reduction with regards to cation changes and crude oil contact angles are limited to a qualitative comparison. It is likely that the similarities between crude oil contact angle values of NAu-2 and IMt-2, were not because of a similar interlayer cation but rather due to the increased reduction extent of IMt-2 that compensated for the otherwise limited effects of chemical reduction of the low iron clay. It can be said that since the amount of iron is not similar, then the changes measured were due to the uptake of Na (see ICP-OES data in Chapter 7). Free radicals were more abundant in the case of IMt-2 due to the increased sodium dithionite offer, ultimately leading to similar post reduction effect on cations present and wettability.

Ballah and co – workers (2016) suggested that the hydration energies of the cations are the main driving force of the clay's wettability. Hydration enthalpy of Ca is greater than Na, however for these clays the ratio of Na:Ca is 2:1, hence a balance is maintained. Based on the above, it can be said that the predominant mechanism accounting for the changes in wettability is that of a change in the cations concentrations due to the cation exchange occurring as a result of a chemical reduction by sodium dithionite. As a consequence, the clays' enthalpy of hydration changed leading to dehydration of the clay minerals. This affected the surface of the clays available for adhesion by means of reducing the cations' availability to form bonds with crude oil. Coupled with the subsequent changes induced by clay reduction in clay minerals, such as layer collapse (see Chapter 2: Literature and references therein), after a post-reduction sodium saturation, in an attempt to retain its hydrophilic domains, the clay's affinity towards water shifted its wetting state

to a less – oil wet. While the clay remained sodium-saturated, that shift accounted for the increase in contact angles and changes of wettability of crude oil on the reduced clays.

Within the context of an oil reservoir, the altered wetting of the clay surface, can impact on clay swelling and ultimately reservoir parameters, such as permeability and porosity. This has been shown with swelling (montmorillonites) and non-swelling clays (kaolinite) – clay grain size as well as quartz should also be factored in when measuring porosity and permeability parameters. It was shown that in samples with larger clay grains the permeability decline was not significant after swelling occurred (Aksu et al 2015). Following on tests with water wetting conditions should be performed, also within the redox context, to firther understand how wetting and clay swelling can impact on reservoir parameters. Ultimately, clay wetting and subsequently clay swelling through water interlayer retention, also controlled by redox, can impact reservoir performance.

5.5 Conclusions

An understanding of the changes in the wettability of iron-bearing clay films at the clay film-crude oil interface as function of reduction extent was gained. It was proven that reduction extent is important in terms of changes at the surface of both swelling and non-swelling types of clay minerals. The sensitivity of the wetting state of the clay films to the reduction extent was tested by performing partial chemical reduction on clay minerals. By using small reduction extents for nontronite and illite (i.e. 28% and 46% respectively) to study their wettability, the starting point for the study of changes of the properties of iron-bearing clay minerals with regard to greater reduction extents within the context of fines migration was set.

Contact angle measurements showed that when iron is present in the clay structure allowing for a control over the reduction extent, the increase in crude oil contact angle on the clay films is 10 degrees on average, making the clay substrates less oil wet. Partially reduced nontronite NAu-2 and illite IMt-2 with iron content of 23 wt% and 7 wt% respectively, showed a 10 degree increase in the crude oil contact angle when compared with the native – oxidized clay films. Further work is needed so that homoiionic calys and effects of redox on those are understood in terms of crude oil wetting. Montmorillonite SCa-3 (CMS) with bellow 1 wt% iron in its structure showed no change in the contact angle of crude oil, verifying that in the absence of iron, no changes in wettability are evident. The decreased oil-wetting of the clay films can be attributed to post-reduction changes of cation enthalpy of hydration and clay dehydration, leading to changes at the surface of the clay minerals and clay films, having an immediate effect on the interface of clay and crude

oil. Ultimately, it can be said that fines migration can be induced in redox environments be means of a decreased adhesion at the clay-oil interface inside clastic reservoirs.

Concluding it can be said that reduction extent is important for changing the surface wetting of both swelling and non-swelling types of clay minerals, also present inside clastic reservoirs. The sensitivity of the wetting state of the clay films to the reduction extent was tested by performing partial chemical reduction on iron clay minerals. Based on the results i.e. reduced wettability post-reduction, it could be thought that adhesion forces at the clay/crude oil interface in the reduced conditions of a reservoir are in favor of fines mobility. By deploying LSWF previous equilibrium is disrupted and the mobilization of fines affected by the mechanisms explained above.

Future work:
In terms of clay film preparation, both a qualitative and quantitative surface characterization post-reduction could be used to elucidate the degree to which surface topography (i.e. roughness and waviness) is changed. At present, the roughness of the oxidised prepared film is assumed to reflect the roughness of the reduced film. Consequently, an understanding of the effect of chemical reduction on the surface of clay films will be gained. For that, both contact and non-contact techniques are suitable: atomic force microscopy and scanning electron microscopy could be used to probe changes at the clay film surface.

Regarding iron reduction extent, clay films could be further reduced to larger extents – up to complete iron reduction, in order to better quantify the changes of the wetting state of the clay films via their crude oil contact angles in further reduced states. Ultimately, contact angle values relative to the entire reduction extent spectrum could be gained.

In addition to the sessile drop method, other wettability measuring techniques could be utilized to assess the wetting state of the films relative to reduction extent: The captive bubble method could be used; where the clay film is immersed in a liquid, with its surface positioned underside and the wetting state is measured by means of the formation of a gass-bubble. In the case of Low Salinity Water Flooding, the liquid could be brine. To achieve anaerobic conditions, constant purging with nitrogen should occur during the run time of the experiment.

5.6 References

1. Aksu, I., E. Bazilevskaya, and Z. T. Karpyn. "Swelling of clay minerals in unconsolidated porous media and its impact on permeability." *GeoResJ* 7 (2015): 1-13.
2. Apeiranthitis, N., Neumann, A., Greenwell H. C., Redox dependency of wettability of iron-bearing clay minerals: implications for enhanced oil recovery. Energy and Fuels, 2021 (under submission)
3. Apeiranthitis, Nikolaos. Understanding enhanced oil recovery (EOR) in sandstone reservoirs: the role of redox changes in clay minerals on wettability, Department of Earth Sciences, Durham University, United Kingdom, 2021
4. Borysenko, Artem, Ben Clennell, Rossen Sedev, Iko Burgar, John Ralston, Mark Raven, David Dewhurst, and Keyu Liu. "Experimental investigations of the wettability of clays and shales." *Journal of Geophysical Research: Solid Earth* 114, no. B7 (2009).
5. Butler, Benjamin M., and Stephen Hillier. "Automated full-pattern summation of X-ray powder diffraction data for high-throughput quantification of clay-bearing mixtures." *Clays and Clay Minerals* 69, no. 1 (2021): 38-51.
6. Gailhanou, Hélène, Philippe Vieillard, Philippe Blanc, Arnault Lassin, Renaud Denoyel, Emily Bloch, Guy De Weireld et al. "Methodology for determining the thermodynamic properties of smectite hydration." *Applied Geochemistry* 82 (2017): 146-163.
7. Haines, S. H., van der Pluijm, B. A., Ikari, M. J., Saffer, D. M., and Marone, C. (2009), Clay fabric intensity in natural and artificial fault gouges: Implications for brittle fault zone processes and sedimentary basin clay fabric evolution, *J. Geophys. Res.*, 114, B05406
8. Hillier, Stephen. "Quantitative analysis of clay and other minerals in sandstones by X-ray powder diffraction (XRPD)." *Clay mineral cements in sandstones* (1999): 213-251.
9. Hillier, Steve. "Use of an air brush to spray dry samples for X-ray powder diffraction." *Clay Minerals* 34, no. 1 (1999): 127-135.
10. Huamin, Gan, Joseph W. Stucki, and George W. Bailey. "Reduction of structural iron in ferruginous smectite by free radicals." *Clays and Clay Minerals* 40, no. 6 (1992): 659-665.
11. Jackson, Matthew D., Dawoud Al-Mahrouqi, and Jan Vinogradov. "Zeta potential in oil-water-carbonate systems and its impact on oil recovery during controlled salinity water-flooding." *Scientific reports* 6, no. 1 (2016): 1-13.
12. Jańczuk, Bronisław, Emil Chibowski, Mieczysław Hajnos, Tomasz Białopiotrowicz, and Janusz Stawiński. "Influence of exchangeable cations on the surface free energy of

kaolinite as determined from contact angles." *Clays and Clay Minerals* 37, no. 3 (1989): 269-272.

13. KAREEM, RIKAN, and ALI MOHAMMED. "Nano Geochemistry of Low Salinity Enhanced Oil Recovery." PhD diss., Durham University, 2017.
14. Keeling, John L., Mark D. Raven, and Will P. Gates. "Geology and characterization of two hydrothermal nontronites from weathered metamorphic rocks at the Uley graphite mine, South Australia." *Clays and Clay Minerals* 48, no. 5 (2000): 537-548.
15. Ksiezniak, Katarzyna, Andrzej Rogala, and Jan Hupka. "Wettability of shale rock as an indicator of fracturing fluid composition." *Physicochemical Problems of Mineral Processing* 51 (2015).
16. Lebedeva, Evgenia V., and Andrew Fogden. "Adhesion of oil to kaolinite in water." *Environmental science & technology* 44, no. 24 (2010): 9470-9475.
17. Lebedeva, Evgenia V., Andrew Fogden, Tim J. Senden, and Mark A. Knackstedt. "Kaolinite Wettability—The Effect of Salinity, pH and Calcium." *Society of Core Analysts* (2010).
18. Liu, Chao, A. M. Omer, and Xiao-kun Ouyang. "Adsorptive removal of cationic methylene blue dye using carboxymethyl cellulose/k-carrageenan/activated montmorillonite composite beads: Isotherm and kinetic studies." *International journal of biological macromolecules* 106 (2018): 823-833.
19. Marsh, Alastair, Andrew Heath, Pascaline Patureau, Mark Evernden, and Pete Walker. "Alkali activation behaviour of un-calcined montmorillonite and illite clay minerals." *Applied Clay Science* 166 (2018): 250-261.
20. Miller, J. D., S. Veeramasuneni, J. Drelich, M. R. Yalamanchili, and G. Yamauchi. "Effect of roughness as determined by atomic force microscopy on the wetting properties of PTFE thin films." *Polymer Engineering & Science* 36, no. 14 (1996): 1849-1855.
21. Morrow, Norman R. "Wettability and its effect on oil recovery." *Journal of petroleum technology* 42, no. 12 (1990): 1476-1484.
22. Neumann, Anke, Michael Sander, and Thomas B. Hofstetter. "Redox properties of structural Fe in smectite clay minerals." In *Aquatic Redox Chemistry*, pp. 361-379. American Chemical Society, 2011.
23. O'Loughlin, Edward J., Maxim I. Boyanov, Kenneth M. Kemner, and Korbinian O. Thalhammer. "Reduction of Hg (II) by Fe (II)-Bearing Smectite Clay Minerals." *Minerals* 10, no. 12 (2020): 1079.
24. Oliver, J. P., C. Huh, and S. G. Mason. "An experimental study of some effects of solid surface roughness on wetting." *Colloids and surfaces* 1, no. 1 (1980): 79-104.

25. Omotoso, Oladipo, Douglas K. McCarty, Stephen Hillier, and Reinhard Kleeberg. "Some successful approaches to quantitative mineral analysis as revealed by the 3rd Reynolds Cup contest." *Clays and Clay Minerals* 54, no. 6 (2006): 748-760.
26. Strand, Skule, Tina Puntervold, and Tor Austad. "Effect of temperature on enhanced oil recovery from mixed-wet chalk cores by spontaneous imbibition and forced displacement using seawater." *Energy & Fuels* 22, no. 5 (2008): 3222-3225.
27. Stucki, Joseph W. "A review of the effects of iron redox cycles on smectite properties." *Comptes Rendus Geoscience* 343, no. 2-3 (2011): 199-209.
28. Stucki, Joseph W., D. C. Golden, and Charles B. Roth. "Preparation and handling of dithionite-reduced smectite suspensions." *Clays and Clay Minerals* 32, no. 3 (1984): 191-197.
29. Wei, Bing, Jian Ning, Jielin He, Laiming Lu, Yuanyuan Wang, and Lin Sun. "Relation between brine-crude oil-quartz contact angle formed on flat quartz slides and in capillaries with brine composition: Implications for low-salinity waterflooding." *Colloids and Surfaces A: Physicochemical and Engineering Aspects* 555 (2018): 660-667.
30. Yan, Laibin, and Joseph W. Stucki. "Effects of Structural Fe Oxidation State on the Coupling of Interlayer Water and Structural Si− O Stretching Vibrations in Montmorillonite." *Langmuir* 15, no. 13 (1999): 4648-4657.
31. Yan, Laibin, and Joseph W. Stucki. "Structural perturbations in the solid–water interface of redox transformed nontronite." *Journal of Colloid and Interface Science* 225, no. 2 (2000): 429-439.
32. Yesufu-Rufai, Sherifat, Fons Marcelis, Apostolos Georgiadis, Steffen Berg, Maja Rücker, Johannes van Wunnik, and Paul Luckham. "Atomic Force Microscopy (AFM) study of redox conditions in sandstones: Impact on wettability modification and mineral morphology." *Colloids and Surfaces A: Physicochemical and Engineering Aspects* 597 (2020): 124765.
33. Young, Thomas. "An essay on the cohesion of fluids." In *Abstracts of the Papers Printed in the Philosophical Transactions of the Royal Society of London*, no. 1, pp. 171-172. London: The Royal Society, 1832.

Chapter 6. Infrared Spectroscopy Studies on Native and Reduced Clay Minerals: Implications for Hydration Changes as a Redox Controlled Process

6.1 Introduction

In Chapter 5, it was determined that reduction of ferruginous clay minerals resulted in a marked change in clay wettability to crude oil, not exhibited by similar clay minerals with negligible iron. This change did not relate with the previously determined clay film roughness (Chapter 4), and was determined to be either due to the increased clay mineral charge, or the exchange and uptake of Na^+ ions from the reducing chemistry. To probe these latter effects further, this chapter focuses on the hydration state of clay minerals as a function of their redox state with the use of infrared (IR) spectroscopy. The aim of this study is to understand hydration of iron clay minerals as well as the reversibility of hydration in specific reservoir simulated states (i.e. hydrated after water saturation using relative humidity conditions or dehydrated by vacuum, after production stage), also by using redox as a controlling factor. At a clay mineral level, the idea of varying the RH is to probe which parts of the IR are related to hydration of the cations. Understanding cation hydration helps to understand changes observed during chemical reduction and cation effects vs charge effects.

Hydration of clay minerals is directly linked to their physical properties such as their swelling capacity and wettability (Ballah et al 2016). Cation exchange capacity and cation affinity along with the cations' enthalpies of hydration are all interlinked with the wetting state of the clay mineral that plays an important part in oil recovery (Ballah et al 2016). Tests on the hydration state were performed on natural, untreated clay minerals sourced from the Clay Minerals Repository (Clay Mineral Society, Chantilly, VA, USA). Comparison was made between the obtained IR spectra of oxidized (as received) and of partially reduced and fully reduced clays (using chemical reduction).

Section 6.1 aims at giving a brief introduction to infrared spectroscopy of clay minerals and to the various structural bands that correspond to different regions in the crystal structure of clays. These regions are subjected to stretching and bending phenomena with characteristic vibrational modes, which absorb with characteristic frequencies in the infrared region of the electromagnetic spectrum. Following the introductory part, the materials used, the results and interpretation of the spectra are given in Sections 6.2, 6.3 and 6.4, respectively. The data were obtained in two different areas of the IR spectra; near – infrared (NIR 8000 to 4000 cm^{-1}) and mid – infrared (MIR 4000 to 400 cm^{-1}) for oxidized, partially reduced and fully reduced samples.

Data interpretation was based on the following: a) the targeted region of the specific functional group vibration or bend, how the region shifted from its original position and the intensity associated with the shift, and b) the structural changes in the crystal lattice associated with the redox and hydration states of the clays, expressed as vibrations of the various structural groups.

This interpretation of the IR spectra aims at gaining a better understanding of the differences between oxidized and reduced clays in the clay structure in terms of hydroxyl groups, cations and associated water. Using this approach, conclusions can be reached regarding their relative hydration and dehydration corresponding to the clays' different redox states.

The typically studied IR spectrum of clay minerals covers the MIR and NIR areas. The MIR infrared covers the area between 4000 to 400 cm^{-1} and the NIR the area between 8000 and 4000 cm^{-1} (also see Chapter 2 and references therein).

Nontronite NAu2: The relative bending or stretching of its functional groups can be estimated according to its chemical type that is $(M+_{.97})[Si_{7.57}\ Al._{01}\ Fe_{.42}][Al_{.52}\ Fe_{3.32}\ Mg_{.7}]O_{20}(OH)_4$ (Keeling, J.L.et al. 2000), based on the percentage of each cation included in its structure. It is likely that some vibration bands are masked under the stretching or bending of other more dominant functional groups. In the MIR infrared spectrum, the main group of interest with regards to water are seen in the 3000 – 3500 cm^{-1} (OH^- bands) and in the 3500 – 3700 cm^{-1} (Frost et al 2001). In the

NIR spectra of the dioctahedral NAu2, the band appearing at around 6960 cm^{-1} represents the $2\nu(Fe_2^{3+}OH)$ group (Madejova et al 2000b). In the 4375 cm^{-1} region, a strong $(\nu+\delta)Fe_2^{3+}OH$ band exists (Madejova et al 2017). These bands are of particular interest, especially for the smectite group of minerals, since they show overtones of the hydroxyl groups tied to the structural iron of the minerals.

Typically, in the nontronite structure, octahedral Al^{3+} is totally substituted by Fe^{3+}, resulting in the filling up of site occupancies of the clay (Frost et al 2000). Moreover, during reduction of structural iron in the nontronite, Fe^{2+} gradually takes up the place of octahedral Fe^{3+}, followed by loss of OH^- groups (Rozenson and Kallai 1977). In addition, Stucki and Roth (1977) suggested that during iron reduction, electron transfer from the reducing agent occurs before or during loss of H_2O. Subsequently, they suggested that lower intensity in the curves that correspond to hydroxyl groups (3000 – 3500 cm^{-1} and 4000 – 5000 cm^{-1}) are to be expected in the case of chemical reduction of reduced smectites.

Illite IMt2: The IMt – 2 illite belongs to the family of dioctahedral non – expandable clays. Potassium predominantly takes up site occupancies in the interlayer of the mineral without water molecules attached to it (Gualtiery et al 2008). It is possible that in natural systems NH_4^+ may take up the sites previously occupied by K. In the MIR spectrum, this is seen as a δ(N – H) vibration in the region between 1400 and 1430 cm^{-1} as suggested in the works of Sucha and co – workers (1994), Petit and co – workers (1999a) and Pironon and co – workers (2003). Dioctahedral illites show a vibrating band at 3623 cm^{-1} that corresponds to an OH^- stretch (Madejova et al 2017). A stretching vibration of the Si – O band is visible at 1030 cm^{-1}. Farmer (1974b) suggested that an Al^{IV} – O vibration exists at 831 cm^{-1}. This vibration might also be a result of a AlMgOH stretch. At 756 cm^{-1}, a plane vibration of Al – O – Si is also present (Farmer 1974 b). Van der Marel and Beutelspacher (1974) suggest that the Al – O – Si vibration is also present at 696 cm^{-1} specifically for the IMt2 illite. They also suggested that Al – O – H exists at 901 cm^{-1}. In the NIR section, the main overtones as described by Madejova and co – workers (2017) are as follows: at 7071 cm^{-1}, the overtone band of 2ν(OH), at 4500 the combination of the structural OH^- group, at 4257 cm^{-1} the OH^- combination band that possibly corresponds to ν(SiOAl) and ν(OH) vibrations (Baron and Petit 2016). For the IMt2, changes shown in its spectra are expected to be subtle. That is due to the low percentage of structural iron present. Moreover, since illite is, in most cases, a non – swelling and non – expandable clay due to the potassium or NH_4^+ present inside its interlayer, the presence of initial structural water is minimal (Gualtiery et al 2008).

In terms of the effect of iron reduction on the IR spectra of illite IMt2, to this day, there is no literature covering the topic, since, conventionally, smectite high iron content clay minerals (i.e. NAu2, SWa1, Garfield nontronites), have been used to understand redox processes due to their high iron content. However, in this study, we approached illite IMt2 as a mixed swelling clay with low iron content, with the ability to partially withhold water in site occupancies similar to those of the swelling high iron content nontronite NAu2. Interestingly, as shown in Ch. 5, despite the lower Fe content in IMt2, the contact angle change was similar in magnitude to NAu2. Consequently, the spectral bands measured and interpreted were in the 3000 – 3500 and 3700 cm^{-1} (OH^- stretch), 4000 – 5000 and 5000 cm^{-1} (combination of the structural OH^- group), 6000 and 7000 cm^{-1} (overtone band of 2v(OH)) regions. The specific band descriptors for the IR spectral features for NAu2 and IMt2 in the MIR and NIR spectra are shown in Table 6.1.

Table 6.1: Specific band descriptors for the NAu2 and IMt2 in the MIR and NIR spectra (Frost et al 2001; Sucha and co – workers (1994); Petit and co – workers (1999a); Pironon and co – workers (2003); Neumann et al 2011; Baron and Petit 2016).

Nontronite NAu2 MIR infrared	
3568	Al FeOH stretch
3419	Water OH stretch
1630	HOH bends
Nontronite NAu2 NIR infrared	
7082	Overtone OH stretch (1) (2x) AlFe-OH
5244	H_2O combination
4531	Combination OH stretch and OH deformation of Fe, FeOH
Illite IMt2 MIR infrared MIR infrared	

3623	OH stretch
1800	OH combination
1430	δ(N – H) vibration
Illite IMt2 MIR infrared NIR infrared	
7071	overtone band of 2v(OH)
4500	combination of the structural OH group
4257	OH combination band; possibly corresponds to v(SiOAl) and v(OH) vibrations

6.2 Materials and methods

Materials: The clay minerals were sourced from the Clay Minerals Repository, Chantilly VA, USA. These have been previously described in the methods chapter. XRD characterization was the same as the one described in chapter 5.

Chemical reduction method: In total, two different clay minerals were tested with IR; NAu2 and IMt2. The clay minerals were divided into native-as received, partially reduced and fully reduced batches for the NAu2 and into oxidized, partially and fully reduced for IMt2. NIR and MIR infrared spectra were obtained for all nontronite NAu2 samples. For the illiteIMt2, data were acquired for the native-oxidized, partially reduced and fully reduced in the NIR infrared and for the native-oxidized and fully reduced in the MIR infrared. The chemical reduction method has been previously described in methods chapter. Preparation of clay mineral samples for infrared spectroscopy analysis has been described in methods chapter.

Figure 6.1. Setup of IR Spectroscopy studies. a) 8700 Nicolet IR Spectrometer; b) relative humidity (water) and nitrogen control panel operated manually; c)nitrogen and water tanks and pumping system; d) vacuum pump system monitor and control valves.

Table 6.2. Sample nomenclature table for the MIR and NIR Spectroscopy samples. Samples were measured in oxidized (ox) and reduced (red) 30, 50 and 100% states in atmospheric (air), under

vacuum (vac) for 10, 20, 30 and 45 minutes and under 10, 30 and 70% relative humidity conditions (rh).

Samples	**MIR**	**NIR**
Native nontronite Nau2 (oxidized)	Nau2_ox_air	Nau2_ox_air
	Nau2_ox_vac45min	Nau2_ox_vac45min
	Nau2_ox_rh10	Nau2_ox_rh10
	Nau2_ox_rh70	Nau2_ox_rh70
Native nontronite Nau2 (reduced 30%)	Nau2_red30_air	Nau2_red30_air
	Nau2_red30_vac30min	Nau2_red30_vac30min
	Nau2_red30_rh10	Nau2_red30_rh10
	Nau_red30_rh70	Nau_red30_rh70
Native nontronite Nau2 (reduced 100%)	Nau2_red100_air	Nau2_red100 air
	Nau2_red100_vac20	Nau2_red100_vac20min
	Nau2_red100_rh10	Nau2_red100_rh30
	Nau2_red100_rh70	-
Native illite Imt2 (oxidized)	Imt2_ox_Air	Imt2_ox_air
	Imt2_ox_vac30min	Imt2_ox_vac30min
	Imt2_ox_rh10	Imt2_ox_rh10
	Imt2_ox_rh70	Imt2_ox_rh70
Native illite Imt2 (reduced 50 %)	-	Imt2_red50_air
	-	Imt2_red50_vac20min
	-	Imt2_red50_rh10
	-	Imt2_red50_rh70
Native illite Imt2 (reduced 100%)	Imt2_red100_air	Imt2_red100_air
	Imt2_red100_vac30min	Imt2_red100_vac10min
	Imt2_red100_rh30	Imt2_red100_rh30

6.3 Results

Nontronite NAu2 MIR Infrared: sourced from the CMR, was studied using MIR spectroscopy. Figure B.6.1 shows the MIR spectra of NAu2. As this is a non – homoionized clay that has not undergone any size fractionation process, it is important to note that it includes all the cations found in its native form along with a limited amount of impurities (see Quant% XRD analysis in Materials and Methods section of this chapter). The spectra were acquired after subjecting the sample to various degrees of hydration – relative humidity percentage, dehydration (vacuum), air and nitrogen conditions. The main vibrations in the annotated areas are as seen in Fig B.6.1.

The dehydration of NAu2 starts after the 2356 cm^{-1} (annotated in Fig B.6.1) is developed within the 2500 – 3500 cm^{-1} region (Fig B.6.2), corresponding to the stretching of hydroxyl water found in the FeFeOH group. This is evident in the vacuum curve compared with ambient conditions and RH curves. A small intensity decrease in the same band can be seen in the rehydration curve of RH 10%. Highest rehydration of the sample was achieved in RH 70% conditions. In RH 70%, rehydration is evident in the 2500 – 3140 cm^{-1} as a sharp increase of the intensity, followed by bending of the band between 3140 and 3500 cm^{-1}.

Following the measurements of native NAu2 in oxidized conditions, are the MIR spectra of the partially reduced (30%) nontronite (Fig B.6.3). The achieved iron reduction was 30% as indicated by Mössbauer spectroscopy (see Chapter 5 for Mössbauer analysis). In the MIR spectra shown in Fig (6.4), dehydration of the partially reduced clay is evident in the annotated structural bands.

Dehydration is evident in the band between 2000 and 3200 cm^{-1}, with a clear starting point of dehydration annotated at 2043 cm^{-1} (Fig B.6.4) and in the 3000 and 3600 cm^{-1} in ambient conditions. After 30 minutes of vacuum, further dehydration is noticeable in the following regions: between 1710 and 1800 cm^{-1} shown as a flattened curve, 1800 and 2250 cm^{-1} shown as lower intensity curve, 2250 and 3200 cm^{-1} shown as near – flat curve followed by structural band, between 3200 and 3600 cm^{-1} shown with significantly less intensity than in ambient conditions. Re – hydration of the sample took place in RH 10% and RH 70% conditions, with the latter achieving the highest rehydration in the structural band of the stretching FeFeOH group in the 3200 to 3600 cm^{-1} band.

Following partial reduction, totally reduced NAu2 nontronite (Fig B.6.5) by chemical reduction with the use of sodium dithionite was tested with IR spectroscopy. The annotated bands are, again, showing dehydration through de – hydroxylation and H_2O loss in the structural groups in ambient and vacuum conditions. More specifically, dehydration is evident in the 30 minute vacuum curve, following the measurement of MIR spectrum in ambient conditions (air).

Dehydration is seen in the 1600 cm^{-1} band as bending in the low intensity curve (annotated at 1601 cm^{-1}). Secondly, dehydration in the band between 3000 and 3400 cm^{-1} (Fig B.6.6) is seen as flattened curve of lower intensity as opposed to the same band corresponding to the spectrum measured in ambient conditions. The third visible dehydrated band is in the 3542 cm^{-1} in the FeFeOH functional group. Re – hydration is mostly seen in the RH 70% curve, as a sharp intensity increase in the 1600 cm^{-1} bending group, as a smoother intensity increase in the 1900 cm^{-1} (see Fig 6.6, 1923 cm^{-1} annotation) region and as another sharp intensity increase starting at 3000 cm^{-1} and reaching 3600 cm^{-1}, possibly between the Al – OH and FeFeOH groups. For clarity, the OH^- bands are shown in appendix B.1.

Following the spectra of the total reduction process, the combined spectra of native NAu2 in oxidized, partially reduced and fully reduced conditions are seen in Figures 6.2,a,b,c,d,e,f . The comparison is made between measurements taken in ambient conditions, vacuum conditions and conditions of 70% relative humidity. The main trend is lower intensity of the spectra in the partially and fully reduced samples compared with the oxidized sample in ambient and vacuum conditions. The opposite is true for the rehydrated samples. More specifically, in the spectra measured in ambient conditions, lower intensity in the reduced nontronites is evident in the band just before 1800 cm^{-1} and until the 2000 cm^{-1} as a gradual flattening of the curve, in the band between 2000 cm^{-1} until 2200 cm^{-1}, again as a lower intensity curve compared with the oxidized sample. Moreover, intensity decrease is evident in the 3000 – 3500 cm^{-1} seen as less a steep curve in comparison with the respective curve of the oxidized sample. In vacuum conditions, both partially and fully reduced curves show lower intensity than that of the oxidized sample. The main bands where this is visible are between the 1600 – 1700 cm^{-1} range, 1800 – 2000 cm^{-1} and 3000 – 3500 cm^{-1}. Rehydration of the clays was proven possible in the RH 70% curves. Highest rehydration and re – entering of OH^- and H_2O was possible in the 100% reduced sample compared with oxidized and 30% reduced. This can be seen in the following bands: 1600 cm^{-1}, 2000 – 2200 cm^{-1} and 3000 – 3600 cm^{-1}. The main areas of interest regarding the interpretation of the various spectra lies between 3000 and 4000 cm^{-1} that correspond to dehydrated hydroxyl groups of the clay minerals. Dehydration in this range is expressed as vibrations in the cation – H_2O group, water OH^- stretch, FeFeOH and AlFeOH stretch. Due to the fact that the NAu2 used is a non – homoionized, non – size fractionated clay, the interpretation (see discussion section below) can only be done in approximation and relative to the shape of the various spectra (see section on materials and methods for bulk composition of clay minerals given by XRD analysis).

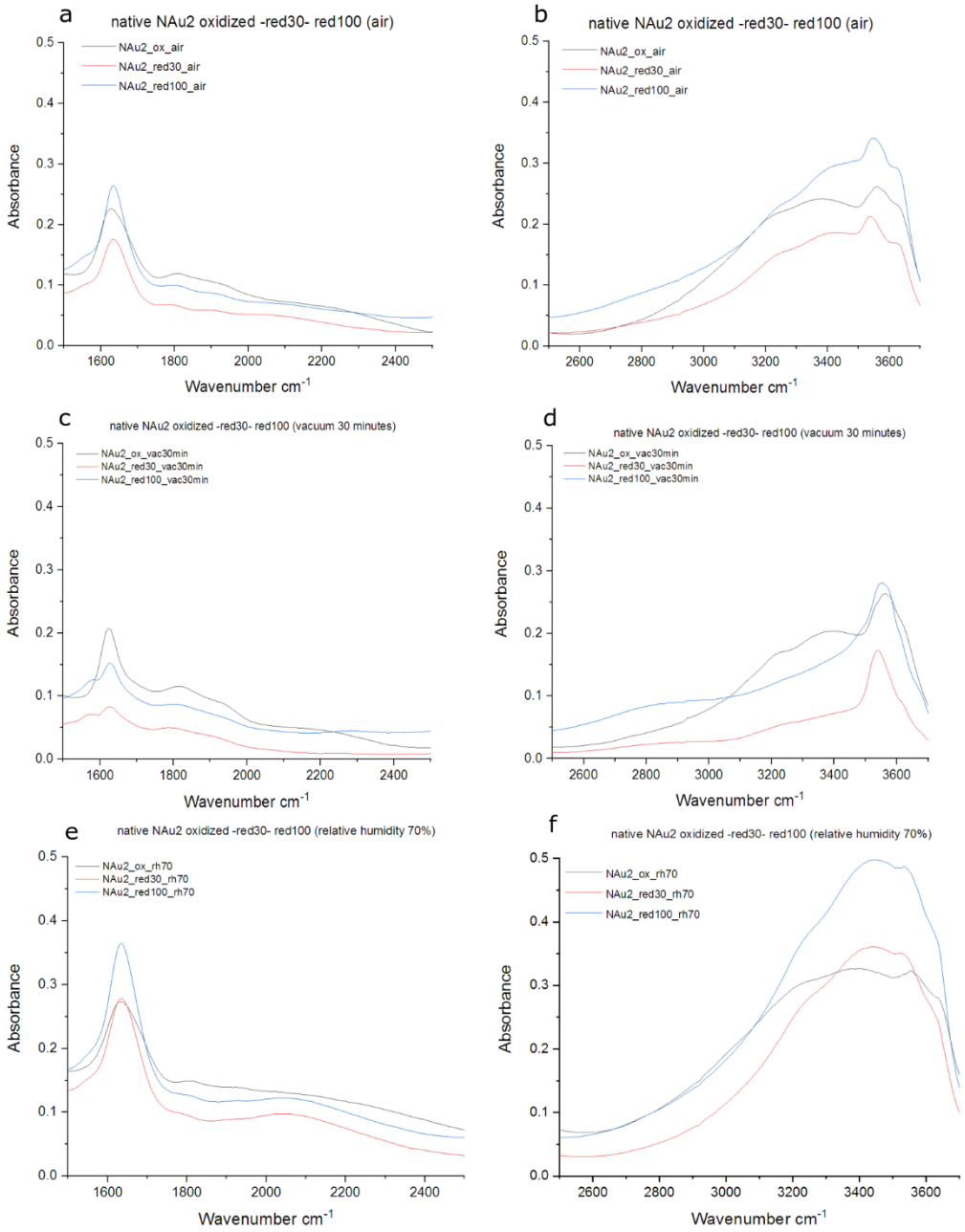

Figure 6.2. MIR spectra for the oxidized, partially and fully reduced nontronite NAu2 in air (a,b), vacuum (c.d) and rehydration state of RH 70% (e,f). Rehydration increases in proportion to the reduction state; higher reduction corresponds to increased rehydration seen as higher intensity curves in the spectra.

Nontronite NAu2 NIR Infrared: Following MIR infrared spectra measurements, NIR infrared measurements were taken for oxidized, partially and fully reduced samples. Data gathered and processed are presented in this section. NIR spectrum measurements were taken for the bands in the 4000 – 7000 cm^{-1} region. Once again, the main dominating trend was dehydration of the reduced samples when compared with the oxidized NAu2. The main overtones of NIR infrared spectra (see annotations in appendix Fig.B.6.8) appear in the bands existing between 4064 cm^{-1} and 4500 cm^{-1}, 5261 cm^{-1} and 7023 cm^{-1}. A clear smoothening of the curve is evident in the vacuum spectrum compared with ambient conditions. After rehydration of the sample in 10% and 70% relative humidity, it is clear that the highest re – hydration was achieved in 70% conditions.

According to Frost and co – workers (2002), the overtones that appear in the NIR spectrum, correspond to the following groups: between the combination of stretching of OH^- and deformation of iron in the FeOH group at 4531 cm^{-1}, in the H_2O combination of deformation and stretching at 5244 cm^{-1} and in the 7082 cm^{-1} overtone of the OH^- stretch (see introduction section and discussion of this chapter). These are found in better detail in appendix B.

Native partially reduced (30%) NAu2 NIR spectra show same perturbations in the 4000 to 7000 cm^{-1} range. More specifically in the 4072 cm^{-1}, 4268 cm^{-1} and 5263 cm^{-1}. The curve under vacuum conditions shows band overtones with extremely low intensity compared with those in ambient conditions. Hydration under 70% of relative humidity is clearly higher than that of 10% of relative humidity in the same annotated bands.

Fully reduced NAu2 NIR spectra are shown in Figure B.6.12. The measured spectra shown are in ambient conditions, in rehydration conditions of 30% RH and after exposure to vacuum for 20 minutes. Overtones appear mainly in the 4404 cm^{-1} band of OH^- deformation and in the 5241 cm^{-1} of H_2O deformation. Dehydration is shown in the vacuum curve as lower intensity in the 4404 cm^{-1} band. Moreover, the flattening of the curve at 5241 cm^{-1} shows further overtone of the H_2O group. That was expressed as an overtone in the 4404 cm^{-1} band. . Overtones are seen in the 4000 – 5000 and in the 5000 – 6000 cm^{-1} region (see appendix B).

A compilation of the NIR spectra between the oxidized, reduced and partially reduced samples is shown in Figure 6.3. Comparisons are made between the spectra in ambient, vacuum and re – hydration conditions. After measurements in ambient conditions, the samples were put under vacuum for 10 minutes to allow for further dehydration. Rehydration of the samples followed in relative humidity conditions of 30%. Subtle structural changes occurred that were expressed as overtones in similar wavenumbers throughout the spectral sets. As a general observation, lower intensity and loss of OH^- structural bands are visible in the reduced samples compared with the

oxidized sample. In ambient conditions, changes in overtones appeared in the 4000 – 5000 cm^{-1}, 5000 – 6000 cm^{-1} regions and around the 7000 cm^{-1}, with lower intensity appearing in the reduced samples in air. In vacuum conditions, overtones appeared again in roughly in the same regions, indicating lower intensity for the partially and fully reduced samples. Finally in the re – hydrated samples, overtones can be seen around the 4200 cm^{-1} – 4500 cm^{-1} and 5000 cm^{-1} – 5400 cm^{-1} with the oxidized sample achieving the most rehydration seen as increased intensity in the respective regions.

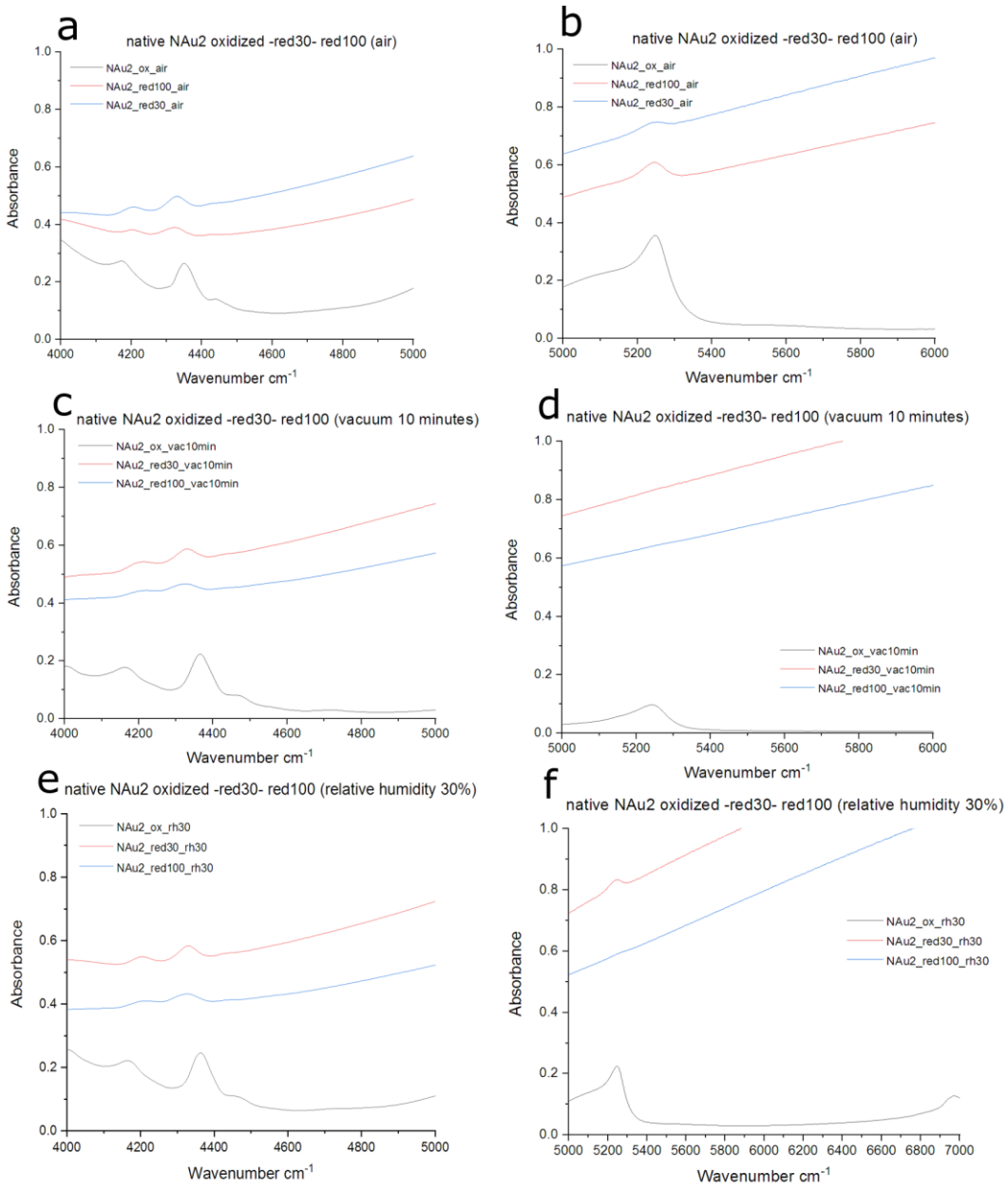

Figure 6.3 NIR spectra of the oxidized, partially and fully reduced NAu2 in ambient, vacuum and relative humidity (RH 30%) rehydration conditions. Overtones recorded in the 4000 – 5000, 5000 – 6000 and 7000 regions as intensity shifts indicating dehydrtation of the reduced samples in air and vacuum conditions and rehydration of the oxidized sample in RH 30%.

Illite IMt2 MIR infrared: The spectra of the native oxidized IMt2 seen in Figure 6.16 were measured in ambient (air), vacuum for 30 minutes and in re – hydration conditions of 10% and 70%. Changes in vibrations are shown in the annotated regions at 1590, 1961, 2998 and at 3400 cm^{-1} respectively. In the vacuum curve, vibrations are indicative of dehydration compared with the spectrum in ambient conditions. This is mainly seen in the 3200 and 3400 cm^{-1} region. After 30 minutes under vacuum, rehydration is evident mainly in RH 70% in the same region. This is expressed as higher intensity in the region. Rehydration curve in the 10% relative humidity conditions only shows a small increase in intensity in the 3200 to 3400 cm^{-1} region. Vibrations of the hydroxyl groups located in the 3000 – 3700 cm^{-1} region. Specific bands showing vibration are annotated and shown as follows. Higher intensity in the region of 1657 cm^{-1} in the air measurement than in vacuum. Higher intensity in the region between 3000 cm^{-1} and 3500 cm^{-1} (Fig B.6.18) is also evident in the air measurement compared with vacuum, indicating dehydration of the clay. After vacuum conditions, gradual rehydration took place at 10% and 30% relative humidity. The same annotated bands show increased intensity in the 30% relative humidity curve.

The spectra between the native oxidized and the native fully reduced IMt – 2 show subtle changes in the spectra indicating a dehydrated reduced clay compared with the oxidized in all conditions. In ambient conditions, vibration changes appear between the 1600 and 2000 cm^{-1} region and in the 3000 and 3600 cm^{-1} region. The H_2O stretching vibrations appearing with lower intensity found in the second region indicate dehydration. After exposure to vacuum for 30 minutes, subtle changes can be seen in the region between 1500 and 2000 cm^{-1} that are intensified in the 3000 – 3500 cm^{-1} region; less intensity curves is evident for the fully reduced sample in this region. Similar changes in the 3000 – 3500 cm^{-1} are present in the rehydration curves with less changes occurring in the 1600 – 2500 cm^{-1} region.

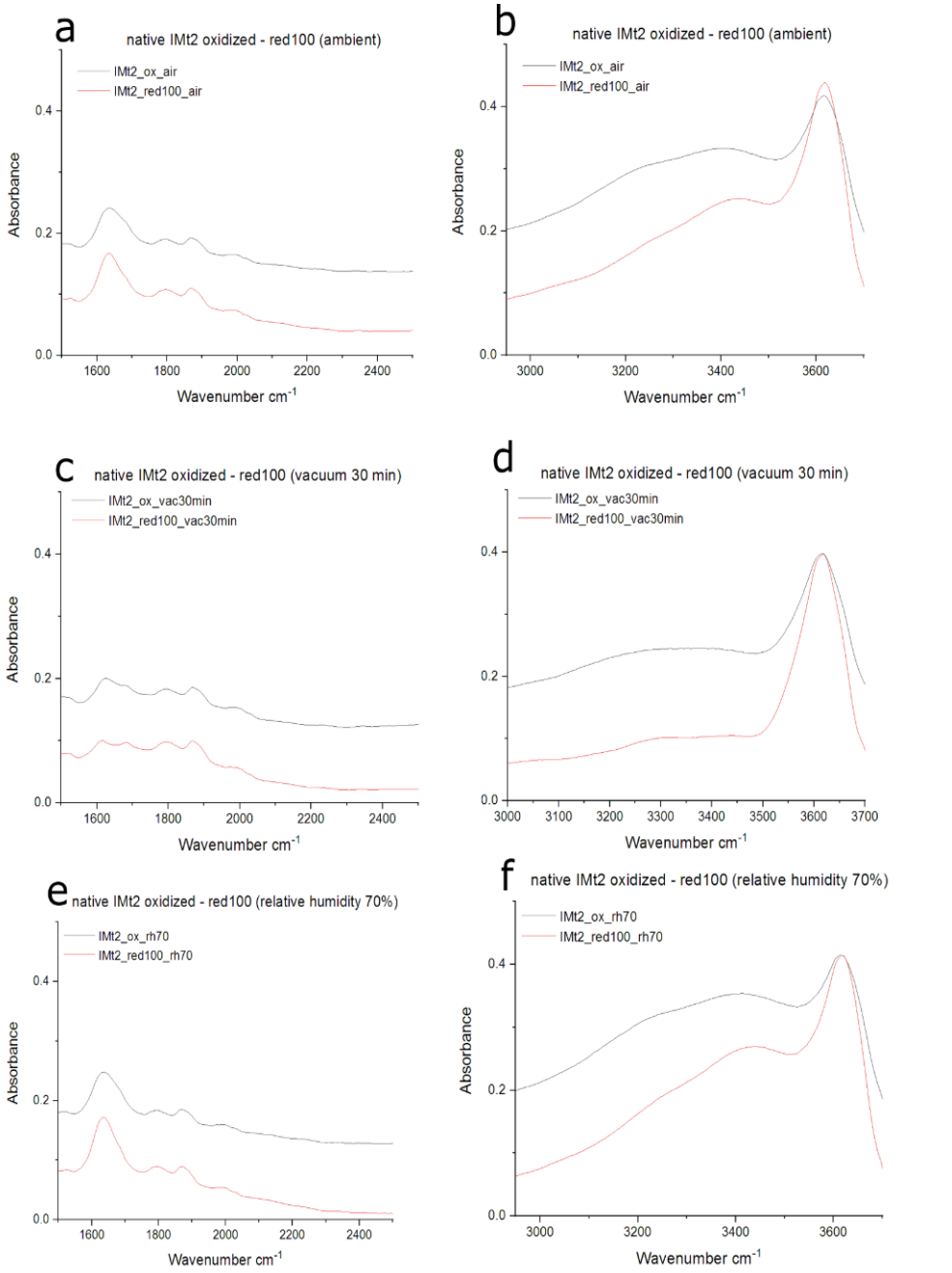

Figure 6.4. Comparison of MIR spectra between oxidized and fully reduced illite IMt2 in ambient (a,b), vacuum (c,d) and rehydration conditions RH 70% (e.f).

Illite IMt2 NIR infrared: Following measurements of the MID spectra of IMt – 2, NIR spectra were measured for the oxidized, partially reduced and fully reduced samples. In the measured native oxidized IMt – 2 spectra, the main vibrations appear in the 4000 – 5500 cm^{-1} and in the 6500 – 7200 cm^{-1} regions. The most significant intensity discrepancies are seen in the vacuum curve, signaling the overtones in the structural OH^- group, along with a combination of the stretching of OH^- group. Moreover in the 7145 cm^{-1} region the bending and stretching of the OH^- indicated

further dehydration of the sample. Subtle changes in intensity between the vacuum, RH 10% and RH 70% curves are seen in the same regions.

The NIR spectra of the partially (50%) reduced IMt2 is shows main overtones appear around the 4216 cm^{-1}, in the 4423 cm^{-1}, in the 5050 cm^{-1} and around 7200 cm^{-1}. Only subtle changes can be seen between the spectra in ambient and vacuum conditions, indicating a low vibration in the NIR region. Small changes in intensity do however indicate a subtle dehydration and a hydration in RH 10% and RH 70% conditions. Overall, the spectral profile of the partially reduced IMt2 does not show dramatic changes between measurements.

In the fully reduced (100%) IMt2 spectra, overtones appear in the regions between 4337 cm^{-1} and 4487 cm^{-1} and in the 5267 cm^{-1}. In the 4437 cm^{-1} lower intensity in vacuum indicates a vibration of the OH^- group. Overall, there are small changes in intensity between the air and RH 30% curve. A noticeable intensity shift exists in the 5267 cm^{-1} between all three curves. Highest intensity in this region is shown in ambient conditions, followed by RH 30% and then vacuum conditions (Figure 6.23).

The compilation of the NIR spectra of the native oxidized, partially reduced and fully reduced IMt2 is shown in Figure 6.5. The overall observation is subtle changes in the intensity of the overtones

between the spectra. That is seen in all three sets of data presented. In ambient conditions, subtle changes are evident in the 4500 – 5300 and around 7000 cm^{-1} regions. Highest intensity is seen in the spectra of the oxidized IMt2. Further dehydration of the samples achieved by exposure to vacuum shows that the most dehydrated clay is the fully reduced IMt2 with a very low intensity at 5200 cm^{-1}. Although the time of exposure to vacuum conditions varies for each sample, it is still clear that with gradual reduction and dehydroxilation, dehydration becomes dominant in the reduced samples. The compared vacuum spectra were measured after 30 minutes exposure for

the oxidized sample, 20 minutes exposure for the 50% reduced sample and after 10 minutes exposure for the 100% reduced sample. Although the changes in intensity are indeed subtle between the 50% and 100% spectra, there are clear intensity discrepancies of both spectra when compared with the oxidized IMt2. Similarly to the vacuum spectra, relative humidity curves show low intensity changes between the oxidized and the reduced samples. Overall, the rehydration occurred more intensely in the oxidized sample compared with the 50% and 100% reduced samples. That is evident near the 4500 cm^{-1} and between the 5200 and 5400 cm^{-1} regions (Fig 6.5).

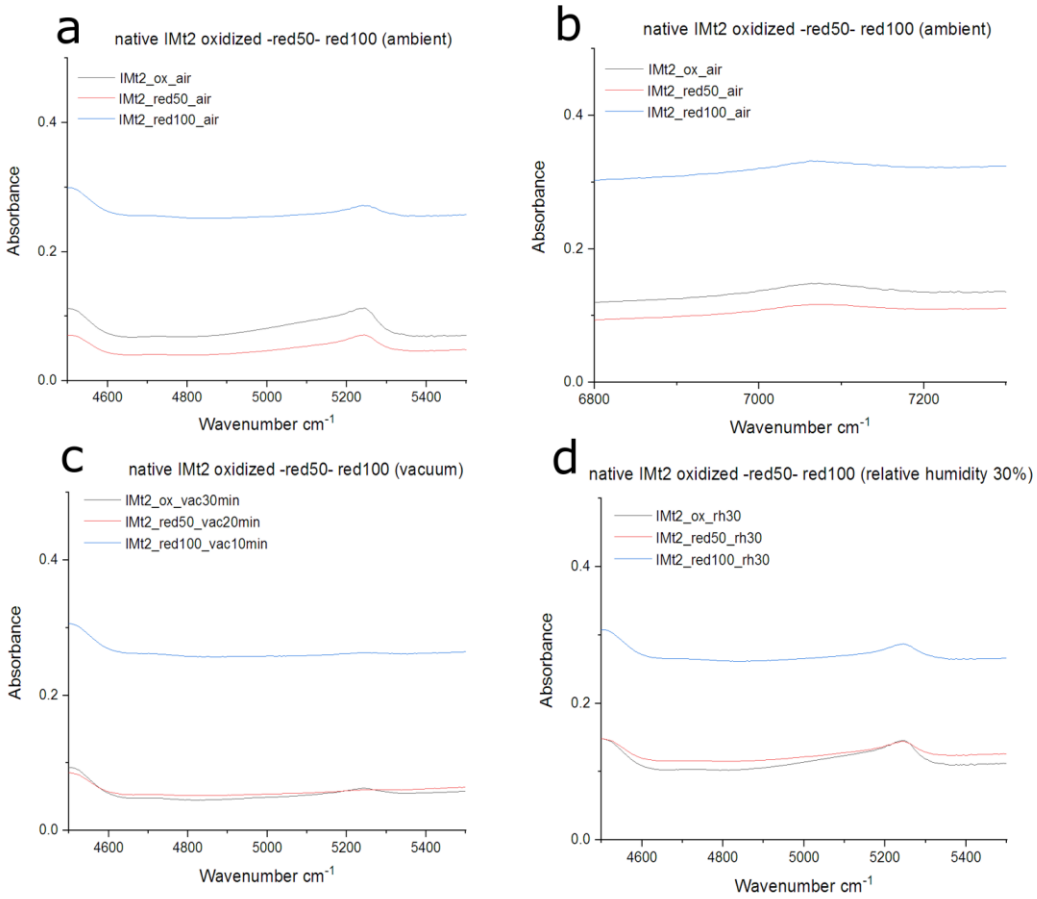

Figure 6.5. Comparison of NIR spectra between the oxidized, partially (50%) reduced and fully (100%) reduced native IMt2; spectra measured in ambient conditions (a,b), vacuum (c) and in rehydration conditions (RH 30%) (d).

6.4 Discussion

In this chapter, the MIR and NIR spectra of the native, non – size fractionated NAu2 and IMt2 clays (CMR Chantilly, VA, USA) were presented after measurements were taken in different redox states.

Changes in the spectra of NAu2 after chemical reduction: The bending and stretching as well as the first overtones expressing either OH^- or H_2O loss are present in the MIR and NIR regions of the spectra for the NAu2 oxidized samples. However, site occupancies changed in the reduced samples due to the rearrangement of the lattice after electron transfer from the donor (sodium dithionite).

More specifically, in ambient conditions, the results of reduction in the MIR spectra was dehydration of the MM – OH combination seen in the 3000 – 3600 cm^{-1} region for both partially

and fully reduced NAu2 samples. In the NIR spectra, dehydration was mainly evident in the 4000 – 4600 cm^{-1} regions for samples in partial and total reduction states.

The well documented dehydroxylation that occurred during chemical reduction of NAu2 as a result of lattice rearrangement is in agreement with findings in the literature regarding reduction of smectite clay minerals (NAu2, SWa1, Garfield nontronites). Loss of the structural OH^- groups has been suggested by workers in the past (Stucki and Roth 1977, Lear and Stucki 1985, Kallai 1997, Drits and Manceau 2000, Neumann et al 2011). These previous findings suggest that during iron reduction, gaining of electrons leads to a change in the Fe^{2+} - Fe^{3+} ratio, results in transferring of ferrous iron to trioctahedral sites, leading to a change in the cation exchange capacity of the clay mineral. Ultimately these changes directly affect the bonding with hydroxyl groups, seen as dehydration and expressed as lower intensity curves.

In vacuum conditions, further loss of water was seen in all spectra of both partially and fully reduced NAu2 samples in comparison to the oxidized samples in the MM – OH bands. These measurements represented extreme dehydration, without heating of the stage.

In terms of the reversibility of dehydration, measurements were taken in various RH degrees show reappearance of hydroxyls groups to a considerable extent. Rehydration was evident mostly in RH conditions of above 30%, by means of the reappearance of OH^- bands in the 3000 – 3600 cm^{-1} and in the 5000 cm^{-1} regions in the MIR and NIR spectra respectively. This rehydration corresponds well with previous work that suggests that rehydration is achieved by rehydroxylation, once IR spectra is similar to the initial spectra (Komadel et al 1990, Fialips et al 2002, Dong et al 2003, Lee et al 2006, Ribeiro et al 2009, Neumann et al 2011). It has been thought that rehydration that occurs as re – entering of OH^- groups, is possibly an indication of pre – existing iron that had remained in the lattice after reduction (Neumann et al 2011), that was ultimately re – hydroxylated in relative humidity (RH) conditions. The rehydration by means of rehydroxylation was in proportion to the reduction state; the more reduced – dehydroxylated NAu2 was significantly more rehydrated through rehydroxylation. After partial reduction and exposure of NAu2 to RH conditions, rehydration was also present as was after total reduction, indicating that the beginning of reversibility of the process is in proportion to the reduction extent. These findings are particularly true for the dioctahedral smectites such as the NAu2 nontronite with high structural Fe^{2+} content indicating the reversibility of the process of dehydration to a considerable extent. Rehydroxylation was increasing in proportion to the increased reduction state; this can be thought of as the effect of the swelling nature of NAu2 nontronite. The more water depleted NAu2 will more readily uptake water in its attempt to replenish its water deficit.

In the MIR spectra, both dehydration and rehydration are more visible than in the NIR for the NAu2. That could be attributed to the combination of the following: a) due to the single stretching motion of the OH – group in the 3500 – 3700 cm^{-1} region that can be more easily visualized, b) to the existence of both lattice and –H - group combined movements that occur between 4000 – 4300 cm^{-1} and 4200 – 4600 cm^{-1} respectively, complicating in this way the spectral visualization and c) to the non – size fractionated used clay minerals, leading to either a noise or masking of such lattice and –H - group movements due to the existence of multiple MM – OH groups.

In the NIR spectra, in ambient conditions, the main changes in intensity of overtones between the oxidized, partially and fully reduced samples, are seen in the 4200 – 4600 cm^{-1} and in the 5200 cm^{-1} regions. These indicate changes in the combination of OH^- stretch combination and OH^- deformation of FeFeOH (Frost et al 2001; Neumann et al 2011).

Measurements in vacuum conditions in the NIR spectra showed lower intensity for the reduced samples in comparison to the oxidized. This was evident in the same regions that were dehydrated in ambient conditions. Rehydration was inversely proportionate to the reduction state in the NIR spectra; overtones in the 4200 – 4600 cm^{-1} and around the 5200 cm^{-1} regions reappeared with lower intensity for the reduced samples.

Although changes in the lattice were evident through significant dehydroxylation both in MIR and NIR spectra, an overall preservation of the silicate structure did appear by means of partial rehydration, especially for the NAu2 smectite that is also in agreement with previous studies (Stucki et al 1984a; Komadel et al 1995; Ribeiro et al 2009, Neumann et al 2011).

Changes in the spectra of IMt2 after chemical reduction: Similarly to NAu2 nontronite, changes are evident in the non – smectite IMt2 lattice. The results of reduction in the MIR spectra was, again, dehydration in the 3000 – 3600 cm^{-1} region of the MM – OH combination for the fully reduced illite. However, due to the low iron content, MIR spectra were only measured for the oxidized and fully reduced illite samples.

Although illite is known to partially uptake water, it is clear that its dehydration through the mechanism of dehydroxylation is evident in its spectra after measurements taken in air (see results section 6.4). Since the IR Spectroscopy method can only detect octahedral Fe^{2+} that forms bonds with hydroxyl groups (Neumann et al 2011), the loss of water should account for the loss of OH^- groups. These hydroxyl groups possibly exist in the interlayer of the IMt2, attributing for a partially hydrated illite (Wentworth 1970).

After vacuum conditions were applied, dehydroxylation in the 1600 – 2000 cm^{-1} (OH combination) and 3000 – 3600 cm^{-1} (OH stretch) regions became mostly evident in the fully reduced IMt2. For illite IMt2, this is indicative of further dehydration.

Subtle rehydration is evident by the reappearance of OH^- groups in the previously dehydrated bands during exposure of IMt2 to relative humidity conditions of 70%. The reversibility of the iron reduction process is not as dominant as in the case of NAu2, although OH^- groups do reappear, confirming both the existence of remaining iron and the partial water uptake present inside the IMt2. Rehydration of the fully reduced IMt2 was not as dominant as the one seen in the fully reduced NAu2. In this regard, re – entering of hydroxyl bands is not in proportion to the reduction state of the illite. The oxidized illite was more readily rehydrated than the fully reduced in the MIR spectra. This can be thought of as the effect of the non – swelling nature of IMt2, limiting its potential to hold water. Based on the IR spectra of the rehydrated IMt2, it can be said that hydration through iron reduction is not entirely a reversible process. These findings are consistent throughout the MIR and NIR spectra of IMt2, making them internally consistent (this study).

In the NIR spectra, overtones in the 4200 – 4600 cm^{-1} corresponding to the bending and stretching combination of hydroxyl groups are seen with lower intensity for the reduced IMt2 samples. The 5200 cm^{-1} peaks are possibly a continuation of the the structural (v+δ) OH combination that occurs around 4500 cm^{-1} (Madejova et al 2017). Similar trends in the overtone intensities are seen in the vacuum and rehydration conditions, indicating dehydration and subsequent rehydration signaling reversible changes in the clay mineral.

As a general observation, both MIR and NIR spectra correlate well, indicating that changes in illite, with the predominant one being the loss of OH^- groups due to chemical iron reduction, is possible and reversible in iron bearing smectites and partially - swelling clays. Partial reduction had the same effects, mainly for NAu2, possibly due to the high Fe^{2+} - Fe^{3+} ratio that accounted for better discerned changes, whereas the effects were less evident in the IMt2 spectra due to low structural iron present The main mechanism of dehydration that could be suggested based on this study, is the loss of hydroxyl groups as a direct effect of reduction process. Along with this, numerous studies mainly in smectite clay minerals (i.e. SWa1, Garfield nontronites) suggest that a direct effect of reduction, either chemical or biological, is the collapse of the interlayer. Therefore water room becomes less available for the smectites in an initial reduced environment (see Chapter 1: Literature Review and references therein). The dehydration effect appears consistent across illite and nontronite, though less reduction possible in illite.

The documented dehydroxylation responsible for dehydration, is also important for oil extraction, mainly from coal and shales as it typically follows the extraction (Frost and Vassallo 1996). As this is a mechanism mostly studied for kaolinite (White et al 1970), little comparison is possible with nontronite and illite due to their different interlayer cation and surface properties (i.e. surface water retention). Constraining dehydroxylation by applying different reduction states to the clay minerals, deepens the understanding of this mechanism.

6.5 Conclusions

Reduction seems to account for less water present in both swelling and non-swelling types; both clay types chosen for this study hold less water if initial conditions are reduced conditions as was qualitatively seen in the MIR and NIR spectra. Less water was visualized as lower intensity curves indicating the dehydroxylation that was consistent throughout the measurements. Higher dehydration was achieved by nontronite NAu2, possibly due to its swelling nature, existing cations and the higher iron present. Illite IMt2 was dehydrated in proportion to the increased reduction, however subtle intensity changes indicate less hydration, again, in proportion to the significantly lower iron present. Both clay minerals allowed for rehydration to occur after they were introduced to relative humidity conditions, proving the reversibility of the process of chemical reduction.

Implications for EOR and Fines Migration in clastic reservoirs: In petroleum reservoirs, where the conditions are thought to be anoxic and reduced, clay minerals exist in a reduced state. Based on the measured IR spectra relative to reduction states shown above, it is now understood that the clay minerals are also dehydrated, with less hydroxyls available when found in those initial reduced conditions - the main mechanism of dehydration was the loss of hydroxyl groups as a direct effect of reduction process. It can be therefore thought that the swellability both at the surface and in the bulk of the clays (i.e. interlayer) will be significantly affected in relation to the reduction state. Ultimately, the swellability of the clay minerals will have a direct impact on the potential migration of fines (i.e. clay – water –oil), making swelling an important process that is redox controlled. The relevant reservoir conditions in which clay minerals appear to be in varying hydration states can now be identified as follows: a) initial reservoir conditions – reduced state with dehydrated clay minerals in the interlayer followed by b) hydration - an intermediate state during Low Salinity deployment with hydration shifting towards a more hydrated clay in all sites; c) production stage with totally oxidized/0fullyhydrated clays.

6.6 Further work

Based on the above, it is important to understand how the adsorption properties of clay minerals change relative to reduction states. This way the surface properties of the clay minerals relative to reduction will be constrained. An understanding of what happens at the interface of the fluid – solid (i.e. vapor gas - clay mineral surface) is critical in order to quantitatively measure the changes at the surface of the clay minerals as a redox controlled process. These changes should be then coupled with what happens deeper into the clay structure (i.e. interlayer) with regards to reduction state. Both of these further studies would eventually culminate in the development of a more holistic view on how redox active clay minerals behave relative to their swellability at the surface and in the bulk. Ultimately that would potentially provide an understanding with regards to their migration in reservoir conditions during the deployment of EOR methods.

6.7 References

1 Ballah, J., M. Chamerois, S. Durand-Vidal, N. Malikova, P. Levitz, and L. J. Michot. "Effect of chemical and geometrical parameters influencing the wettability of smectite clay films." *Colloids and Surfaces A: Physicochemical and Engineering Aspects* 511 (2016): 255-263.

2 Baron, Fabien, Sabine Petit, Emmanuel Tertre, and Alain Decarreau. "Influence of aqueous Si and Fe speciation on tetrahedral Fe (III) substitutions in nontronites: A clay synthesis approach." *Clays and Clay Minerals* 64, no. 3 (2016): 230-244.

3 Dong, Hailiang, Joel E. Kostka, and Jinwook Kim. "Microscopic evidence for microbial dissolution of smectite." *Clays and Clay Minerals* 51, no. 5 (2003): 502-512.

4 Drits, V. A., and A. Manceau. "A model for the mechanism of Fe3+ to Fe2+ reduction in dioctahedral smectites." *Clays and Clay Minerals* 48, no. 2 (2000): 185-195.

5 Frost, R. L., J. Kristof, E. Horvath, and J. T. Kloprogge. "Kaolinite hydroxyls in dimethylsulphoxide-intercalated kaolinites at 77 K–a Raman spectroscopic study." *Clay Minerals* 35, no. 2 (2000): 443-454.

6 Frost, Ray L., Oliver B. Locos, Huada Ruan, and J. Theo Kloprogge. "Near-infrared and mid-infrared spectroscopic study of sepiolites and palygorskites." *Vibrational Spectroscopy* 27, no. 1 (2001): 1-13.

7 Frost, Ray L., and Anthony M. Vassallo. "The dehydroxylation of the kaolinite clay minerals using infrared emission spectroscopy." *Clays and Clay minerals* 44, no. 5 (1996): 635-651.

8 Gualtieri, Alessandro F., Simone Ferrari, Matteo Leoni, Georg Grathoff, Richard Hugo, Mouath Shatnawi, Gianluca Paglia, and Simon Billinge. "Structural characterization of the clay mineral illite-1M." *Journal of Applied Crystallography* 41, no. 2 (2008): 402-415.

9 Keeling, John L., Mark D. Raven, and Will P. Gates. "Geology and characterization of two hydrothermal nontronites from weathered metamorphic rocks at the Uley graphite mine, South Australia." *Clays and Clay Minerals* 48, no. 5 (2000): 537-548.

10 Komadel, Peter, Paul R. Lear, and Joseph W. Stucki. "Reduction and reoxidation of nontronite: Extent of reduction and reaction rates." *Clays and Clay Minerals* 38, no. 2 (1990): 203-208.

11 Madejová, J. "FTIR techniques in clay mineral studies." *Vibrational spectroscopy* 31, no. 1 (2003): 1-10.

12 Madejová, J., W. P. Gates, and S. Petit. "IR spectra of clay minerals." In *Developments in clay science*, vol. 8, pp. 107-149. Elsevier, 2017.

13 Neumann, Anke, Michael Sander, and Thomas B. Hofstetter. "Redox properties of structural Fe in smectite clay minerals." In *Aquatic Redox Chemistry*, pp. 361-379. American Chemical Society, 2011.

14 Nieto, Fernando, Marcello Mellini, and Isabel Abad. "The role of H3O+ in the crystal structure of illite." *Clays and Clay Minerals* 58, no. 2 (2010): 238-246.

15 Petit, S., D. Righi, J. Madejova, and A. Decarreau. "Interpretation of the infrared spectrum of the-clays: application to the evaluation of the layer charge." *Clay Minerals* 34, no. 4 (1999): 543-549.

16 Pironon, J., M. Pelletier, P. De Donato, and Régine Mosser-Ruck. "Characterization of smectite and illite by FTIR spectroscopy of interlayer NH 4+ cations." *Clay Minerals* 38, no. 2 (2003): 201-211.

17 Ribeiro, Fabiana R., José D. Fabris, Joel E. Kostka, Peter Komadel, and Joseph W. Stucki. "Comparisons of structural iron reduction in smectites by bacteria and dithionite: II. A variable-temperature Mössbauer spectroscopic study of Garfield nontronite." *Pure and Applied Chemistry* 81, no. 8 (2009): 1499-1509.

18 Rozenson, I., and L. Heller-Kallai. "Mössbauer spectra of dioctahedral smectites." *Clays and Clay Minerals* 25, no. 2 (1977): 94-101.

19 Stucki, J. W., and C. B. Roth. "Oxidation-reduction mechanism for structural iron in nontronite." *Soil Science Society of America Journal* 41, no. 4 (1977): 808-814.

20 Stucki, Joseph W., D. C. Golden, and Charles B. Roth. "Effects of reduction and reoxidation of structural iron on the surface charge and dissolution of dioctahedral smectites." *Clays and Clay Minerals* 32, no. 5 (1984): 350-356.

21 Šucha, V., I. Kraus, and J. Madejova. "Ammonium illite from anchimetamorphic shales associated with anthracite in the Zemplinicum of the Western Carpathians." *Clay Minerals* 29, no. 3 (1994): 369-377.

22 Van der Marel, Herman Willem, and Hans Beutelspacher. *Atlas of infrared spectroscopy of clay minerals and their admixtures*. Elsevier Publishing Company., 1976.

23 Wentworth, Sally A. "Illite." *Clay Science* 3, no. 6 (1969): 140-155.

24 White, Joe L., Anitra Laycock, and Maribel Cruz. "Infrared studies of proton delocalization in kaolinite." *Bulletin du Groupe français des Argiles* 22, no. 2 (1970): 157-165.

Chapter 7. Effect of Redox State on Water Sorption by Swelling and Non-Swelling Clay Minerals

This is a paper chapter that has been accepted for publication in MDPI Minerals. The format of tables, style and referencing has been changed for overall consistency within the PhD thesis – the paper version (online) follows the MDPI Minerals publishing guidelines.

Abstract**:** Ferruginous clay minerals in saturated soils and within hydrocarbon deposits are likely to exist in a reduced state. Upon introduction of dissolved oxygen, or other oxidants, the clay minerals will oxidise and changes in mineral sorption capacity may occur, resulting in changes in hydration as well as flux in intercalated species. Here we examine the sorption of water to the Fe-containing clay minerals nontronite NAu-2 (23 wt% Fe) and illite IMt-2 (7 wt% Fe) as a function of Fe oxidation state and exchangeable cations by means of water vapour volumetry and N_2 BET method. The clay minerals were chemically reduced using sodium dithionite. Sorption isotherms of water vapour and nitrogen, controlled relative humidity diffractograms, and chemical analyses were recorded. The results show that, after reduction, increased amounts of water vapour and nitrogen were adsorbed to the high Fe content nontronite, despite decreased interlayer distances. Little change was observed for the non-swelling and low Fe content illite. Calcium cations were also found to exchange with sodium from the reducing agent, and sodium balanced the additional mineral charge generated during reduction. The findings presented in this study deliver improved understanding of sorption at the surface of the reduced clay minerals, which will aid constraining the role of clay minerals in subsurface environments.

7.1 Introduction

Water adsorption–desorption isotherms are used as an important tool for measuring water kinetics and the thermodynamic state at the surface of the clay–water vapour system. Early work on factors important in controlling clay hydration suggested that the initial hydration state of the clay was important (Thomas 1921, 1921a). This was determined by wetting and drying treatments of clay mineral rich soil prior to measuring the vapour pressure–moisture relationship. The degree of aggregation of the clay prior to hydration was also found to be a key parameter that affected the moisture content of the clay, as shown by Josheph (1927). By studying submicroscopic samples from centrifugation of soil samples, Josheph showed that there was a significant difference in water capacity between the original clay, the colloid and the residue. By isolating the colloidal material from soils and undertaking washing and performing cation substitution experiments, Anderson concluded that oxide and salt concentration within the clay are also controlling factors (Anderson 1929). It is clear that clay mineral hydration also depends on the interlayer cations that readily exchange in the presence of water (Foster 1954; Noreish 1954; Zhang 1989). In these studies, it was shown that clay mineral hydration by means of the exchangeable interlayer cation occurred as hydrating the interlayer cation forces clay mineral layers apart, leading to either crystalline or osmotic swelling. The underpinning mechanism has been extensively studied and reviewed comprehensively (Anderson et al 2010). In short, during swelling discrete integer-layer hydrates form within the clay mineral interlayers (Mooney et al 1952). The accumulation of hydrate layers forms quasi-crystal structures in the interlayer space, thus creating stepwise increased spacing in the interlayer. Computational chemistry simulations have confirmed this mechanism of clay hydration (Karaborni et al 1996; Hensen et al 2002) and indicated that accumulation of layer hydrates occurs gradually, leading to the adsorbed water molecules forming discrete hydration layers in the interlayer during initial swelling.

Clay hydration by means of water vapour adsorption is a dynamic and progressive process that is also controlled by the pressure of water vapour, the temperature at which the clay–water system equilibrates, the type of clay mineral, the chemical composition of the system and the water activity during equilibrium (Tardy and Touret 1987). The surface hydration and dehydration of clay minerals exhibit a complete solid solution between the hydrated and dehydrated end members of the clay mineral(Tardy and Fritz 1981). In addition to the work of Tardy and Touret (1987), clay hydration energies also correlate with the layer charge, as shown by Tardy and Duplay (1992).

Hydration, either at the surface or in a bulk material, is a time-dependent condition, and this is also the case in clay mineral–water systems, where the shifting from dry to wet states occurs gradually and equilibrium sorption experiments are important tools to defining hydration. Calculating the free energy of hydration, ΔG_{HYD}, is key in determining whether equilibrium is attained. Based on the observations made by Tardy and Touret (1987), Tardy and Duplay (1992) proposed a model for measuring the ΔG_{HYD} for a series of smectite and non-smectite clay minerals. The authors concluded that stability fields, meaning the distinct, individual phases of these minerals (solid, liquid, colloidal), the equilibrium constant and concentration of the phases (solubility products) and the corresponding chemical composition of the clay minerals, were primarily controlled by the following factors: the size of the crystal grain, the composition of layer charge and nature of the interlayer cation and, ultimately, the hydration state of the clay. Subsequent to these studies, considerable research has been undertaken to understand clay swelling and stability under hydration (Smalley 2006).

To quantitatively measure adsorption of gases at clay mineral surfaces, the principles of the Brunauer-Emmett-Teller (BET) method are used. These principles are based on a previous model proposed by Langmuir (1918), used to describe the dynamic equilibrium in adsorbent–adsorbate systems based on the kinetics of sorption and desorption of a gaseous phase to and from a surface. The theory of the more evolved BET model (Brunauer et al 1938) is based on the premise that the mineral surface is homogeneous and lateral interactions do not occur between adsorbate molecules. Moreover, adsorption energy is the same for all sites and adsorption can occur in an infinite number of layers, whereas Langmuir's theory was limited to one surface layer of adsorbate molecules. Based on the type of material, the generated isotherms can vary in type. In general, there are five distinct types of isotherms (Brunauer et al 1938), describing the creation of mono- or multi-layers at different pressures and constant temperature.

Although much research has highlighted the importance of layer charge and type of interlayer cation on the hydration and swelling behaviour of clay minerals, less effort has focused on understanding how these properties might be affected in anaerobic conditions typical for saturated soils and hydrocarbon reservoirs. In these reducing environments, structural Fe in clay minerals becomes reduced, increasing the clay mineral's layer charge, which is balanced by the uptake of cations, and/or subsequent dehydroxylation in case of high Fe content clay minerals reduced to high extents. However, the effect of these structural changes on the sorption characteristics of ferruginous clay minerals have not been explored.

In this study, we combine water vapour volumetry and nitrogen BET methods with X-ray diffraction analyses to investigate the effects of clay mineral Fe reduction on (1) bulk water

adsorption, (2) changes in clay mineral surface area and pore structure and (3) the relative contribution of clay mineral interlayers and micro/macro-pores for water uptake.

7.2 Materials and Methods

7.2.1. Clay mineral preparation:

To allow comparison with previous studies, the clay minerals were sourced from the Clay Minerals Society's Source Clay Repository (www.clays.org) (Nieto et al 2010). The minerals have been previously described in chapter 3 (methods) Similar values were obtained with minor discrepancies from ICP-OES analysis of fully digested samples, as shown in the supplementary information (see Table S1 in supplementary material). The mineralogy of the clay minerals used has previously been described by others, with the nontronite NAu-2 described as 95% nontronite, 5% plagioclase and below 1% quartz (Keeling et al 2000), whereas the Illite IMt-2 has a bulk mineralogy of illite 89.3%, followed by 7.5%, 2%, 0.9% and 0.3% quartz, microcline, rutile and kaolinite, respectively (Chang et al 2011). Each sample obtained was also analysed for mineralogy as detailed below. The method for clay sample preparation for XRD has been described previously.

Both clay minerals were chemically reduced using dithionite as the reductant following the method described by Neumann et al. (2011). The method for chemical reduction has been described previously (methods chapter).

The nomenclature for the samples prepared is: Oxidised nontronite NAu-2 = NAu-2 OX; Partially reduced nontronite NAu-2 (50%) = NAu-2 PARED; 100% Reduced nontronite NAu-2 = NAu-2 RED; Oxidised illite IMt-2 = IMt-2 OX; Partially reduced illite IMt-2 (50%) = IMt-2 PARED; Reduced illite IMt-2 = IMt-2 RED.

7.2.2 X-ray diffraction analysis

For each of the clay minerals used, quantitative bulk and clay fraction powder X-ray diffraction analysis (XRD) was undertaken at the James Hutton Institute, Aberdeen to verify mineralogical composition. For bulk (whole sample) quantitative analysis samples were wet ground for 12 minutes (in ethanol or water) in a McCrone mill and spray dried to produce random powder specimens (Hihllier 1999). X-ray powder diffraction (XRPD) patterns were recorded on a Bruker D8 Advance instrument from 4-70 °2θ using Ni filtered Cu radiation and counting for 96 s per 0.019° step. Quantitative analysis was made by a normalised full pattern reference intensity ratio (RIR) method as described in Omosoto et al. (2003) and Butler and Hillier (2021). Unless stated

otherwise, expanded uncertainty using a coverage factor of 2, i.e. 95% confidence, is given by ±X 0.35, where X = concentration in wt.%., e.g. 30 wt.% ±3.3 (Hillier 2003). Note also, that for phases present at the trace level (< 1%) there may also have been uncertainty as to whether or not the phase was truly present in the sample.

For semi-quantitative analysis of clay minerals based on their basal reflections, clay fractions of <2 µm were obtained by timed sedimentation, prepared as oriented mounts using the filter peel transfer technique and scanned from 2.5-45 °2θ using the Bruker D8 Advance instrument and counting for 16.5 s per 0.019° step. Three scans were made, one in the air-dried state, one after glycolation (vapour pressure 24 hours), and one after heating to 300 °C for one hour. Clay minerals identified were quantified using a mineral intensity factor approach based on calculated XRPD patterns (Hillier 2003). For clay minerals present in amounts >10 wt% uncertainty is estimated as better than ±5 wt% at the 95% confidence level.

In order to understand the clay mineral hydration further, controlled relative humidity XRD was undertaken on both clay minerals, in both the reduced and oxidized states, also carried out at the James Hutton Institute, Aberdeen. Duplicate XRD analyses were carried out on further samples of each clay mineral to ensure reproducibility. Humidity was adjusted in approximately 25% steps at ~3%, ~25-30%, ~48-53% and ~70-78% relative humidity. XRPD patterns were recorded on a Panalytical Xpert Pro diffractometer using Fe filtered, Co Kα, radiation, and an X-celerator position sensitive detector with active length set to 2.12°. Specimens were mounted in powder cavity holders in an Anton Paar XRK 900 reactor chamber and purged with N_2 gas at various relative humidities controlled by an external Sycos H gas humidifier. Automatic divergence and antiscatter slits were set to illuminate a constant 6 mm wide area of the specimen and patterns were collected from 3-15° 2θ counting for 250 s per 0.017° step so that each scan took approximately 30 min to collect. Successive runs were made from low to high humidity, and prior to each run the specimen was equilibrated at the given relative humidity for one hour. Peak parameters were measured using Bruker Diffrac Eva software.

7.2.3 Water and nitrogen adsorption measurements

The water and nitrogen isotherms were generated at the Laboratory of Physical Chemistry and Microbiology for Materials and the Environment (LCPME), National Centre for Scientific Research (CNRS), Nancy, France by a volumetric method for the native oxidized and fully reduced samples of NAu-2 and IMt-2. The method for generating adsorption isotherms have been described in the methods chapter.

The determination of a clay mineral's textural changes due to water vapour volume sorption was achieved with the calculation of the specific surface area of water vapour (SSA_w). The SSA_w is defined as the portion of the surface area of the clay mineral that is available to adsorb (Kuila and Prasad 2013) and is, by definition, proportional to the amount of sorption of the volume of water vapour by the clay mineral. An increased uptake of water vapour by the clay is followed by an increase in the SSA_w.

The BET measures the surface area. When nitrogen or water gas is not present, no layer of gas is created. A layer of one molecule thick (monolayer) is expected to be formed after gas molecules are present. After nitrogen saturation has occurred, layers of multiple molecule thickness (multilayer) are formed. Calculations of BET specific surface area for water vapour and nitrogen require the use of Eq.7.1:

$$\frac{1}{V[\left(\frac{P_0}{P}\right)-1]} = \frac{1}{V_m C} + \frac{C-1}{V_m C}\left(\frac{P}{P_0}\right) \quad , (7.1)$$

where the adsorbed volume of gas is V (cm^3/g), P/P_0 (kPa) is the relative pressure, V_m (cm^3/g) is the monolayer volume of adsorbate and C (dimensionless constant related to the enthalpy of adsorption of the adsorbate vapour on the powder sample) is the BET energetic constant (Brunauer et al 1940). Pore size and pore volume were calculated using the Gurwitch rule (D = 4V/S, where D is the average pore diameter, V is the total pore volume and S the specific surface area obtained using the BET model). The assumptions made are that the pores must be homogeneous in diameter, cylindrical and rigid.

7.2.4 Composition analysis of clay minerals

Cation composition of the oxidized and reduced clay minerals was measured using inductively coupled plasma optical emission spectroscopy (ICP-OES) analysis at the University of Greenwich. Samples were fused using a lithium metaborate flux at a sample:flux ratio of 1:5. The resultant melt was dissolved in weak nitric acid and made to volume. Instrumental analysis was performed

using a Thermo ICAP 6500 ICP-OES with calibration established using matrix matched synthetic calibration standards made from ICP grade single element stocks.

7.3 Results

7.3.1. NAu-2 and IMt-2 Water Adsorption Isotherms

Figure 7.1(a) shows the water adsorption for the NAu-2 samples followed the trend of NAu-2 RED > NAu-2 PARED > NAu-2 OX. This is evident at all partial pressures. Hysteresis was evident in both the oxidized and the two reduced NAu-2 samples. Adsorption of water vapour for the partially reduced NAu-2 PARED tracked the NAu-2 OX from 0 to 0.2 P/P_0, but then followed the NAu-2 RED curve from ca 0.4 to 1.0 P/P_0. Water desorption isotherms exhibited similar behavior. At all pressures, the desorption isotherm of NAu-2 RED was higher than both NAu-2 PARED and NAu-2 OX. The NAu-2 PARED desorption followed that of NAu-2 OX from 0 to 0.2 P/P_0, as with the adsorption curve, but this changed from 0.2 to 0.7 P/P_0 where the NAu-2 OX desorption isotherm showed higher sorption than that of NAu-2 RED. The opposite occurred in the 0.6 to 0.9 P/P_0 range, just before the desorption isotherms of both samples intersected at a pressure of 1 P/P_0.

Figure 7.1(b) shows adsorption and desorption isotherms for oxidized and reduced illite IMt-2. Overall, significantly less water vapour adsorption was observed than for nontronite NAu-2 samples (maximum xx% vs yy% mass of water/mass of dry clay), with relatively little hysteresis present in the oxidized sample. Adsorption values appeared higher for the oxidized sample (IMt-2 OX) in the 0-0.65 P/P_0 range, while the IMt-2 RED was higher from 0.65 to 1 P/P_0. The desorption isotherm of IMt-2 RED had higher values for water sorbed at above 0.50 P/P_0 and displayed greater hysteresis than the IMT-2 OX. Below 0.50 P/P_0, the desorption curves of both oxidized and reduced IMt-2 were very similar.

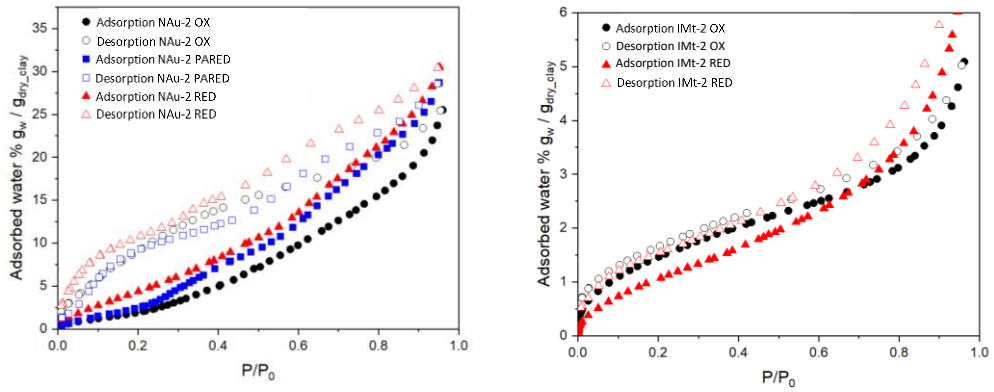

Figure 7.1. Water vapour adsorption-desorption isotherms for (a) oxidized nontronite (NAu-2 OX), 50% reduced nontronite (NAu-2 PARED) and 100% reduced nontronite (NAu-2 RED), and (b) oxidized illite (IMt-2 OX) and reduced illite (IMt-2 RED).

Table 7.1 presents the water adsorption–desorption parameters of nontronite NAu-2 and illite IMt-2 obtained by water vapour volumetry. The specific surface area (SSA_w) was calculated from the water adsorption isotherm at 298 K by the Brunauer, Emmett and Teller (BET) method through multipoint calculation by choosing the result given by the best linear fit in the 0.1 to 0.3 P/P_0 range. The calculated BET SSA_w for the adsorption branch (Table 1) were based on a classic adsorbate cross-sectional area (σ), for which a water molecule area of 14.8 Å² was used (Hagymassy et al 1969; McClellan et al 1967). The SSA_w increased for the NAu-2 samples, correlating with extent of reduction, more than doubling from 115 m²/g to 270 m²/g, whereas the SSA_w for IMt-2 decreased slightly when reduced, from 68 m²/g to 53 m²/g. The C_{BET} water affinity constant, remained at 8 for the NAu-2, irrespective of oxidation state and decreased from 23, for IMt-2 OX, to 13 for the totally reduced IMt-2 RED.

Table 7.1. BET Surface area and energetic constant from water vapour isotherms at 298 K; V_m (cm^3 /g STP) is monolayer volume, S_{BET} (m^2/g) is the water specific surface area and C_{BET} is the energetic constant of water.

	BET		
Samples	**V_m**	**SSA_w**	**C_{BET}**

	(cm³/g STP)	(m²/g)	
IMT-2 OX	17	68	23
IMT-2 RED	13	53	13
NAu-2 OX	28	115	8
NAu-2 PARED	36	140	8
NAu-2 RED	68	270	8

7.3.2 NAu-2 and IMt-2 Nitrogen BET Isotherms

Figure 2a shows the nitrogen adsorption isotherms exhibited a Type IV behavior, as has been first classified by Brunauer et al. (1938). In a Type IV isotherm, the main characteristic is the hysteresis loop that is thought to be associated with capillary condensation occurring in the mesopores of the sample. Moreover, a Type IV isotherm is indicative of a sample's capacity to adsorb in a range of high pressure [30]. In both oxidized and fully reduced nontronite, adsorption hysteresis was evident in the P/P_0 0.48-0.99 pressure range. The monolayer–multilayer formation limit was indicated in the first part of the isotherms at a P/P_0 of 0.04 and 0.06 for NAu-2 OX and NAu-2 RED, respectively, as shown in Figure 2. A very sharp knee seen in the NAu-2 RED sample is indicative of the monolayer completion (Fig. 7.3). The less distinctive knee in the NAu-2 OX isotherm is indicative of monolayer overlapping. Capillary condensation occurred at around 0.8 P/P_0 for both samples. According to the classification of

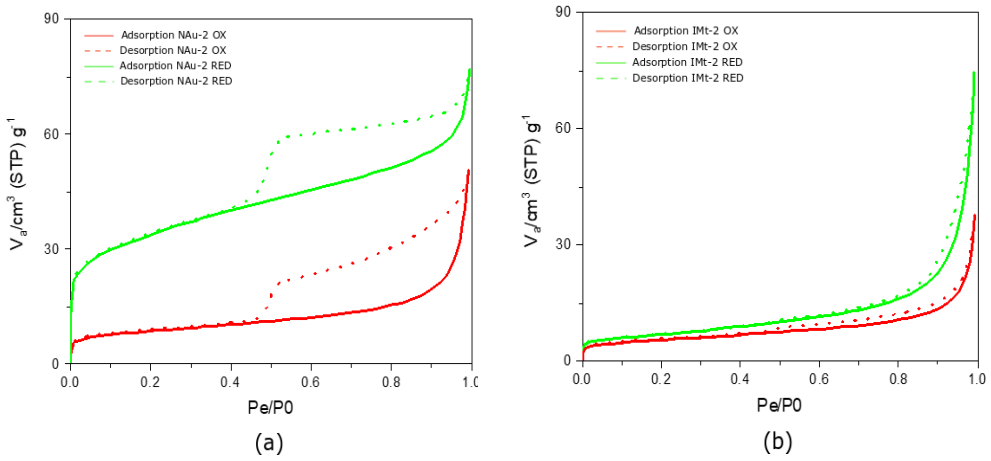

Figure 7.2. Nitrogen Adsorption isotherms for the NAu-2 and IMt-2 oxidized and reduced samples

hysteresis loops suggested by Sing (1982), both NAu-2 samples exhibit a H4 loop type. The almost horizontal isotherms of the H4 type, remain parallel over a range of pressure. The pore structure associated with an H4 loop is narrow slit-like pores.

In contrast, the illite IMt-2 isotherms is classified as Type II, with no hysteretic effect present (Figure 7.2b). Adsorption isotherms of this type are present in non-porous materials, with pore diameter larger than micropores. Based on the classification of physisorption data presented by Sing (1982), Type II indicates an unrestricted monolayer–multilayer adsorption. The mono–multilayer transition point was at a very low pressure of approximately 0.03 P/P_0. However, due to the indistinct knee present at 0.03 P/P_0, it is possible that an onset of the multilayer adsorption had occurred, along with an overlap of the monolayer coverage (see Figure 7.2b). Capillary condensation appeared at mid to high pressures of 0.8 P/P_0. The near-zero hysteresis indicated reversibility of nitrogen adsorption on IMt-2. Nitrogen adsorption isotherms generated for partially and fully reduced IMt-2 (Figure S4) show insignificant differences compared to the adsorption isotherm of IMt-2 OX and indicate a limited effect of clay mineral Fe reduction.

Table 7.2. Nitrogen SSA BET and porosity parameters derived for oxidized and fully reduced NAu-2 and IMt-2 clays. The values were automatically generated using Belsorp Adsorption/Desorption Data Analysis Software (BEL Japan, Inc).

Samples	**V_m (STP) [cm^3/g]**	**Specific Surface Area SSA_{N2} [m^2/g]**	**BET C [constant]**	**Mean pore diameter [nm]**	**Total pore volume (P/P_0 =0.99) [cm^3/g]**
NAu-2 OX	7.2	31	240	9.5	0.074
NAu-2 RED	27.9	121	212	3.6	0.111
IMt-2 OX	4.5	20	198	11.0	0.054
IMt-2 RED	5.6	24	250	18.4	0.112

Table 7.2 summarises BET parameters (SSA and C-constant) and porosity parameters for the oxidized and fully reduced nontronite NAu-2 and illite IMt-2. SSA_{N2} of fully reduced samples increased when compared with oxidized samples, from 31 to 121 m^2/g, a significant 118% increase and from 20 to 24 m^2/g, corresponding to a 22% increase, for NAu-2 and IMt-2, respectively. The mean pore diameter data showed mesopores decreasing in size from 9.5 to 3.6 nm and increasing from 11 to 18.3 nm for NAu-2 and IMt-2 upon reduction, respectively. An increase of the total available pore volume followed the trend in the SSA_N BET increase in the fully reduced samples. More specifically, in the nontronite NAu-2 total pore volume increased from 0.074 to 0.111 cm^3/g and, in illite IMt-2, from 0.054 to 0.112 cm^3/g (P/P_0=0.990), corresponding to a 40% and 70% total pore volume increase respectively.

Figure S1(a) shows the linear regression diagram for nontronite NAu-2 (OX) and Figure S1(b) for NAu-2 (RED). Linear regression of both oxidized and fully reduced samples were plotted in the pressure range of 0-0.25 P/P_0. The corresponding C_{BET} constant values were calculated to be 240 and 212 for NAu-2 OX and NAu-2 RED, respectively (see Table 7.2). Figures S2 and S3 shows the linear regression diagrams for nitrogen adsorption on IMt-2, for the oxidized (Figure S2a), partly reduced (Figure S3) and reduced (Figure S2b) sample. The BET data were plotted for the range of

0-0.24 P/P_0 using the multipoint method. The C_{BET} constant values are 198 and 250 for oxidized and fully reduced illite, respectively (see Table 2).

7.3.3 X-ray Diffraction Analyses of Oxidised and Reduced NAu-2 and IMt-2 At Varying Relative Humidity

The quantitative bulk and clay size fraction analysis data for the oxidised NAu-2 and IMt-2 clay minerals used within this study are given in Table 7.3 and the accompanying X-ray diffraction patters are presented in Figure S5. XRD analysis of both bulk sample and clay size fraction confirmed that the NAu-2 bulk sample was greater than 99% pure nontronite, with trace quartz, which was absent in the clay fraction. In contrast, the IMt-2 bulk sample contained 17% quartz, 5% feldspar and 77% illite. Analysis of the clay size fraction of IMt-2 confirmed very little change between XRD patterns recorded in the air dried, glycolated and heated states, but nonetheless some changes were apparent and indicate a small proportion (<5%) of expandable/swelling layers as per the definition of illite in a broader sense.

Table 7.3. Bulk mineralogy and clay-sized fraction quantitative analysis by X-ray diffraction of the oxidized clay mineral samples NAu-2 and IMt-2.

BULK SAMPLE COMPOSITION

	Quartz	**K-Feldspar**	**Plagioclase**	**Calcite**	**Anatase**	**Nontron.**	**Illite**
NAu-2 OX	0.5	-	-	-	-	99.5	-
IMt-2 OX	17.1	4.9	0.3	0.3	0.6	-	76.8

CLAY SIZE FRACTION COMPOSITION

	Illite	**Nontronite**	**Chlorite**	**Kaolinite**
NAu-2 OX	-	99.5	-	-
IMt-2 OX	99.0	-	trace	1.0

The effect of relative humidity (RH) on the positions of the 001 basal reflections, and thus interplanar spacing, of the oxidized and reduced clay minerals is shown in Figure 7.3. With increasing hydration, the basal spacing showed negligible increase from 14.97 Å to 15.17 Å for NAu-2 OX, and a similarly small increase for NAu-2 RED from 12.52 Å to 12.70 Å. This data also indicates a significant decrease in basal spacing in NAu-2 upon reduction from around 15 Å to 12.5 Å. In illite IMt-2, in contrast, basal spacing remained constant with increasing humidity for both oxidized and reduced sample (10.09-10.04 Å and 10.13-10.10 Å, respectively) and was unaffected by clay mineral Fe reduction. However, changes in peak shape were apparent as measured by the full width at half maximum (FWHM) of the 3% RH samples. Using the Scherrer equation, we calculated the crystallite domain sizes along the c* direction, which increased from 76.3 Å to 111.1 Å for NAu-2 upon reduction and from 111.0 Å to 132.5 Å for the reduction of IMt-2. Similar trends were noted in the other hydration states, although the exact RH reached varied slightly across samples.

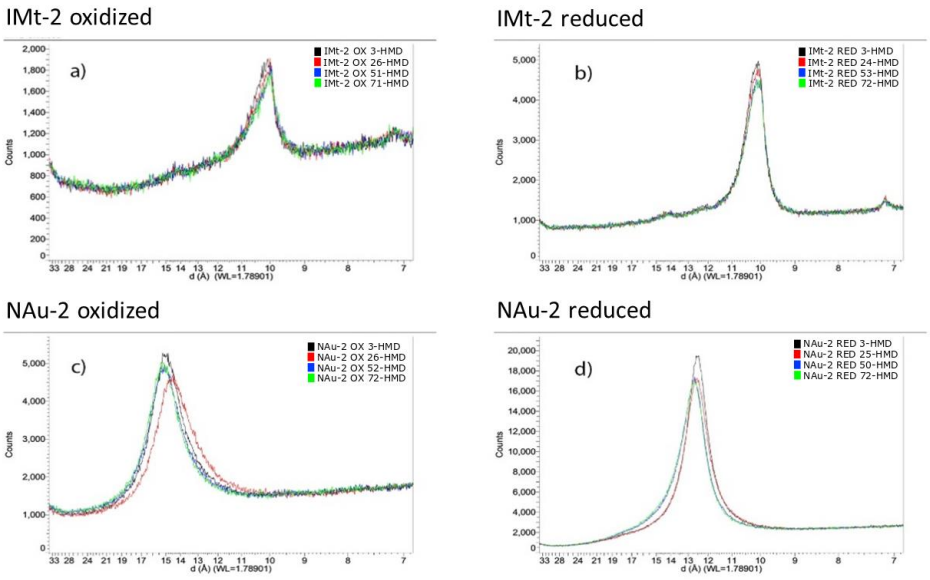

Figure 7.3. X-ray diffraction patterns showing the 001 basal reflection for the clay minerals (a) IMt-2 OX (b) IMt-2 RED (c) NAu-2 OX and (d)NAu-2 RED, as a function of relative humidity (RH) with black = 3% RH; red = ca 25% RH; blue = ca 50% RH and green = ca 75% RH. Actual RH values are given in the legends of each figure.

7.3.4. NAu-2 and IMt-2 charge-balancing cation composition

The amount of charge-balancing cations (Na^+, K^+ and Ca^{2+}) before and after the reduction is shown in Table 7.4. From Table 3, bulk XRD analysis showed the NAu-2 sample was 99.5% nontronite, with a minor ~0.5% mass contribution of quartz, and thus the cation composition is representative of the exchangeable cation composition of the clay mineral phase. For IMt-2, the illite clay mineral fraction accounted for 76.8% by mass of the bulk sample (Table 7.3) with significant quartz (17.1%) and K-feldspar (4.9%) content, indicating contributions of exchangeable, and even more importantly, non-exchangeable cations from phases other than illite.

Table 7.4. Exchangeable cation (Ca^{2+}, Na^+, K^+) amounts and exchangeable cationic charge of oxidised and reduced NAu-2 and IMt-2 measured with ICP-OES, expressed as mmol/100 g. Overall surface charge was calculated based on Ca^{2+}, Na^+ and K^+ amounts and charge; given in meq/100 g.

	Ca^{2+}	**Na^+**	**K^+**	**Overall surface charge**
NAu-2 OX	27.6	8.16	0.740	64.0
NAu-2 RED	4.11	84.3	1.50	94.0
IMt-2 OX	6.97	2.80	162	179
IMt-2 RED	2.01	14.2	164	182

Reduced samples of both NAu-2 and IMt-2 exhibit higher overall surface charge as determined by the relative amounts of charge-balancing cations (taken as Na^+, K^+ and Ca^{2+}) compared to the oxidized samples. The overall surface charge in high Fe content clay mineral NAu-2 increased from 64.0 meq/100 g (NAu-2 OX) to 94.0 meq/100 g (NAu-2 RED), much greater than observed for low Fe content clay mineral IMt-2, for which an increase from 179 meq/100 g (IMt-2 OX) to 182 meg/100 g (IMt-2 RED) was observed. The apparent high overall charge of the IMt-2 samples arises from the presence of the ca 5% K-feldspar in the sample, contributing disproportionately to the overall and constant K^+ content. Changes in charge-balancing cation composition in both clay minerals mainly arise due to an increase in Na^+ content and a decrease in Ca^{2+} content.

7.4 Discussion

The relative hydration properties of reduced and oxidised ferruginous clays have been an area of some interest as these minerals are important in soil horizons and petroleum reservoirs and the hydration of the minerals is a key control on transport of solutes within these systems (Stucki 2011). However, owing to variable results being obtained according to different methodologies used, and size-scales considered, some uncertainty exists over whether ferruginous clay minerals hydrate more when reduced or when oxidised. Here, we attempt to understand the macroscopic hydration of Fe containing clay minerals using water vapour adsorption in relation to the changes in crystal structure/organisation using relative humidity X-ray diffraction and relate this to the changes in surface and pore structures using nitrogen adsorption-desorption volumetry and chemical changes by ICP-OES analysis.

7.4.1. Effect of Reduction and Clay Mineral Type on Water Vapour Adsorption of NAu-2 and IMt-2

Increased water vapour adsorption is evident upon increasing structural Fe reduction in nontronite NAu-2, with an increase from 28 cm^3/g for NAu-2 OX to 36 cm^3/g for NAu-2 PARED and 68 cm^3/g in the case of NAu-2 RED. However, for illite IMt-2, a small decrease was noted upon reduction. More specifically, the increased uptake in NAu-2 is seen in mid to high P/P_0 values that contributes significantly for the total increase of adsorbed water $(\%)g_w/g_{clay}$ after iron reduction (see water adsorption values in Table 7.1 and Figure 7.1).

In terms of hysteresis effects, both reduced and oxidized NAu-2 nontronites show similar trends (Figure 7.1a), with the hysteresis of oxidized NAu-2 being more dominant in the mid-range pressures and the hysteresis of the reduced NAu-2 dominating in high and low pressures. Hysteretic trends arise due to changes in pore size distribution, Table 7.1, and due to the hydration enthalpy of the exchangeable cations. Hence, the cation type is likely to dominate and thus, with higher charge, more cations are present as discussed further below. During depressurising, the NAu-2 surfaces returned to their initial state in proportion to the slow water kinetics.

Similar to the case of NAu-2, the totally reduced IMt-2 adsorbed more water vapour than the oxidized sample in higher P/P_0 values, as observed in Figure 1b. An increase in water volume uptake is also concomitant to an increase in the water specific surface area (SSA_w) (Table 7.1) (Kuila and Prasad 2013). Low to mid pressures may not be sufficient to cause vapour sorption onto the internal clay mineral surfaces, therefore higher pressure is needed. Potentially, the barrier of hydration in this regard can be attributed to large hydration heterogeneities due to differences in layer charge distributions (Ferrage et al 2010). Another reason for our observation may be the

need to overcome the initial hydration energy required to form sequential hydration layers in the collapsed K^+-containing interlayer of illite (Salles et al 2009).

Although illites and other potassium bearing clays do not swell owing to the low hydration enthalpy of K^+, and only partially hold water [34], water vapour adsorption changes between the oxidized and reduced IMt-2 can be clearly seen in Figure 1b. Overall, IMt-2 OX shows almost no hysteresis due to the non-expandable interlayers and low hydration enthalpy of the K^+ cations. Upon reduction, there is a more pronounced hysteresis in IMt-2 RED, though this is smaller than the effects noted for NAu-2, reflecting the small changes in layer charge of this low Fe content clay mineral and negligible change in cation composition upon reduction (see Table 4) in IMt-2.

Relatively few macroscopic studies on ferruginous clay hydration have been undertaken, with several reporting lower uptake of water by the reduced form (Wentworth 1970). However, attempting to understand the hydraulic conductivity in consolidated ferruginous smectite clay barriers, Shen et al.(1992) noted that if the clay minerals were reduced post compaction, despite no change in bulk density upon reduction, the hydraulic conductivity increased. The authors rationalised this in terms of regions of collapsed interlayers in the reduced clay minerals creating micropores within the structure, holding more water and improving transport (Shen et al 1992). Other work, looking at contact angles of different fluids on NAu-2 and IMt-2 clay mineral films to indicate wettability, also noted increased water wetting preference upon reduction, relative to the oxidized sample (Apeiranthitis et al 2021, in submission). Taken with the data presented here, both the NAu-2 and IMt-2 ferruginous clay minerals, with high and low Fe content, respectively, and with different exchangeable and fixed interlayer ions (Na^+ vs K^+, see below), showed increased wettability upon reduction relative to their oxidized state.

7.4.2. Crystal Chemistry Controls on Hydration of NAu-2 and IMt-2 Upon Reduction

It has previously been shown that a decrease in swelling capacity of the clay occurs as a result of structural Fe reduction in nontronite NAu-2 (Manceau et al 2000). Structural Fe reduction in this high Fe content clay mineral was accompanied by structural rearrangements within the dioctahedral sheet, with the resulting Fe^{2+} forming trioctahedral domains and causing dehydroxylation of the mineral structure and a subsequent collapse of interlayers (Manceau et al 2000; Stucki et al 1984; Stucki et al 1987; Gates et al 1996; Kostka et al 1999; Stucki and Kostka 2006). The X-ray diffraction data for NAu-2 in Figure 7.3(c) and Figure 7.3(d) confirms this, with a basal spacing of 14.97-15.17 Å, becoming 12.52-12.70 Å upon reduction, with negligible variation in either sample across the range of applied relative humidity values. The reduction process

dominated basal spacing shift in the NAu-2, rather than extent of hydration. The lower Fe content illite IMt-2 showed no apparent change in basal spacing due to either humidity changes or Fe oxidation state change, as expected owing to the lack of removal of K^+, as evidenced in Table 7.4. This data confirmed that the uptake of water in the reduced ferruginous clay minerals, NAu-2 and IMt-2, was not driven by interlayer expansion and increase in the interlayer surface area for water sorption, further confirmed by the water sorption isotherm analysis in Table 1, in which neither the surface area nor pore volume increased upon reduction.

Previous studies have shown that in both biologically and chemically reduced sodium saturated nontronites (Stucki and Kostka 2006; Favre et al 2006; Lear and Stucki 1989; Gates et al 1993) less water adsorption occurs, at all partial pressures, upon Fe reduction when compared to the oxidized nontronite. That was evident both in the bulk, seen with gravimetric water content analysis and through assessing the effect of the cation by using trimethylphenylammonium (TMPA) to measure changes in the bulk, and at the clay mineral surface using ethylene glycol-monoethyl ether, EGME, specific surface area measurements analysis to measure the surface swelling of reduced samples (Kostka et al 1999; Stucki and Kostka 2006). This previous research suggested that decreased swelling upon reduction is due to the layer charge increase leading to fewer available interlayers participating in the swelling, as may be expected. Hitherto, we are unaware of previous studies of illite reduction and illite is generally considered a non-swelling clay mineral owing to the low enthalpy of hydration of the K^+ cation and a higher net negative layer charge.

Analysis of the crystallite size in the c* direction from the FWHM data showed that the reduced samples consistently showed a narrower peak width, indicating increased crystallite domain size. The crystallite size of NAu-2 OX was 76.3 Å, which indicates crystallite domains of approximately 5 layers in total, with basal spacings recorded of ca 15 Å. In contrast, NAu-2 RED was found to have a crystallite domain length of 111.1 Å, which for a basal spacing of ca 12.5 Å yields a crystal domain containing 9 layers. Similar analysis for IMt-2 OX and IMt-2 RED (111.0 Å and 132.5 Å crystallite domain size, and basal spacing of ca 10 Å), gives 11 layers and 13 layers, respectively. A similar effect was noted by Stucki and Tessier, who studied a ferruginous smectite (SWa-1) using scanning electron microscopy and noted that upon reduction, 'consolidation' of smectite particles occurred and an extensive network of small crystals (1-6 layers thick) formed distinct particles about 20-40 layers thick (Stucki and Tessier 1991). Though the aggregation of layers is not as pronounced in the data in this present study, it nevertheless follows a similar trend. It was further noted that the XRD data also showed consistent increased intensity in the reduced samples, which may be indicative of more overall face-to-face contact/registration of clay (2:1) layers.

Additional hydration will arise from the increased levels of Na^+ in the reduced sample, owing to Na^+ balancing the additional charge caused by the reduction process (Fe^{3+} to Fe^{2+} conversion) and the exchange of Na^+ from the sodium dithionite with other, less hydratable, cations such as K^+ and Ca^{2+}. ICP-OES analysis (Table 7.4) showed an increase in overall surface charge (based on charge-balancing cation content) upon reduction, from 64 to 94 meq/100 g for NAu-2 upon reduction, and from 179 to 182 meq/100 g for IMt-2, a much smaller change. Na^+ content increased as a direct effect of the reduction in both NAu-2 and IMt-2 clay minerals as a result of this additional charge and cation exchange. Cation substitutions occurred mainly between Ca^{2+} and Na^+, for both clay mineral types, with loss of Ca^{2+} and gain of Na^+. The change to monovalent ions resulted in a significantly higher content of hydratable cations (see Table 7.4). The increased layer charge and exchange selectivity for Na^+ within the chemical reduction process contributes to the increased water uptake in NAu-2 when reduced.

There is a scarcity of literature about the cation exchange capacity of the IMt-2 as a function of structural Fe reduction. Table 7.4 shows that illite IMt-2 also underwent Ca^{2+}/Na^+ exchange, however the change in K^+ content was negligible. The K-rich interlayer must have remained relatively unaltered in the reduced conditions as the oxidized and reduced illite have consistent K^+ content and negligible change in CEC. Despite the increase in Na^+, from 2.8 to 14.2 mmol/100g in the IMt-2 (Table 4), no increase in water sorption was noted.

Total $\Delta H_{hydration}$ is therefore expected to vary for the nontronite NAu-2 and illite IMt-2, since clay mineral hydration is also directly controlled by clay mineral composition and the type of cations present (Pons 1980; Haitlim et al1984; Ben et al 1986; Touret 1988). The $\Delta H_{hydration}$ of the clay minerals can be attributed to the cations that balance the negative excess charge, located at the basal planes and interlayers and also on their accessibility and availability for hydration. Specifically, it is the effect of the increased layer charge, balanced by reagent Na^+, and the exchange of Ca^{2+} with Na^+ that may correlate with changes in NAu-2 swelling and water uptake. In the case of illite, though there is evidence of some exchange of Ca^{2+} with Na^+, the majority of K^+ ions are unchanged and IMt-2 remains non-swelling (Table 7.4).

7.4.3. Effect of Clay Mineral Fe Reduction on Nitrogen Adsorption to NAu- 2 and IMt-2

Nitrogen sorption was notably higher in the case of nontronite NAu-2 in terms of sorption isotherms (Figure 7.2a), when compared with to illite IMt-2 (Figure 7.2b), for both the reduced and oxidized cases. Nitrogen adsorbs to external surfaces of the clay mineral particles, without penetrating into the interlayer domains, in contrast to water vapour [Kraehenbuehl et al 1987;

Srodon and McCarty 2008). Hence, lower specific surface area values were observed for nitrogen (SSA_N, Table 7.1) compared to water vapour sorption (SSA_w, Table 7.2).

Hysteresis was mainly present in the NAu-2 desorption isotherms, as opposed to the near-zero hysteresis seen in IMt-2 desorption. This can be attributed to the higher degree of structural change in the high Fe, fully reduced NAu-2, resulting in an approximately 4-fold increased pore volume (Table 7.2) and surface area after reduction. Illite IMt-2 showed almost no hysteresis effect during desorption as well as only a small change in nitrogen adsorption, pore volume and surface area increase upon reduction.

Increased nitrogen adsorption occurred at the surfaces, mainly for the reduced swelling NAu-2 as the result of textural and possibly surface changes (i.e. increased pore volume and aggregation of clay layers) due to reduction (see Table 7.2). The nitrogen adsorption method showed an increase in specific surface area and pore volume for the reduced clay minerals, as derived from the isotherm information. A Type IV and Type II curves indicate a hysteresis loop that is associated with capillary condensation occurring in the mesopores and a reversible unrestricted monolayer–multilayer adsorption for NAu-2 and IMt-2 respectively. A decrease in mean pore diameter was evident after the reduction for NAu-2 and an increase for IMt-2 reduced samples, with their porosity remaining in the mesoporosity category. These findings were in line with and correlate well with the water vapour volumetry data, supporting the present understanding that chemical reduction can both suppress clay mineral swelling (whether through cation exchange (Brindley and Brown 1980) or structural changes (Stucki 2011), as evidenced in the X-ray diffraction analysis under different humidities, and yet result in increased water wettability (Apeiranthitis et al 2021-manuscript in submission) and water vapour sorption.

7.4.4. Implications of increased adsorption as a redox function for fines migration

The documented increased water retention at surface of the clay minerals seen in reduced conditions, sets a new basis on studying fines migration in the liquid/soild system (i.e. crude oil/brine/clay). By reverse-engineering the properties of clay minerals, and understanding how the redox state affects water retained by clay surfaces, interfacial tension at the fluid/clay interface can be understood. Hence, fines migration can be explained using the physisorption mechanism (i.e. change of specific surface area and wetting upon reduction). The redox factor has therefore been introduced as the new mechanism controlling fines migration in clastic reservoirs. Further tests on the crude oil/clay mineral should be conducted, using redox as a control, to understand changes in the SSA of oil.

7.5 Conclusions

In this study, the effect of structural Fe reduction on water uptake of two different Fe containing clay minerals, nontronite NAu-2 and illite IMt-2, has been examined at a crystal scale and at bulk sample scale. Crystal chemistry effects on water sorption were studied using variable relative humidity X-ray diffraction to probe basal spacing and crystallite size, and ICP-OES analysis on digested samples to identify changes in cation composition of the oxidized and reduced samples. At a powder scale, macroscopic water vapour and nitrogen sorption volumetry methods gave insight into vapour adsorption (hydration), specific surface area and pore structure changes arising due to reduction. The clay minerals have different structures and differ in the amount of iron present and the type of the charge balancing cation, yet similar trends were observed upon reduction, showing the importance of redox processes in controlling hydration properties of ferruginous clay minerals. The findings presented improve understanding of water vapour sorption at the surface of the reduced clay minerals that is key in constraining processes at the clay mineral–fluid interface and critical to understanding transport of solutes and water retention.

For high Fe content NAu-2 after iron reduction, X-ray diffraction analysis showed that the interlayer distance decreased and crystallite size (coherent diffraction domain size) increased through aggregation of more clay layers, whereas for low Fe content IMt-2, there was little change in interlayer distance, though some aggregation of more clay layers was also noted. ICP-OES analysis showed that cation retention occurred in IMt-2 upon reduction and the K^+ was not exchanged by Na^+ [54]. For both NAu-2 and IMt-2, the Ca^{2+} content decreased upon reduction, while the amount of Na^+ increased through cation exchange with Na^+ from the chemical reducing agent, potentially accounting for the change in interlayer distance reported above. Though interlayer distance decreased in NAu-2, water sorption was found to increase upon Fe reduction, which indicates that the increased water uptake was not due to uptake into the interlayer space. Rather, porosity analysis confirmed that more interparticle spaces became available through increased pore volume and surface area in the reduced Fe clay mineral, relative to the oxidized.

Overall, it can be concluded that chemical reduction of both low Fe and high Fe clay minerals can result in increased water sorption, even though interlayer swelling may not change or even be suppressed. This is due to changes in textural properties with increased pore volume and surface area observed, coupled with uptake of additional Na^+ from the surrounding fluids during reduction to balance the additional layer charge. In order to resolve the relative effects of interlayer cation

composition and textural changes, nontronite that is cation saturated while oxidized, and post reduction, will be studied.

Understanding the causes of changes in hydration upon reduction/oxidation in clay minerals has implications for both water retention in anoxic horizons of soils containing significant ferruginous clay fraction and also in terms of fines mobility in oil and gas reservoirs, which may start in a reduced state and then oxidize during production.

The relevant reservoir conditions that this study simulated along with the respective changes can be summarized as follows: a) initial reservoir conditions – reduced state and more surface hydration; b) intermediate state found in Low Salinity deployment with hydration shifting towards a more hydrated interlayer and less water holding surface; c) production stage with oxidized and hydrated clays, followed by expansion of interlayer and reduced crystallite, cation exchange capacity and very low surface hydration.

Acknowledgments**:** The authors would like to thank Professor David Wray (University of Greenwich) for providing the ICP-OES data, Kuhan Chellappah (BP) for advising on the project, and Helen Pendlowski who ran the RH clay samples and the editors and anonymous reviewers for their input.

7.6 References

1. Thomas, M. D. Aqueous Vapour Pressure of Soils. Soil Science 1921, 11, 409-434.

2. Thomas, M. D., Aqueous vapour pressure of soils: II Studies in dry soil. Soil Science 1921a, 17, 1-18.

3. Josheph, A.F. The Moisture Equivalent of Heavy Soils II. The Journal of Agricultural Science 1927, 17, issue 1, 12-20.

4. Anderson, M. S. The influence of Substituted Cations on the Properties of Soil Colloids. Journal of Agricultural Research 1929, 38, 505-584.

5. Foster M.D.; The relation between Composition and Swelling in Clays. Clays and Clay Minerals 1954, 3, 205-220.

6. Norrish, K.; The swelling of montmorillonite. Faraday Soc. Discussion 18 1954, 120–134.

7. Zhang Z.Z.; Low P.F. Relation between the heat of immersion and the initial water content of Li-, Na-, and K-montmorillonite. Journal of Colloid and Interface Science 1989, 133, 2, 461-472

8. Anderson R.L.; Ratcliffe I.; Greenwell H.C.; Williams P.A.; Cliffe S.; x Coveney S. Clay swelling — A challenge in the oilfield. Earth-Science Reviews 2010, 98, 3–4, 201-216

9. Mooney, R.W.; Keenan, A.G.; Wood, L.A. Adsorption of water vapour by montmorillonite. II. Effect of exchangeable ions and lattice swelling as measured by X-Ray Diffraction. Journal of the American Chemical Society 1952, 74, 1371–1374.

10. Karaborni, S.; Smit, B.;Heidug,W.; Urai, J.; van Oort, E. The swelling of clays: molecular simulations of the hydration of montmorillonite. Science 1996, 271, 1102–1104.

11. Hensen, E.J.M.; Smit, B. Why clays swell. Journal of Physical Chemistry 2002, B 106 12664–12667.

12. Tardy, Y.; Touret, O. Hydration Energies of Smectites: A Model for Glauconite, Illite and Corrensite Formation. Clay Conference, Denver 1987, 46-52.

13. Tardy, Y.; Fritz, B. An Ideal Solid Solution Model for Calculating Solubility of Clay Minerals. Clay Minerals 1981, 16, 361-373.

14. Tardy, Y.; Duplay, J. A Method of Estimating the Gibbs Free Energies of Formation of Hydrated and Dehydrated Clay Minerals. Geochimica et Cosmochimica Acla 1992, 56, 3007-3029.

15. Smalley, M.V. Clay Swelling and Colloid Stability (1st ed.) 2006, CRC Press.

16. Langmuir, I. The Adsorption of Gases on Plane Surfaces of Glass, Mica and Platinum. Journal of American Chemical Society 1918, 40, 1361.

17. Brunauer, S.; Emmett, P.H.; Teller, E. Adsorption of Gases in Multimolecular Layers, Journal of American Chemical Society 1938, 60, 309.

18. Keeling, J.L.; Raven, M.D.; Gates, W.P. Geology and Characterization of Two Hydrothermal Nontronites from Weathered Metamorphic Rocks at the Uley Graphite Mine, South Australia. Clays Clay Miner 2000, 48, 537–548

19. Nieto, F.; Mellini, M.; Abad, I. The Role of H_3O^+ in the Crystal Structure of Illite. Clays Clay Miner 2010, 58, 238–246

20. Chang P.H.; Li Z.; Jean W.T.; Wang C.J.; Lin K.H.; Adsorption of tetracycline on 2:1 layered non-swelling clay mineral illite. Applied Clay Science 2011, 67-68, 158-163

21. Neumann A.; Petit S.; Hofstetter T.B. Evaluation of redox-active iron sites in smectites using middle and near infrared spectroscopy. Geochimica et Cosmochimica Acta 2011, 75, 2336-2355.

22. Hillier, S.; Use of an air brush to spray dry samples for X-ray powder diffraction. Clay Minerals 1999 34, 127–135

23. Omotoso, O.; McCarty, D. K.; Hillier, S.; Kleeberg, R. Some successful approaches to quantitative mineral analysis as revealed by the 3rd Reynolds Cup contest. Clays Clay Miner. 2003, 54, 748-760

24. Butler, B.; Hillier, S.; Automated full-mattern summation of X-Ray powder diffraction data for high-throughput quantification of clay-bearing mixtures. Clays Clay Miner. 2021 69, 38–51

25. Hillier, S.; Quantitative analysis of clay and other minerals in sandstones by X-ray powder diffraction (XRPD). International Association of Sedimentologists Special Publication 2003, 34, 213-251.

26. Kuila, U.; Prasad, M. Specific Surface Area and Pore – Size Distribution in Clays and Shales; Geophysical Prospecting 2013, 61, 341-362.

27. Brunauer S.; Deming L.S.; Deming W.E.; On a Theory of the van der Waals Adsorption of Gases. Jurnal of American Chemical Society 1940, 62, 7, 1733-1732

28. Hagymassy, Jr., J.; Brunauer, S.; Mikhail, R.S. Pore Structure Analysis by Water Vapour Adsorption: I. t-Curves for Water Vapour. Journal of Colloid Interface Science 1969, 29, 485-491.

29. McClellan, A.L.; Harnsberger, H.F. Cross-Sectional Areas of Molecules Adsorbed on Solid Surfaces. Journal of Coilloid and Interface Science 1967,23, 577-599.

30. Sing, K.S.W. Reporting Physisorption Data for Gas/Solid Systems with Special Reference to the Determination of Surface Area and Porosity. Pure and Applied Chemistry 1982, 54, no. 11, 2201-2218.

31. Stucki J.W. A review of the effects of iron redox cycles on the properties of smectites. Geoscience Reports 2011, 343, 2-3, 199-209

32. Ferrage E.; Lanson B.; Michot L.J.; Robert J.L. Hydration Properties and Interlayer Organization of Water and Ions in Synthetic Na-Smectite with Tetrahedral Layer Charge. Part 1. Results from X-ray Diffraction Profile Modeling. Journal of Physical Chemistry C, American Chemical Society 2010, 114, 4515-4526.

33. Salles, F.; Douillard, J.M.; Denoyel, R.; Bildstein, O.; Julien, M.; Beurroies, I.; Van Damme, H. Hydration Sequence of Swelling Clays: Evolutions of Specific Surface Area and Hydration Energy. Journal of Colloid and Interface Science 2009, 333, 510-522.

34. Wentworth, S.A. Illite. Clay Science 1970, 3, no. 6, 140-155

35. Shen; Siyuan; Stucki, J. W.; Boast, C. W.Effects of structural iron reduction on the hydraulic conductivity of Na-smectite. Clays and Clay Minerals 1992, 40.4, 381-386.

36. Apeirantitis, N.; Neumann, A.; Greenwell, H.C. Redox dependency of wettability of iron bearing clay minerals; implications for enhanced oil recovery. Energy and Fuels 2021 (in submission)

37. Manceau, A.; Lanson, B.; Drits, V.A.; Chateigner, D.; Gates, W.P.; Wu, J.; Stucki, J.W. Oxidation-Reduction Mechanism of Iron in Dioctahedral Smectites: I. Crystal Chemistry of Oxidized Reference Nontronites. *American Mineralogist* 2000, 85, (1), 133-152.

38. Stucki, J.W.; Golden, D.C.; Roth, C.B. Effect of Reduction and Reoxidation of Structural Iron on The Surface Charge and Dissolution of Dioctahedral Smectites. *Clays and Clay Minerals* 1984, 32, no.5, 350-356.

39. Stucki, J.W.; Komadel, P.; Wilkinson, H.T. Microbial Redcution of Structural Iron(III) in Smectites. *Soil Science Society of America Journal* 1987, 6,1663-1665.

40. Gates, W.P.; Stucki, J.W; Kirkpatrick, R.J. Structural Properties of Redcued Upton Montmorillonite. *Physics and Chemistry of Minerals* 1996, 23, 535-541.

41. Kostka, J.E.; Wu, J.; Nealson, K.H.; Stucki, J.W. The impact of structural Fe(III) Reduction by Bacteria on the Surface Chemistry of Smectite Clay Minerals. *Geochimica et Cosmochimica Acta* 1999, 63, 3705-3713.

42. Stucki, J.W.; Kostka, J.L. Microbial Reduction of Iron in Smectite. *C. R. Geoscience* 2006, 338, issues 6-7, 468-475.

43. Favre, F.; Stucki, J.W.; Pascal, B. Redox Properties of Structural Fe in Ferruginous Smectite. A discussion of the Standard Potential and Its Environmental Implications. *Clays and Clay Minerals* 2006, 54, no 4, 466-472.

44. Lear, P.R.; Stucki, J.W. Effects of Iron Oxidation State on The Specific Surface Area of Nontronite. *Clays and Clay Minerals* 1989, 37, 547-552.

45. Gates, W.P.; Wilkinson, H.T.; Stucki, J.W. Swelling Properties of Microbially Reduced Ferruginous Smectite. *Clays and Clay Minerals* 1993, 41, 360-364.

46. Stucki, J. W.; Tessier, D. Effects of iron oxidation state on the texture and structural order of Na-nontronite gels. *Clays and Clay Minerals* 1991 39.2, 137-143.

47. Pons, C.H. Evidence of Relationships Between Texture and Structure in Smectite Systems by Small Angle Synchotron X Ray Scattering. PhD Thesis, INIS 1980, 48, issue. 22

48. Haitlim, A.; Robert, M.; Tessier, R.; Prost, R. Influence of Exchangeable Cations (Na, Ca, Mg) and Salt Concentration on The Physical Properties (Water Retention, Hydraulic Conductivity) of Montmorillonite. agris.fao.org 1984, Agronomie, 4, 451-459.

49. Ben Rhaiem, H.; Tessier, D.; Pons, C.H. Comportement Hydrique et Evolution Structurale et Texturale des Montmorillonites au Cours D'un Cycle De Dessiccation-Humectation Partie I Cas des Montmorillonites Calciques. *Clay Minerals* 1986, 21, 9-29.

50. Touret, O. Structure of hydrated clays: thermodynamics of dehydration and compaction of smectites. PhD Thesis, www.theses.fr/1988STR13026 1988

51. Kraehenbuehl, F.; Stoecki, H.F.; Brunner, F.; Kahr, G.; Muller-Vonmoos, M. Study of the Water-Bentonite System by Vapour Adsorption, Immersion Calorimetry and X-ray Techniques: 1. Micropore Volumes and Internal Surface Areas, Following Dubinin's Theory. *Clay Miner* 1987, 22, issue 1, 1-9.

52. Środoń, J.; McCarty, D.K. Surface Area and Layer Charge of Smectite from CEC and EGME/H2O-Retention Measurements. *Clays Clay Miner* 2008, 56, issue 2, 155-174

53. Brindley, G.H.; Brown, G.; Quantitative X-ray mineral analysis of clays. *Crystal structures of clay minerals and their X-ray identification* 1980, 5, 411-438.

54. Cervini-Silva, J.; Larson, R.A.; Stucki, J.W. Hydration/Expansion and Cation Charge Compensation Modulate the Brønsted Basicity of Distorted Clay Water. *Langmuir* 2006, 22, 7, 2962-2965.

Supplementary material

Article

Effect of Redox State on Water Sorption by Swelling and Non-Swelling Clay Minerals

Christos Vasilopanagos [1*], Cedric Carteret [2], Stephen Hillier [3,4], Anke Neumann [5], and Hugh Christopher Greenwell [1*]

S1. Methods

S1.1. Calculation of sodium dithionite for use in the clay mineral Fe reduction method

For the reduction of structural iron in clay mineral, the amount of sodium dithionite was calculated based on the following: The amount of total iron was first converted into mmol/g taking into account the total Fe content (NAu-2: 23 wt%, IMt-2: 7 wt%) and the molecular mass of iron (55.85 g/mol). Dithionite is a two-electron donor, whereas Fe^{3+} is a one-electron acceptor. Therefore, the reaction stoichiometry is 1:2 and half the number of dithionite molecules is needed per Fe^{3+} to be reduced. Last, the desired reduction extent of the clay mineral Fe was considered and the

molecular mass of sodium dithionite (174.107 g/mol) was used to yield the mass to be used. The amount of sodium dithionite used for NAu-2 partial reduction (30% Fe(II)/Fe(total)) was 0.172 g/g

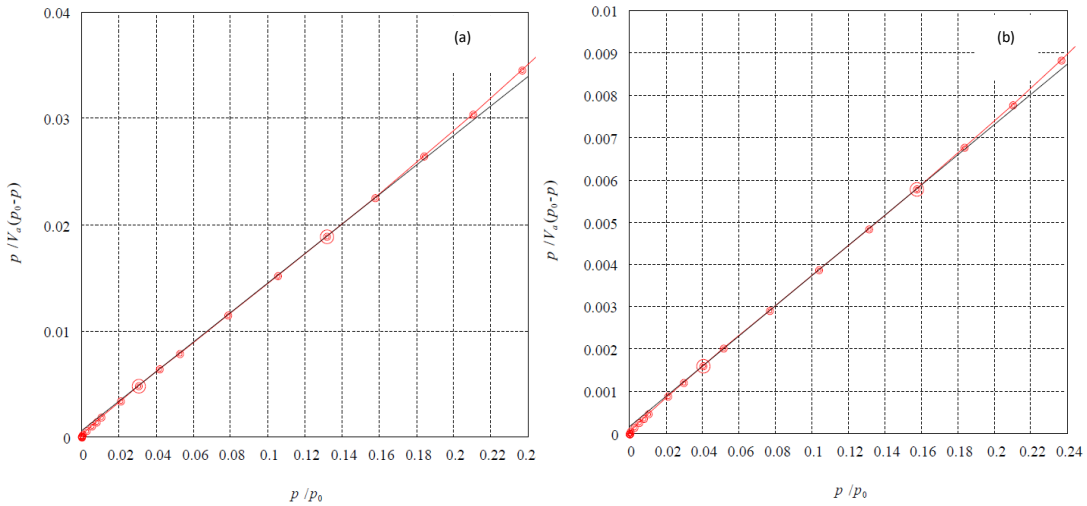

clay mineral and for IMt-2 0.054 g/g clay mineral. For complete reduction of all structural Fe, the amount of sodium dithionite was three times the mass of the clay mineral.

S1.2. Chemical reduction of clay mineral Fe using the sodium dithionite method

To reduce the structural iron in clay minerals, all equipment and reagents were transferred to an anaerobic glovebox a minimum 12 h prior to start of the reaction. For both NAu-2 and IMt-2, 1 g of powdered clay mineral was suspended in a sodium citrate and bicarbonate buffer overnight to create a homogenous mixture. Then, the suspension heated to 70 °C, sodium dithionite was added and the suspension was stirred for 2-4 hours at 70 °C. Once cooled to room temperature, the suspension was transferred into 250 mL centrifuge tubes, which were sealed with PTFE tape, and centrifuged at 10000 rpm for 10 minutes at 10 °C. The centrifuge tubes were transferred back into the glovebox, the supernatant discarded and the solids equilibrated with 1 M NaCl solution overnight. The homoionisation solution was removed by centrifugation (10000 rpm, for 10 minutes at 10 °C) and the reduced solids were placed inside plastic Corning® centrifuge tubes.

Figure S1. *BET linear regression plots, generated by multipoint calculation: (a) for NAu-2 OX; (b) for NAu-2 RED samples.*

Figure 1(a) shows the linear regression diagram for nontronite NAu-2 OX and Figure 1(b) NAu-2 RED. Linear regression of both oxidized and fully reduced samples were plotted in the pressure

range of 0-0.25 P/P_0. The corresponding C_{BET} constant values were calculated to be 240 and 212 for NAu-2 OX and NAu-2 RED, respectively (see Table 2).

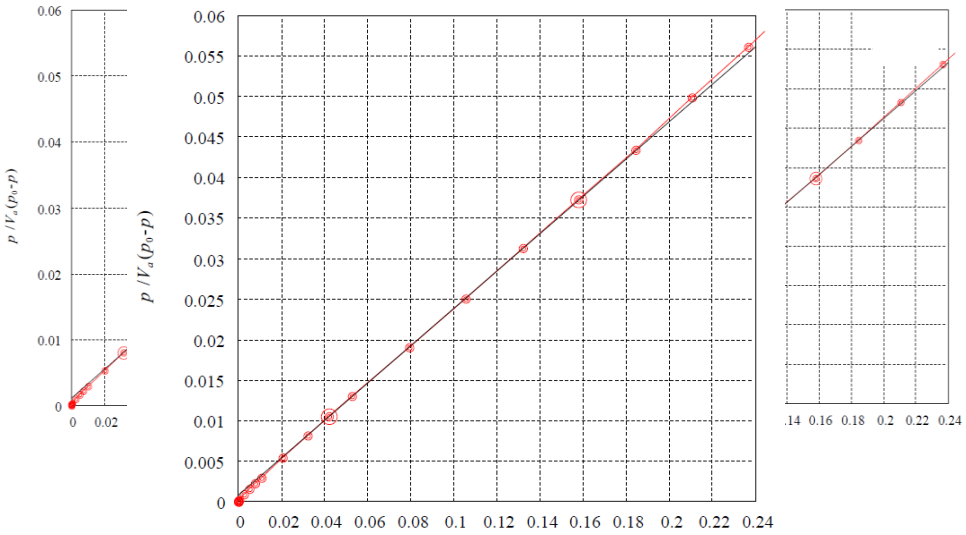

Figure S2. BET linear regression plots, generated by multipoint calculation: (a) the IMt-2 OX; (b) reduced samples.

Figure S3. BET linear regression plots, generated by multipoint calculation for the partially reduced IMt-2 sample.

Figure S4. Nitrogen Adsorption isotherms for the oxidized, partially and fully reduced IMt-2 illite

S2. ICP-OES analysis of acid-dissolved mineral melts from lithium metaborate flux treatment.

Table S3. Cation composition of the oxidized and fully reduced clay minerals NAu-2 and IMt-2

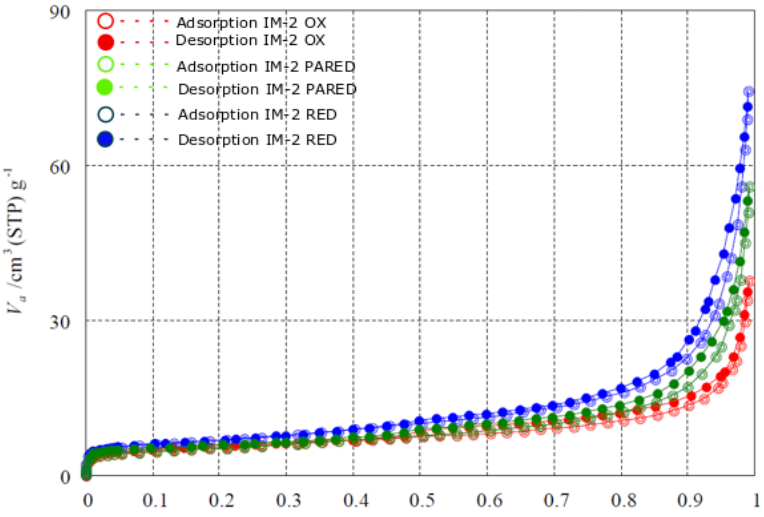

		Al_2O_3	CaO	Fe_2O_3t	MgO	MnO	Na_2O	K_2O	P_2O_5	SiO_2	TiO_2
Data are mean	LoD	0.41	0.53	0.35	0.19	0.05	0.16	0.68	0.08	0.64	0.12

blank subtracted											
Mean blank		0.002	0.020	0.005	0.006	0.0014	0.005	0.002	0.000	-0.048	0.001
P21 023 21 0400	IMt2 oxidised	20.197	0.383	6.208	2.127	0.0306	0.085	7.498	0.079	57.033	0.782
P21 023 21 0401	NAu2 oxidised	2.172	1.366	32.300	0.725	0.0019	0.224	0.031	0.010	47.117	0.114
P21 023 21 0402	IMt2 reduced	20.369	0.110	5.267	1.995	0.0122	0.431	7.557	0.072	58.135	0.749
P21 023 21 0403	NAu2 reduced	1.949	0.207	34.220	0.248	0.0002	2.345	0.063	0.003	46.164	0.034

Chapter 8. Microfluidics – a method for direct visualization of *in situ* iron reduction in a microfabricated sandstone proxy

8.1 Introduction

Models are used in every field of research to ensure that complex systems, such as petroleum reservoirs, are reproduced in a laboratory environment in a simplistic way so that a basic understanding of the system can be gained. That is possible by ruling out parameters and focusing on selected controlling factors each time an experiment is conducted. The more constrained the system, the more definitive and accurate the results. Petroleum research is no exception when it

comes to using models to help simplify experimental processes. Previous studies on enhanced oil recovery have included various parameters found *in situ* during core – flooding, such as pressure and temperature of the injected water, salinity levels, mineralogy and original oil in place properties amongst other. However, the one parameter that has been systematically excluded from the studies is that of free oxygen conditions. Petroleum reservoirs exist at a depth of 5 kilometers, where near zero levels of free oxygen are found and bacterial activity exists (Voordouw et al 1996). The very small percentage of free oxygen is taken up by existing bacteria that are high pressure and temperature resistant, leading to almost total depletion of any remaining free oxygen. Therefore, the initial conditions of a reservoir can be thought to be anoxic and reduced (see Chapter 1 for literature on redox state of oil reservoirs). Due to the systematic use of this convention, it can be said that there is a gap in understanding the mechanisms associated with the migration of fines and the low salinity effect during low salinity water flooding (LSWF) deployment.

The aim of the work presented here is twofold. First, an attempt is made to create an experimental set up that allows direct imaging of *in situ* reduction of clay minerals in a sandstone micromodel. Second, the work aims to provide a method for simulating the initial conditions of a reservoir with regards to free oxygen levels and reduction potential during LSWF in a 2 D micromodel. The suggested experimental method regarding the study of reservoir micromodels in anaerobic and anoxic environments presented aims to provide a basis for further research in this topic.

The main challenge lies in the complexity of simulating and maintaining an oxygen – free environment throughout the experiment. That implies the following challenges: a) in assembling the appropriate experimental apparatus or designing and building the apparatus if necessary, b) in ensuring oxygen free conditions while introducing fluids, c) a challenge of the complexity associated with coordinating the various individual parts of the apparatus to maintain oxygen free conditions while monitoring the experiment and d) in the creation of a protocol for correctly setting up the apparatus. Finally, e) a challenge lies in the creation of a protocol that establishes the method for direct visualization of the reduction process and ensures its repeatability. The set up described here can be used in any experimental work on enhanced oil recovery core flooding after the appropriate modifications are made. It is possible that other hydrous systems, such as aquifers can also be studied by using this experimental set up.

It is important to note that the designing and building of the cell was completed in March 2020, just as lockdown restrictions due to the Covid-19 pandemic started. A year of the ongoing Covid-19 pandemic and the necessary restrictions in place made the follow on experiments as well as

fine-tuning of the experimental setup impossible. However, the progress made set the basis for further study on the fines migration as a redox controlled process using the novel flow cell. The follow-on experiments, to be conducted in a future research project, are described in the future work section in the final chapter (see Chapter 9).

The use of rock micromodels is a method first developed by Mattax and Kyte (1961). At the time, the micromodel was etched onto glass substrates. These micromodels were built simplistically to have a uniform pore network. Improvements on this convention were later made by Davis and Jones (1968). They used photoresist to coat the surface of the glass substrate and add more detail to the micromodels. Chambers and Radke (1990) showed that using photoresist can give a realistic pore network (5-10 μm), making it more appealing to researchers. Later on Hornbrook et al (1991) created the first micromodel proxy of a Berea Sandstone. It can be said that sandstones have a typical average porosity 20% (Cardoso and Balaban 2015), which makes the creation of their proxy less complicated.

Unquestionably, the most important advantage of using 2 D micromodel proxies lies in the fact that they allow for direct imaging and visualization of their surface and any changes during experiments. In traditional core – flooding experiments, visualization requires the use of X – Ray computed tomography or low field nuclear magnetic resonance scans. Although these techniques provided insights with regard to what happens inside the core, the need to see how in-flow affects the core *in situ* culminated in the creation of 2D micromodels. Micromodels can easily overcome that boundary and fit under a microscope once appropriate modifications of the micromodel holder are made. Some examples of microscopes suited for studying micromodels are stereo microscopes, standard optical microscopes and confocal microscopes. The disadvantages of using a proxy however include: the relatively unrealistic pore connectivity mainly due to micro fabrication limitations, the discrepancies between the 3 D pore network of a real rock and the 2 D pore network of the micromodel and the complexity associated with the process of making a micromodel.

Based on the previous studies, the most widely used material for micromodel creation is silicon, as it allows for high control over etching and represents the silicate matrix of a sandstone. The benefits of using a micromodel as a proxy can be summarized as follows: a) due to the robustness of the material, they allow high repeatability of the experiments, b) they allow total control over the composition of the proxy through controlled mineral injection techniques, c) they work as an inexpensive mean of studying complex systems, d) they provide total control over wettability of their surface.

In previous work on microfabricated proxies using wafers, etching was the preferred method for micromodel creation (Oren et al 1992, Dossary and Kovscek 2012, Kovscek and Song 2016). With etching, the printing of a pattern is performed by either wet etching or plasma etching (Chekurov et al 2010) controlled either by electron transfers of acid-base reactions. Previous workers preferred this technique as it does not require an intermediate material such as a photoresist, therefore it simplifies the fabrication process. However, in this study, a novel approach with regard to sandstone micromodel creation was used – photolithography using a photoresist material. The photoresist SU-8 was chosen due to its excellent aspect ratios that are important for the application studied as well as being an excellent material for achieving thicknesses (see details on the SU-8 polymer in Section 8.2.1).

In more recent years, micromodel proxies have been used in EOR research as seen in the numerous works of Kovscek and co – workers and Wei et al (2020). Specifically, fines migration and their effect on wettability were first studied with the use of microfluidics in the work of Song and Kovscek (2016). Using a 2D silicon etched micromodel and confocal microscopy, they tracked pore blocking induced by the mobilization of kaolinite and montmorillonite inside a microfabricated proxy.

Within the context of optimizing EOR microfluidics imaging, the *in situ* imaging of microfluidic devices becomes important in terms of directly visualizing fluid flow, oil and clay minerals migration. Due to the most recent increasing interest in the effects of redox processes in the wettability of oil reservoirs (Yesufu-Rufai et al 2020, Unsal et al 2020), the need for the creation of a microfluidic setting that allows for direct imaging of wettability and fines migration as a redox controlled process has arisen.

The steps necessary to meet the above-mentioned objectives can be grouped into the following parts. The first part consists of the creation of a sandstone proxy that includes imaging of a Berea sandstone (Section 8.1.1), mask creation (Section 8.1.2) and wafer creation (Section 8.1.3) using scanning electron microscopy and photolithography. The second part consists of the creation of an anaerobic flow cell (section 8.2) that works as a holder for the microfabricated sandstone proxy. This device allows flooding of the micromodel under anaerobic conditions as well as direct imaging under a microscope. Techniques to create a chip device consisting of the micromodel sealed with glass are reviewed and presented (Section 8.2. The third step consists of the apparatus for changing and monitoring oxygen levels, as well as monitoring the pressure of the microfluidic system (Section 8.3). In the following sections, the methods along with the basic terms and the necessary theoretical background associated with these steps are presented. Original designs of

microfabricated sandstone proxies and microfluidic devices are shown and the microfluidics setup used are explained. Finally, the suggested setup for executing in – situ reduction and direct visualization is presented (Section 8.4). The results are discussed along with further limitations presented in Section 8.5. The steps can be seen in the flow chart below (Figure 8.1).

8.2 Creation of a Sandstone Proxy

In research, a proxy is a term used to describe a unit that represents something of specific interest. The proxy is therefore tested instead of the unit of interest. In petroleum research a proxy can replace a rock, a mineral, crude oil or any item that exists in the system under study. For the development of the setup explained in the introduction of this chapter, a proxy for Berea Sandstone was designed and built.

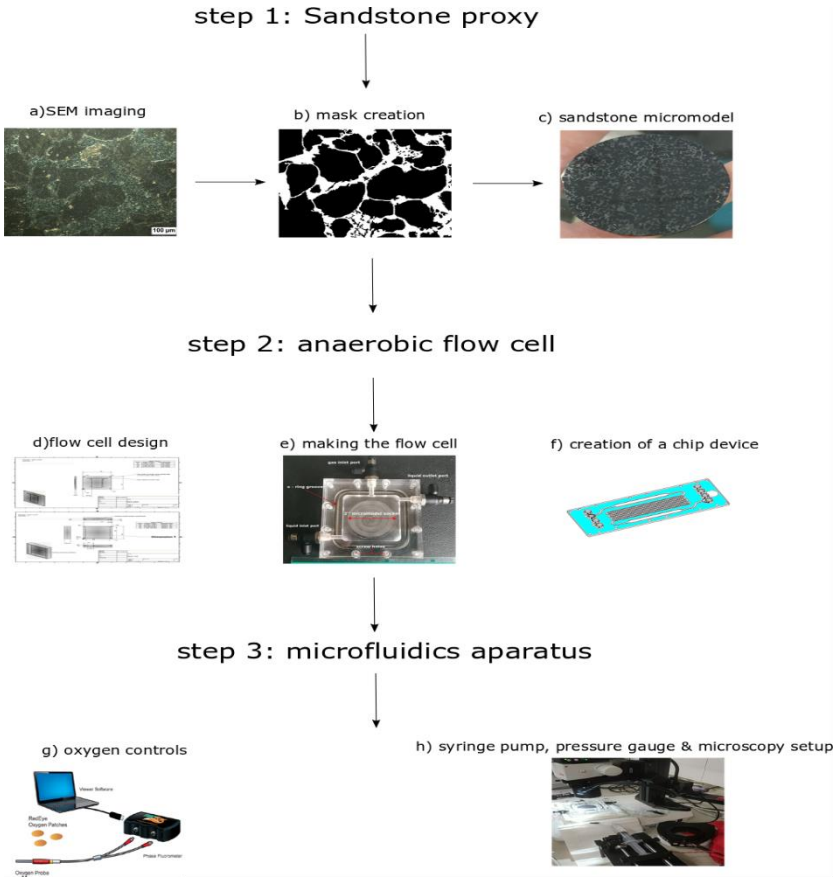

Figure 8.1. Flow chart of the creation of the EOR microfluidics experimental setup.

8.2.1 Microfabrication – Process Overview

Microfabrication is the process of building devices that are microscopic in size. Most commonly the devices built have features that are in the micron size (μm) range, however fabrication of nanometer – sized features (nm) is also associated with the term microfabrication (Tavakoli et al 2005). Microfabrication has many applications in fields such as biology, medicine and engineering.

It has been extensively used in the fields of Micro – Electro – Mechanical Systems (MEMS), cosmetics, drug development and petroleum research to name a few (Skinner et al 1997). Microfabrication by patterning was used to create the sandstone micromodel (see Figure 8.1.b). This technique involves photolithography and soft lithography. Specifically for the creation of the sandstone micromodel, photolithography, known as optical lithography which is the most widely used technique (Reichmanis et al 2001), was used. Photolithography is used to transfer a desired pattern from a photomask to a surface. In photolithography, a photoinitiator and a hydrogel precursor react in a crosslink fashion when they are exposed to ultraviolet light (Figure 8.3). After photocrosslinking, the pattern is transferred to the surface and any excess polymer material is carefully flushed out. The mask created is the reverse image of the initial image taken (i.e. SEM image of the Berea sandstone; see Figure 8.1.a).

Microfabrication work was carried out under cleanroom conditions, in the cleanroom laboratory, at the Department of Engineering, Durham University. The process for microfabricating the sandstone micromodel is shown in Figure 8.1. The first stage of microfabrication includes substrate pretreatment that is followed by coating and edge bead removal (EBR). The material then undergoes soft baking, exposure to UV light and a post exposure bake (PEB). Once the post exposure bake is complete, the material is placed in a developer liquid for a time that depends on the desirable thickness of features. The process is complete after rinsing and drying. More specifically, substrate preparation includes the cleaning and drying of the substrate before the photoresist material is applied. Typically, substrates are cleaned in a Piranha bath, which is a mixture of H_2SO_4 and H_2O_2, and rinsed with de – ionized water. Coating includes applying the photoresist material onto the substrate. Various resists exist in different viscosities that suit different applications. For this study the SU – 8 2000 resist was used. More details on the SU – 8 are given in the following section. During EBR, a thick bead is carefully removed to avoid contamination of the hotplate. The spin coating technique was used to evenly coat the substrate with the SU-8. The spin coating method was used so that the SU-8 mass is transferred transiently to the substrate through flow (Bornside et al 1987). It is used as a standard method in photolithography for spreading a liquid onto a surface by utilizing a centrifugal force (Larson and Rehg 1997). Contamination might occur during spin coating as an excess of photoresist on the sides of the substrate may form. Removal of the bead that forms on the edges also improves contact between the photomask and the wafer. Soft baking includes the baking of the wafer with the applied mask at different temperatures and duration, depending on the thickness of features. During exposure stage the resist, photomask and wafer are exposed to UV light, followed by a Post Exposure Bake (PEB) that occurs immediately after exposure. The PEB time and temperature

varies, again, according to the thickness of the features (Table 8.1). The development stage includes immersion of the wafer, mask and resist and simultaneous agitation. Development times are calculated based on the thickness of features. The final stage is rinsing with de – ionized water for 10 seconds, spraying with isopropanol and air drying with pressurized air. Schematically, the typical process flow chart can be seen in Fig 8.2.

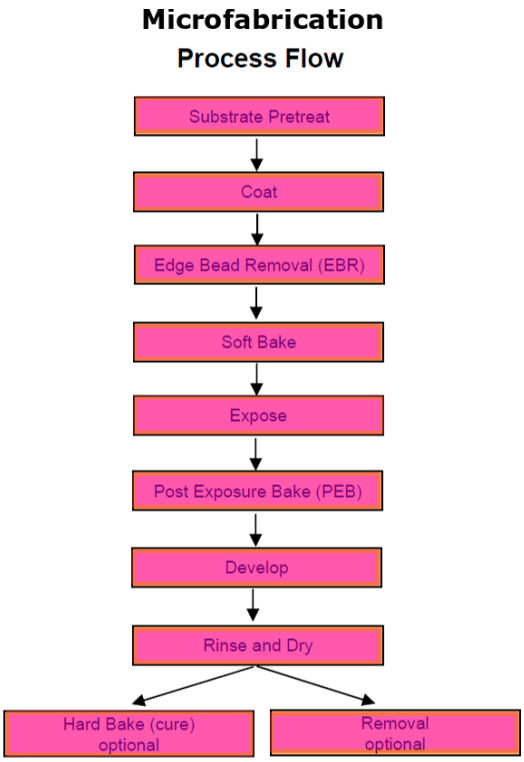

Figure 8.2. Microfabrication work – flow diagram (modified after Microchem: processing guideline guide for permanent Epoxy Negative Photoresist)

Table 8.1. Exposure energy, baking times and development times for SU – 8 negative photoresist. Highlighted are the desired thickness of the features (microns) and the respective times (modified after Microchem processing guideline guide for Epoxy Negative Photoresist).

Thickness [microns]	**Exposure Energy [mJ/cm2]**	**Thickness [microns]**	**PEB Time (65 C)* [minutes]**	**PEB Time (95 C)* [minutes]**
25-40	150-160	25-40	1	5-6
45-80	150-215	45-80	1-2	6-7
85-110	215-240	85-110	2-5	8-10
115-150	240-260	115-150	5	10-12
160-225	260-350	160-225	5	12-15

Thickness [microns]	Development Time [minutes]	Thickness [microns]	65 C [minutes] 95 C [minutes]	Soft bake times
25-40	4-5	25-40	0-3	5-6
45-80	5-7	45-80	0-3	6-9
80-110	7-10	85-110	5	10-20
115-150	10-15	115-150	5	20-30
160-225	15-17	160-225	7	30-45

8.2.1.1 Selection of the photoresist material

As indicated in the introduction, previous work on petroleum microfluidics involved the use of silicon wafers. However etching silicon wafers with high aspects ratios (deep reactive ion etching, DRIE), becomes problematic when the maximum achievable aspect ratio, otherwise known as critical aspect ratio (Blauw et al 2001; Kim et al 2003) is reached. When this plateau is reached, the etch rate (i.e. the ratio of etching/elapsed time) becomes zero (Yeom et al 2005). As a consequence, the microfabrication of high aspect ratio (i.e. the length to width ratio) structures becomes limited. Specifically the SU-8 negative photoresist was chosen for the fabrication of the micromodels due to its ability to surpass this limitation.

With regard to the wettability, the SU-8 is known to be hydrophobic when compared with silicon (see below in this section for details), glass and PDMS (polydimethylsiloxane) (Silveiro et al 2019). However, surface wettability modification (SWM) of the SU-8 is possible by means of polymerization of its surface using a polymeric hydrogel layer (Gao et al 2008).

In terms of textural roughness both etching and building with SU – 8 create additional surface roughness. The new topography carved into the wafer after etching will have values that represent the depth of the features that will be subject to any defects embedded in the manufacturing process. The SU – 8 resist coats the surface uniformly and after exposure and bake, layers of material are left on the wafer, without altering the silicon or glass surface. In this case, additional surface roughness is created that can easily be controlled using surface activation methods depending on individual needs.

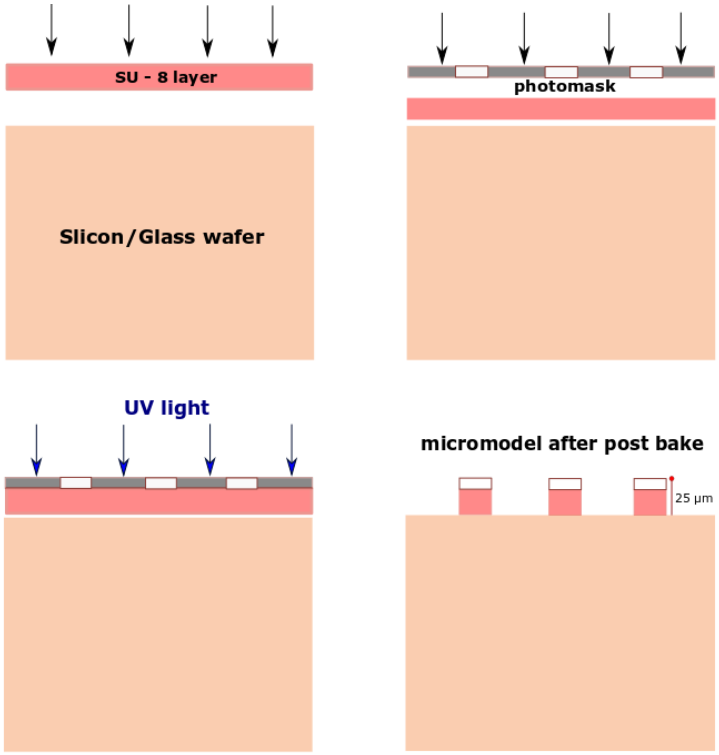

Figure 8.3. Schematic illustration of micromodel fabrication using the SU – 8 negative photoresist and the chrome mask. Opposite to etching, the SU – 8 is a building layer – by – layer technique without altering the surface of the wafer. An SU – 8 layer is applied onto the wafer, a photomask is then added and UV light source used. After exposure and developing time, the wafer is baked and the micromodel is ready for use.

The SU – 8 is a negative photoresist invented by IBM in 1989. The first commercial SU – 8 products became available in 1996 from MicroChem (LaBianca N C and Gelorme 1995). This epoxy – type resist has been increasingly used for microfabrication purposes, especially for MEMS devices due to its robustness and excellent aspect ratio (Xu et al 2016). The SU – 8 consists of Bisphenol A Novolak epoxy oligomer and a photoacid generator triarylsulfonium hexafluroantimonate salt (A del Campo, C Greiner 2007). When the resist is exposed to UV irradiation, hexafluoroantimonic acid is produced due to decomposition of the photoacid generator. Produced protonated oxonium ions then react with neutral epoxides by means of crosslinking reactions after heating (Teh W H et al 2005). A negative tone is created after photothermal activation has taken place.

Consequently, the SU – 8 becomes mechanically and thermally stable (A del Campo and Greiner 2007). The resist can be used for fabricating features of various thickness, from 2 to 300 μm. It can absorb UV light above 360 nm (Yang and Wang 2005) increasingly as the occurring chemical changes take place (Gaudet et al 2006). It gives high aspect ratio (width/height) features (A del Campo and Greiner 2007) and its mechanical robustness makes it excellent material for many applications. The SU – 8 is a relatively hydrophobic material with a water static contact angle droplet varying from 100 to 79 ± 1° that may need to undergo further treatment depending on the purpose of use (Gao et al 2008). Achieving quartz-like wettability (i.e. a water contact angle of 54 degrees when measured in dry quartz plate; Janczuk et al 1984 and crude oil contact angle of 50 degrees when measured after aging in brine at 25 °C; Xie and Morrow 1999), the polymerization method can be used (Gao et al 2008), and the contact angle can be reduced to 36 ± 1° relative to the extent of polymerization. Common treatments for wettability enhancement such as oxygen plasma activation and other have been used to change the chemistry of the SU – 8 and make it hydrophilic. By SWM of the SU-8, a micromodel that represents the wettability of a quartz surface can be built that has the potential to provide a variety of oilfield wetting states in terms of brine wetting.

8.2.1.2 Fluorescence of SU-8

Fluorescence microscopy has been extensively used in the field of life sciences to examine living cells. Similarly to living cells, activators (Rost 1992), known as quantum isolated defects are found in many minerals (Tisler et al 2009). For these particular minerals, the term fluorescing minerals is used (King 2020). Therefore, fluorescence microscopy can be, and has been, used in mineral science. Examples of this are coal petrology (Rost 1995) and petroleum research (Burrus 1991; Ryder 2005). Specifically in microfluidics petroleum research, fluorescence microscopy has been increasingly used by a number of workers (Buchgraber et al 2012; Guateplass et al 2015, Song and Kovscek 2016; Yun et al 2020).

As an organic material, the SU-8, exhibits autofluorescence in visible wavelengths (Pai et al 2007). Although its other properties make it a good alternative option to simple etching, the existing background fluorescence can have a limiting effect on biological applications and more importantly to this study, on EOR microfluidic simulations. That is due to the autofluorescence of crude oil, most commonly used in water flooding and imbibition studies. Therefore, in the case were both crude oil and the SU-8 fluoresce with the same intensity, the possibility that oil migration cannot be distinguished increases.

To test the emitted fluorescence intensity of the SU – 8 relative to different treatment methods, three different samples were prepared as follows: Sample a – fully resist coated silicon wafer, Sample b – resist coated glass wafer that was baked with no later exposure to UV light and Sample c – resist coated glass wafer that was baked and UV exposed. The aim was to identify a basic treatment method relative to baking and UV irradiation that would minimize autofluorescence of the resist without the need for special treatment. The samples were scanned using the ZEISS 800 Confocal Microscope (details of the instrument are given in Chapter: 3) and snapshots were taken as shown in Figure 8.4.

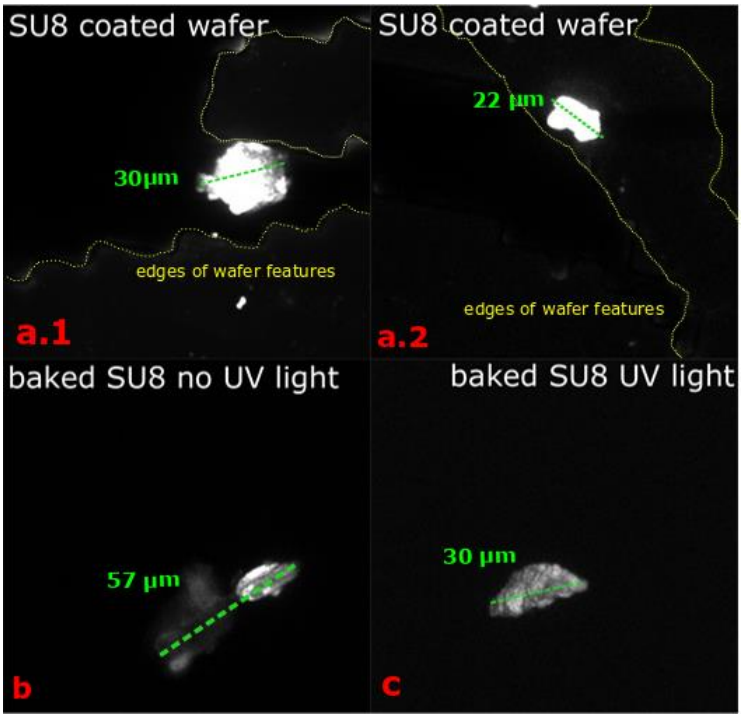

Figure 8.4. Snapshots of SU – 8 coated silicon (a.1, a.2) and glass (b, c) samples using the ZEIS 800 Confocal Microscope. Sample a.1, a.2 – UV light excited areas up to 30 µm on coated silicon wafer between features that represent sandstone grains. Samples b, c – UV light excited areas up to 57 µm in glass substrates, with and without post – exposure to UV light.

As shown in Figure 8.4, all samples contained fluorophore particles that were excited after a UV laser light at 493 nm was used. In each case, the entire sample was exposed to UV light and the selected areas where the ones exhibiting fluorescence. This implies that the autofluoresence of the SU – 8 photoresist is not controlled by baking or exposure to UV light. Rather, the UV – sensitive fluorophore particles are embedded into the SU – 8 resist and the elimination of them calls for a more sophisticated treatment method. An example of such a method is found in the work of Cao et al (2011). They showed that coating the SU – 8 with a thin layer (20 nm) of gold

nanoparticles (AuNPs), reduces the fluorescence of the photoresist. However, no additional layer was used to buffer fluorescence as that would later complicate the flow experiment.

8.3 Photomask creation

Mask creation is an essential part of microfabrication. As was explained in previous sections, a patterned mask is a prerequisite to any micro machining and photolithography application that calls for the study of a specific system. For the purposes of this study, a mask represents an image of the Berea sandstone. Once a desired image of the sandstone was taken and processed, it was sent to commercial contractors (Jd Photomask) in a tiff format. The mask was made and then written onto the wafer by the method of photolithography, as described in section (8.1.2). There is an abundance of software for graphically designing a sketch of a mask for various applications. Namely, CorelDraw (Sharma and Jha 2010), AutoCad (Singh et al 1991), LayoutEditor (Georg et al 2018) and CleWin (Wijdeven et al 2019) are some of the most common options for graphic designing. The Berea Sandstone images were processed using Fiji/ImageJ software (Schindelin et al 2012). Specifically the Fiji 2.0.0 – rc – 69/1.52p version was used. In total, two masks were created due to defects detected in the first one.

The masks used were 7 cm long by 7 cm wide, made of low reflective chrome (LRC) material. Soda lime glass, a low cost alternative to quartz, was used as base material that gave the masks a CrO coating layer that prevents any light reflections. The resolution was Class 2 (128 k dpi; as set by the manufacturer, JD Photodata), the higher the class, the higher the quality of the mask, class, giving the mask high quality parameters such as edge roughness, alignment accuracy and addressability. In the Class 2 resolution, pixel lines can be as small as 4 µm in width (therefore when converted into a micromodel the smallest features, in this application a pore or grain, can be 4 µm), with only a small pixilation. The selection of the resolution was based on what size had been used in previous microfluidic settings (Rangel-German and Kovscek 2006). The polarity of the masks was negative with the chrome side facing down (see Figure 8.5). This means items drawn on the image file (.tiff) will be clear on the mask and the rest will be chrome (see Section 8.2.2, Figure 8.3).

Mask creation was performed in the following steps (see Figure 8.5 for workflow and Figure 8.6): An image (pattern) showing the desired patter was created and then transferred to the mask writer via Gerber software. The pattern was then exposed onto the substrate (soda lime) used for the mask creation. After exposure, the mask underwent the development process which allowed for the final mask to become visible. The imager used was a flat granite surface with the ability to

expose glass substrates. The granite flat surface was capable of transporting the photohead to the mask, specifically where the imaging should be placed. A laser was used to expose light towards the modulating digital micro-mirror (DMM). The mirrors can be tilted and caused the light to travel through the optical system and reach and write the mask by imaging it. The chrome coating acted as a paper for the writing of the mask. The mask images (frames) were captured by the lenses, and were then put together one by one onto the chrome surface. After this stage, the chrome side of the mask was coated with an anti-reflecting (typically SiO oxides such as a potassium silicate solution; Ling et al 2014) coating and photosensitive photoresist (polydimethylsiloxane, PDMS; Qin et al 1997). After development, the photoresist layer was removed using etching and the mask was ready for use (see Figure 8.6).

The first image was unedited when it was sent to the commercial contractors in a tiff format. The image was then converted to a binary image by their technical team, which is typical prerequisite manipulation of an image prior to mask creation. Converting the image to binary, minimizes gray scales and ensures maximum optical contrast between pore network and grains. Details of imaging and further modifications are described in the sections below.

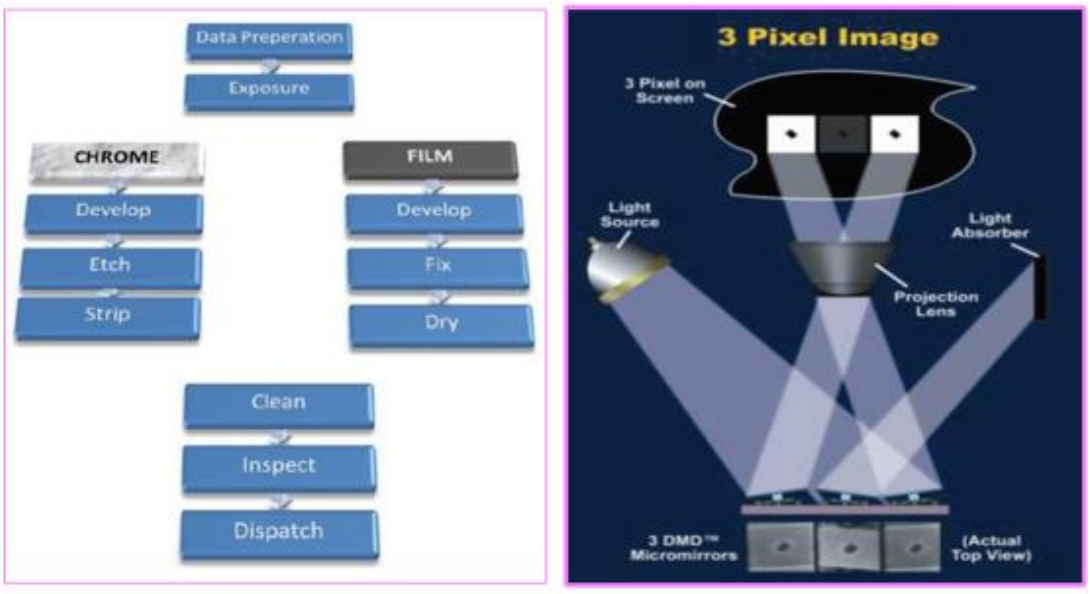

Figure 8.5. Workflow of the photomask creation (left); schematic representation of mask imaging using light source, DMM micromirrors and light absorber (modified after JD Photodata photomask guide 2018).

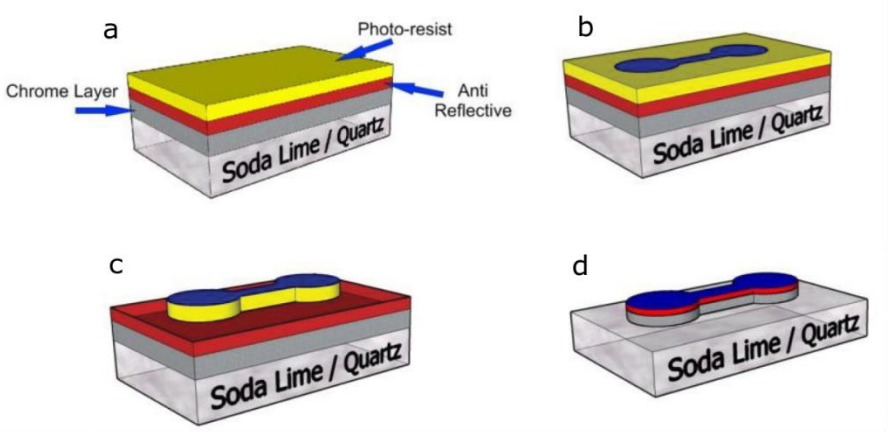

Figure 8.6. Mask creation: a) application of antireflective coating and photoresist; b) use of a mask writer – imaging of the mask; c) development stage; stripping of the remainng photoresist (Modified after after JD Photodata photomask guide 2018.

8.4 Sample preparation and scanning electron microscopy imaging

Thin sections were cut out of a Berea sandstone sourced from Cleveland Quarries in Vermilion, Ohio, USA. Berea was specifically used as it Is one of the typical model cores used that can be obtained within defined permeability and porosity ranges. Berea sandstones have been extensively used in a number of petroleum studies, including for EOR (Bryant and Douglas 1988; Seright et al 2009; Li et al 2013; Hendraningrat et al 2013;Zhang et al 2014). The sections were impregnated with diglycidyl ether epoxy resin (Sigma Aldrich) and were left under vacuum for 45 minutes to create a resin impregnated sample. Resin impregnation works as an excellent method for filling up pores and providing an easy way to quantitatively analyze the porosity of a sample. After the samples were impregnated, they were polished using various diamond suspensions to

smooth out the surface and make it appropriate for imaging (fig 8.5). The job was carried out at the thin section and sample preparation room, at the Department of Physics, Durham University.

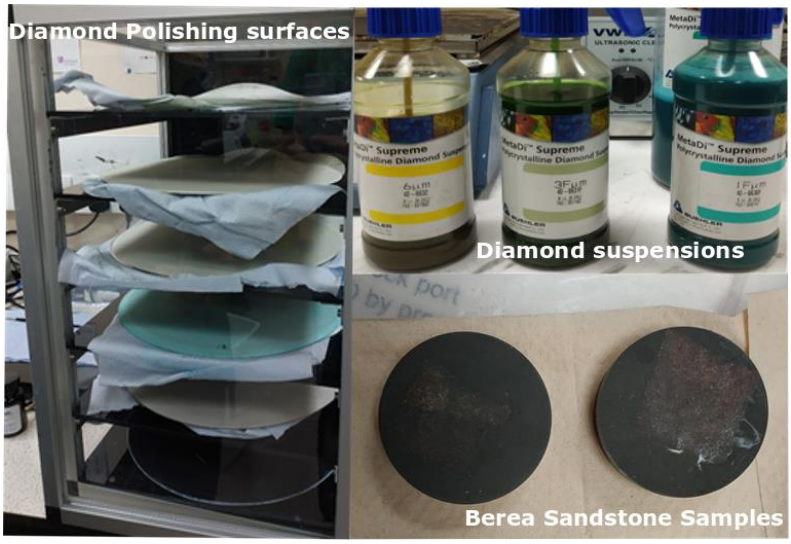

Figure 8.7. Berea Sandstone sample preparation for SEM imaging; diamond polishing surface and suspensions of different µm.

For the imaging a Hitachi SU-70 FEG SEM Scanning Electron Microscope in backscattered mode in the department of Physics, at Durham University, was used (see details of the instrument in Chapter 3). A 10 mm square was broken down into 12 by 12 array and scanned as individual squares before being reassembled. Imaging of a 10 × 10 mm was performed as follows: 12 * 12 images were scanned and re-combined by montage mode. The end result was an image of 7247 pixels wide by 6608 pixels high. Total scanning time was 10 hours. The raw sandstone image was then used for the creation of the first mask that was then written onto a wafer using photolithography techniques. Figure 8.6 shows the raw SEM image in backscattered mode. A cropped out section of the same image was used for the creation of the second mask, after several modifications were made (see Section 8.1.2.2.2).

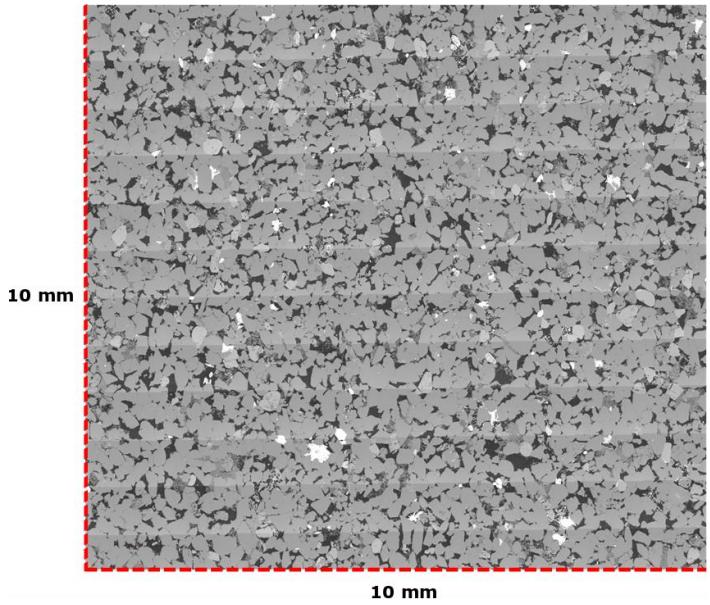

Figure 8.8. Raw SEM image of a Berea Sandstone in backscattered mode, 12 x 12 image montage (7247 x 6608 pixels).

8.5 Complications and updated image processing

Insufficient editing created limitations that were not considered in the first place. These can be summarized as follows: A) a large scanned area led to a 7 * 7 cm mask that did not fit into a 5 * 5 cm wafer. As a result, the mask had to be cut specifically to fit the wafer leading to many of the features written on the mask to be excluded. B) Gray scales that remained on the image later became features on the pattern of the mask. That led to poor connectivity between the pores of the wafer that was due to the technical limitation of converting gray sketches to wafer features. C) Finally, poor permeability was also a result of insufficiently editing of the image; limited pore connection with isolated pores and large grains taking up most space preexisted in the image. That became apparent after visual inspection and initial tracer fluid tests (see following sections for details on the tracer fluid tests).

To overcome those complications a second mask was created after necessary modifications were made on the image. These include the following: re – scaling of the image using smaller – sized image for the mask, improving permeability by manually connecting isolated pores when possible and adding artificial grid – like channels for enhancing laminar flow (Figure 8.11). Upscaling was then performed to ensure pore connectivity was achieved and to avoid any defects occurring due to the mask making system. Upscaling has been used before to avoid photomask creation and microfabrication limitations that would be detrimental to the flow experiments. The upscaling has been done either by increasing pixel dimensions of the original image resulting in increased

porosity – permeability (Buchgraber et al 2012), or by means of manually improving porosity by creating pore networks, leading to a 54% porosity in a 5 * 5 cm sandstone micromodel (Song and Kovscek 2012). Once the necessary modifications were made and the optimal image was created, it was arrayed three times horizontally and vertically (Figure 8.11). That was to constrain the larger, complicated sandstone system and make comparison between preferential flow paths easy.

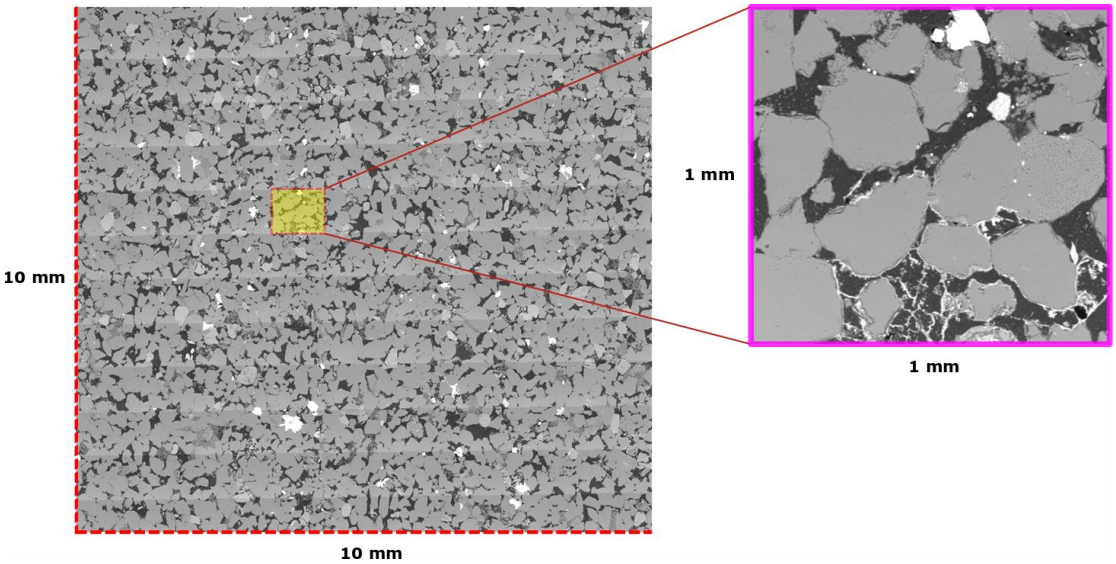

Figure 8.9. Raw, backscattered SEM images of the Berea Sandstone. Left: Initial Berea Sandstone 10 x 10 mm image used for mask 1; right: cropped – out and enlarged 50×50 mm Berea Sandstone 1 x 1 mm image used for mask 2.

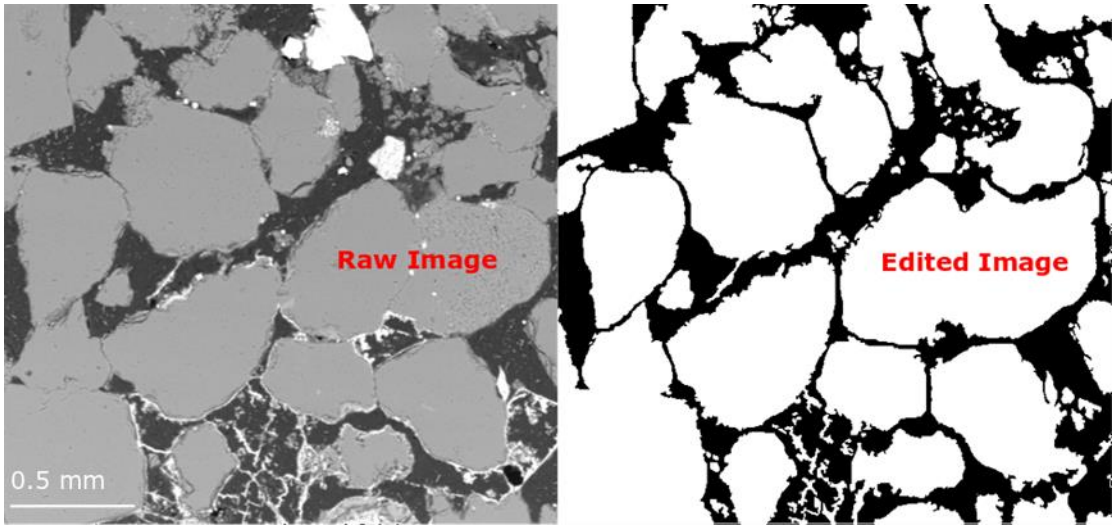

Figure 8.10. Left: raw image of the Berea Sandstone used for mask 2; right: edited with Fiji software, image of the Berea Sandstone – binary (black and white) image, edited for improved permeability by connecting pores where possible and completely removing grey scales.

Additionally to the modifications on the image, a certificate of conformity of the mask was created before manufacturing was complete. The certificate of conformity that verifies the features (channels, grains) on the mask were produced as per order was necessary to ensure upscaling of the image in terms of dimensions was done correctly. Specific areas were chosen for measuring (grains and channels) to ensure the improved permeability would provide enough space for liquid to flow. In total, eleven areas were chosen for size testing. These included large and small grains and more importantly, inlets and outlet ports for fluid injection and exit. Figure 8.11 shows the edited image, arrayed three times horizontally and vertically and the measured areas. The certificate of conformity (COC) was created and provided by JD Photodata (Figure 8.1; Table 8.2).

It can be said that mask 1 represents the actual sandstone more accurately than mask 2. That is due to the unedited SEM image used for the creation of the mask. Since the image used for the second mask was heavily modified as described in the section above, there are considerable discrepancies with the backscattered image of the sandstone.

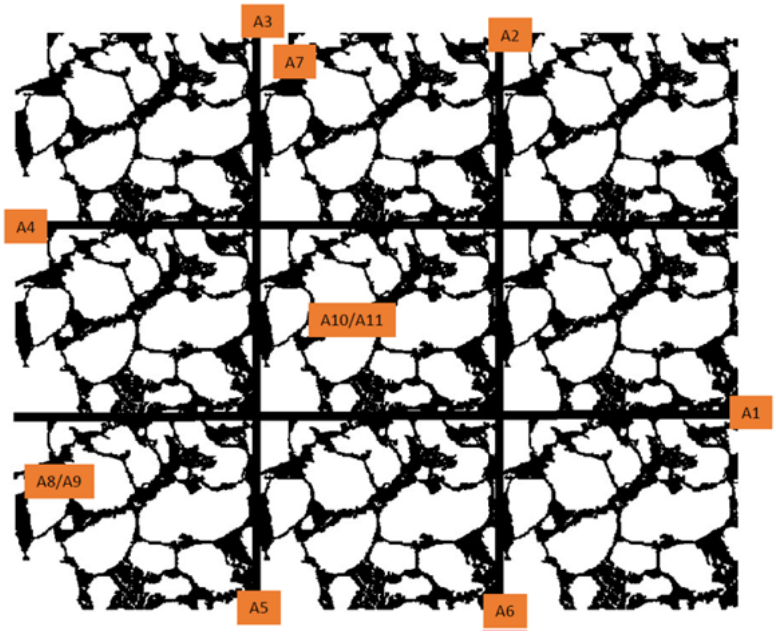

Figure 8.11. Edited enlarged Berea sandstone image in an array of 3 x 3. Initial size was 50 * 50 mm. Artificial grid was added to the array to ensure maximum connectivity and laminar flow between individual images.

Table 8.2. Selected measurements on Chrome mask that correspond to the selected areas measured as seen in Figure 8.11 for the primarily measured are seen in Fig.8.9.

	Nominal [mm]	Measured	Tol +/- um	Error um	Polarity of feature
A1	0.36	0.3597	1.6	-0.3	Positive
A2	0.33	0.3295	1.6	-0.5	Positive
A3	0.33	0.3298	1.6	-0.2	Positive
A4	0.36	0.3598	1.6	-0.2	Positive
A5	0.33	0.33	1.6	0	Positive
A6	0.33	0.3294	1.6	-0.6	Positive
A7	0.06	0.0598	1.6	-0.2	Positive
A8	0.09	0.0903	1.6	0.3	Positive
A9	0.09	0.0908	1.6	0.8	Positive
A10	0.03	0.0307	1.6	0.65	Positive
A11	0.09	0.091	1.6	1	Positive

8.6 Microfabrication; wafers

Two photomasks were created from images taken using a SEM. The photomasks were later written onto silicon and glass wafers, with a 5 cm diameter using the method of photolithography

(see Section 8.2.1). The features built on the wafers were 25, 35 and 45 µm in height (also consistent with literature; Song and Kovscek 2016). All wafers were first optically examined for any defects or discrepancies between the initial image and the fabricated wafer under a Leica Stereo Fluor M165 FC microscope using a 1.0 x objective lens. Below are pictures of the silicon and glass wafers bearing the first mask taken with the Leica Stereo microscope for optical comparison.

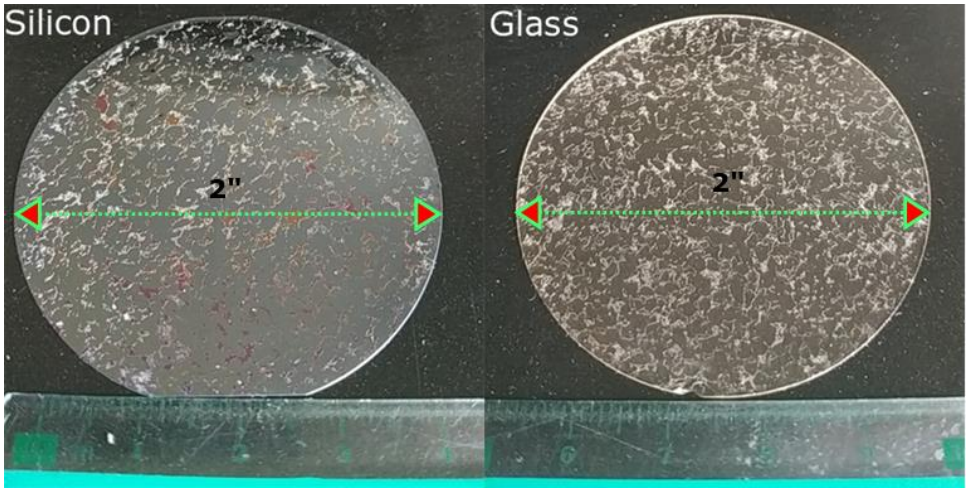

Figure 8.12. Micromodels with a microfabricated mask 1 on silicon wafer (left) and on glass wafer (right).

8.7 Creation of a microfluidic system; anaerobic flow cell and fluid flow apparatus

As explained in the introduction section of this chapter, near – zero oxygen free environments are where reservoirs are most commonly found. The simulation of such conditions is the main objective that this section focuses on. The rationale behind the design and the making of two prototype flow cells is presented along with original designs. Several modifications made on the flow cells are explained. Fluid tests results are shown and the limitations of the flow cells explained. Finally, suggestions for adequate sealing of mircomodels to achieve maximum microfluidic conditions are made.

Conventional methods for simulating anaerobic conditions in a laboratory setting include the use of anaerobic chambers, commonly known as glovebox. There are many types of commercially available gloveboxes in terms of size, material, ventilation system, vacuum chambers and other specifications. Gloveboxes have been traditionally used for radiochemical and radiometallurgical applications as well as for biological studies, plant science and for any anoxic – reduction potential related study. For the experiments described in previous chapters (Chapter 5, 6 and 7) chemical reduction of iron – bearing clay minerals was performed in anaerobic chamber conditions. More

specifically, surface adhesion measurements of the clay – crude oil interface were taken inside a glovebox (Chapter 5). For the infrared spectra of clays, and water sorption studies, described in Chapters 6 and 7 respectively, the clay minerals used were reduced using a chemical reduction protocol (see Chapter 5) inside an anaerobic chamber. Depending on the manufacturing quality, a glovebox can create near – zero free oxygen conditions at ppm levels which are significantly low, allowing for high accuracy of near – zero free oxygen measurements. Even though a glovebox is the ideal mean to study oxygen – free systems, limitations occur with increasing complexity of an experiment. Clay reduction inside anaerobic chambers is a well established method that requires the use of clay samples in powder form, buffers agents, a reducing agent, a thermometer, a hot plate and appropriate Pyrex glassware. Therefore, it can be said that clay reduction is a rather simple process in terms of the apparatus needed and execution. In a more advanced setting such as one required for core flooding experiments, the use of a glovebox becomes problematic. That is due to a number of reasons: the limited space available inside a glove box that does not allow for a complex setup or any imaging of the experiment, including using traditional optical microscopes or micro CT scanners, the cost and maintenance of a high-end glovebox, the access point is not sufficiently large to include the instrument and allow for a good seal. That implies that the microfluidic system has to be mobile to be studied with different microscopy methods so that the option of switching between optical and confocal microscopy becomes possible. In this way, preferential flow paths of brine and oil can be assessed with minimum effort using two microscopy methods. Moreover, opposite to the straightforward method of clay reduction, the complexity of microfluidics lies in the different parts of apparatus. Fluid injection is performed with a syringe pump. Although a syringe pump is operated remotely through a terminal using a computer, the filling and refilling of syringes, change of syringes and preparation of solutions as well as the adjustment or replacement of tubing has to be performed manually. In addition, all solutions that are used in glove box conditions have to be deoxygenated before use. That adds a considerable amount of time and complexity to the experimental process. Considering the significant technical difficulties these issues can create with regard to the basic conduction of the experiment, the use of a glovebox was excluded.

8.7.1 Anaerobic flow cell for microfluidics; designs and devices

Due to the complications explained in the section above, a new method for simulating near – zero free oxygen conditions had to be developed. A new anaerobic flow – cell had to be created that met the following criteria: a) be a host to the microfluidic experiments on the Sandstone micromodel, b) provide a way to include the necessary inlet and outlet ports and tubing for liquid

injection and exit, c) be gas tight in order for the simulation of oxygen – free conditions, d) provide a clear space for imaging under a microscope – to allow for direct visualization of the experiment and allow total mobility of the apparatus and setup. As this was a novel approach in building oxygen controlling flow cells for microfluidic experiments in petroleum research, there was scarcity of literature in anaerobic simulation methods. The idea of designing a flow cell in which oxygen levels could be controlled came from a patented device designed and created by Lee and Yang (2018). They created a lid device for conventional culture dishes with the purpose of *in situ* reducing oxygen levels, creating and maintaining hypoxia for studying microbial activity insider conventional cell cultures (Figure 8.13). Although their paper provided the basic concept for creating such an anaerobic device, the design of the microfluidic cell for flooding sandstone micromodels had to be significantly different.

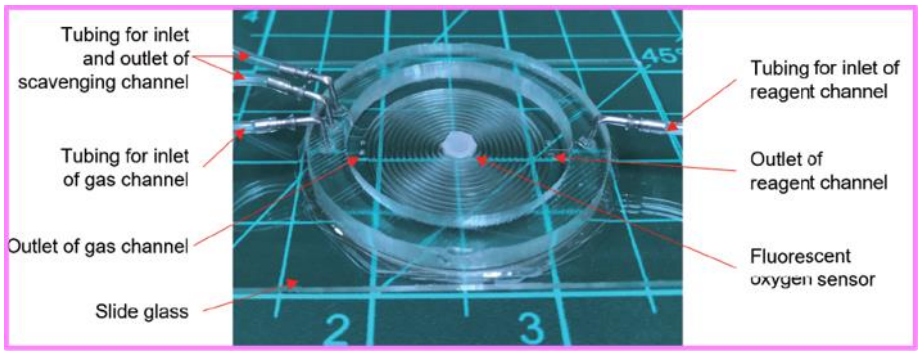

Figure 8.13. Patented device for in situ reducing oxygen levels, creating and maintaining hypoxia in culture cells (modified after Lee and Yang 2018).

Additionally to the main specifications required, the cell had to provide the following: a) robust material that could withstand frequent handling and carrying, optical clarity, b) the ability to withstand temperatures above 70 °C, c) chemical stability and d) very low water absorption. For the abovementioned reasons, the material selected for building the flow cell was clear acrylic. It has a density of 1.19, g/cm^3 (ISO 1183) and 0.2% water absorption index (ISO 62), a Vicat softening temperature of above 110 °C (ISO 306) and a refractive index of 1.49 (ISO 489/A).

The anaerobic flow cell was built in the Physics Workshop, at the Department of Physics, Durham University. Prior to building the flow cell, various designs were created and then modified using the Inventor software. The device consists of two parts: a base unit and a top unit (Figure 8.14). It had to be such that allowed for control over fluid injection and exit and ensure turbulent flow is

minimized. For that purpose inlet – outlet ports were designed to be opposite to each other (B1, B2 in Figure 8.14). In addition to fluid flow ports, a gas inlet port was designed (C1 in Figure 8.14). There was no need for a gas outlet port since any excess gas, oxygen or nitrogen, would exit the cell through the liquid outlet along with the liquid. A socket for holding the sandstone micromodel was designed in the middle of the device (D1 in Figure 8.14). To ensure it was gas – tight, a groove (E1 in Figure 8.14) for holding an o – ring was designed in the base unit. Multiple screw hole positions were designed (A1 – A4 in Figure 8.14) in the top unit to ensure tight sealing and to avoid any liquid or gas leaks. Various dimensions of the base and top units were initially considered, but only designs with the smallest dimensions were selected for manufacture. The most heavily modified section of the device was the main cavity area that was going to hold the micromodel. The design modifications were such that allowed flushing to the top of the cell so that fluid flow had to follow the pore network. Once the optimal design was selected, the manufacturing process began. The figures below show the first flow cell device and the initial designs of its base and top units.

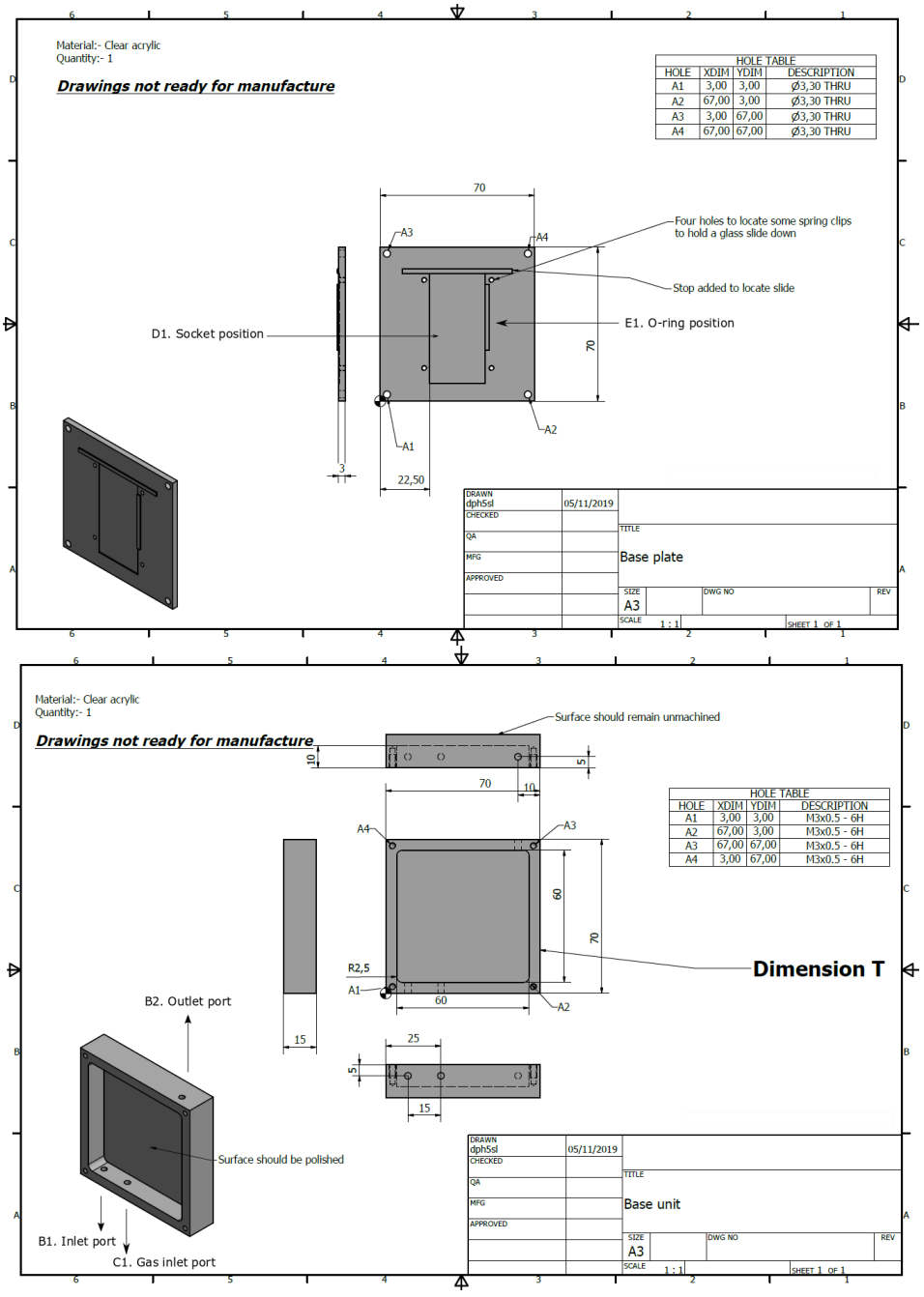

Figure 8.14. First design of base unit (top) and top unit (bottom) of the flow cell using the Inventor software (Waguespack 2014).

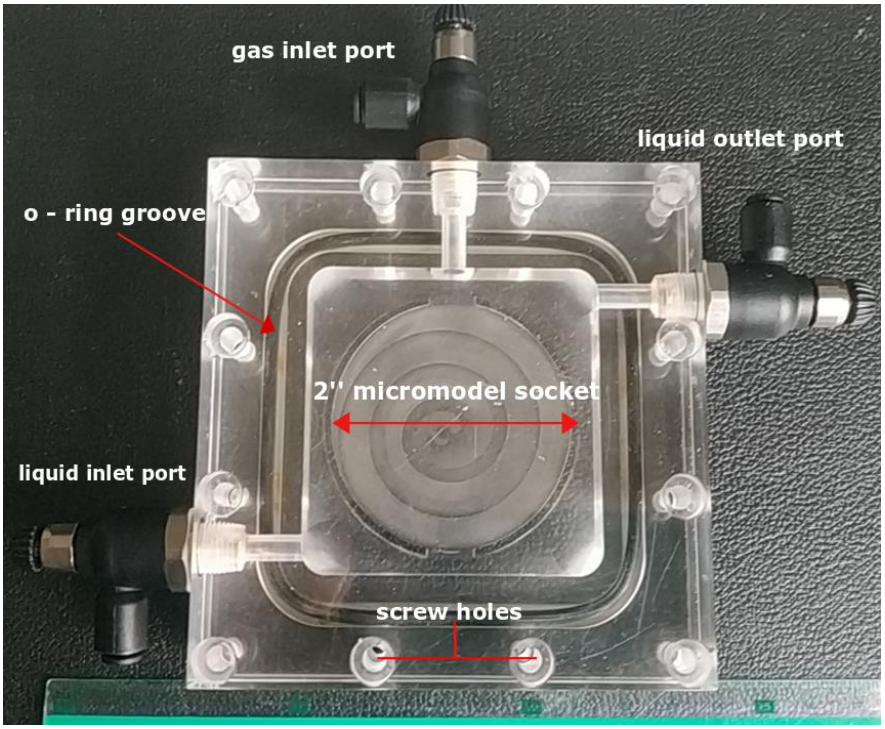

Figure 8.15. Modified flow cell device prototype made of clear acrylic. Rubber O – ring located in the groove around the main socket for ensuring gas – tight conditions. Twelve screw – holes for secure sealing and three flow regulators are attached (Legris) – two for fluid flow and one for gas flow; improved-manufactured version.

The design shown in Figure 8.14 represents the first flow cell device made. However, the end – up flow cell device was modified before manufacture, specifically in the main section of the base plate (Figure 8.15); the shape of the cavity – socket was changed from rectangular to circular so that the micromodels fit inside the cavity. Moreover, there were no spring – clips included in the base plate as that would be problematic both for fluid flow and imaging. The stop was modified to hold the circular wafer securely. Additionally, eight screw holes were added to support the existing four and ensure maximum sealing of the case. Figure 8.15 shows the modified version of the first flow cell.

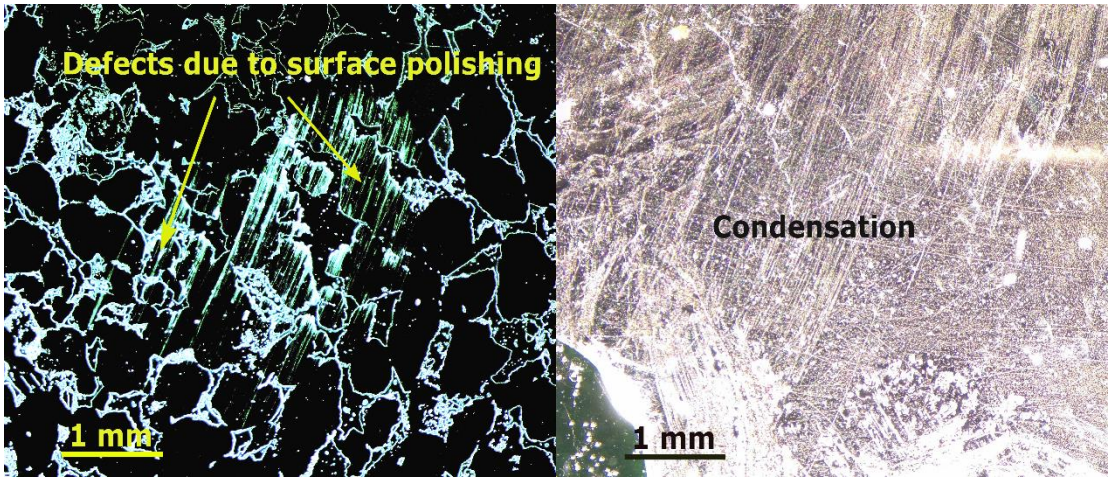

Figure 8.16. Initial tracer fluid testing of prototype flow cell. SU-8 negative photoresist coated micromodel (left); tracer fluid testing and major condensation on the top unit of the device (right). Images taken with a Leica Stereo Fluor M165 FC, using a 1.0 x objective lens.

8.7.2 Second flow cell; design and testing

Due to the limitations of the prototype flow cell explained previously, a second flow cell device was designed and manufactured. The flow cell was heavily modified in terms of dimensions and positioning of the inlet and outlet port and flow regulators. The volume of the main cavity was significantly decreased. That was to allow more control over flow and prevent turbulence, along with ease of flow across its surface. The thickness of the base and top units was also decreased as shown in (Figure 8.17). Overall the second design was improved to a considerable extent with regards to achieving a more controlled fluid flow and gradual filling of the pores. No condensation was created after micro – flooding, leaving a clear area for imaging.

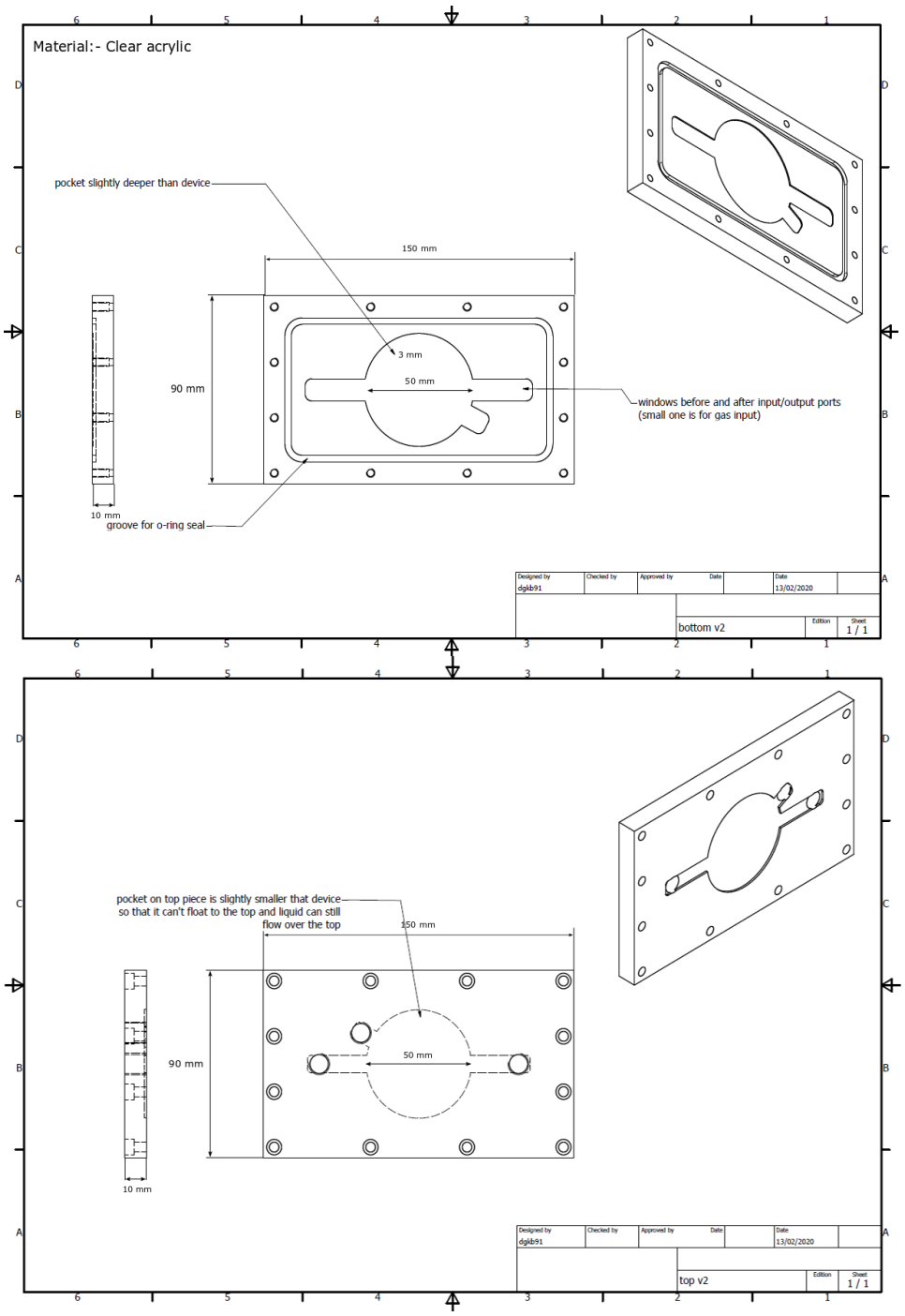

Figure 8.17. Second design of the flow cell device. Modifications include a thinner base and top units, repositioning of inlet and outlet ports for fluid flow and gas injection and decreased cavity volume.

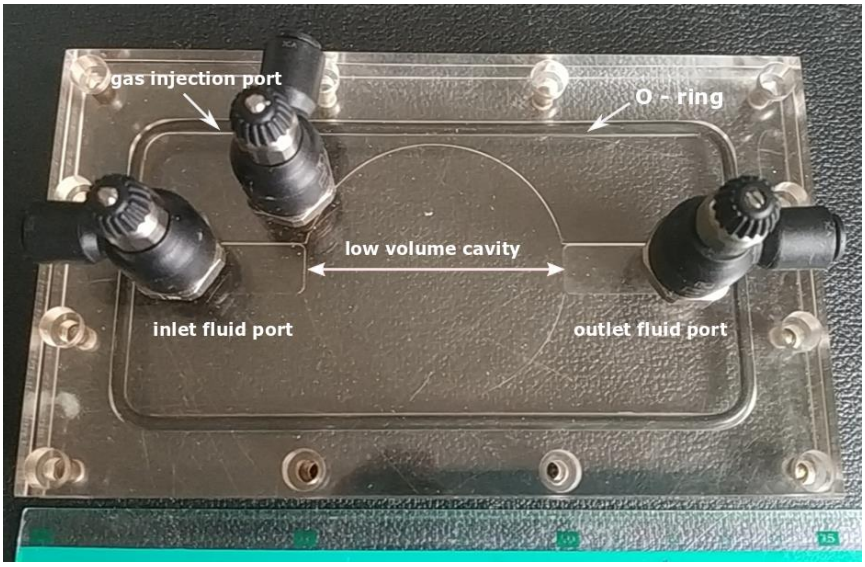

Figure 8.18. Second flow cell device. Thin base and top units, significantly reduced volume in the main cavity, repositioning of inlet and outlet ports for fluid flow and gas injection. The shape of the injection ports is changed; cylindrical ports are replaced.

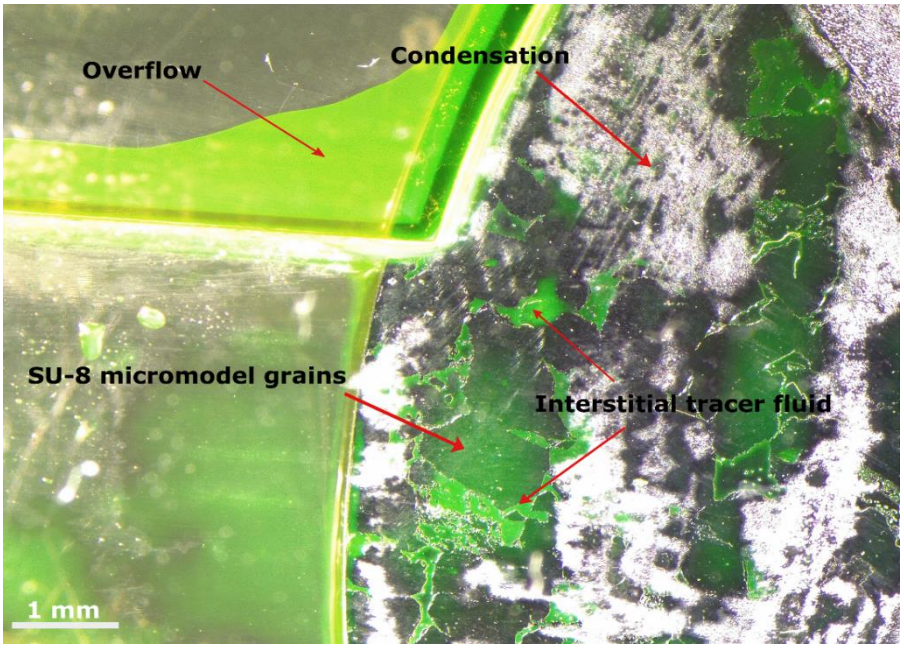

Figure 8.19. Initial tracer fluid micro – flooding test on a sandstone micromodel using second flow cell. For the test, a silicon substrate wafer is used bearing mask 1 written using the SU – 8 photoresist method. The height of features is 25 µm. Over flooding in the side areas of the device led to limited control over flow. Vapor condensation prevented clear imaging as can be seen above. The image was taken with a Leica Stereo Fluor M165 FC, using a 1.0 x objective lens.

8.7.3 Limitations of the flow cells

Limitations of the flow cells were realized after initial micro – flooding tests under a stereo microscope using a syringe pump. Details on the syringe pump and fluidics apparatus are given in Section 8.3. The limitations can be summarized as follows. Excess volume in the cavity located in the middle section of the prototype flow cell caused over flooding and limited control over fluid flow. In addition to the large volume cavity in the center of the device, the large – volume cylindrical inlet and outlet ports provided excessive amount of liquid during flooding that far exceeded the capacity of the pores of the micromodel. That enhanced uncontrollable turbulent flow and overflow. As a result significant condensation was created after an initial test using a tracer fluid on Flow Cell 1 (Figure 8.16) preventing clarity in imaging. Although the second device provided better clarity than the prototype, condensation was still present after flooding. Overflow was still present (Figure 8.19), preventing gradual pore filling. The inlet and outlet channels that replaced the cylindrical ports of the prototype, were once again feeding the micromodel liquid in greater volumes than its capacity. The thickness of base and top plates made imaging possible under a stereo microscope, however further modifications of the flow cell were needed to allow imaging with a confocal microscope.

8.8 Sealing the micromodel; wafer bonding and advanced microfluidics flow cell

So far the attempts to create a controlled micro – flooding system with regards to achieving laminar flow and gradual filling of pores were proven to be inadequate. The limitations mentioned in Section 8.3 were the reasons why the system was unable to provide the desired experimental conditions. Namely, those were poor connectivity resulted from the first unedited image of the Berea sandstone that was written on a photomask, the excess volume of the flow cell main cavity along with the design of inlet – outlet ports and the poorly sealed surface of the micromodel. Since there was no previous work conducted on microfluidic models in combination with anaerobic flow cells, the initiative was taken to explore other possible ways of sealing the micromodel. This was undertaken to simplify the design of the flow cell and avoid adding any unnecessary parts to it. Initially, the top unit of the flow cell was used to seal the wafer by trying out various thicknesses and distances from the surface of the micromodel. Setbacks were only realized after that initiative had been taken. As that was proven to be problematic, other methods for wafer bonding were reviewed and are presented in the discussion section of this chapter. A new setup of the sealed wafer was designed that incorporated the second mask bearing the edited image of the Berea Sandstone. A cross section of the abovementioned sealed wafer is shown in Figure 8.20.

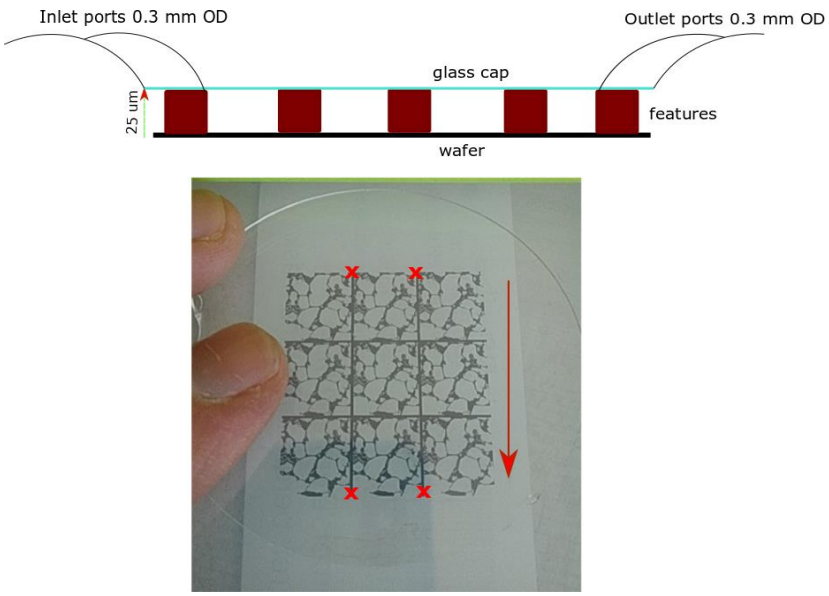

Figure 8.20. Top: Schematic cross section of the combined glass wafer – mask, glass cap and positioning of inlet and outlet ports for fitting of appropriate tubing. Bottom: Modified mask on a glass wafer, to be sealed using wafer bonding. Cross points indicate the inlet and outlet ports, red arrow indicates laminar flow direction.

8.9 Microfluidics; apparatus – syringe pump, tubing, oxygen sensor, portable inert gas (nitrogen) tank and pressure gauge

For the microfluidics experiment the Terumo OEM syringe pump by Chemyx for microfluidic applications was used. The syringe pump has a capacity between 0.5 µL to 60 ml. It operates on a 2.3 cm Stepper Motor – stepping and has a step resolution of 0.098 µm/step and an operating temperature from 4 to 40 °C. The syringe pump was operated manually and remotely using a terminal to access its applications. The specific software used for these experiments was Tera Term, which is open source. All the commands were given manually to the syringe pump as serial command lines through the terminal. The basic commands include start, stop and setting various parameters such as rate of flow and volume. Other commands include help, setting the diameter of the syringe of use and viewing the parameters. Minimum and maximum flow rates vary according to model, syringe size and inner diameter of the syringe and tubing. For the Terumo OEM syringe pump, the minimum and maximum rates are as shown in Table 8.3.

Table 8.3. Minimum and maximum flow rates depending on the syringe size and inner diameter (I.D) (mm) for the Terumo OEM model (Modified after chemyx.com, syringe support library).

Syringe Size	**ID inner diameter [mm]**	**Minimum flow rate [uL/hr]**	**Maximum flow rate [uL/hr]**
1mL	4.93	0.55	1792.32
3mL	9	1.99	6489.02
5mL	13.04	4.18	13622.26
10mL	15.79	6.14	19973.69
20mL	20.18	10.02	32623.94
30mL	23.36	13.43	43715.93
60mL	29.45	21.35	69480.78

The tubing used in all connections was a fluoropolymer (PTFE) Teflon. The benefits of using Teflon for fluidics studies is that it is thermally stable at temperatures ranging from -223 to 360 °C and has excellent electrical properties including a dielectric constant of 2.1 F/m. It is an insulating material with surface resistivity of 3.6×10^{12} ohms. It is also a non – stick material allowing for ease of movement of liquid. The flow regulators connected with the tubing were purchased by Legris. Specifically for the setup shown in Figures 8.11 and 8.15, the 7010 flow regulators with an outer diameter of 4 mm were used. These are Banjo type flow regulators with a recessed screw. They offer stability during flow and their robust construction makes them ideal for extended use. For tracer liquid testing, the BD Plastipak™ 50 mL syringes were used (Fisher Scientific). For clay

injection and reducing solution, borosilicate glass 50 mL Luer Lock Metal tip syringes were used (Chem Stores, Department of Chemistry, Durham University). These syringes were used to ensure gas tight conditions during in situ – clay reduction.

8.9.1 Monitoring oxygen levels

To measure free oxygen levels and ensure near – zero free oxygen conditions are maintained during the in – situ reduction, a free – oxygen meter was required. Due to the complexity of the experiment, monitoring free oxygen levels in this case requires a non – intrusive method for measuring free – oxygen conditions. For this particular study the selected non – intrusive method is based on the use of a fluorescent optical sensor. For this task, the NeoFox Optical Oxygen Sensor (FOXY) was purchased by Ocean Optics. FOXY measures fluorescent lifetime with the use of excitation of LED light along with photodiode detection. Measurements are taken with the use of probes that are optic fibre fluorescent. The tip of the probes contains an oxygen – sensing thin film. The probe is positioned perpendicularly to a patch that is attached to the inside wall of the vessel under study. The probe measures free oxygen percentages between 0 – 100% and dissolved oxygen between 0 – 40 ppm. It has a O_2 resolution between 0.001 – 0.05% and a dissolved oxygen resolution between 4 – 20 ppb. For this application a below 20 ppb dissolved oxygen resolution would be the acceptable level – EOR deployment is performed after using oxygen scavengers to deoxygenate injection water down to 20 ppb (details on EOR deployment provided by BP). The accuracy of the readings is 5% and the minimum detectable free – oxygen level varies between 0.01 – 0.05%. It can operate at temperatures between -50 and +80 °C. The patch has the same specifications as the probe in terms of free oxygen and dissolved oxygen detection range, O_2 resolution, dissolved oxygen resolution, accuracy of reading and minimum detectable limit. It operates at a temperature range between -20 and +60 °C. This makes it perfect for this application – fluid flow experiments to be conducted at ambient temperature of +20 °C. Temperature will be kept constant throughout the runs.

Calibration of the probe can be done either for two points (two – point calibration) or more (multipoint calibration). For this experiment, a two – point calibration is required for further work. For the calibration, two oxygen concentrations must be known, including the 0% free oxygen concentration. The probe must first be exposed to the 0% free oxygen environment until the value is read and saved in the FOXY software. For this reading, the vessel must be purged with nitrogen until the probe reads 0%.The second concentration is usually that of ambient conditions at 20.9% oxygen. Once the reading is saved in the FOXY software, the calibration is complete. The FOXY software can be operated manually and remotely through a computer. It saves the concentrations

of free oxygen at a given point and displays charts that can be reviewed in the future. An additional pre – calibrated probe for measuring the temperature of the system comes with the package.

8.9.2 Purging with nitrogen

Nitrogen purging for creating near zero free oxygen conditions has been used in previous studies focused on the redox effects on iron-bearing sandstones (Yesufu-Rufai et al 2020; Unsal et al 2020). The same method can be used to keep oxygen levels below 20 ppb inside the flow cell holder of the sandstone micromodel. Due to the small size of the flow cell, the tubing attached to the nitrogen tank must be such that allows small volumes of gas to enter. A standard nitrogen gas tank can be used for the purging along with Teflon tubing. A pressure gauge is also necessary to keep track of the applied gas pressure inside the flow cell. For this task a standard analogue pressure gauge with a range of 0 – 140 psi is recommended. Keeping track of the pressure of the system is critical to monitor flow rates.

8.9.3 Suggested setup, *in situ* reduction and visualization

As it was mentioned in the introduction of this chapter, the final section aims to present the setup for simulating a reduced environment in a microbricated sandstone proxy. Following the setup, the protocol for the in – situ reduction is presented. Once that is established, increased complexity

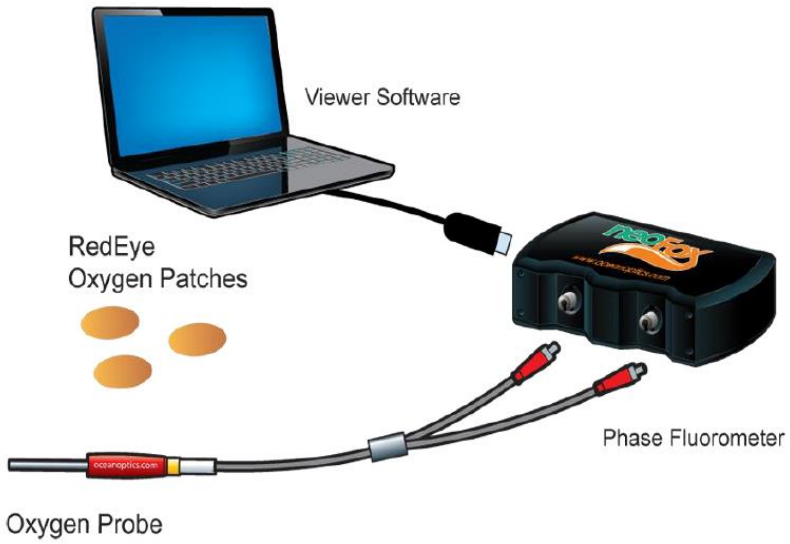

Figure 8.21. FOXY oxygen probe setup (Ocean Optics Oxygen Sensing Manual, modified).

regarding the salinity of the injected water, oil injection and reoxydation of the micromodel is possible. The setup consists of the sandstone micromodel and sealed microchip, the flow cell device, the syringe pump and tubing, a fitted pressure gauge, the free – oxygen sensor and the

nitrogen tank with tubing. In addition, a heating plate is needed to heat the flow cell holding the sandstone micromodel in order for the in – situ reduction to take place. For the clay reduction, sodium dithionite, sodium bicarbonate and sodium citrate by Sigma Aldrich and nontronite NAu – 2 powder from the Clay Mineral Repository, Chantilly VA, USA are needed for the iron – bearing clay chemical reduction. For the direct imaging, a Leica Stereo Fluor M165 FC microscope with a mounted camera (FLEXACAM C1) and a computer. Imaging under a Stereo Microscope can set the basis for more complex imaging, such as that possible with the use of confocal microscopy, once the process is refined.

8.10 Discussion

Sandstone proxy: Micromodel features are up – scaled and do not represent a realistic pore system, calling for better resolution of images and nanoscale fabrication. Due to the technical limitations embedded in the equipment in the MEMS microfabrication lab at the Department of Engineering, Durham University, nanoscale structures are not possible to manufacture. Deviations from real sandstone flooding are expected to be seen during micro – flooding relative to the following: fluid flow and preferential flow paths and overall pore connectivity and pore blocking. Although the possibility of discrepancies between the micromodel and the Berea sandstone is well understood and expected, up – scaling the features and improving connectivity serve as an excellent way of ensuring optimal visualization of the *in situ* reduction. Consequently, a better understanding of migrating fines in the micromodel proxy can be gained and comparison between individual pores can be enhanced. In terms of overall pore connectivity, the microfabricated proxy was made taking the work of Buchgraber and co-workers (2012) and Song and Kovscek (2016) into account. The overall depth (in our micromodel this is equal to the height of a feature) features was 25 µm and 30 µm in the 2012 and 2016 studies respectively and dimension-wise the smallest was roughly 4 µm in diameter. Additional modifications were manually performed to ensure good pore connectivity was achieved. That was possible with the use of an artificial pore network (2012 study) and the upscaling of pixels size (2016 study). The end product as was presented in earlier sections of this chapter was the outcome of the combined methods used by the previous workers.

In terms of the micromodel's material, using the SU-8 polymer gives an edge over traditional silicon or glass etching by introducing, for the first time, a polymer-based micromodel with excellent aspect ratio properties for EOR microfluidics. In addition, wettability is easily controlled with surface wettability modifications methods as described in Section 8.2.2. Compared with the work done using silicon and glass etching, the wettability of the SU-8 will start off as hydrophobic

as indicated in Section 8.2.2. However, it can easily be manipulated and e comparable to the less hydrophobic wettabilities of silicon and glass. The wettability of the SU-8 polymer is going to have an effect on the adhesion of water, clay and crude oil to the surface of the microstructures. As this material has not been used for petroleum research purposes before, there are no references with regard to its mixed wetting behaviour and affinity towards clay, low salinity water and crude oil. Techniques for altering the wetting state and the adhesion forces between various oils and of SU – 8 structures are known. However, how an altered SU – 8 surface will behave during a chemical reduction process that involves heating and injection of a reducing solution remains unknown. Even if the wettability is changed with the use of surface activation methods, it is unclear whether it will remain the same after chemical reduction and injection of nitrogen gas into the flow cell.

The autofluorescence in visible wavelengths of SU – 8 and of crude oil can be confusing during imaging under a confocal microscope or even after simple tracer fluid tests using UV light as an excitation source. However, it should be possible to tack the movement of clay minerals as each seems to fluoresce at different wavelengths (Harasawa 2020, M.Res thesis).

Overall, the production of the SU-8 micromodel requires more steps than the traditional etching (i.e. application of the polymer, development and baking stage; see Section 8.2.1) that would make the process more time consuming. However, it can be said that the very high aspect ratio and robustness of the SU-8 structures compensate for the longer production times.

Flow cell device: EOR microfluidics have been used in previous studies as mentioned in the sections of this chapter. The 2 D micromodels have been successfully mounted onto holders that allow for fluid injection in ambient conditions. However, redox conditions have been neglected in a 2 D micromodel setting. Redox processes and effects on wettability have only recently started to gain attention (Yesufu-Rufai et al 2020; Unsal et al 2020). To this day, there is no complete study done on microfluidics, redox processes and their effect by means of direct visualization under a microscope. The novel flow cell designed and presented here, has a potential for delivering 2 D imaging of mines migration as a redox controlled process.

Visualisation of oil, fines and redox changes: Tracking of fluid flows can be achieved, both in quantity and quality, using standard imaging techniques, previously used in microfluidics. These include standard optical microscopy (Yu et al 2019; Mejia et al 2020). These workers used standard optical microscopes and mounted cameras to track fluid flow for EOR applications. Also, specifically, fluorescence microscopy can also been used to look at flow paths, either of tracer fluids (Buchgraber et al 2012), crude oil or clay minerals (Harasawa 2020, M.Res thesis), as has been used in previous studies. Gauteplass et al (2015) used fluorescence microscopy to track pore-

level foam generation in micromodels simulating fractured systems. Another example of using UV excitation microscopy is found in the work of Song and Kovscek (2016) that used confocal microscopy to track kaolinite induced formation damage.

In situ reduction can be documented easily using a model clay such as nontronite NAu – 2 due to its color change, typical for nontronite clay minerals (Stucki 2011), following crystal lattice rearrangements as these have been described in chapters 5, 6 and 7. In that way, mineral migration can also be easily tracked under a microscope in this 2 D setup. That is not possible in the case of testing other clays, such as illite IMt – 2 that does not exhibit color changes after iron reduction. Although near zero free oxygen conditions are achievable, identifying the reduction potential of the entire system and the degree of possible reoxidation of the clays can be a difficult task. The recommended running time of the iron reduction experiment is long (6 – 8 hours) and it requires constant and steady supply of nitrogen to ensure free oxygen levels inside the flow cell remain 0% at all times. Although these limitations should be taken into consideration, the abovementioned designs and trials provide the first suggestion to realistically monitor clay reduction in a 2 D microfluidic simulation of a sandstone. That could potentially lead to a more accurate and better quantitative elucidation of fines migration behaviour as a redox controlled process.

8.11 Conclusions

The methods described throughout this chapter can set the basis for studying micromodels in an anaerobic environment and directly visualize changes regarding their redox state, flow paths, water and oil emulsions and fines migration. In the above sections, the methods for preparation of a sandstone proxy were presented, along with the original designs and models of wafers. The SU – 8 polymer was introduced as a novel material for microfluidics flooding simulation. Original designs of anaerobic flow – cells were presented along with tracer fluid tests that tested the models for their suitability. An optimal experimental setup is suggested in Chapter 9 that could help with the monitoring of in – situ reduction of clay minerals in a microfabricated sandstone proxy. The peripherals included in the apparatus section and the suggestions mentioned can monitor and regulate free oxygen levels inside the anaerobic flow cell. However the method bears limitations that are subject to refining and optimization. This study provides the basis for further development on the EOR microfluidics.

8.12 Future work

Wafer bonding methods; suggestions for microchip creation: Many microfabrication applications require sealing of the wafer for the creation of microfluidic or microelectromechanical systems (MEMS), therefore calling for an advanced method of wafer bonding. In previous studies in microfluidics where sandstone or limestone masks were written on wafers, anodic bonding was used as the sealing method (Buchgraber et al 2012, Song and Kovscek 2016). This method is most commonly used for the bonding a borosilicate glass (Pyrex) and silicon wafers. The bonding occurs at temperatures between 300 °C and 450 °C after microfabrication is complete (Lapadatu, Jakobsen 2015). Bonding is achieved by the polarization of alkali glass used to seal the wafer by heating both the silicon and the glass wafer up to 450 °C and applying DC voltage between the range of 400 and 1000 V. As a result, bonding is achieved after the glass wafer gains opposite charge to that of the silicon wafer. Another widely used method for wafer sealing is direct bonding. Conventional direct bonding utilizes the flat and smooth surface of the wafers so that they can elastically be brought into contact through short – range adhesion forces without any intermediate bonding material (Turner and Spearing 2006). As described by Tong and Gosele (1999), the wafers are first joined at ambient temperature followed by heating that leads to the formation of primary bonds between them. The abovementioned techniques for wafer bonding are mainly used for etched wafers, with no other intermediate materials used for the bonding. Since the SU – 8 negative photoresist was used to create the features of the sandstone micromodel onto the silicon wafer, the sealing was requiring a more sophisticated method of wafer sealing. The following experimental microchip setup by Garcia et al (2009), is the recommended method for sealing a silicon wafer bearing SU – 8 features with glass. In their work, they created a multi-layered micromodel chip that consisted of SU – 8 microstructures. The micro – engineered channels were sandwiched between a base silicon wafer with an additional layer of SU – 8 2 and a top SU – 8 2 layer sealed by a layer of glass. The silicon base was thermally oxidized in order for surface activation to take place. Once that was achieved, the bottom SU – 8 layer was applied. The SU – 8 microstructures were bonded with the upper SU – 8 layer with the use of air – brushing coating technique. The final layer of glass was bonded with the upper SU – 8 layer by means of post exposure bake at around 60 °C for approximately one hour. This multilayer system provides an excellent alternative to traditional bonding of etched micromodels. The method described can be used as a protocol to seal micromodel proxies built with SU – 8 negative photoresist.

The creation of the microchip as described above requires the redesigning of the flow cell holder. That is necessary in order for the microchip to properly sit inside the holder without additional

forces applied due to confined space. Also, due to the new design of the microchip, inlet and outlet ports have to be drilled through the top part of the holder for the fitting of the appropriate tubing as seen in Figure 8.22.

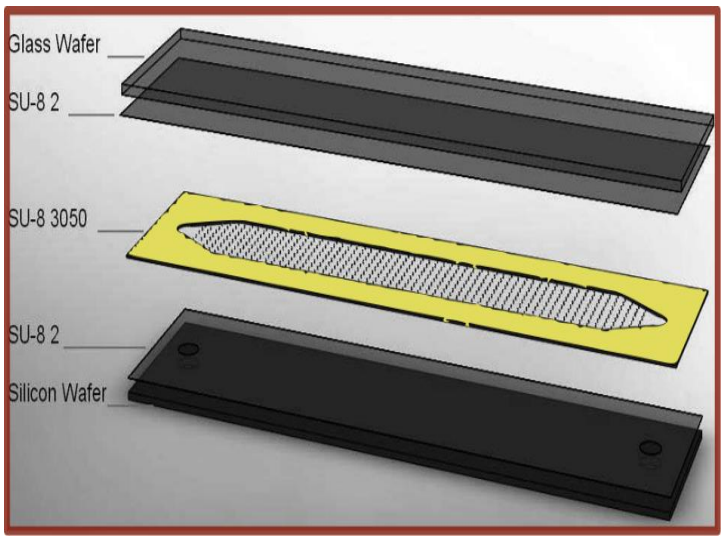

Figure 8.22. Multilayer micromodel by Garcia and co – workers (2009) (SENSOR+TEST Conference 2009 - SENSOR 2009 Proceedings, modified).

8.13 References

1. Blauw, M. A., T. Zijlstra, and E. W. J. M. van der Drift. "Balancing the etching and passivation in time-multiplexed deep dry etching of silicon." *Journal of Vacuum Science & Technology B: Microelectronics and Nanometer Structures Processing, Measurement, and Phenomena* 19, no. 6 (2001): 2930-2934.
2. Bornside, D. E., C. W. Macosko, and L. E. Scriven. "MODELING OF SPIN COATING." *Journal of imaging technology* 13, no. 4 (1987): 122-130.
3. Bryant, Rebecca S., and Jonell Douglas. "Evaluation of microbial systems in porous media for EOR." *SPE reservoir engineering* 3, no. 02 (1988): 489-495.
4. Buchgraber, M., M. Al-Dossary, C. M. Ross, and Anthony R. Kovscek. "Creation of a dual-porosity micromodel for pore-level visualization of multiphase flow." *Journal of Petroleum Science and Engineering* 86 (2012): 27-38.
5. Burruss, Robert C. "Practical aspects of fluorescence microscopy of petroleum fluid inclusions." (1991).
6. Cao, Cuong, Sam W. Birtwell, Jonas Høgberg, Anders Wolff, Hywel Morgan, and D. Duong Bang. "Surface modification of photoresist SU8 for low autofluorescence and bioanalytical applications." In *15th International Conference on Miniaturized Systems for Chemistry and Life Sciences (Seattle, Washington, USA, 2011)*, pp. 1161-1163. 2011.
7. Cardoso, Oldemar Ribeiro, and Rosangela de Carvalho Balaban. "Comparative study between Botucatu and Berea sandstone properties." *Journal of South American Earth Sciences* 62 (2015): 58-69.
8. Chambers, K. T., and Clayton John Radke. *Micromodel foam flow study*. No. DOE/SF/00098-T17. California Univ., Berkeley, CA (USA). Dept. of Chemical Engineering, 1990.
9. Chekurov, Nikolai, Kestutis Grigoras, Lauri Sainiemi, Antti Peltonen, Ilkka Tittonen, and Sami Franssila. "Dry fabrication of microdevices by the combination of focused ion beam and cryogenic deep reactive ion etching." *Journal of Micromechanics and Microengineering* 20, no. 8 (2010): 085009.
10. Davis, J. A., and S. C. Jones. "Displacement mechanisms of micellar solutions." *Journal of Petroleum Technology* 20, no. 12 (1968): 1415-1428.
11. del Campo, Aránzazu, and Christian Greiner. "SU-8: a photoresist for high-aspect-ratio and 3D submicron lithography." *Journal of micromechanics and microengineering* 17, no. 6 (2007): R81.

12. Gao, Zhan, David B. Henthorn, and Chang-Soo Kim. "Enhanced wettability of an SU-8 photoresist through a photografting procedure for bioanalytical device applications." *Journal of Micromechanics and Microengineering* 18, no. 4 (2008): 045013.
13. Garcia-Blanco, Sonia, Patrice Topart, Karine Le Foulgoc, Jean-Sol Caron, Yan Desroches, Christine Alain, Francois Chateauneuf, and Hubert Jerominek. "Hybrid wafer-level vacuum hermetic micropackaging technology for MOEMS-MEMS." In *Reliability, Packaging, Testing, and Characterization of MEMS/MOEMS and Nanodevices VIII*, vol. 7206, p. 720602. International Society for Optics and Photonics, 2009.
14. Gaudet, Matthieu, Jean-Christophe Camart, Lionel Buchaillot, and Steve Arscott. "Variation of absorption coefficient and determination of critical dose of SU-8 at 365 nm." *Applied Physics Letters* 88, no. 2 (2006): 024107.
15. Gauteplass, Jarand. "Pore-to-core Laboratory Upscaling and Visualization of Enhanced Oil Recovery and CO2 Storage." (2015).
16. Georg, Maximilian, Tamara Fernandez-Cabada, Natalia Bourguignon, Paola Karp, Ana B. Peñaherrera, Gustavo Helguera, Betiana Lerner, Maximiliano S. Pérez, and Roland Mertelsmann. "Development of image analysis software for quantification of viable cells in microchips." *Plos one* 13, no. 3 (2018): e0193605.
17. HARASAWA, YU,EMMA (2021) Imaging Fines Migration Induced by Salinity Changes, Durham theses, Durham University. Available at Durham E-Theses Online: http://etheses.dur.ac.uk/13907/
18. Hendraningrat, Luky, Shidong Li, and Ole Torsæter. "A coreflood investigation of nanofluid enhanced oil recovery." *Journal of Petroleum Science and Engineering* 111 (2013): 128-138.
19. Hornbrook, J. W., L. M. Castanier, and P. A. Pettit. "Observation of foam/oil interactions in a new, high-resolution micromodel." In *SPE Annual Technical Conference and Exhibition*. OnePetro, 1991.
20. Jańczuk, Bronislaw, Emil Chibowski, and Tomasz Białopiotrowicz. "Interpretation of the contact angle in quartz/organic liquid film-water system." *Journal of colloid and interface science* 102, no. 2 (1984): 533-538.
21. Kim, Bumsuk, Jongjin Lee, and Insuk Yu. "Electrical properties of single-wall carbon nanotube and epoxy composites." *Journal of Applied Physics* 94, no. 10 (2003): 6724-6728.

22. King, H., 2020. Fluorescent Minerals And Rocks: They Glow Under UV Light!. [online] Geology.com. Available at: <https://geology.com/articles/fluorescent-minerals/> [Accessed 27 August 2020].
23. LaBianca, Nancy C., and Jeffrey D. Gelorme. "High-aspect-ratio resist for thick-film applications." In *Advances in Resist Technology and Processing XII*, vol. 2438, pp. 846-852. International Society for Optics and Photonics, 1995.
24. Lapadatu, Adriana Cozma, and Henrik Jakobsen. "Anodic bonding." In *Handbook of Silicon Based MEMS Materials and Technologies*, pp. 599-610. William Andrew Publishing, 2015.
25. Larson, Ronald G., and Timothy J. Rehg. "Spin coating." In *Liquid Film Coating*, pp. 709-734. Springer, Dordrecht, 1997.
26. Lee, Seung Yeob, and Sung Yang. "A microfluidic-based lid device for conventional cell culture dishes to automatically control oxygen level." *BioTechniques* 64, no. 5 (2018): 231-234.
27. Ling, Gee Chong, Min Hui Low, Martina Erken, Sharon Longford, Shaun Nielsen, Andrew J. Poole, Peter Steinberg, Diane McDougald, and Staffan Kjelleberg. "Micro-fabricated polydimethyl siloxane (PDMS) surfaces regulate the development of marine microbial biofilm communities." *Biofouling* 30, no. 3 (2014): 323-335.
28. Mattax CC, Kyte JR (1961) Ever see a water flood? Oil Gas J 59:115–128
29. Mejia, Lucas, Peixi Zhu, Jeffrey D. Hyman, Kishore K. Mohanty, and Matthew T. Balhoff. "Coreflood on a chip: Core-scale micromodels for subsurface applications." *Fuel* 281 (2020): 118716.
30. Oren, P. E. "of Waterflood by Gas flnjection for Water-Wet ‘Conditions." *Evaluation* (1992): 71.
31. Pai, Jeng-Hao, Yuli Wang, Gina To'A. Salazar, Christopher E. Sims, Mark Bachman, G. P. Li, and Nancy L. Allbritton. "Photoresist with low fluorescence for bioanalytical applications." *Analytical chemistry* 79, no. 22 (2007): 8774-8780.
32. Qin, Dong, Younan Xia, and George M. Whitesides. "Elastomeric light valves." *Advanced Materials* 9, no. 5 (1997): 407-410.
33. Rangel-German, E. R., and A. R. Kovscek. "A micromodel investigation of two-phase matrix-fracture transfer mechanisms." *Water resources research* 42, no. 3 (2006).
34. Reichmanis, Elsa, Omkaram Nalamasu, and Francis M. Houlihan. "Polymers for microlithographic applications: new directions and challenges." In *Macromolecular Symposia*, vol. 175, no. 1, pp. 185-196. Weinheim: WILEY-VCH Verlag GmbH, 2001.
35. Rost, Fred WD. *Fluorescence microscopy*. Vol. 2. Cambridge University Press, 1992.

36. Ryder, Alan G. "Analysis of crude petroleum oils using fluorescence spectroscopy." In *Reviews in Fluorescence 2005*, pp. 169-198. Springer, Boston, MA, 2005.
37. Schindelin, Johannes, Ignacio Arganda-Carreras, Erwin Frise, Verena Kaynig, Mark Longair, Tobias Pietzsch, Stephan Preibisch et al. "Fiji: an open-source platform for biological-image analysis." *Nature methods* 9, no. 7 (2012): 676-682.
38. Seright, Randall S., J. Mac Seheult, and Todd Talashek. "Injectivity characteristics of EOR polymers." *SPE Reservoir Evaluation & Engineering* 12, no. 05 (2009): 783-792.
39. Silverio, Vania, Miguel Amaral, João Gaspar, Susana Cardoso, and Paulo P. Freitas. "Manipulation of Magnetic Beads with Thin Film Microelectromagnet Traps." *Micromachines* 10, no. 9 (2019): 607.
40. Skinner, Jack Lindon. *Diffractive optical MEMS technology for tunable filters and modulators*. University of California, Davis, 2007.
41. Song, Wen, and Anthony R. Kovscek. "Direct visualization of pore-scale fines migration and formation damage during low-salinity waterflooding." *Journal of Natural Gas Science and Engineering* 34 (2016): 1276-1283.
42. Stucki, Joseph W. "A review of the effects of iron redox cycles on smectite properties." *Comptes Rendus Geoscience* 343, no. 2-3 (2011): 199-209.
43. Tavakoli, S. M., D. A. Pullen, and S. B. Dunkerton. "A review of adhesive bonding techniques for joining medical materials." *Assembly Automation* (2005).
44. Teh, Su Fern, Tianxi Liu, Lei Wang, and Chaobin He. "Fracture behaviour of poly (ethylene terephthalate) fiber toughened epoxy composites." *Composites Part A: applied science and manufacturing* 36, no. 8 (2005): 1167-1173.
45. Tisler, Julia, Gopalakrishnan Balasubramanian, Boris Naydenov, Roman Kolesov, Bernhard Grotz, Rolf Reuter, Jean-Paul Boudou et al. "Fluorescence and spin properties of defects in single digit nanodiamonds." *ACS nano* 3, no. 7 (2009): 1959-1965.
46. Tong, Q-Y., and Ulrich M. Gösele. "Wafer bonding and layer splitting for microsystems." *Advanced Materials* 11, no. 17 (1999): 1409-1425.
47. Turner, K. T., and S. M. Spearing. "Mechanics of direct wafer bonding." *Proceedings of the Royal Society A: Mathematical, Physical and Engineering Sciences* 462, no. 2065 (2006): 171-188.
48. Unsal, Evren, Hilbert van der Linde, and Ove B. Wilson. "Redox effects on relative permeability in Fe-rich clay bearing sandstones." *Marine and Petroleum Geology* 115 (2020): 104251.

49. van de Wijdeven, Rosanne, Ola Huse Ramstad, Vibeke Devold Valderhaug, Peter Köllensperger, Axel Sandvig, Ioanna Sandvig, and Øyvind Halaas. "A novel lab-on-chip platform enabling axotomy and neuromodulation in a multi-nodal network." *Biosensors and Bioelectronics* 140 (2019): 111329.
50. Voordouw, Gerrit, Stephen M. Armstrong, Monika F. Reimer, Benjamin Fouts, Anita J. Telang, Y. I. N. Shen, and Diane Gevertz. "Characterization of 16S rRNA genes from oil field microbial communities indicates the presence of a variety of sulfate-reducing, fermentative, and sulfide-oxidizing bacteria." *Applied and Environmental Microbiology* 62, no. 5 (1996): 1623-1629.
51. Wei, Xuemei, Wenchao Jiang, Yanyu Zhang, Zhao Wang, Xiaojun Li, and Feipeng Wu. "Investigation of Clay Type on Low Salinity Water Flooding Using a Glass Micromodel." *Frontiers in Energy Research* (2020): NA-NA.
52. Xie, X., and N. R. Morrow. "Contact angles on quartz induced by adsorption of heteropolar hydrocarbons." *Journal of adhesion science and technology* 13, no. 10 (1999): 1119-1135.
53. XU, Ke, Peixi Zhu, Colon Tatiana, Chun Huh, and Matthew Balhoff. "A microfluidic investigation of the synergistic effect of nanoparticles and surfactants in macro-emulsion based EOR." In *SPE Improved Oil Recovery Conference*. OnePetro, 2016.
54. Yang, Ren, and Wanjun Wang. "A numerical and experimental study on gap compensation and wavelength selection in UV-lithography of ultra-high aspect ratio SU-8 microstructures." *Sensors and Actuators B: Chemical* 110, no. 2 (2005): 279-288.
55. Yeom, Junghoon, Yan Wu, and Mark A. Shannon. "Critical aspect ratio dependence in deep reactive ion etching of silicon." In *TRANSDUCERS'03. 12th International Conference on Solid-State Sensors, Actuators and Microsystems. Digest of Technical Papers (Cat. No. 03TH8664)*, vol. 2, pp. 1631-1634. IEEE, 2003.
56. Yesufu-Rufai, Sherifat, Maja Rücker, Steffen Berg, Sarah F. Lowe, Fons Marcelis, Apostolos Georgiadis, and Paul Luckham. "Assessing the wetting state of minerals in complex sandstone rock in-situ by Atomic Force Microscopy (AFM)." *Fuel* 273 (2020): 117807.
57. Zhang, Hua, Alex Nikolov, and Darsh Wasan. "Enhanced oil recovery (EOR) using nanoparticle dispersions: underlying mechanism and imbibition experiments." *Energy & Fuels* 28, no. 5 (2014): 3002-3009.

Chapter 9: Summary of findings and future work

9.1 Introduction

There are now many studies examining low salinity water flooding to increase oil recovery. However very few consider the oxidation state. This PhD work was focused on shedding light onto the following: a) understanding manufactured surface roughness on coated clay films using contact and non-contact techniques; b) understanding the wettability and interplay at the clay-crude oil interface by making thin films of clays to represent reservoir mineral surfaces and understanding how they wet when reduced and oxidised by measuring the contact angle of different wetting phases; c) understanding swelling capacity and hydration state of reservoir clay minerals as a function of reduction extent in the bulk (interlayer) and at surface (surface hydration) along with the cation budget of the clay minerals in reduced and oxidized conditions, That was possible by probing the mechanisms of the changes observed by water sorption and IR spectroscopy; d) developing a flow cell apparatus to study fines migration *in situ* as a function of redox state. Having understood how redox state effects hydration of clay minerals and wettability, the subsequent impact on fines migration, detachment and mobilisation of fines can be better understood by *in situ* visualization. In this final chapter the findings of the work are presented and discussed within the context of Low Salinity Water Flooding. Future work is included in studying LSWF in anoxic conditions.

9.2 Summary

9.2.1 Understanding engineered surface roughness of coated clay films

The aim of this study was the overall characterization of the topography of the clay substrates. The basic methods for obtaining the roughness profile were the atomic force microscopy, white light interferometry and confocal microscopy, which was used as a complementary and novel approach to characterize the surface texture of the substrates. Surface characterization was critical in order to create a roughness profile of the casted clay films and ensure discrepancies did not occur between the clay substrates. The collected data and their interpretation provided a quantitative estimation of the surface topography.

Results from the CCI Talysurf showed the topographic highs and lows of the selected cross section in nm. The topography of NAu-2 substrates varied in terms of the shape of the coating. The coating appeared as lumps that vary in quantity. Most aggregates were found in NAu-2 – 2 substrate. Despite the different shapes of the coated material, there was no significant variation in the

primary roughness values (see appendix A.1). Therefore, it can be said that the difference in the shape of the topography was not followed by a significant change in roughness. The coating of the surface did not show a significant variation among the substrates. Most variations could be seen in white yellow as scattered material that represented higher topographic points, mainly in SCa-3 – 3. The coating of IMt-2 appeared in different shapes; IMt-2 – 1 and IMt2 – 3 coatings for valleys that appeared across or in the center of the substrate's surface whereas IMt2 – 2 and IMt2 – 4 had scattered accumulations of coating.

Results from the AFM showed that NAu-2 – 1 and NAu-2 – 2 had similar primary Ra values that average 58.45 and 78.9 nm respectively. NAu-2 – 3 showed small variation in primary Ra values compared to the first two substrates. NAu-2 – 3 substrate appeared to be relatively rougher, averaging a primary Ra value of 253 nm. That can be seen in NAu-2 – 3 that had created wavy coatings as opposed to NAu-2 – 1 and NAu-2 – 2 where the shape was more irregular and the features were spikes instead of waves. SCa-3 – 1 and SCa-3 – 2 had similar primary Ra values that average 134.65 and 153.18 respectively. Similarities in surface texture were clear in SCa-3 – 1 and SCa-3 – 2 in the 2 D profiles. The first two substrates showed patches of clay material almost equally coating the glass surface, whereas SCa-3 – 3 showed that the material had coated the surface in waves, forming a different surface texture. That was also shown in the 3 D images of SCa3 substrates. The wavy – darker profile showed an increased primary Ra compared to SCa3 – 1 and SCa3 – 2. IMt-2 showed primary Ra values that average 114.17 and 81.83 for IMt-2 – 1 and IMt-2 – 2 and 79.66 nm for IMt-2-3. All substrates had similar texture.

Confocal microscopy results showed SCa-3 substrates averaged fluorescence intensities that had values up to 750 Arbitrary Units (AU). Substrates SCa3 – 1 and SCa3 – 2 had similar intensity values whereas SCa3 – 3 averaged 300 AU. The intensity profiles did not vary significantly. The average fluorescence intensity of IMt2 – 1 and IMt2 – 3 values reached up to 580 AU and 500 AU respectively with a dissimilar distribution of intensity between the substrates. NAu2 substrates had the lowest fluorescence intensity values. NAu2 – 1 and NAu2 – 3 averaged 20 AU and NAu2 – 2 averaged intensity did not exceed 12 AU. In terms of the intensity's distribution, all three substrates had a relatively flat surface with few peaks.

Based on this study, the important conclusion that be reached is as follows: Although roughness found in natural environments such as clay nano – surfaces in rocks and roughness expressing irregularities caused by a manufacturing process are different types of roughness, the methods and approach used allowed a complete surface characterization. Consistency was proven across all substrates with small discrepancies between them, therefore objective was attained.

9.2.2 Understanding wettability at the clay-crude oil interface as a redox function

Having constrained surface roughness on clay thin films, the focus of this work became the wettability of clay minerals with regard to the clay – crude oil interface. This was tested as a function of the reduction extent of structural iron. The contact angle measurements indicated less surface tension at the surface of the clay films is induced chemical reduction. In the three-phase system which characterizes the system under study; i.e. clay film, crude oil and nitrogen as the vapor phase or air in the case of oxidizing conditions, the angle between the solid and liquid increased. More specifically in oxidized conditions the NAu-2, with a calcium-rich interlayer cation, showed crude oil contact angle values ranging from 21-23 degrees. The potassium-rich IMt-2 illite showed crude oil contact angle values ranging from 24-25.6 degrees and the sodium-rich Sca-3 smectite showed crude oil contact angles between 22.7-24.6 degrees.

The conclusion to be drawn is that reduction extent is important in terms of changes at the surface of both swelling and non-swelling types of clay minerals. The sensitivity of the wetting state of the clay films to the reduction extent was tested by performing partial chemical reduction on clay minerals. It would be therefore expected that adhesion forces at the clay/crude oil interface in the reduced conditions of a reservoir are in favor of fines mobility. By deploying LSWF previous equilibrium is disrupted and the mobilization of fines affected.

9.2.3 Infrared Spectroscopy studies on iron clays: Implications for hydration changes as a redox controlled process

Having understood how the interplay of clay surface and crude oil changed due to iron reduction, the focus of this part of the study became the hydration state of clay minerals as a function of their redox state. This was explored with the use of infrared (IR) spectroscopy. The important water and hydroxyl bands were monitored in the mid infrared (MIR) and near infrared (NIR) spectra. That gave an important insight on the hydration state of the iron clay minerals in oxidized, partial and fully reduced conditions.

The bending and stretching as well as the first overtones expressing either OH^- or H_2O loss were present in the MIR and NIR regions of the spectra for the NAu-2 oxidized samples. In ambient conditions, the results of reduction in the MIR spectra was dehydration of the MM – OH combination seen in the 3000 – 3600 cm^{-1} region for both partially and fully reduced NAu-2 samples. In the NIR spectra, dehydration was mainly evident in the 4000 – 4600 cm^{-1} regions for samples in partial and total reduction states.

In vacuum conditions, further loss of water was seen in all spectra of both partially and fully reduced NAu2 samples in comparison to the oxidized samples in the MM – OH bands.

Measurements taken in various RH degrees revealed reappearance of hydroxyl groups to a considerable extent. Rehydration was evident mostly in RH conditions of above 30%, by means of the reappearance of OH^- bands in the 3000 – 3600 cm^{-1} and in the 5000 cm^{-1} regions in the MIR and NIR spectra, respectively. After partial reduction and exposure of NAu-2 to RH conditions, rehydration was also present as was after total reduction, indicating that the beginning of reversibility of the process was in proportion to the reduction extent. These findings were particularly true for the dioctahedral smectites such as the NAu2 nontronite with high structural Fe^{2+} content indicating the reversibility of the process of dehydration to a considerable extent. Rehydroxylation was increasing in proportion to the increased reduction state; this can be thought of as the effect of the swelling nature of NAu2 nontronite.

In the NIR spectra, in ambient conditions, the main changes in intensity of overtones between the oxidized, partially and fully reduced samples, were seen in the 4200 – 4600 cm^{-1} and in the 5200 cm^{-1} regions. These indicated changes in the combination of OH^- stretch combination and OH^- deformation of FeFeOH.

Measurements in vacuum conditions in the NIR spectra showed lower intensity for the reduced samples in comparison to the oxidized. This was evident in the same regions that were dehydrated in ambient conditions. Rehydration was inversely proportionate to the reduction state in the NIR spectra; overtones in the 4200 – 4600 cm^{-1} and around the 5200 cm^{-1} regions reappeared with lower intensity for the reduced samples. Although changes in the lattice were evident through significant dehydroxylation both in MIR and NIR spectra, an overall preservation of the silicate structure did appear by means of partial rehydration, especially for the NAu-2 smectite.

Similarly to NAu-2 nontronite, changes wre evident in the non – smectite IMt-2 lattice. The results of reduction in the MIR spectra was, again, dehydration in the 3000 – 3600 cm^{-1} region of the MM – OH combination for the fully reduced illite. However, due to the low iron content, MIR spectra were only measured for the oxidized and fully reduced illite samples.

After vacuum conditions were applied, dehydroxylation in the 1600 – 2000 cm^{-1} (OH combination) and 3000 – 3600 cm^{-1} (OH stretch) regions became mostly evident in the fully reduced IMt-2. For illite IMt-2, this is indicative of further dehydration.

Subtle rehydration was evident by the reappearance of OH^- groups in the previously dehydrated bands during exposure of IMt-2 to relative humidity conditions of 70%. The reversibility of the iron

reduction process was not as dominant as in the case of NAu-2, although OH^- groups did reappear, confirming both the existence of remaining iron and the partial water uptake present inside the IMt-2. Rehydration of the fully reduced IMt2 was not as dominant as the one seen in the fully reduced NAu-2. In this regard, re – entering of hydroxyl bands is not in proportion to the reduction state of the illite. The oxidized illite was more readily rehydrated than the fully reduced in the MIR spectra.

In the NIR spectra, overtones in the 4200 – 4600 cm^{-1} corresponding to the bending and stretching combination of hydroxyl groups were seen with lower intensity for the reduced IMt-2 samples. The 5200 cm^{-1} peaks were possibly a continuation of the the structural (ν+δ) OH combination that occurs around 4500 cm^{-1}. Similar trends in the overtone intensities were seen in the vacuum and rehydration conditions, indicating dehydration and subsequent rehydration signaling reversible changes in the clay mineral.

What can be derived from this study is the following: As a general observation, both MIR and NIR spectra correlated well, indicating that changes in illite, with the predominant one being the loss of OH^- groups due to chemical iron reduction, was possible and reversible in iron bearing smectites and partially - swelling clays. Partial reduction had the same effects, mainly for NAu-2, and possibly due to the high Fe^{2+} - Fe^{3+} ratio that accounted for better visualization, whereas the effects were less evident in the IMt2 spectra due to low structural iron present. The main mechanism of dehydration that could be suggested based on this study, was the loss of hydroxyl groups as a direct effect of reduction process. The dehydration effect appeared consistent across illite and nontronite, though less reduction was possible in illite. Dehydration was evident in both spectra for both clay mineral types and objective attained.

9.2.4 Effect of redox state on water sorption by swelling and non-swelling clay minerals

After having looked at the hydration state of iron clays by means of vibration of hydroxyl groups, further understanding of surface properties such as water sorption became important. To elucidate that, the aim became to compare the water adsorption and specific surface area of reduced ferruginous clays with that of the oxidized clays so that an understanding on surface hydration, pore structure and adsorption could be gained. To further understand how changes in the clay mineral microstructure correlate with changes in the reduction state, and hydration, analysis of changes in cation composition before and after reduction were made. The data generated were coupled with controlled relative humidity (RH) X-ray diffraction (XRD) analysis to

further assess the relative contribution of interlayer swelling changes and pore water uptake to the water sorption isotherms.

Water adsorption for the iron-rich nontronite NAu-2 samples followed the trend of NAu-2 fully reduced > NAu-2 partially reduced > NAu-2 oxidized. This was evident at all partial pressures, with hysteresis being evident in both the oxidized and the reduced NAu-2 samples. Adsorption of water vapor for the partially reduced NAu-2 PARED tracked the NA-2 OX from 0 to 0.2 P/P0, but then followed the NAu-2 RED curve from ca 0.4 to 1.0 P/P0 with a similar behavior seen in the water desorption isotherms. At all pressures, the desorption isotherm of NAu-2 RED was higher than both NAu-2 PARED and NAu-2 OX. The NAu-2 PARED desorption followed that of NAu-2 OX from 0 to 0.2 P/P0, as with the adsorption curve, with the trend changing from 0.2 to 0.7 P/P0 where the NAu-2 OX desorption isotherm showed higher sorbtion than that of NAu-2 RED. The opposite occurred in the 0.6 to 0.9 P/P0 range, just before the desorption isotherms of both samples intersected at a pressure of 1 P/P0. Significantly less water vapor adsorption was observed than for nontronite NAu-2 samples, and with relatively little hysteresis present in the oxidized sample. Adsorption values appeared higher for the oxidized iron-poor sample of (IMt-2 OX) in the 0 – 0.65 P/P0 range, while the IMt-2 RED was higher from 0.65 P/P0 upwards. The desorption isotherm of IMt-2 RED had higher values for water sorbed at above 0.50 P/P0 and displayed greater hysteresis than the IMT-2 OX. Below 0.50 P/P0, the desorption curves of both oxidized and reduced IMt-2 were very similar.

Nitrogen adsorption isotherms exhibited a Type IV behaviour. In both oxidized and totally reduced nontronites, adsorption hysteresis was evident in the P/P_0 0.48 – 0.99 pressure range. Monolayer – multilayer formation limit was indicated in the first part of the isotherms at a P/P_0 of 0.04 and 0.06 for the NAu-2 OX and NAu-2 RED, respectively. Monolayer completion was seen as a very sharp knee in the NAu-2 RED sample. The less distinctive knee in the NAu-2 OX isotherm was indicative of monolayer overlapping. Capillary condensation occurred at around 0.8 P/P_0 for both samples - both NAu-2 samples exhibited a H4 loop type. The almost horizontal isotherms of the H4 type, remained parallel over a range of pressure. The pore structure associated with an H4 loop was narrow slit – like pores. The specific surface area of nitrogen of fully reduced samples increased when compared with oxidized samples, from 31.1 to 121.3 m^2/g, a significant 118% increase and from 19.6 to 24.4 m^2/g, corresponding to a 22% increase, for NAu-2 and IMt-2, respectively. The mean pore diameter data showed mesopores decreasing in size from 9.5 - 3.6 nm, and increasing from 11 – 18.3 nm for NAu-2 and IMt-2 upon reduction, respectively. An increase of the total available pore volume followed the trend in the SSA_N BET increase in the fully reduced samples. More specifically, in the nontronite NAu-2 total pore volume increased from

0.074 to 0.111 cm^3/g and, in illite IMt-2, from 0.054 to 0.112 cm^3/g (P/P_0=0.990), corresponding to a 40% and 70% total pore volume increase respectively.

The effect of relative humidity (RH) on the positions of the 001 basal reflections, and thus interlayer spacing, of the oxidized and reduced clay minerals was as follows: With increasing hydration, for NAu-2 OX, the interlayer spacing showed negligible increase from 14.97 Å to 15.17 Å, while NAu-2 RED changed from 12.52 Å to 12.70 Å. For the illite, IMt-2, no significant increase in basal spacing, 10.09 Å to 10.04 Å and 10.13 Å to 10.10 Å, was observed for the oxidized or reduced samples, respectively. Changes in peak width were apparent within the full width at half maxima (FWHM) data for the 3% RH samples indicating crystallite domain sizes along the *c** direction, according to the Scherrer equation, as 76.3 Å and 111.1 Å, for NAu-2 OX and NAu-2 RED, respectively, and 111.0 Å and 132.5 Å for IMt-2 OX and IMt-2 RED, respectively. Similar trends were noted in the other hydration states, though the RH varied across samples, and the 3% was consistent, allowing a meaningful comparison to be made.

In terms of the cation budget in reduced and oxidized conditions the following were shown: The reduction process resulted in increased overall surface charge as determined by the relative amounts of exchangeable cations (taken as Na+, K+ and Ca2+) in both samples, with the higher Fe content nontronite NAu-2 increasing exchangeable cation charge from 63.044 (NAu-2 OX) to 93.977 meq/100g (NAu-2 RED). For illite IMt-2, the change in overall cation charge was significantly smaller, moving from 178.859 meq/100g to 182.253 meg/100g, reflecting the low Fe content. The apparent high overall charge arose owing to the presence of the ca 5% K-feldspar in the sample contributing dis-proportionately to the overall K+ content. Changes in cation composition mainly arose in the Na+ content, which increased significantly in both clay minerals upon reduction, and a loss of Ca2+.

The important conclusions that can be drawn from this study is as follows: At a powder scale, macroscopic water vapor and nitrogen sorption volumetry methods gave insight into vapor adsorption (surface hydration), specific surface area, pore structure changes arising due to reduction. The clay minerals have different structures and differ in the amount of iron present and the nature of the charge balancing cation, yet similar trends were observed upon reduction, showing the importance of redox processes in controlling hydration properties of ferruginous clay minerals. The findings presented improve understanding of sorption mechanisms of water vapour at the sur-face of the reduced clay minerals that is key in constraining clay behavior in the fluid – solid interface, and critical to understanding transport of solutes and water retention. For the high Fe NAu-2, the interlayer swelling decreased and crystallite size (coherent diffraction domain size)

grew through aggregation of more clay layers, while for low Fe IMt-2, there was little change in interlayer swelling, though some aggregation of more clay layers was also noted. ICP analysis showed that cation retention occurred in IMt-2 upon reduction and the K^+ was not exchanged by Na^+.For both NAu-2 and IMt-2, the Ca^{2+} content decreased upon reduction, while the amount of Na^+ increased through cation exchange with Na^+ from the chemical reducing agent, potentially accounting for the change in swelling reported above. Though interlayer swelling decreased in the oxidised NAu-2, water sorption was found to increase upon Fe reduction and given the increased water uptake was not due to interlayer swelling, porosity analysis confirmed more interparticle spaces became available through increased pore volume and surface area in the reduced Fe clay minerals, relative to the oxidized.

In this study we showed consistency with previous studies in dehydration of interlayer domains of the clay minerals. The CEC changes were the opposite of those indicated in literature (CEC increases upon reduction in this present study), followed by an increase in water adsorption at surface. We constrained the hydration profile of the clay minerals at surface and in the bulk, while finding discrepancies between our findings and the literature.

9.2.5 Creation of a flow-cell device for direct visualization of *in situ* iron reduction in a microfabricated sandstone proxy

Thus far, the wetting behavior of static clay minerals films and clay mineral powders have been studied. However, a key next step would be to understand whether the redox state and wettability affect the release of fine particles from quartz surfaces. In this section, a flow cell was designed and, prior to CoVID, manufactured in order to ascertain how the clay minerals behaved under flow when moving from reduced to oxidized conditions. The aim of the work was twofold: a) an attempt was made to create an experimental set up that allows direct imaging of *in situ* reduction of clay minerals in a sandstone micromodel; b) the work aimed to provide a method for simulating the initial conditions of a reservoir with regards to free oxygen levels and reduction potential during low salinity water flooding in a 2-D micromodel. The suggested experimental method regarding the study of reservoir micromodels in anaerobic and anoxic environments presented, aimed to provide a basis for further research in this topic.

The SU – 8 polymer was introduced as a novel material for microfluidics flooding simulation. Original designs of anaerobic flow – cells were presented along with tracer fluid tests that tested the models for their suitability. The flow cell allows gas and liquid tight conditions suitable for reducing iron clays *in situ*. In combination with the peripherals (i.e. syringe pump, nitrogen gas tank, microscope setup, pressure gauge and free oxygen meter), and the suggestions mentioned in terms of the setup and protocol for clay injection, can be used to monitor and regulate free

oxygen levels inside the anaerobic flow cell. However the method bears limitations that are subject to refining and optimization. This study provided the basis for further development on the EOR microfluidics.

9.3 Implications of results

Throughout this thesis the main objective was to identify how changes at the clay mineral level induced by the reduction of iron impacted on clay mineral wetting, and subsequent mobilization. Through investigating this process, an insight on the properties of iron clay minerals, both for the swelling and non-swelling types, in oxidized and reduced states was obtained. Therefore a correlation with the relevant reservoir conditions was made possible. These conditions can now be identified as follows: a) initial reservoir conditions – reduced state with dehydrated clay minerals in the interlayer and more surface hydration; b) intermediate state during Low Salinity deployment with hydration shifting towards a more hydrated interlayer and less water holding surface; c) production stage with hydrated clays, ferric iron species and complete hydration and expansion of interlayer, reduced cation exchange capacity and very low surface hydration (Fig 9.1). Understanding of hydration in the bulk and at the surface of clay minerals has been possible with the use of IR spectroscopy, water vapor volumetry, ICP-OES and relative humidity XRD studies that provided a fundamental understanding of the changes in the iron clay structure during different reduction states. Applying such surface science techniques to geochemistry problems is still rather in its infancy.

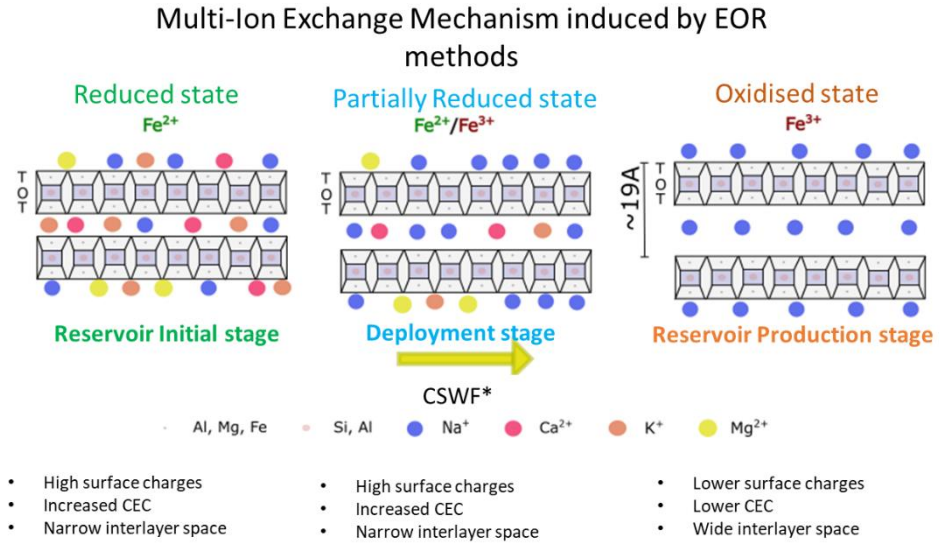

Figure 9.1, Changes induced at surface and interlayer of iron clays, in reduced-initial reservoir conditions (green), partial reduction-LSWF deployment conditions (blue) and oxidized-production stage conditions (orange).

Based on this work, there is now, for the first time, evidence on which the following can be answered: do oxidized and reduced clay minerals, such as in an oil reservoir, have different water uptake and wetting properties and if so, what is causing these changes? Based on research presented in this thesis, this can now be partially answered by ICP-OES data revealing cation exchanges occurring after reduction of iron species. Though Na may have been exchanged from the introduced chemical reductant, ion exchange may also occur owing to the salinity of the water flood fluids or connate brines as salinity – salinity levels may be low during LSWF but there is still a considerable amount (i.e. 4000 ppm NaCl) (Fjelde et al 2012; Sheng 2014), and a diminished amount of Ca^{2+}. Exchange induced by chemical reduction alters CEC and interlayer cation of iron clays leading to changes in cation site occupancies. Although this does explain relative hydration states of iron clays, it leaves some uncertainty with regards to why textural changes are induced by iron reduction. To answer this, more work is needed, although important ground has been covered in this present work (see water sorption and specific surface area study).

The water sorption studies were coupled with wettability studies that elucidated the interplay between clay and crude oil, providing evidence of lower surface adhesion in reduced-initial reservoir conditions. It can therefore be said that initial-reservoir conditions can provide more mobilized clay-crude oil colloids.

Upscaling was attempted to understand the colloidal system of clay-crude oil-water by creating *in situ* conditions of iron reduction within a 2 D microfabricated silicon proxy. Building on recent findings of others, who have been working on LSWF microfluidics, the aim was to develop a flow cell device capable of hosting anoxic conditions, so that redox changes could be visualized directly. Significant process was made towards that direction by creating unique flow cell devices and micromodels with adjustable wetting properties as demonstrated in Chapter 8. However, there are still embedded limitations in the process that should be taken into account in future attempts of creating anoxic LSWF microfluidic conditions.

9.4 Future work

Throughout this PhD project the focus has been on the fundamental properties of iron clay minerals such as wettability, swelling capacity and surface hydration within the context of low salinity water flooding during EOR operations. While this research was conducted, a number of other studies were undertaken that addressed some of these items. This highlights the attention that redox controlled processes within petroleum reservoir research are gaining. In 2020, Shell funded work was published in collaboration with Imperial College, UK, focusing on the alteration

of wettability of sandstone cores as a function redox extent of iron clays. Yesufu-Rufai et al (2020), created anoxic conditions, performed core flooding and measured surface alterations using AFM microscopy. Their results indicated that wettability is redox-dependent and that crude oil wetting in anoxic conditions is less than in oxidized. This topic should be explored further and redox conditions in core flooding experiments should be constrained. It is also important to understand the reversibility of the process of iron reduction and the extent to which iron clay minerals can return to their initial state. Another work conducted by Unsal et al (2020) was focused on understanding how permeability is affected due to altering the redox state of iron clay sandstones. Their findings suggest that upon oxidation, clay swelling is induced, altering the morphology and ultimately permeability of the rock.

Earlier in 2021, a study performed at Durham University by Apeiranthitis et al (2021, in review), showed that crude oil wettability at a clay film scale, depends heavily on the redox extent. Using clay film substrates they showed that crude oil wetting is less in reduced-anoxic conditions, whereas water wetting increases in the same conditions. This is complementary to the findings presented in this present work in Chapter 7, where surface hydration was shown to increase relative to the increased reduction states. In this context, future work should aim to constrain changes in wetting in a more realistic 2D setting. For that, micromodelling work has been gaining attention, especially in the last five years. Mainly it has been the work conducted by Kovscek and co-workers at Stanford University, USA, where innovative 2D micromodels have been used for core flooding experiments, with the most recent published in 2019 (Aldousari and Kovscek 2019). An introduction of redox-anoxic conditions would be the next step, in order to simulate a more realistic reservoir environment during Low Sal deployment and track changes *in situ*.

Harasawa's M.Res work at Durham University (2020), aimed to identify how confocal microscopy can be used to monitor clay aggregation and fines migration during low salinity water flooding. Fines migration and clay-oil-water emulsions induced by redox changes could be studied using confocal microscopy in more detail in future work. For such studies, advanced apparatus should be used as mentioned in Chapter 8.

The effect of redox changes during production of petroleum reservoirs is gaining attention. Oil majors such as BP (this work, see also Vasilopanagos et al 2021) and Shell (see Unsal et al 2020) are funding and publishing redox related research. Although it has been, hitherto, almost entirely neglected, possibly due to the complexity of the surface chemistry involved, the effect of redox on the release of oil and/or fine particles during production is an emerging topic, especially within the field of low salinity water flood research. Potentially, these environmentally friendly EOR

methods have a significant role to play in helping the energy transition go forward. Oil is likely to be an important resource, for materials and feedstocks, if not for fuel into the future (Keyße and Lenzen 2021). Increased use of existing assets will replace exploration for new, and thus EOR methods will come to the fore to ensure maximum extraction, maintaining production of each reservoir for as long as possible.

9.5 References

1 Keyßer, Lorenz T., and Manfred Lenzen. "1.5 C degrowth scenarios suggest the need for new mitigation pathways." *Nature communications* 12, no. 1 (2021): 1-16.

Appendix A.1

Table 1. AFM data obtained by constant force mode for nine areas on NAu-2 coated substrates. Primary Ra (roughness average) values are shown in red. RMS stands for Root mean Squared roughness values and PVR stands for Peak versus Valleys values; the distance between highest and lowest point at the surface of the substrate at the point of the measurement.

	NAu2 – 1								
Scan	1	2	3	4	5	6	7	8	9
Ra (*nm*)	69.27	68.3	53.02	55.76	56.7	51.72	70.15	53.23	47.9
RMS(*nm*)	96.19	85.88	68.24	71.25	73.16	67.31	86.96	67.09	63.22
PVR (*nm*)	886.7	556.2	565.8	642.1	1013	528.2	616	549.2	641
	NAu2 – 2								
Scan	1	2	3	4	5	6	7	8	9
Ra (*nm*)	87.4	77.95	94.64	77.66	76.5	95.76	68.05	57.79	74.4
RMS(*nm*)	123.6	97.63	130.8	104.5	97.71	130.4	85.59	76.18	94.44
PVR (*nm*)	1441	1449	1132	1648	951	1616	608.9	609	987.9
	NAu2 – 3								
Scan	1	2	3	4	5	6	7	8	9
Ra (*nm*)	194.8	232.1	191.8	239.4	287.7	349.1	228.8	267.6	286.6
RMS(*nm*)	243.1	289.8	240.6	302.1	368.7	457	322	351.2	356.9
PVR(*nm*)	1.770	2.100	2.208	2.750	3.810	4.590	1.800	1.962	4.127

Table 2. AFM data obtained by constant force mode for SCa-3 coated substrates. Primary Ra (roughness average) values are shown in red. RMS stands for Root mean Squared roughness

values and PVR stands for Peak versus Valleys values; the distance between highest and lowest point at the surface of the substrate.

	SCa3 – 1								
Scan	0	1	2	3	4	5	6	7	8
Ra(*nm*)	94.49	111.5	108.4	141.2	139.6	124.4	143.6	192.5	156.2
RMS(*nm*)	118	140.9	137.7	176	175	155.8	179.2	238.1	196
PVR (*nm*)	0.952	1.114	1.063	1.508	1.563	1.436	1.396	0.227	1.325

	SCa3 - 2								
Scan	0	1	2	3	4	5	6	7	8
Ra(*nm*)	114.1	159.7	119	173.1	138.7	136	210.6	201.2	126.3
RMS(*nm*)	142.3	204.2	148.7	216.8	173.4	171.1	265.1	250.7	156.1
PVR (*nm*)	1.051	1.590	1.350	2.630	2000	1.830	3.190	0.208	1.330

	SCa3 – 3								
Scan	0	1	2	3	4	5	6	7	8
Ra (*nm*)	422.4	258.1	240.5	348.9	309.8	223.9	218.8	168.4	169
RMS(*nm*)	521.7	325.6	321	428.9	375.9	280.5	270	210.4	218.6
PVR (*nm*)	2.750	2.603	3.865	3.534	2.990	2.490	1.954	1.950	2.200

Table 3. AFM data obtained by Quantitative Imaging mode for IMt-2 coated substrates. Primary Ra (roughness average) values are shown in red. RMS stands for Root mean Squared roughness values and PVR stands for Peak versus Valleys values; the distance between highest and lowest point at the surface of the substrate.

	IMt2 - 1								
Scan	1	2	3	4	5	6	7	8	9
Ra(*nm*)	50.43	53.24	42.24	106.8	379.8	101	93.62	51.12	149.3
RMS(*nm*)	69.32	69.23	55.61	143.8	490.7	166.7	136.8	65.89	267.2
PVR (*nm*)	892.5	822.6	1179	1690	3832	2631	1773	880.4	3958
	IMt2 - 2								
Scan	1	2	3	4	5	6	7	8	9
Ra(*nm*)	133.8	74.32	77.09	87.07	74.95	79.22	71.4	75.17	63.52
RMS(*nm*)	168.2	98.7	96.75	112	93.38	99.78	89.69	95.12	82.19
PVR (*nm*)	1430	982.3	1232	3145	1012	1155	848.1	1229	1494
	IMt2 – 3								
Scan	1	2	3	4	5	6	7	8	9
Ra(*nm*)	88.07	113	100.2	110.4	37.34	56.53	77.86	69.29	64.29
RMS(*nm*)	115	144.5	184.6	138.8	77.81	72.27	100.6	87.42	83.21
PVR (*nm*)	1374	997.9	3110	1004	687.4	1037	923.9	772.1	902.5

Table 4. Primary Ra values for the Nau-2 clay films using the CCI Talysurf Interferometer. H0 is the initial positioning of the sample, H1, H2 and H3 are the following positions of the scans each at a distance of 1 mm from the previous scan, moving along the X axis. Primary Ra values are elevated in H1 position for every substrate.

Primary Ra (µm)	***Nau2-1***	***Nau2-2***	***Nau2-3***	***Nau2-4***

H0	0.000326	0.000363	0.000345	0.00039
H1	0.000466	0.000489	0.000464	0.00042
H2	0.000357	0.000473	0.000446	0.000373
H3	0.00025.5	0.000378	0.000452	

Table 5. Primary Ra values for the SCa-3 substrates using the CCI Talysurf Interferometer. H0 is the initial positioning of the sample, H1, H2 and H3 are the following positions of the scans each at a distance of 1 mm from the previous scan, moving along the X axis. Primary Ra values are elevated in SCa-3 – 2 substrate. Primary Ra values are elevated in H0 position for every substrate.

Primary Ra (µm)	***SCa3-1***	***SCa3-2***	***SCa3-3***	***SCa3-4***
H0	0.000156	0.000274	0.000182	0.000202
H1	0.000148	0.000156	0.000119	0.000184
H2	0.000119	0.000257	0.000136	0.00013
H3	0.000127	0.000169	0.000113	0.000106

Table (6) Primary Ra values for the IMt-2 substrates using the CCI Talysurf Interferometer. H0 is the initial positioning of the sample, H1, H2 and H3 are the following positions of the scans each at a distance of 1 mm from the previous scan, moving along the X axis. Primary Ra values are elevated in IMt2 – 2 substrate. Primary Ra values are elevated in H0 position for every substrate.

Primary Ra µm	***Imt-2-1***	***Imt-2-2***	***Imt-2-3***	***Imt-2-4***

H0	0.0002529	0.000369	0.000365	0.0003274
H1	0.0002386	0.0002774	0.00022	0.0002585
H2	0.0003051	0.0002337	0.000113	0.0001595
H3	0.0001196	0.0002531	0.000105	0.0001141

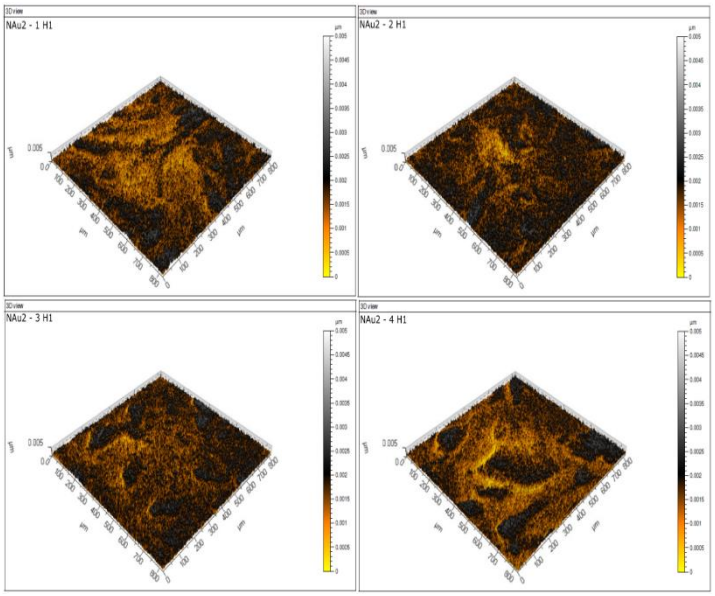

Figure 1. 3 D view of NAu0-2 substrates in the H1 position in a 800 × 800 um area in the X, Y axis. The height difference in topography can be seen by the change in colors. Yellow shades show lower topography and gray shades show higher topography. All substrates show similar features, such as lumps (dark gray color), unevenly coating the surface. The size of lumps varies from 100 to 500 µm. NAu-2 – 1 has lumps covering 40% of its surface, NAu-2 – 2 has increased accumulation of material appearing as lumps coating the surface almost in its entirety. Lumps coat the surface of NAu-2 – 3 up to 35% and up to 30% in NAu-2 – 4 substrate.

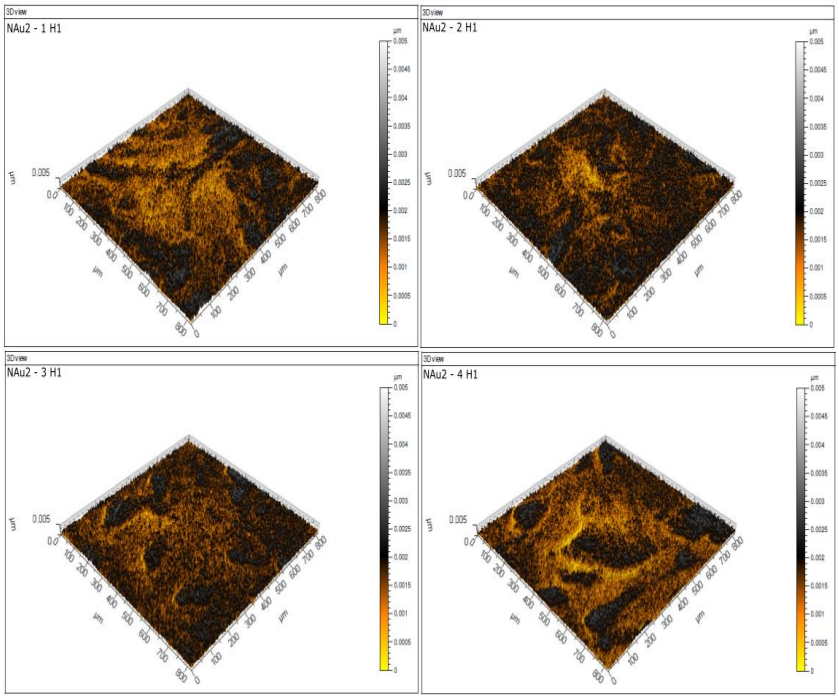

Figure 2. 3 D view of NAu-2 substrates in the H1 position in a 800 × 800 µm area in the X, Y axis. The height difference in topography can be seen by the change in colors. Yellow shades show lower topography and gray shades show higher topography. All substrates show similar features, such aggregates (dark gray color), unevenly coating the surface. The size of aggregates varies from 100 to 500 µm. NAu-2 – 1 has aggregates covering 40% (visually estimated) of its surface, NAu-2 – 2 has increased accumulation of material appearing as aggregates coating the surface almost in its entirety. Lumps coat the surface of NAu-2 – 3 up to 35% and up to 30% in NAu-2 – 4 substrate (visually inspected).

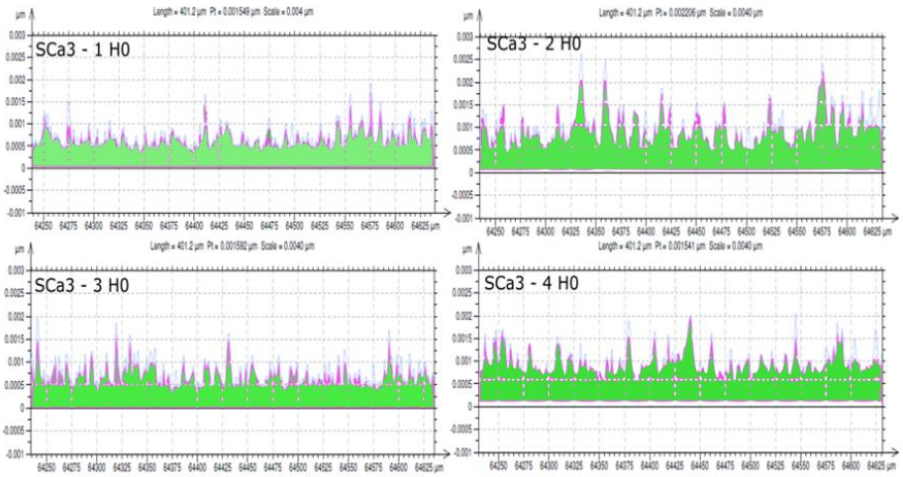

Figure 3. Extracted profile through the 400 × 400 µm zoomed area with a centerline along the X axis for the SCa-3 substrates. Selected cross sections are shown in yellow in fig (8). Primary

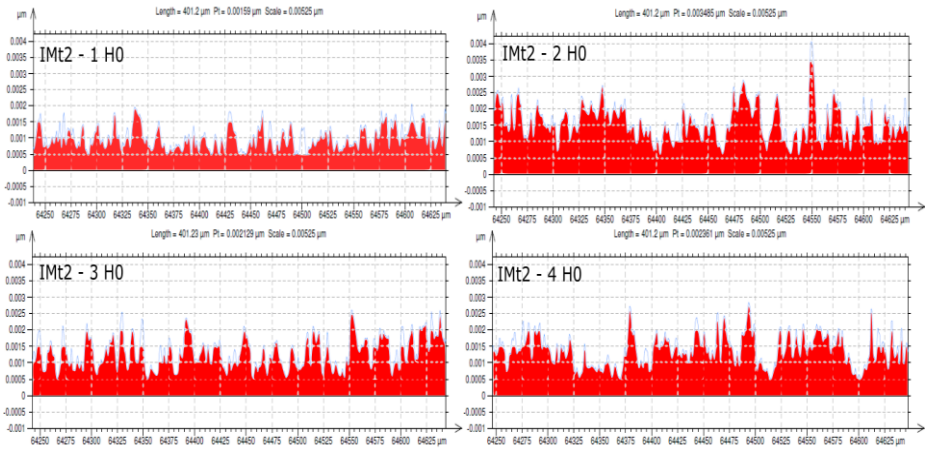

Figure 4. Extracted profiles through the 400 × 400 um zoomed area with a 237 centreline along the X axis for the IMt-2 substrates.

Appendix B.1

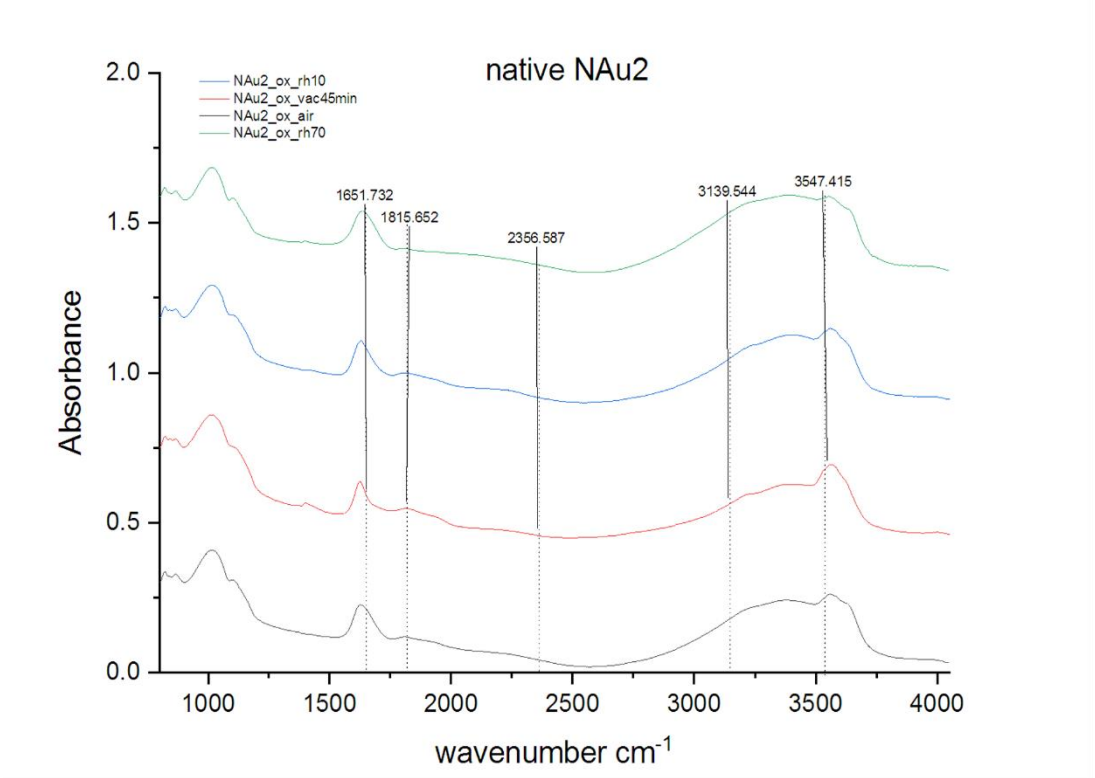

Figure B.6.1. MIR spectra of native NAu2 nontronite; measurements taken in ambient conditions (air), humidity at 10% and 70% and in vacuum after 45 minutes of exposure.

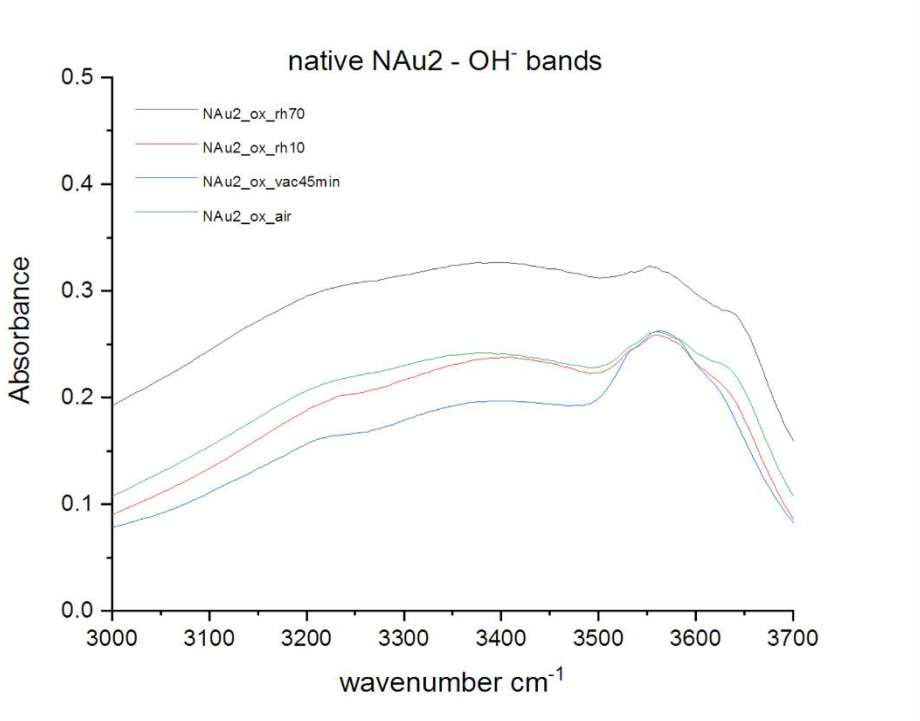

Figure B.6.2. MIR spectra of OH^- bands in the native oxidized nontronite (NAu2) ; measurements were taken in ambient conditions (air), humidity at 10% and 70% and in vacuum after 45 minutes of exposure.

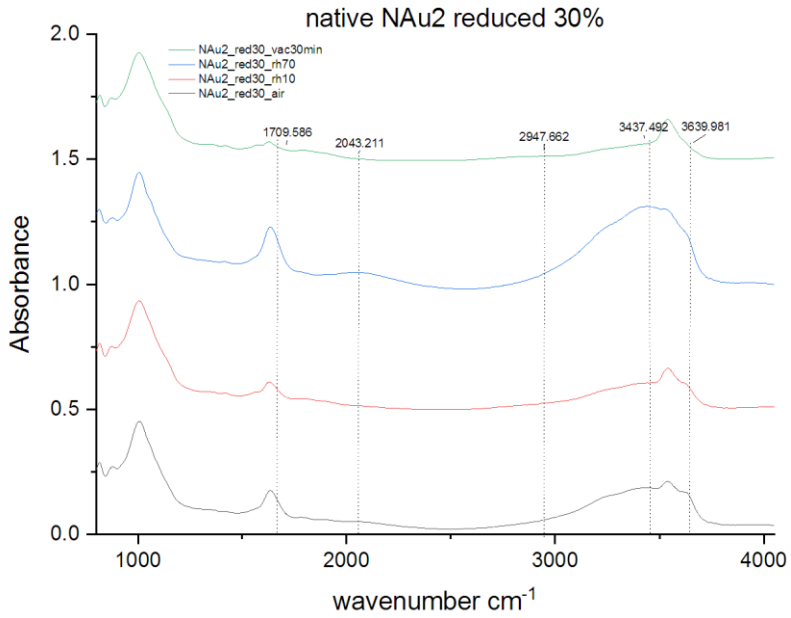

Figure B.6.3. MIR spectra for the native NAu2 nontronite after partial (30%) chemical reduction by dithionite; measurements taken in ambient (air), relative humidity 10% and 70% respectively and after drying under vacuum for 30 minutes.

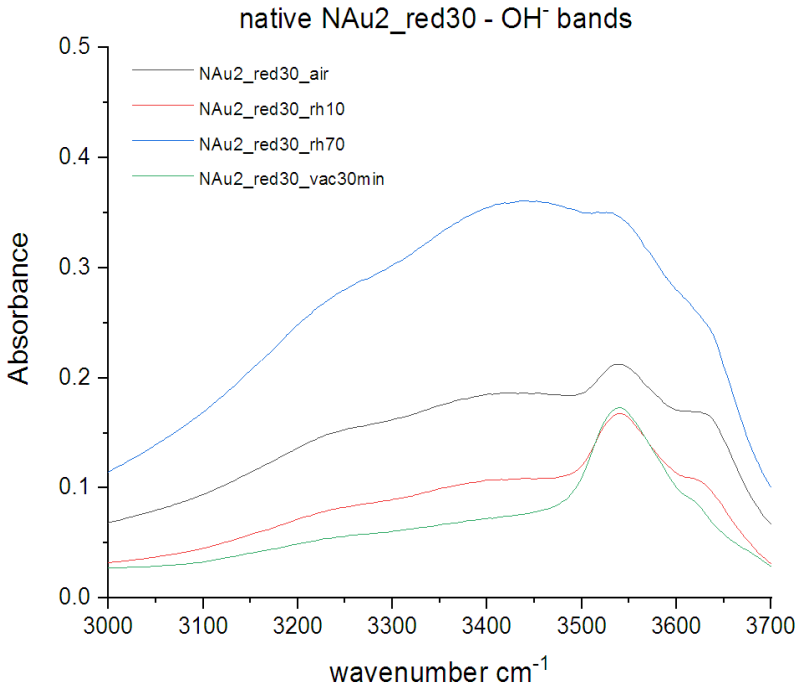

Figure B.6.4. MIR spectra of the OH^- bands of the native NAu2 nontronite after partial (30%) chemical reduction by dithionite; measurements taken in ambient (air), relative humidity 10% and 70% respectively and after drying under vacuum for 30 minutes

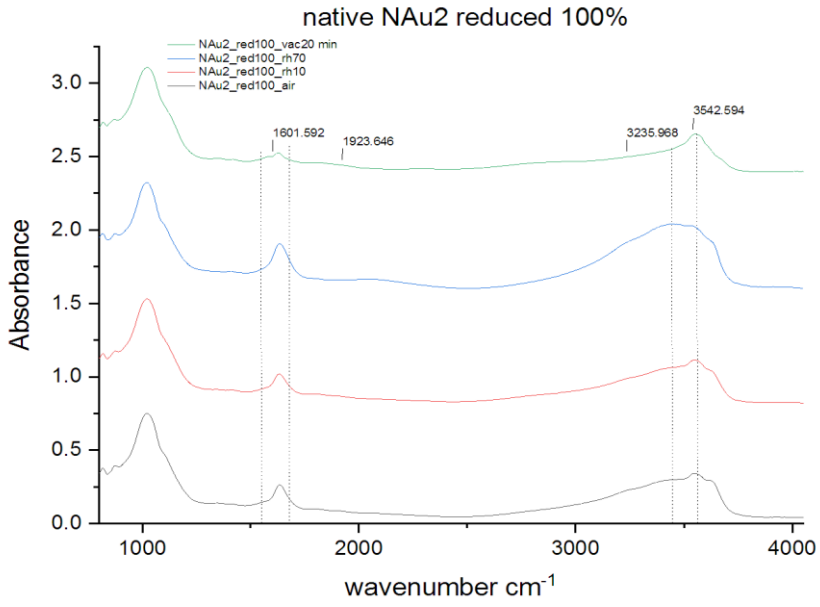

Figure B.6.5. MIR spectra of totally reduced nontronite NAu2 in air, vacuum, relative humidity 10% and 70% conditions.

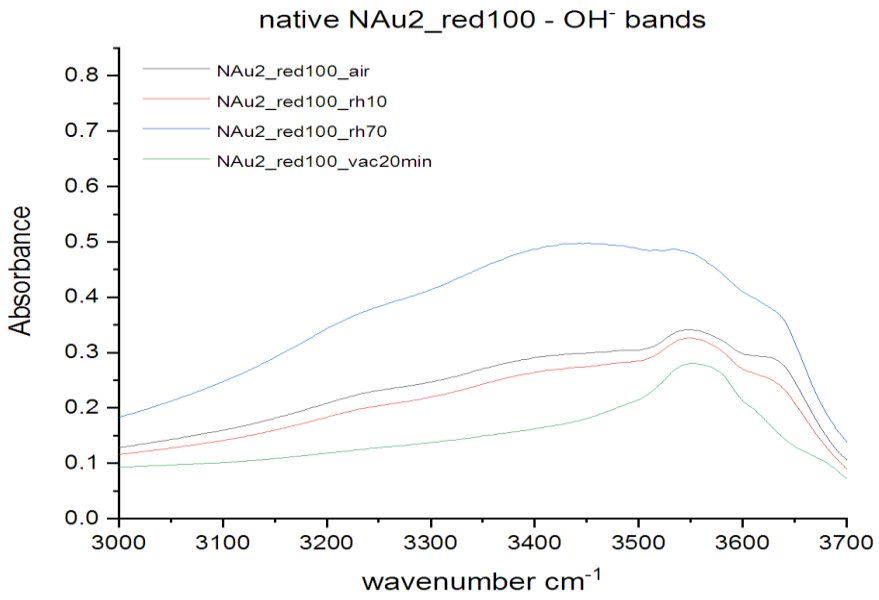

Figure B.6.6. MIR spectra of OH^- bands in the native fully reduced (100%) nontronite (NAu2); measurements were taken in ambient conditions (air), humidity at 10% and 70% and in vacuum after 20 minutes of exposure.

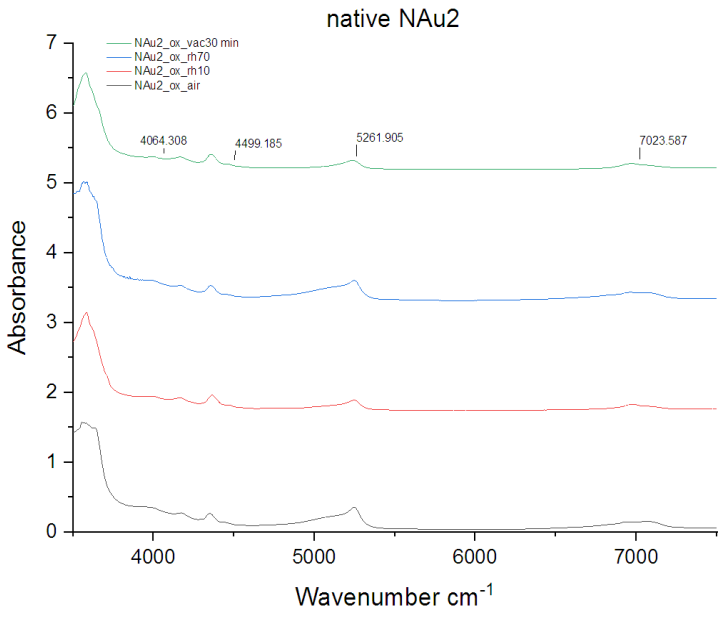

Figure B.6.7. NIR spectra of the native oxidized NAu2 nontronite, in air, vacuum and relative humidity conditions.

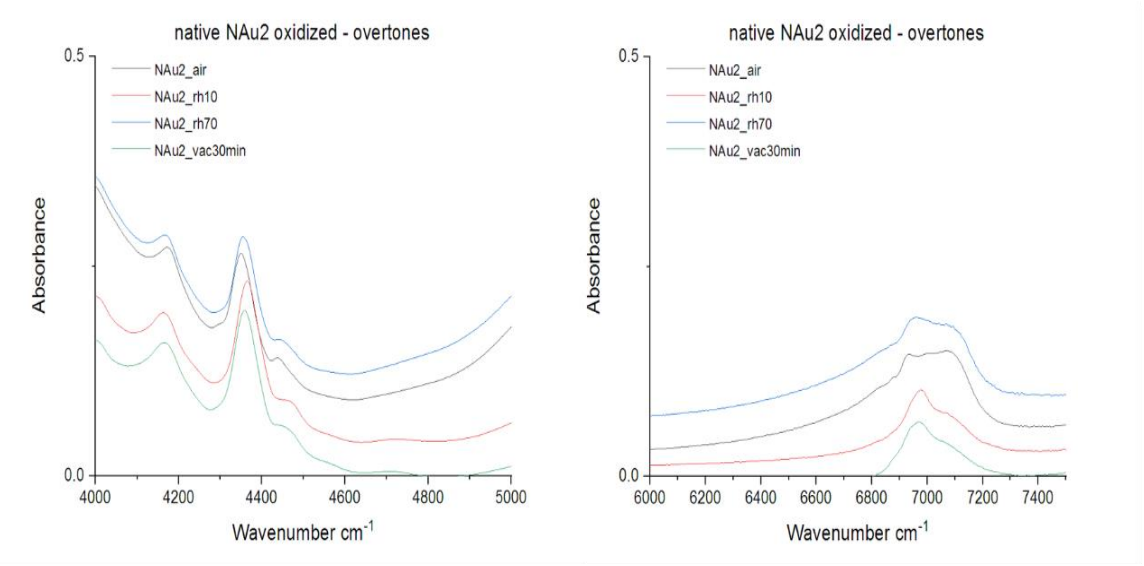

Figure B.6.8. NIR spectra of the native oxidized NAu2 nontronite, in air, vacuum and relative humidity conditions. Overtones are seen in the 4000 – 5000 and in the 6000 – 7000 cm^{-1} region.

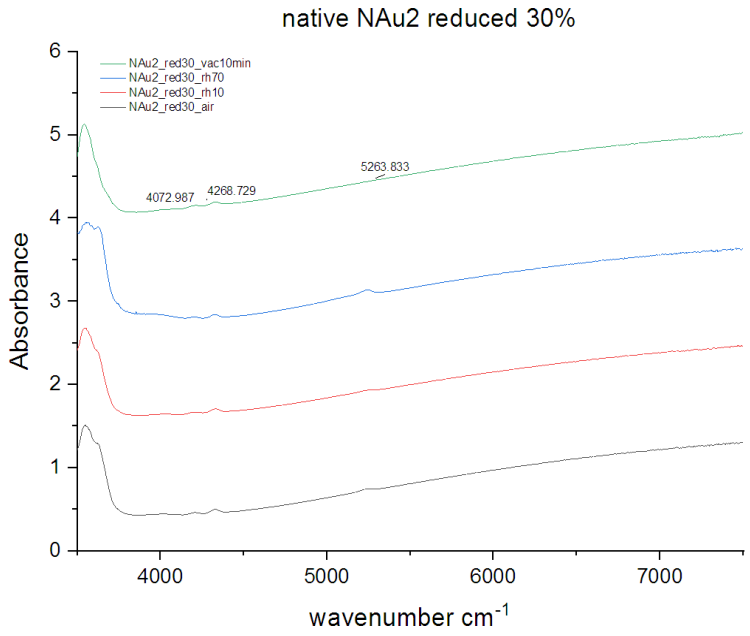

Figure B.6.9. NIR spectra of the native partially reduced (30%) NAu2 nontronite, in air, vacuum and relative humidity conditions.

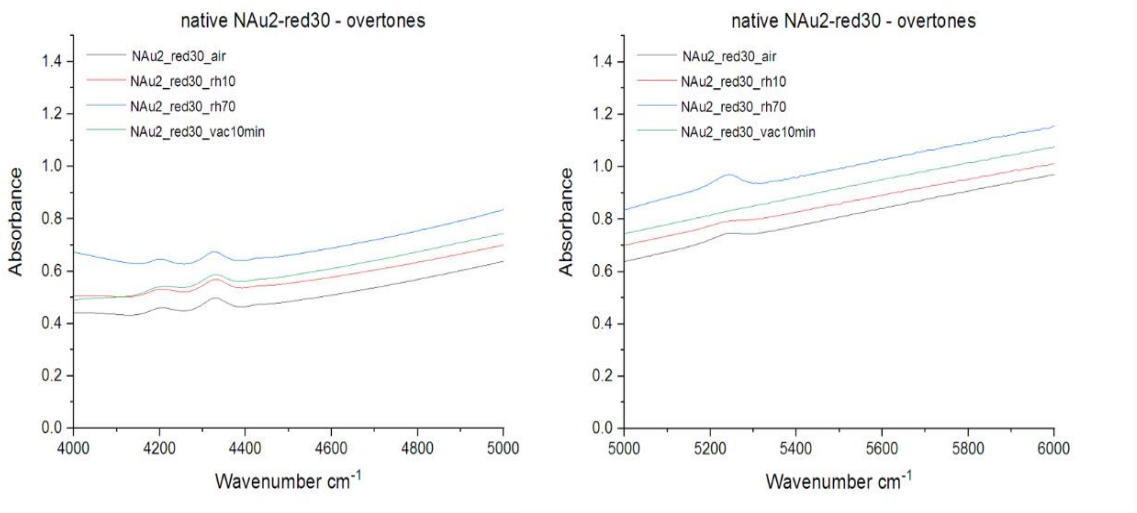

Figure B.6.10. NIR spectra of the native partially reduced (30%) NAu2 nontronite, in air, vacuum and relative humidity conditions. Overtones are seen in the 4000 – 5000 and in the 5000 – 6000 cm^{-1} region.

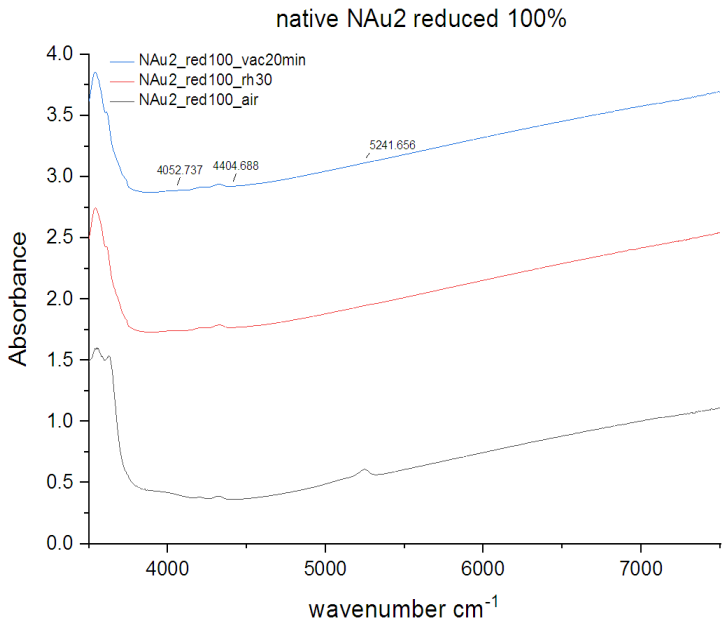

Figure B.6.11. NIR spectra of the native fully reduced (100%) NAu2 nontronite, in air, vacuum (20 minutes) and relative humidity conditions (RH 30%).

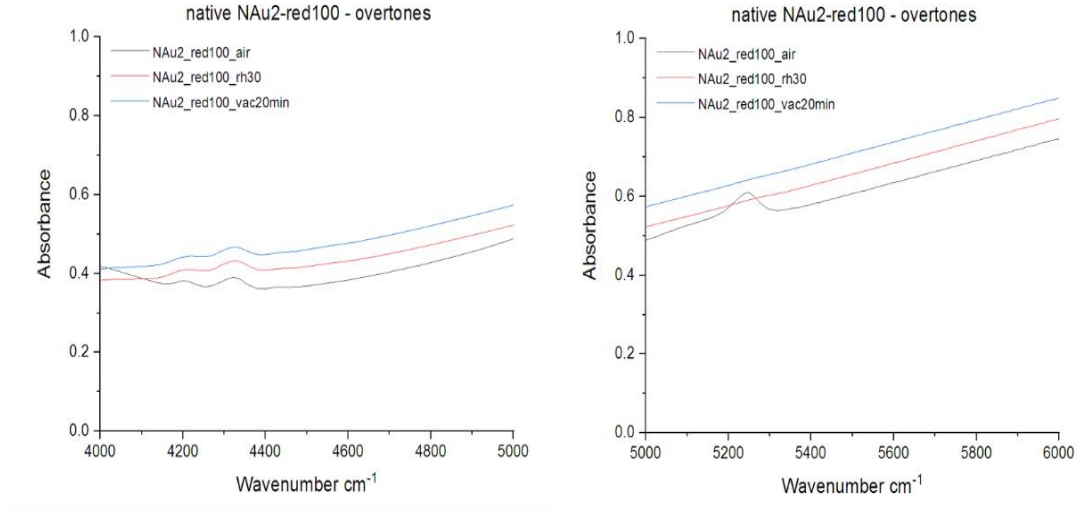

Figure B.6.12. NIR spectra of the native fully reduced (100%) NAu2 nontronite, in air, vacuum and relative humidity conditions. Overtones are seen in the 4000 – 5000 and in the 5000 – 6000 cm^{-1} region.

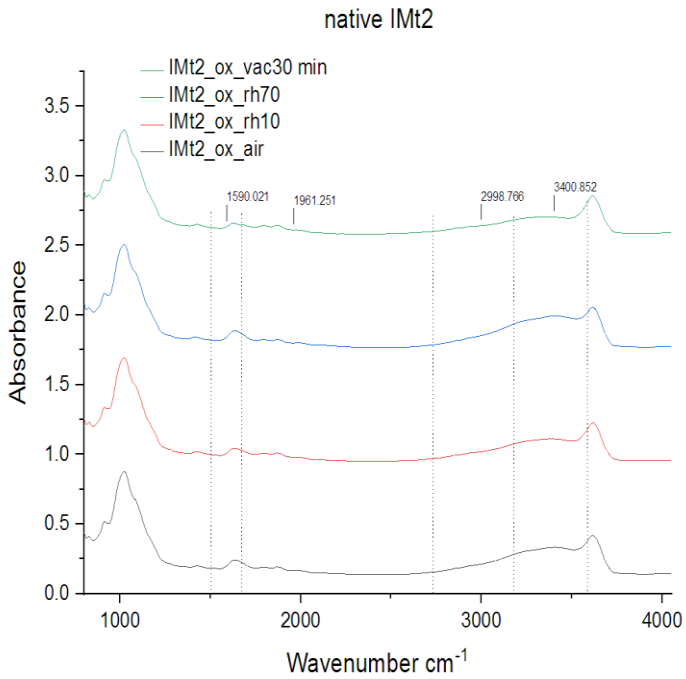

Figure B.6.13 MIR spectra of the native oxidized IMt2 spectrum; spectra measured in ambient (air) conditions, after 30 minutes exposure to vacuum and in rehydration conditions of 10% and 70%.

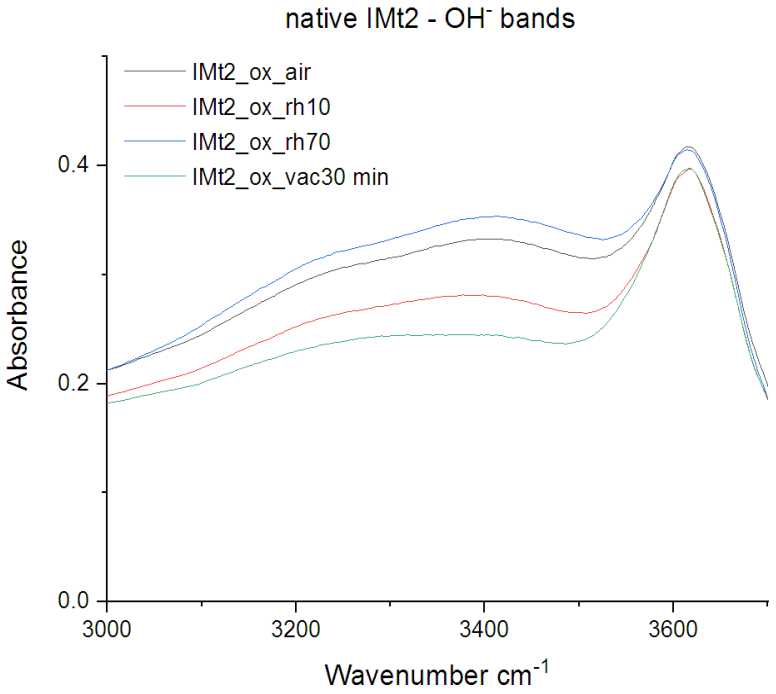

Figure B.6.14. MIR spectra of hydroxyl bands in the 3000 – 3700 region of the native oxidized IMt2 spectrum; spectra measured in ambient (air) conditions, after 30 minutes exposure to vacuum and in rehydration conditions of 10% and 70%.

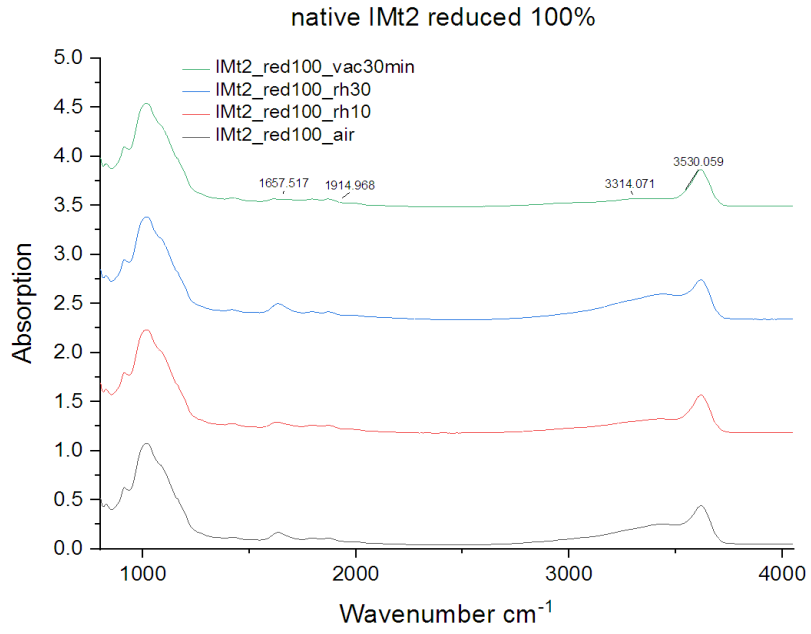

Figure B.6.15. MIR spectra of the native fully reduced IMt2; spectra measured in ambient (air), vacuum (30 minutes) and rehydration conditions of 10% and 30%.

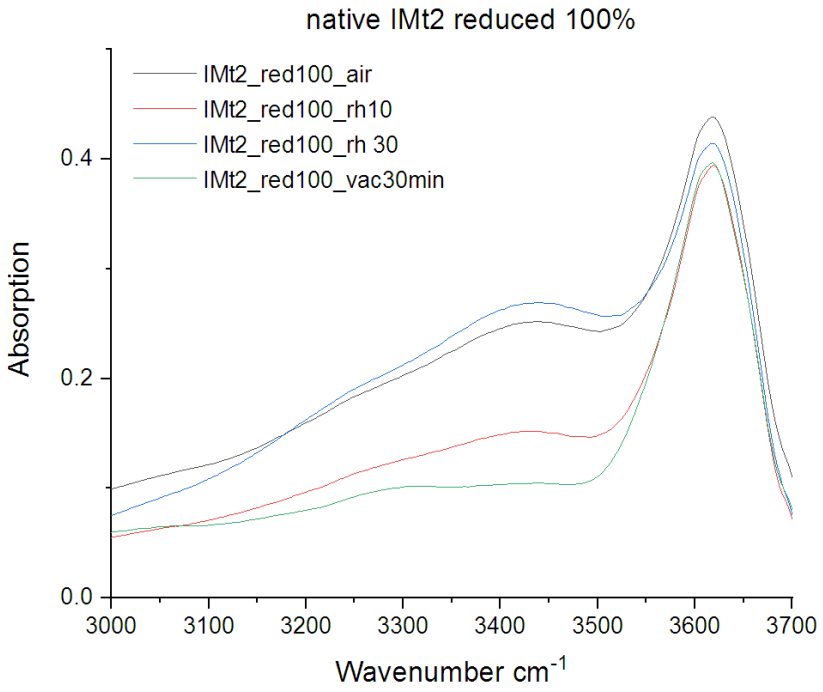

Figure B.6.16. MIR spectra of the native fully reduced IMt2 in the hydroxyl bands region; spectra measured in ambient (air), vacuum (30 minutes) and rehydration conditions of 10% and 30%.

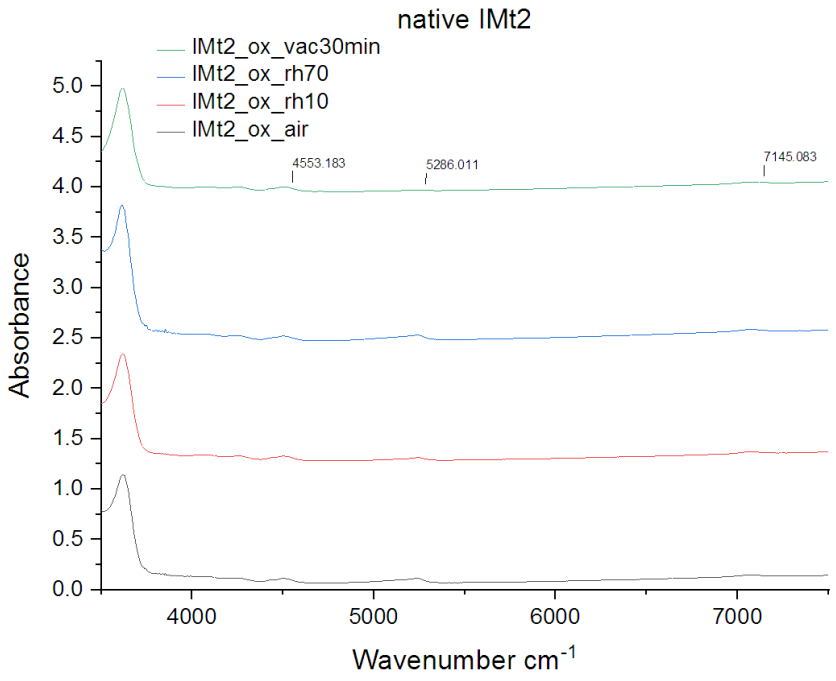

Figure B.6.17. NIR spectra of native NAu – 2; measurements taken in ambient (air) conditions, after exposure to vacuum for 30 minutes and in rehydration conditions of RH 10% and RH 70% respectively.

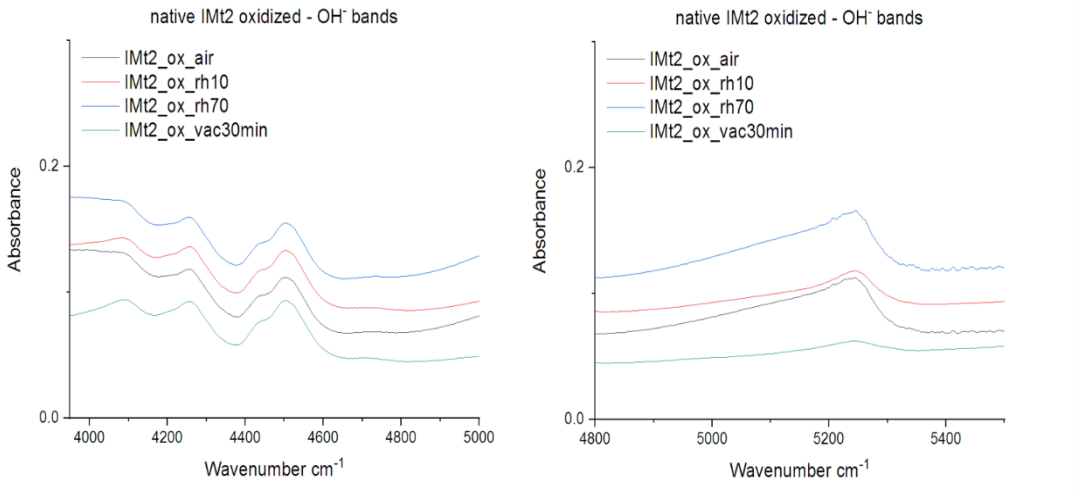

Figure B.6.18. NIR spectra of native IMt2; measurements taken in ambient (air) conditions, after exposure to vacuum for 30 minutes and in rehydration conditions of RH 10% and RH 70% respectively.

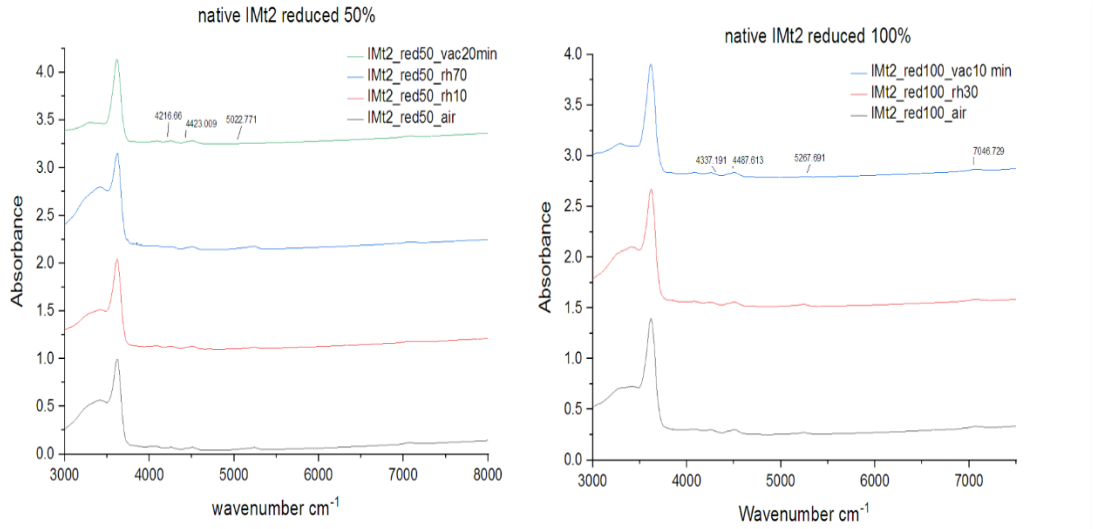

Figure B.6.19. NIR spectra of the partially (50%) and fully reduced (100%) native illite IMt2. Spectra for the partially reduced (left) were measured in air, vacuum (20 minutes), RH 10% and RH 70% conditions; spectra for the fully reduced (right) were measured in air, vacuum (10 minutes) and RH 30% conditions.